

Mechanisms and mitigation of short pitch rail corrugation

Zhang, P.

DOI

[10.4233/uuid:1da4c818-dc1a-44d7-a89d-a4047184d854](https://doi.org/10.4233/uuid:1da4c818-dc1a-44d7-a89d-a4047184d854)

Publication date

2022

Document Version

Final published version

Citation (APA)

Zhang, P. (2022). *Mechanisms and mitigation of short pitch rail corrugation*. [Dissertation (TU Delft), Delft University of Technology]. <https://doi.org/10.4233/uuid:1da4c818-dc1a-44d7-a89d-a4047184d854>

Important note

To cite this publication, please use the final published version (if applicable).
Please check the document version above.

Copyright

Other than for strictly personal use, it is not permitted to download, forward or distribute the text or part of it, without the consent of the author(s) and/or copyright holder(s), unless the work is under an open content license such as Creative Commons.

Takedown policy

Please contact us and provide details if you believe this document breaches copyrights.
We will remove access to the work immediately and investigate your claim.

MECHANISMS AND MITIGATION OF SHORT PITCH RAIL CORRUGATION

MECHANISMS AND MITIGATION OF SHORT PITCH RAIL CORRUGATION

Dissertation

for the purpose of obtaining the degree of doctor
at Delft University of Technology
by the authority of the Rector Magnificus Prof.dr.ir. T.H.J.J. van der Hagen
Chair of the Board for Doctorates
to be defended publicly on
Wednesday 7 December 2022 at 10:00 o'clock

By

Pan ZHANG

Master of Science in Road and Railway Engineering
Southwest Jiaotong University, China
Born in Henan, China

This dissertation has been approved by the promotor.

Composition of the doctoral committee:

Rector Magnificus,
Prof. dr. ir. Z. Li,
Dr. A.A. Núñez Vicencio,

chairperson
Delft University of Technology, promotor
Delft University of Technology, copromotor

Independent members:

Prof. dr. ir. A.R.M. Wolfert
Prof. dr. ir. C. Jommi
Prof. dr. X. Jin
Prof. dr. E. Garcia Vadillo
Prof. dr. ir. R.P.B.J. Dollevoet

Delft University of Technology
Delft University of Technology
Southwest Jiaotong University, China
University of Basque Country, Spain
Delft University of Technology



Printed by Gildeprint

Copyright © by Pan Zhang (zhang.tudelft.994@gmail.com)

ISBN 978-94-6419-652-8

An electronic version of this dissertation is available at
<http://repository.tudelft.nl/>.

To my family

Pan Zhang

CONTENTS

Summary	xi
Samenvatting	xv
1 Chapter 1	1
Introduction	1
1.1 Overview of short pitch corrugation	2
1.2 Consequences of short pitch corrugation	3
1.3 Development mechanism of short pitch corrugation	3
1.3.1 Theoretical studies of short pitch corrugation	4
1.3.2 Experimental study of short pitch corrugation	5
1.4 Mitigation of short pitch corrugation	6
1.5 Identification and constraint of rail vibration modes	7
1.5.1 Identification of rail vibration modes	7
1.5.2 Constraint of rail vibration modes	8
1.6 Research questions	9
1.7 Outline of this dissertation	9
References	11
2 Chapter 2	17
MULTIMODAL DISPERSIVE WAVES IN A FREE RAIL: NUMERICAL MODELING AND EXPERIMENTAL INVESTIGATION	17
2.1 Introduction	18
2.2 Numerical simulation of multimodal dispersive waves in free rail.	19
2.2.1 3D FE model	20
2.2.2 Modal results	21
2.2.3 Dispersion relations	23
2.3 Methods of experimental investigation	25
2.3.1 Sensor distribution.	25
2.3.2 Experimental setup	26
2.3.3 Experimental methods.	27
2.4 Experimental results	30
2.4.1 Results of ODS measurement	30
2.4.2 Results of SMAW measurement	32
2.5 Discussion	35
2.5.1 Discussion of ODS and SMAW measurement	35
2.5.2 The effectiveness of ODS measurement and SMAW measurement in field track	35

2.6	Conclusions and future work	38
	References	39
3	Chapter 3	43
	VIBRATION MODES AND WAVE PROPAGATION OF THE RAIL UNDER FASTENING CONSTRAINT	43
3.1	Introduction	44
3.2	Methodology	45
3.2.1	Experimental investigation	46
3.2.2	3D FE model	50
3.2.3	Rail vibration control by fastening parameters	51
3.3	Experimental results	53
3.3.1	Results of ODS measurement	53
3.3.2	Results of SMAW measurement	57
3.4	Validation and analysis of 3D FE model	60
3.4.1	Validation of FRFs and ODSs	60
3.4.2	Validation of group velocities and attenuation coefficient	62
3.4.3	Analysis of rail vibrations by wavenumber-frequency dispersion curves	63
3.5	Rail vibration control by fastening parameters	65
3.5.1	Rail vibration modes	65
3.5.2	Wave propagation characteristics	67
3.6	Discussions	69
3.6.1	Field SMAW measurement of wave propagation characteristics	69
3.6.2	The influences of rail lengths on rail vibration modes	71
3.7	Conclusions	72
	References	73
4	Chapter 4	79
	Parametric investigation of railway fastenings into the development and mitigation of short pitch corrugation	79
4.1	Introduction	80
4.2	Methodology	82
4.2.1	3D FE vehicle-track interaction model	82
4.2.2	Fastening models	83
4.2.3	Wear model	87
4.2.4	Simulation procedure for corrugation development with different fastening models	87
4.3	The influence of fastening configurations and boundary conditions on corrugation development	88
4.3.1	Fastening configurations	88
4.3.2	Fastening longitudinal boundary conditions	91
4.4	Influence of fastening longitudinal stiffness and damping	93
4.4.1	Influence of fastening longitudinal stiffness	94
4.4.2	Influence of fastening longitudinal damping	94

4.5	Influence of track length on corrugation features	95
4.6	Discussion	96
4.7	Conclusions and future work	99
	References	100
5	Chapter 5	103
	Short pitch corrugation mitigation by rail constraint design	103
5.1	Introduction	104
5.2	Methodology	107
5.2.1	3D FE vehicle-track interaction model for corrugation reproduction	107
5.2.2	ODS approach to identify corrugation initiation mechanism	108
5.2.3	Design and modelling of rail constraints for corrugation mitigation	109
5.2.4	Evaluation of rail constraints for corrugation mitigation	113
5.3	Corrugation reproduction and the initiation mechanism	113
5.4	Experimental results and modelling of rail constraints for corrugation mitigation	116
5.4.1	Experimental results and discussion	116
5.4.2	Validation of FE modelling of rail constraints	121
5.5	Evaluation of rail constraints for corrugation mitigation	122
5.6	Conclusions	124
	References	125
6	Chapter 6	131
	Design, calibration and validation of a wheel-rail contact force measurement system in V-Track	131
6.1	Introduction	132
6.2	Design of the dynamometer in V-Track	134
6.2.1	Structure of V-Track	134
6.2.2	Design of the dynamometer	136
6.3	Static calibration	138
6.3.1	Setup for static calibration	138
6.3.2	Results for static calibration	139
6.4	Validation of running tests	141
6.4.1	The repeatability of measurements in running conditions	141
6.4.2	Validation by a static measurement	142
6.4.3	Validation by wheel torque and spring load measurement	143
6.5	Influencing factors	146
6.5.1	The influence of braking torques on contact forces	146
6.5.2	The influence of running speeds	149
6.6	Measurement and control of contact forces in a 1/7 scaled V-Track	150
6.7	Conclusions and future work	152
	References	153

7 Chapter 7	157
Experimental study on the development mechanism of short pitch corrugation using a downscale V-Track test rig	157
7.1 Introduction	158
7.2 Corrugation experiment in the V-Track	160
7.2.1 Experimental setup	160
7.2.2 Corrugation experiment	161
7.3 The reproduced corrugation in the V-Track	165
7.4 Corrugation development mechanism	168
7.4.1 Corrugation wavelengths	168
7.4.2 Corrugation frequencies	170
7.4.3 Corrugation development mechanism.	170
7.5 Discussions	172
7.5.1 Validation and extension of the new insights in [7][14].	172
7.5.2 Vertical vibration modes and short pitch corrugation	173
7.5.3 The initial excitation for corrugation development.	173
7.5.4 The loading conditions and the excited rail vibration modes.	174
7.6 Conclusions and future work	174
References	176
8 Chapter 8	181
Conclusions and recommendations	181
8.1 Conclusions.	182
8.2 Applications of research findings	186
8.3 Recommendations for future research	187
References	188
Acknowledgements	189
Curriculum Vitae	193
List of Publications	195

SUMMARY

Short pitch corrugation is a (quasi-) periodic rail surface defect with shiny crests and dark valleys. It primarily occurs on tangent tracks or gentle curves with a typical wavelength in the range of 20-80 mm. Short pitch corrugation excites high-frequency wheel-rail dynamic contact forces and generates a high level of noise, which is a nuisance to both the passengers and the residents near the railway lines. The resulting large dynamic forces accelerate the degradation of the track components and may induce other rail defects (such as, squats), which increase the maintenance cost. The goal of this dissertation is to better understand the formation mechanism of short pitch corrugation and develop the root-cause solutions to mitigate it. Three steps are taken to achieve this goal: 1) identification and control of rail vibration modes which are crucial to short pitch corrugation formation; 2) design of a new rail constraint to mitigate short pitch corrugation; 3) experimental study of short pitch corrugation using an innovative V-Track test rig.

1 focuses on the identification and control of rail vibration modes. First, the vibration modes and dispersive waves of a free rail are simulated employing a finite element (FE) approach. The modal behaviors, wavenumber-frequency dispersion relations, and phase and group velocities of six types of propagative waves are derived and discussed in detail in 0-5 kHz. The operating deflection shape (ODS) approach distinguishes different types of rail vibration modes experimentally. A synchronized multiple-acceleration wavelet (SMAW) approach is proposed to experimentally study the propagation and dispersion characteristics of these waves. Both the laboratory and in-situ experimental results demonstrate the effectiveness of the ODS measurement for coupled rail mode identification and the SMAW approach for wave dispersion analysis. Afterward, the ODS and SMAW approaches are further applied to investigate rail vibration modes and wave propagation under fastening constraint. A three-dimensional (3D) FE rail-fastening model is also developed and validated against the ODS and SMAW measurement results. Subsequently, a sensitivity analysis of fastening parameters using this FE model is performed to gain insights into the control of rail vibrations. The results indicate that under fastening constraint, ODS measurement identifies vertical bending modes, longitudinal compression modes and lateral bending modes with shifted frequencies and significantly reduced vibration amplitude compared to free rail. Fastenings constrain the rail longitudinal vibrations less strongly compared to the vertical and lateral directions. The variation of fastening parameters can control rail mode frequencies and their vibration amplitudes, and influence the wave propagation velocities and attenuation along the rail.

Step 2 proposes a methodology to design a new rail constraint to mitigate short pitch corrugation. First, a parametric investigation of fastenings is conducted to understand the corrugation development mechanism and gain insight for a new rail constraint design for corrugation mitigation. A 3D FE vehicle-track dynamic interaction model is

employed, which considers the coupling between the structural dynamics and the contact mechanics, and the damage mechanism is assumed to be differential wear. Various fastening models with different configurations, boundary conditions, and dynamic parameters are built up and analyzed. The results indicate that the fastening longitudinal constraint to the rail is the major factor determining the corrugation development. The fastening vertical and lateral constraints influence corrugation features in terms of spatial distribution and wavelength components. The increase of fastening constraint in the longitudinal dimension helps to mitigate corrugation, and the inner fastening constraint in the lateral dimension is necessary for corrugation alleviation. Based on these insights, a methodology is proposed to mitigate short pitch corrugation by rail constraint design. First, short pitch corrugation is numerically reproduced employing a 3D FE vehicle-track interaction model. Then, the corrugation initiation mechanism is identified by examining the ODSs of rail longitudinal compression modes. Afterward, different rail constraints are designed, and their effects on longitudinal compression modes are analyzed. Models of these rail constraints are also built and validated. Finally, the rail constraint models are applied to the 3D FE vehicle-track interaction model, and their validity on short pitch corrugation mitigation is evaluated. It is found that a relative rigid constraint can completely suppress rail longitudinal compression modes and significantly reduce the fluctuation amplitude of the longitudinal contact force to mitigate corrugation. A direction is pointed out for corrugation mitigation in the field by strengthening the rail longitudinal constraint.

Step 3 performs an experimental investigation of short pitch corrugation using the down-scale V-Track test rig. First, a force measurement system named dynamometer is developed in the V-Track to measure the wheel-rail contact forces for short pitch corrugation experiments. The dynamometer consists of four 3-component piezo-electric force sensors and is mounted between the wheel assembly and the steel frame, enabling it to measure the forces transmitted from the wheel-rail interface to the frame. Static tests are first carried out to calibrate the dynamometer in three directions. Then, several tests are performed in the V-Track to examine the reliability and validity of the dynamometer for measuring the wheel-rail contact forces under running conditions. Experimental results show that the dynamometer is capable of reliably and accurately measuring these forces. Utilizing the measurement results from the dynamometer, the control of the wheel-rail contact forces in V-Track has also been achieved. Afterward, the V-Track test rig is used to investigate the development mechanism of short pitch corrugation experimentally. The loading conditions of the V-Track are designed to simulate the vehicle-track interaction on tangent tracks where short pitch corrugation mainly occurs in the field. Short pitch corrugation is successfully reproduced in the V-Track, and its spatial distribution, wavelength components, and hardness variation are captured by the 3D HandyScan and the hardness tests. Based on the measurement results of wheel-rail contact forces and track dynamic behaviors and observations, the development mechanism of short pitch corrugation is identified. It is found that rail longitudinal and lateral vibration modes contribute to the consistent development of short pitch corrugation.

Overall, the major contribution of this dissertation is threefold: 1) a better understanding of vibration modes and wave propagation of the rail in free condition and under fastening constraint is obtained by ODS and SMAW measurement, which is essential to under-

stand and mitigate short pitch corrugation; 2) a new rail constraint is designed which can effectively suppress rail longitudinal compression modes and mitigate short pitch corrugation; 3) experimental evidence is provided to demonstrate that initial excitation and longitudinal compression modes play a significant role in the consistent growth of short pitch corrugation.

SAMENVATTING

Golfslijtage met een korte golflengte is een (quasi-) periodisch defect op de bovenkant van de spoorstaaf met glimmende toppen en donkere dalen. Het komt vooral voor op rechte sporen of in lichte bogen en heeft een typische golflengte tussen de 20 en 80 mm. Deze golfslijtage zorgt voor hoog frequente wiel-rail dynamische krachten en genereert veel geluid, wat hinder kan veroorzaken voor zowel passagiers als bewoners in de spooromgeving. De resulterende dynamische krachten versnellen ook de degeneratie van de spoorcomponenten en kunnen andere typen defecten veroorzaken (bijv. squats), wat zorgt voor hogere onderhoudskosten. Het doel van dit proefschrift is het verkrijgen van een beter begrip over het ontstaan van deze schade en het ontwikkelen van oplossingen die het probleem bij de bron aanpakken. Er zijn drie stappen gezet om dit doel te bereiken: 1) Identificatie en controle van de vibratiemodi van de spoorstaaf welke cruciaal zijn in de vorming van korte golf golfslijtage; 2) het opstellen van nieuwe ontwerpeisen voor de rail om korte golf golfslijtage te voorkomen; 3) experimentele studie van korte golf golfslijtage met gebruik van een innovatieve V-Track testopstelling.

Stap 1 focust op het identificeren en controleren van de vibratiemodi van de spoorstaaf. Eerst zijn de vibratiemodi en dispersieve golven van een vrij liggende spoorstaaf gesimuleerd met behulp van een eindige elementen (EE) pakket. Het modelgedrag, golfgetal-frequentie dispersie relaties, en fase- en groepssnelheden van zes soorten lopende golven zijn afgeleid en bediscussieerd in detail in de range van 0-5 kHz. De 'operationele deflection shape' (ODS) aanpak identificeert verschillende types van vibratiemodi met behulp van experimenten. Een 'synchronized multiple-acceleration wavelet' (SMAW) aanpak wordt voorgesteld om met behulp van experimenten de voortplanting en dispersie karakteristieken van deze golven te bestuderen. Zowel de laboratorium testen als de testen ter plaatse laten de effectiviteit zien van de ODS meting voor gekoppelde spoorstaafmodi identificatie en van de SMAW aanpak voor golf dispersie analyse. Hierna zijn de ODS en SMAW methodes verder ingezet om de spoorstaaf vibratiemodi en golf voortplanting onder geklemde omstandigheden. Ook is er een 3-dimensionele (3D) EE spoorstem model ontwikkeld en gevalideerd tegen de ODS en SMAW meetresultaten. Daarna is een gevoeligheidsanalyse uitgevoerd van klemparameters met behulp van dit EE model, om een inzicht te krijgen in de beheersbaarheid van spoorstaafvibraties. The resultaten van ODS metingen laten zien dat onder geklemde omstandigheden, de verticale buigmodi, longitudinale compressiemodi, en laterale buigmodi van frequentie veranderen en een significant kleinere amplitude hebben dan bij een vrij liggende spoorstaaf. Spoorstaafklemmen hebben minder invloed op de longitudinale trillingen van de spoorstaaf en vergelijking met de verticale en laterale trillingen. Het variëren van klemparameters kan controle uitoefenen op de spoorstaafmodi frequenties en hun vibratie amplitudes en kan daarmee de golf voortplantingssnelheid en demping in de spoorstaaf beïnvloeden.

Stap 2 introduceert een methode voor het ontwerp van een nieuwe railbevestiging om

korte golf golfslijtage te verminderen. Allereerst is een parametrische studie van railklemmen uitgevoerd om de golfslijtage vormende mechanismes te begrijpen en inzicht te krijgen in een nieuw railbevestiging ontwerp ter voorkoming van golfslijtage. Een 3D EE voertuig-spoor dynamisch interactie model is ingezet, welke rekening houdt met de koppeling tussen de structurele mechanica en contact mechanica, en als schade mechanisme is aangenomen dat er sprake is van differentiële slijtage. Verschillende bevestigingsmodellen met verschillende configuraties, randvoorwaardes en dynamische parameters zijn gebouwd en geanalyseerd. De resultaten laten zien dat de longitudinale beperking die wordt opgelegd door de bevestiging de belangrijkste factor is in het bepalen van de vorming van golfslijtage. De verticale en laterale beperkingen opgelegd door de bevestiging beïnvloeden golfslijtage eigenschappen in de vorm van ruimtelijke spreiding en golflengte componenten. Het verhogen van de inklemkracht in longitudinale richting helpt om golfslijtage te verminderen en de binnenste inklemkracht in de laterale dimensie is nodig voor het verzachten van golfslijtage. Gebaseerd op deze bevindingen wordt een methode voorgesteld om korte golf golfslijtage te verminderen door railbevestigingsontwerp. Als eerste is korte golf golfslijtage numeriek gereproduceerd met behulp van een 3D EE voertuig-spoor interactie model. Daarna is het golfslijtage initiatie mechanisme geïdentificeerd door het bestuderen van de ODSen van de longitudinale compressie modi van het spoor. Hierna zijn verschillende railbevestigingen ontworpen en hun effecten op de longitudinale compressie modi zijn geanalyseerd. Modellen van deze railbevestigingen zijn ook gemaakt en gevalideerd. Als laatste zijn de modellen van deze railbevestigingen toegepast in het 3D EE voertuig-spoor interactie model, en is hun werking in het verminderen van golfslijtage geëvalueerd. De bevindingen hieruit zijn dat een relatief stijve bevestiging in het geheel de compressie modi in longitudinale richting van de rail kan onderdrukken en de fluctuatie in amplitude van de longitudinale contact kracht significant kan verminderen om golfslijtage te verminderen. Een oplossingsrichting is aangewezen voor het verminderen van golfslijtage in het veld, door de longitudinale inklemkracht van de spoorbevestiging te verhogen.

Stap 3 voert een experimentele onderzoek uit naar korte golf golfslijtage met gebruik van de geschaalde V-track testopstelling. Allereerst is een krachtmeting systeem ontwikkeld voor de V-track genaamd dynamometer welke de contactkrachten tussen wiel en spoorstaaf kan meten voor de korte golf golfslijtage experimenten. De dynamometer bestaat uit vier 3-richting piezo-elektrische kracht sensoren en is gemonteerd tussen de wielophanging en het stalen frame, waardoor het de krachten kan meten die van de interface tussen wiel en spoorstaaf worden overgebracht naar het platform. Eerst zijn statische testen uitgevoerd ter kalibratie van de dynamometer in drie richtingen. Daarna zijn verschillende tests uitgevoerd met de V-track om de betrouwbaarheid en de validiteit van de dynamometer voor het meten van contactkrachten tussen het wiel en de spoorstaaf te onderzoeken onder testomstandigheden. De resultaten laten zien dat de dynamometer in staat is deze krachten betrouwbaar en accuraat te meten. Met gebruik van de meetresultaten van de dynamometer is het ook gelukt de contactkrachten tussen wiel en spoor in de V-track te controleren. Hierna is de V-track gebruikt om de vorming van korte golf golfslijtage te onderzoeken met behulp van experimenten. De belasting condities op de V-track zijn ontworpen om de voertuig spoor interactie op recht spoor te simuleren waar korte golf golfslijtage voornamelijk optreed. Korte golf golfslijtage is succesvol gerepro-

duceerd op de V-track en de ruimtelijke distributie, golflengte componenten en hardheid variatie zijn gemeten met behulp van de 3D HandyScan en hardheidstests. Gebaseerd op de meetresultaten van de wiel-rail contact krachten en de dynamische eigenschappen van het spoor, is het ontstaansmechanisme voor korte golf golfslijtage geïdentificeerd. Er is gevonden dat de longitudinale en laterale vibratiemodi van de spoorstaaf bijdragen aan de vorming van de korte golf golfslijtage.

Al met al zijn er drie belangrijke nieuwe bevindingen in deze dissertatie: 1) een beter begrip van de vibratiemodi en golf voortplanting van de spoorstaaf in vrije condities en onder geklemde condities is verkregen met behulp van ODS en SMAW metingen, welke essentieel is voor een beter begrip van en voor het verminderen van korte golf golfslijtage; 2) een nieuwe spoorstaafbevestiging is ontworpen welke effectief de longitudinale compressie modi van de spoorstaaf kan onderdrukken en daarmee korte golf golfslijtage vermindert; 3) bewijs vanuit experimenten is gegeven, waarin gedemonstreerd wordt dat initiële excitatie en longitudinale compressie modi een significante rol spelen in de consistente groei van korte golf golfslijtage.

1

INTRODUCTION

1.1. OVERVIEW OF SHORT PITCH CORRUGATION

Railway has become a major means of transportation worldwide because of being economical, safe, and environmentally friendly. In recent decades, railway trains keep evolving in operation speed and the axle load to meet the increasing demands for a shorter traveling time and a larger transportation capacity. These demands often take the railway infrastructure close to its service limits and cause more defects in the wheels and rails. Short pitch corrugation is one of the major defects that occur in the running band of the rails. It is recognized as a (quasi-) periodic undulation of the rail surface with shiny crests and dark valleys, as shown in Figure 1.1. Short pitch corrugation has a long history, and its first report can date back to the late nineteenth century. A large statistical analysis in the 1950s indicated that 46% of the tracks in Germany suffered from short pitch corrugation[1]. Nowadays, short pitch corrugation remains one of the most severe problems to the railway administrations and has attracted extensive attention from researchers worldwide.

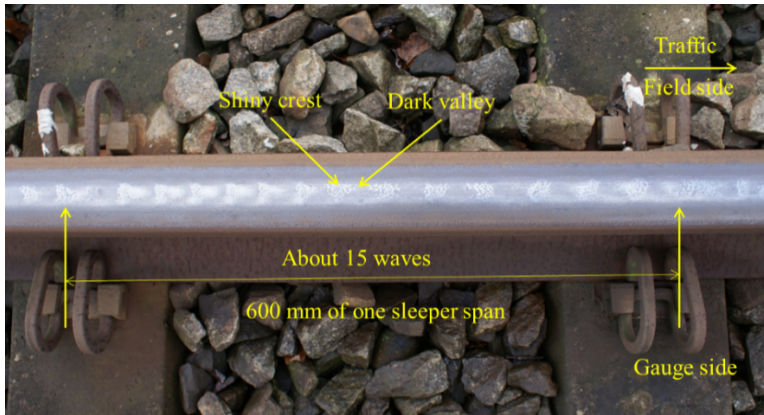


Figure 1.1: Short pitch corrugation with a wavelength of approximately 40 mm in the Dutch railway network. The photo was taken near Steenwijk, the Netherlands.

Field observations and measurements reveal several essential features of short pitch corrugation[2][3]. It primarily appears on tangent tracks or gentle curves with no contact between the wheel flange and the rail gauge corner. These tracks commonly lie in the high-speed main-line railway networks with relatively light axle loads. The wavelength of short pitch corrugation falls typically in the range of 20-80 mm, and it varies little with the train speed. The corrugation amplitude can reach up to 50-100 μm . Besides, it is observed that corrugation can develop in the embedded rail system with continuous support, despite a smaller propensity compared to the traditional discretely-supported track[1]. Metallurgical analysis shows that the microstructure of the corrugated rail varies at the crests and valleys, and white etching layers may develop at the corrugation crest, causing considerably high hardness[4].

1.2. CONSEQUENCES OF SHORT PITCH CORRUGATION

Short pitch corrugation excites high-frequency wheel-rail dynamic contact forces and induces a high level of noise. It is reported that the wheel-rail noise generated by short pitch corrugation can reach up to 15 dB[5], which is a nuisance to both the passengers and the residents nearby the railway lines. Because of the high noise radiation, short pitch corrugation is often referred to in the literature as the “roaring rail”. The resulting large dynamic forces from corrugation transmit through the entire track system and accelerate the degradation of the track components, such as fastenings and sleepers, which increase the maintenance cost. Besides, short pitch corrugation is related to the formation of rolling contact fatigue (RCF) in the field, for instance, rail squats[6][7] (Figure 1.2), which may lead to catastrophic rail breakage. In practice, grinding is a commonly-used measure for short pitch corrugation treatment. However, grinding increases the maintenance cost and meanwhile reduces the service life of the rail. Therefore, it is crucial to understand the formation mechanism of short pitch corrugation and develop the corresponding root-cause solutions for corrugation mitigation.

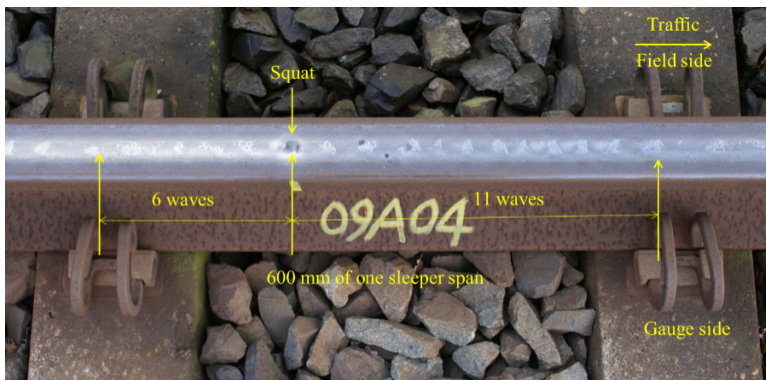


Figure 1.2: Short pitch corrugation with a wavelength of about 35 mm. The squat was induced by corrugation and occurred at around 1/3 sleeper span. The photo was taken near Steenwijk, the Netherlands.

1.3. DEVELOPMENT MECHANISM OF SHORT PITCH CORRUGATION

S.L. Grassie and J. Kalousek [3] presented a general corrugation development mechanism, as illustrated in a feedback loop in Figure 1.3. This mechanism consists of two features, a wavelength-fixing mechanism, and a damage mechanism. Consider that the initial rail profile is not corrugated at the beginning and assume an initial excitation [8] occurs. The initial excitation may result from initial rail roughness, track component degradation (i.e., fastenings), or traction and braking of the trains. With an initial excitation, dynamic loads with certain wavelengths are generated at the wheel-rail interface. The wavelengths are mainly determined by the interplays of the structural dynamics and the contact mechanics, the so-called wavelength-fixing mechanism. The excited dynamic loads cause a particular type of rail damage, therefore modifying the initial rail

profile. Typical damage mechanisms are wear and plastic deformation. The continuous accumulation of differential wear or plastic deformation at particular locations leads to corrugation initiation and growth. According to different wavelength-fixing and damage mechanisms, corrugation is classified into six groups[3]: heavy haul, light rail, booted sleeper, contact fatigue, rutting, and short pitch corrugation, respectively. S. L. Grassie and J. Kalousek[3]reported that the development mechanisms of all types of corrugation are well understood except for short pitch corrugation.

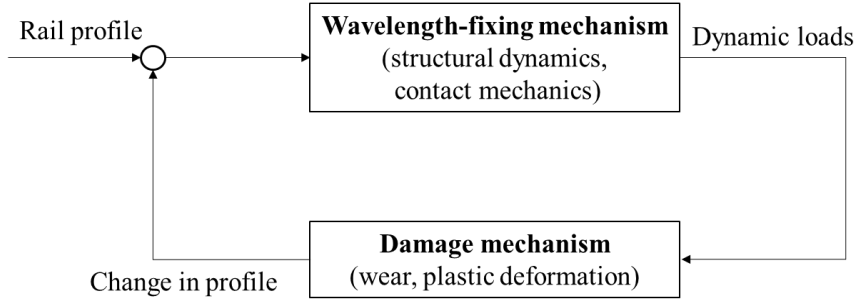


Figure 1.3: The feedback loop of a general corrugation development mechanism[3]

1.3.1. THEORETICAL STUDIES OF SHORT PITCH CORRUGATION

Since 1980, increasing attention has been paid to short pitch corrugation[9]. Based on field observations, wear is commonly considered as the damage mechanism of short pitch corrugation. However, although many hypotheses have been proposed in the literature, a well-validated wavelength-fixing mechanism has not yet been demonstrated. The vertical pinned-pinned resonance, a vertical rail bending mode with the wavelength of two sleeper spans, has been attributed to determine the wavelength-fixing mechanism [10][11][12][13]. Nevertheless, this hypothesis has difficulty in explaining some field observations. For instance, the corrugation wavelength varies little with the train speed in the field instead of in the direct proportion based on the explanation of the vertical pinned-pinned resonance. Additionally, according to this mechanism, corrugation should occur everywhere above the sleeper support after a certain amount of train passages, which is not observed in practice. Corrugation is also formed in the embedded rail system, which eliminates the pinned-pinned resonances due to the continuous support. To explain the slight variation of corrugation wavelength with the train speed, S. Muller[14]introduced a geometrical filter function of the wheel-rail contact that allows corrugation formation within a fixed wavelength band (i.e., 20-100 mm). Besides, except for the vertical pinned-pinned resonance, other structural dynamics, such as vertical rail resonance, lateral 1st and 2nd pinned-pinned resonance, can also contribute to corrugation development. T. X. Wu and D. J. Thompson[15] studied multiple wheel/rail interactions and found that the wave reflections on the rail between multiple wheels cause more vertical resonance frequencies than those of a single wheel/rail interaction, which are associated with several wavelengths of short pitch corrugation.

S. Li et al.[16]and Z. Li et al.[8]employed an advanced and validated three-dimensional

(3D) finite element (FE) model [17][18][19] to study the development mechanism of short pitch corrugation. The main conclusions include: (1) rail longitudinal vibration modes are possibly dominant for corrugation initiation; (2) the consistency in the longitudinal and vertical contact forces, the resulting differential wear, and the existing corrugation should determine the continuous growth of corrugation. Based on these two hypotheses, together with an “initial excitation” from the fastening system, a process for consistent corrugation initiation and growth was proposed in [8][18][19]. Afterward, short pitch corrugation has been successfully reproduced using a 3D FE vehicle-track dynamic model, which shares features similar to the corrugation observed and measured in the field in terms of spatial distribution and major wavelength components. In this dissertation, experimental validation of the development mechanism of short pitch corrugation proposed in [8] is performed.

1.3.2. EXPERIMENTAL STUDY OF SHORT PITCH CORRUGATION

Despite extensive theoretical work in the literature, few experimental studies have been conducted to validate and understand the formation mechanism of short pitch corrugation. P. A. Bellette et al. [20] simulated the corrugation growth rate using a tangent track corrugation model and achieved good agreement with the experimental results of a downscale two disk test rig. They also reported that the speed variation and the friction modifier could considerably reduce the corrugation growth rate. X. Jin and Z. Wen [21] utilized a full-scale test rig to study rail corrugation experimentally. It is found that the high-frequency vibration of the test rig can initiate a corrugation with different wavelengths on the smooth contact surfaces of the wheel with the non-zero steady creepage of the wheelset/rollers. However, it should be noted that most existing test facilities mainly focus on the simulation of the wheel-rail contact, with little consideration their dynamic similarity with real-life vehicle-track interaction system [20][21][22][23][24]. The structural dynamics of the vehicle-track system are crucial to the wavelength-fixing of short pitch corrugation in the field [3]. Therefore, although the natural vibration modes of these test facilities can well explain the wavelengths of the reproduced corrugation [20][21], they may not be comparable to those of the real vehicle-track system because of the dynamic dissimilarity, and thus cannot be used to understand and validate the wavelength-fixing mechanism of short pitch corrugation in the field.

An innovative downscale test rig called ‘V-Track’ has been developed to simulate vehicle-track dynamic interactions [24] to remedy the lack of dynamic similarity between the laboratory facilities and the real-life railways. The V-Track consists of multiple wheel components, running over a horizontal track ring with a radius of 2 m to simulate continuous wheel-rail contact, as shown in Figure 1.4. The vehicle is simplified into the preloaded primary suspension and the wheel, which is acceptable for studying the vehicle-track system dynamics at high frequencies, where the vibration of the sprung mass has a negligible effect [25]. The major components of tracks in the field, consisting of the rail, sleepers, fastenings, and ballast layer or slab, can all be included in the setup, making the track dynamic behaviors almost equivalent to the real system. The wheel and rail materials are identical to the real-life ones. That is to represent the real wheel-rail rolling contact phenomenon as accurately as possible by capturing its nonlinear behaviors. Overall, the V-Track can comprehensively simulate both the wheel-rail contact mechanics and

high-frequency dynamics of the real vehicle-track system, making it a suitable setup for studying short pitch corrugation.

This dissertation aims at validating the development mechanism of short pitch corrugation proposed in [8] using the innovative V-Track test rig. For this purpose, accurate measurement and control of wheel-rail contact forces are prerequisites. Some methods for wheel-rail contact force measurement have been proposed in the literature, mainly direct methods [26][27][28][29] and indirect methods [30][31][32]. Direct methods typically install the dynamometric sensors on an instrumented wheelset to directly measure the contact forces. For instance, P. Gullers et al. [26] equipped a wheel disc with strain gauges to measure the vertical contact force within 2 kHz in the field and identified different classes of rail irregularities using the measured wheel-rail contact force. Indirect methods combine the measurement of the dynamic responses of a vehicle (i.e., acceleration) and the vehicle-track interaction model to obtain the wheel-rail contact forces. For example, F. Xia et al. [30][31] measured the car body responses and estimated the contact forces based on an inverse wagon model. This dissertation aims at developing a contact force measurement system in the V-Track using the direct method for the short pitch corrugation experiment.

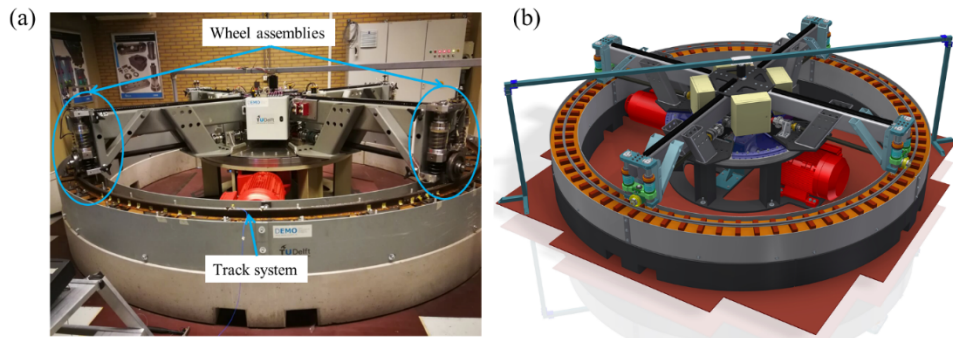


Figure 1.4: The downscale V-Track test rig for the short pitch corrugation experiment. (a) V-Track developed in the laboratory; (b) schematic drawing of V-Track in CAD. (Source: [33]).

1.4. MITIGATION OF SHORT PITCH CORRUGATION

In practice, rail grinding is a widely used method to treat and prevent all types of corrugation [3][34]. Cyclic preventive grinding can keep the railhead irregularity at a low level, which reduces the wheel-rail dynamic contact force, and thus delay the onset of short pitch corrugation. However, in the meantime, it will increase the maintenance cost and reduce the service life of the rail. Rail grinding is also the means of removing the existing corrugation instead of rail replacement. However, in this case, grinding is more like a palliative than a cure. It is reported that short pitch corrugation may reoccur rapidly after the grinding treatment [35]. Therefore, it is necessary to understand the short pitch corrugation formation mechanism further and develop effective root-cause solutions to mitigate it.

Since wear is the damage mechanism, more wear-resistant rails should be a solution to short pitch corrugation mitigation regardless of its wavelength-fixing mechanism. The field testing results indicated that the head-hardened rails with a higher wear resistance significantly delayed short pitch corrugation growth[36]. In addition, friction modifiers, which can control the friction and creep characteristic between the wheel and the rail[37][38], appear to alleviate short pitch corrugation successfully[39][40]. Overall, these solutions mainly delay but can hardly prevent corrugation formation.

Root-cause solutions may be developed to mitigate or even eliminate short pitch corrugation by suppressing the wavelength-fixing mechanism. T. Wu[39] reported that rail vibration absorbers reduce rolling noise and suppress the vertical pinned-pinned resonance. Then, the evolution process of short pitch corrugation was simulated by combining the wheel-track-absorber dynamics, contact mechanics and wear. It is found that the corrugation with the vertical pinned-pinned resonance as the wavelength-fixing mechanism is effectively mitigated by a rail vibration absorber. Experimental evidence has not been provided to support this conclusion. S. Li et al.[16] and Z. Li et al.[8] proposed a new hypothesis for the wavelength-fixing mechanism that rail longitudinal compression modes are dominant for corrugation initiation and verified it by numerical simulations. This new finding points out a promising direction for short pitch corrugation mitigation or even elimination by constraining longitudinal compression modes to suppress corrugation initiation. It is worth emphasizing in[8] that fastening models, which serve as the initial excitation to the vehicle-track system, play an essential role in corrugation formation. Therefore, a systematic parametric investigation of fastenings may provide insights into short pitch corrugation mitigation methods. Further, a new type of rail constraint may need to be designed instead of the current fastenings to better suppress longitudinal compression modes for corrugation mitigation.

1.5. IDENTIFICATION AND CONSTRAINT OF RAIL VIBRATION MODES

1.5.1. IDENTIFICATION OF RAIL VIBRATION MODES

Rail vibration modes are essential to the wavelength-fixing of short pitch corrugation [3][16][40]. For the new design of rail constraints to mitigate corrugation, identification of rail vibration modes is a prerequisite. The frequency range of interest for short pitch corrugation is about 150-2000 Hz, considering the corrugation wavelength of 20-55 mm with the train speed of 30-140 km/h in the Dutch railway network. In this frequency range, five types of rail vibration modes are expected: vertical bending modes, longitudinal compression modes, lateral bending modes, lateral torsion modes, and lateral web 1st bending modes, respectively [42][43], as shown in Figure 1.5 Therefore, rail modal coupling of different directions may occur, making one natural frequency correspond to multiple rail modes. In this case, the widespread experimental method in the railway structure, frequency response function (FRF) measurement[44][45][46], has difficulty in identifying the coupled modes because it can only derive the natural frequencies of the track system. Thus the experimental methods which are capable of distinguishing the coupled rail vibration modes should be employed.

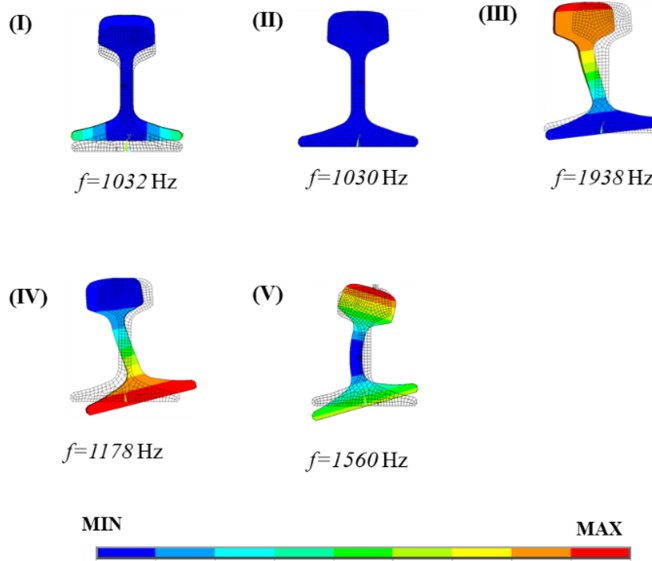


Figure 1.5: Cross-sectional deformation of vertical bending modes (I), longitudinal compression modes (II), lateral bending modes (III), lateral torsion modes (IV), web 1st bending modes (V) of a free rail. (Source:[41])

1.5.2. CONSTRAINT OF RAIL VIBRATION MODES

In railway tracks, fastenings impose significant constraints on rail vibrations. Fastenings mainly consist of two components: railpads and clamps. Railpads are made of resilient materials placed between the rail and the sleeper to reduce vibration and noise by adding track flexibility. Clamps fix the rail to the sleeper to ensure that the rail remains attached to the sleeper under train loads. Railpads and clamps constrain the displacement of the rail in the vertical, longitudinal and lateral directions. Experimental and numerical studies indicate that the fastenings influence the vehicle-track dynamic interaction in a broad frequency range between 50 Hz and 3000 Hz [12][47][48][49][50], covering the frequency range of interest for short pitch corrugation. Therefore, a good understanding of the rail constraint mechanism of fastenings is important to study corrugation formation mechanism and may provide insights for the new design of rail constraint to mitigate corrugation.

Many experimental studies indicate that the dynamic properties of railpads are nonlinear and depend on the preload, excitation frequency, excitation amplitude, temperature, and aging[51][52]. The fastening models were also developed to consider the nonlinearity of railpads, such as Poynting-Thomson (PT) model [53], Prony series model[51], fractional derivative model[54], and solid railpad model[55]. However, most studies mainly focus on the vertical rail vibrations under fastening constraint because the wheel-rail excitation seem to primarily act in the vertical direction. Some researchers also investigate the lateral constraint mechanism of fastenings to study wheel-rail rolling noise[42][46]. However, the constraint mechanism of fastenings on rail longitudinal compression modes, which is considered dominant for corrugation initiation[16][8], has

been barely reported in the literature.

1.6. RESEARCH QUESTIONS

Based on the literature review, the goal of this dissertation is to answer the following research question:

What are the development mechanism and mitigation approaches of short pitch corrugation?

A set of sub-questions are formulated to answer this question, as follows:

Q1. How to identify the coupled rail vibration modes to understand and mitigate short pitch corrugation?

Q2. What is the constraint mechanism of fastening on the rail longitudinal compression modes, which is dominant for short pitch corrugation initiation?

Q3. How do the fastening parameters influence the development and mitigation of short pitch corrugation?

Q4. How to mitigate short pitch corrugation by the new design of rail constraint?

Q5. How to measure the wheel-rail contact forces in the downscale V-track test rig for the short pitch corrugation experiment?

Q6. How to reproduce short pitch corrugation on the downscale V-track test rig to validate the corrugation development mechanism in[8]?

1.7. OUTLINE OF THIS DISSERTATION

This dissertation answers the above research questions in three steps, as shown in Fig. 1.6. In Step 1, the operating deflection shape (ODS) approach and the synchronized multiple-acceleration wavelet (SMAW) approach are employed to investigate rail vibration modes and wave propagation in free condition (Chapter 2) and under fastening constraint (Chapter 3). Insights into the rail vibration control are also gained through a sensitivity analysis of fastening parameters. In Step 2, the influence of fastening parameters on the development and mitigation of short pitch corrugation is numerically studied, employing a 3D FE vehicle-track interaction model (Chapter 4). In light of these results, a new rail constraint is designed to suppress rail longitudinal compression modes and mitigate short pitch corrugation (Chapter 5). In Step 3, a dynamometer is developed in the V-Track test rig to measure the wheel-rail contact forces for short pitch corrugation experiments (Chapter 6). Afterward, the V-Track test rig reproduces short pitch corrugation to understand and validate the corrugation development mechanism proposed in[8] (Chapter 7). A more detailed description of each chapter is presented as follows.

Chapter 2 employs a FE solution to predict the vibration modes and dispersive waves of a free rail. The modal behaviors, wavenumber-frequency dispersion relations, and phase and group velocities of six types of propagative waves are derived and discussed in detail in 0-5 kHz. The ODS measurement approach is applied to distinguish different types of rail vibration modes. A SMAW approach is proposed to experimentally study the propagation and dispersion characteristics of rail vibrational waves.

Chapter 3 proposes a systematic methodology to investigate 3D rail vibration and control under fastening constraint. Through this methodology, rail vibration modes under

fastening constraint are identified by ODS measurement, and the SMAW approach measures wave propagation and dispersion characteristics. Insights into the rail vibration control are also gained through a sensitivity analysis of fastening parameters, including dynamic stiffness and damping.

Chapter 4 performs a parametric investigation of fastenings to understand the short pitch corrugation development mechanism further and gain insight for corrugation mitigation. A 3D FE vehicle-track dynamic interaction model is employed, which considers the coupling between the structural dynamics and the contact mechanics, and the damage mechanism is assumed to be differential wear. Various fastening models with different configurations, boundary conditions, and dynamic stiffness and damping parameters are built up and analyzed.

Chapter 5 proposes a methodology to mitigate short pitch corrugation by rail constraint design. First, short pitch corrugation is numerically reproduced employing a 3D FE vehicle-track interaction model. Then, the corrugation initiation mechanism is identified by examining the ODSs of rail longitudinal compression modes. Afterward, different rail constraints are designed, and their effects on longitudinal compression modes are analyzed. Models of these rail constraints are also built and validated. Finally, rail constraint models are built up and applied in the 3D FE vehicle-track interaction model, and their effectiveness on short pitch corrugation mitigation is evaluated.

Chapter 6 develops a force measurement system named dynamometer in the V-Track to measure the wheel-rail contact forces. The dynamometer consists of four 3-component piezo-electric force sensors and is mounted between the wheel assembly and the steel frame, enabling it to measure the forces transmitted from the wheel-rail interface to the frame. The static and running tests are performed to examine the reliability and validity of the dynamometer for measuring the wheel-rail contact forces.

Chapter 7 presents an experimental study on the development mechanism of short pitch corrugation using the downscale V-Track test rig. The loading conditions of the V-Track are so designed to simulate the vehicle-track interaction on tangent tracks where short pitch corrugation mainly occurs in the field. The corrugation development mechanism is understood based on the measured wheel-rail dynamic contact forces, track dynamic behaviors, and observations.

Chapter 8 presents the main conclusions and recommendations for future work.

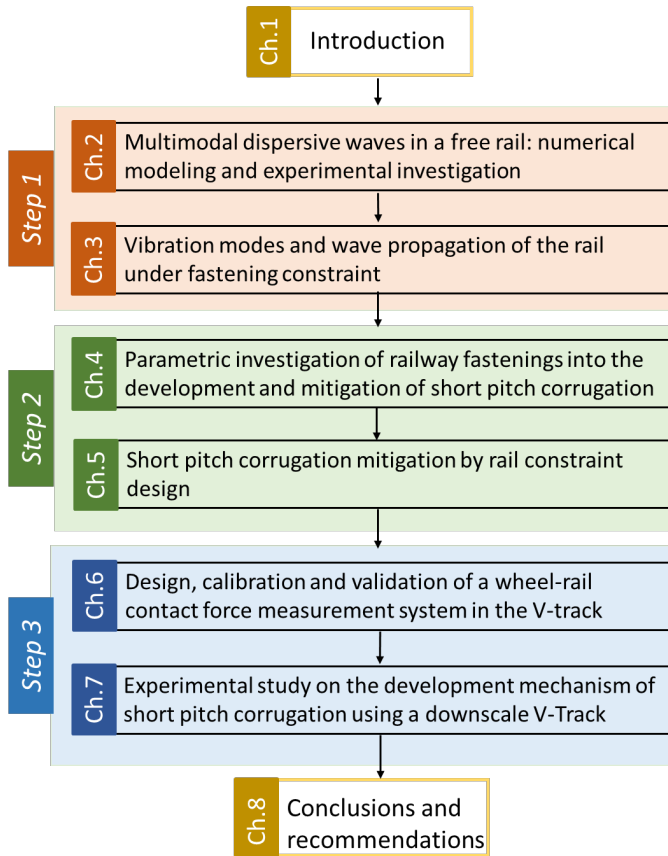


Figure 1.6: Outline of this dissertation.

REFERENCES

- [1] K. Oostermeijer, *Review on short pitch rail corrugation studies*, *Wear* **265**, 1231 (2008).
- [2] S. Grassie, *Rail corrugation: characteristics, causes, and treatments*, *Proceedings of the Institution of Mechanical Engineers, Part F: Journal of Rail and Rapid Transit* **223**, 581 (2009).
- [3] S. Grassie and J. Kalousek, *Rail corrugation: characteristics, causes and treatments*, *Proceedings of the Institution of Mechanical Engineers, Part F: Journal of Rail and Rapid Transit* **207**, 57 (1993).
- [4] E. Wild, L. Wang, B. Hasse, T. Wroblewski, G. Goerigk, and A. Pyzalla, *Microstructure alterations at the surface of a heavily corrugated rail with strong ripple formation*, *Wear* **254**, 876 (2003).
- [5] J. Alias, *Characteristics of wave formation in rails*, *Rail International* (1986).

- [6] Z. Li, X. Zhao, C. Esveld, R. Dollevoet, and M. Molodova, *An investigation into the causes of squats—correlation analysis and numerical modeling*, *Wear* **265**, 1349 (2008).
- [7] X. Deng, Z. Qian, Z. Li, and R. Dollevoet, *Investigation of the formation of corrugation-induced rail squats based on extensive field monitoring*, *International Journal of Fatigue* **112**, 94 (2018).
- [8] Z. Li, S. Li, P. Zhang, A. Nunez, and R. Dollevoet, *Mechanism of short pitch corrugation: Initial excitation and wavelength selection for consistent initiation and growth*, Submitted (2021).
- [9] Y. Sato, A. Matsumoto, and K. Knothe, *Review on rail corrugation studies*, *Wear* **253**, 130 (2002).
- [10] K. Hempelmann and K. Knothe, *An extended linear model for the prediction of short pitch corrugation*, *Wear* **191**, 161 (1996).
- [11] A. Igeland and H. Ilias, *Rail head corrugation growth predictions based on non-linear high frequency vehicle/track interaction*, *Wear* **213**, 90 (1997).
- [12] H. Ilias, *The influence of railpad stiffness on wheelset/track interaction and corrugation growth*, *Journal of Sound and Vibration* **227**, 935 (1999).
- [13] M. Hiensch, J. C. Nielsen, and E. Verheijen, *Rail corrugation in the netherlands—measurements and simulations*, *Wear* **253**, 140 (2002).
- [14] S. Muller, *A linear wheel-track model to predict instability and short pitch corrugation*, *Journal of Sound and Vibration* **227**, 899 (1999).
- [15] T. Wu and D. Thompson, *An investigation into rail corrugation due to micro-slip under multiple wheel/rail interactions*, *Wear* **258**, 1115 (2005).
- [16] S. Li, Z. Li, A. Núñez, and R. Dollevoet, *New insights into the short pitch corrugation enigma based on 3d-fe coupled dynamic vehicle-track modeling of frictional rolling contact*, *Applied Sciences* **7**, 807 (2017).
- [17] X. Zhao and Z. Li, *The solution of frictional wheel-rail rolling contact with a 3d transient finite element model: Validation and error analysis*, *Wear* **271**, 444 (2011).
- [18] M. Molodova, Z. Li, A. Núñez, and R. Dollevoet, *Validation of a finite element model for axle box acceleration at squats in the high frequency range*, *Computers & Structures* **141**, 84 (2014).
- [19] Z. Yang, X. Deng, and Z. Li, *Numerical modeling of dynamic frictional rolling contact with an explicit finite element method*, *Tribology international* **129**, 214 (2019).
- [20] P. Bellette, P. Meehan, and W. Daniel, *Validation of a tangent track corrugation model with a two disk test rig*, *Wear* **271**, 268 (2011).

- [21] X. Jin and Z. Wen, *Rail corrugation formation studied with a full-scale test facility and numerical analysis*, Proceedings of the Institution of Mechanical Engineers, Part J: Journal of Engineering Tribology **221**, 675 (2007).
- [22] Y. Suda, H. Komine, T. Iwasa, and Y. Terumichi, *Experimental study on mechanism of rail corrugation using corrugation simulator*, Wear **253**, 162 (2002).
- [23] A. Saulot, S. Descartes, and Y. Berthier, *Sharp curved track corrugation: From corrugation observed on-site, to corrugation reproduced on simulators*, Tribology International **42**, 1691 (2009).
- [24] M. Naeimi, Z. Li, R. H. Petrov, J. Sietsma, and R. Dollevoet, *Development of a new downscale setup for wheel-rail contact experiments under impact loading conditions*, Experimental Techniques **42**, 1 (2018).
- [25] K. Knothe and S. Grassie, *Modelling of railway track and vehicle/track interaction at high frequencies*, Vehicle system dynamics **22**, 209 (1993).
- [26] P. Gullers, L. Andersson, and R. Lundén, *High-frequency vertical wheel-rail contact forces—field measurements and influence of track irregularities*, Wear **265**, 1472 (2008).
- [27] A. Matsumoto, Y. Sato, H. Ohno, M. Tomeoka, K. Matsumoto, J. Kurihara, T. Ogino, M. Tanimoto, Y. Kishimoto, Y. Sato, *et al.*, *A new measuring method of wheel-rail contact forces and related considerations*, Wear **265**, 1518 (2008).
- [28] P. Urda, S. Muñoz, J. F. Aceituno, and J. L. Escalona, *Wheel-rail contact force measurement using strain gauges and distance lasers on a scaled railway vehicle*, Mechanical Systems and Signal Processing **138**, 106555 (2020).
- [29] S. Meymand and M. Ahmadian, *Design, development, and calibration of a force-moment measurement system for wheel-rail contact mechanics in roller rigs*, Measurement **81**, 113 (2016).
- [30] F. Xia, C. Cole, and P. Wolfs, *An inverse railway wagon model and its applications*, Vehicle system dynamics **45**, 583 (2007).
- [31] F. Xia, C. Cole, and P. Wolfs, *Grey box-based inverse wagon model to predict wheel-rail contact forces from measured wagon body responses*, Vehicle System Dynamics **46**, 469 (2008).
- [32] L. Wei, J. Zeng, P. Wu, and H. Gao, *Indirect method for wheel-rail force measurement and derailment evaluation*, Vehicle System Dynamics **52**, 1622 (2014).
- [33] P. Zhang, J. Moraal, and Z. Li, *Design, calibration and validation of a wheel-rail contact force measurement system in v-track*, Measurement **175**, 109105 (2021).
- [34] S. L. Grassie, *Rail corrugation: advances in measurement, understanding and treatment*, Wear **258**, 1224 (2005).

- [35] C. Frederick and W. Bugden, *Corrugation research on british rail, symposium on rail corrugation problems*, , Berlin, June (1983).
- [36] R. Heyder and G. Girsch, *Testing of hsh® rails in high-speed tracks to minimise rail damage*, *Wear* **258**, 1014 (2005).
- [37] O. Arias-Cuevas, Z. Li, R. Lewis, and E. A. Gallardo-Hernandez, *Rolling-sliding laboratory tests of friction modifiers in dry and wet wheel-rail contacts*, *Wear* **268**, 543 (2010).
- [38] R. Galas, M. Omasta, I. Krupka, and M. Hartl, *Laboratory investigation of ability of oil-based friction modifiers to control adhesion at wheel-rail interface*, *Wear* **368**, 230 (2016).
- [39] T. Wu, *Effects on short pitch rail corrugation growth of a rail vibration absorber/damper*, *Wear* **271**, 339 (2011).
- [40] K. Knothe and A. Groß-Thebing, *Short wavelength rail corrugation and non-steady-state contact mechanics*, *Vehicle system dynamics* **46**, 49 (2008).
- [41] P. Zhang, S. Li, A. Núñez, and Z. Li, *Multimodal dispersive waves in a free rail: Numerical modeling and experimental investigation*, *Mechanical Systems and Signal Processing* **150**, 107305 (2021).
- [42] D. Thompson, *Wheel-rail noise generation, part iii: rail vibration*, *Journal of sound and vibration* **161**, 421 (1993).
- [43] L. Gavrić, *Computation of propagative waves in free rail using a finite element technique*, *Journal of Sound and Vibration* **185**, 531 (1995).
- [44] A. Man, *Dynatrack: A survey of dynamic railway track properties and their quality*. (2004).
- [45] M. Oregui, Z. Li, and R. Dollevoet, *Identification of characteristic frequencies of damaged railway tracks using field hammer test measurements*, *Mechanical Systems and Signal Processing* **54**, 224 (2015).
- [46] Z. Yang, A. Boogaard, R. Chen, R. Dollevoet, and Z. Li, *Numerical and experimental study of wheel-rail impact vibration and noise generated at an insulated rail joint*, *International Journal of Impact Engineering* **113**, 29 (2018).
- [47] S. Grassie, R. Gregory, D. Harrison, and K. Johnson, *The dynamic response of railway track to high frequency vertical excitation*, *Journal of Mechanical Engineering Science* **24**, 77 (1982).
- [48] D. Thompson, C. Jones, T. Wu, and A. De France, *The influence of the non-linear stiffness behaviour of rail pads on the track component of rolling noise*, *Proceedings of the Institution of Mechanical Engineers, Part F: Journal of rail and rapid transit* **213**, 233 (1999).

- [49] M. Oregui, A. Núñez, R. Dollevoet, and Z. Li, *Sensitivity analysis of railpad parameters on vertical railway track dynamics*, *Journal of Engineering Mechanics* **143**, 04017011 (2017).
- [50] K. Wei, F. Wang, P. Wang, Z.-x. Liu, and P. Zhang, *Effect of temperature-and frequency-dependent dynamic properties of rail pads on high-speed vehicle-track coupled vibrations*, *Vehicle System Dynamics* **55**, 351 (2017).
- [51] M. Oregui, A. De Man, M. Woldekidan, Z. Li, and R. Dollevoet, *Obtaining railpad properties via dynamic mechanical analysis*, *Journal of Sound and Vibration* **363**, 460 (2016).
- [52] K. Wei, Q. Yang, Y. Dou, F. Wang, and P. Wang, *Experimental investigation into temperature-and frequency-dependent dynamic properties of high-speed rail pads*, *Construction and Building Materials* **151**, 848 (2017).
- [53] B. Ripke, *Hochfrequente Gleismodellierung und Simulation der Fahrzeug-Gleis-Dynamik unter Verwendung einer nichtlinearen Kontaktmechanik* (VDI-Verlag, 1995).
- [54] Å. Fenander, *A fractional derivative railpad model included in a railway track model*, *Journal of Sound and Vibration* **212**, 889 (1998).
- [55] M. Oregui, Z. Li, and R. Dollevoet, *An investigation into the modeling of railway fastening*, *International Journal of Mechanical Sciences* **92**, 1 (2015).

2

MULTIMODAL DISPERSIVE WAVES IN A FREE RAIL: NUMERICAL MODELING AND EXPERIMENTAL INVESTIGATION

This chapter presents a solution method based on finite element (FE) modeling to predict multimodal dispersive waves in a free rail. As well as the modal behaviors and wavenumber-frequency dispersion relations, the phase and group velocities of six types of propagative waves are also derived and discussed in detail in the frequency range of 0-5 kHz. To experimentally distinguish different types of wave modes, the operating deflection shape (ODS) measurement approach is employed in the laboratory. ODS is measured from the spatial distribution of imaginary parts of the FRFs. We also propose a synchronized multiple-acceleration wavelet (SMAW) approach to experimentally study the propagation and dispersion characteristics of waves in a free rail. The group velocities in the vertical, longitudinal, and lateral directions are estimated from the wavelet power spectra (WPSs). The good agreement between the simulation and measurement in terms of mode shapes and ODSs, wavenumber-frequency dispersion curves, and group velocities indicates that the ODS and SMAW approaches can distinguish different wave modes and measure wave propagation and dispersion characteristics. In situ experimental results further demonstrate the effectiveness of the ODS measurement for coupled modal identification and the SMAW approach for wave dispersion analysis of the rail in a field track.

Parts of this chapter have been published in P.Zhang **150**, 107305 (2021)[1]

2.1. INTRODUCTION

Rail vibrations play an important role in wheel-rail interactions, especially in the high-frequency range. Noise and corrugation problems in railway engineering are related to rail vibrations; for example, the lateral and vertical rail modes dominate rolling noise radiation from 500-1600 Hz and generally remain important at higher frequencies up to 5[2]. Short pitch corrugation has been reported to be related to the 'pinned-pinned' resonance at approximately 1 kHz[3][4], which is a rail vertical bending mode with a wavelength of two sleeper spacings. New insights into short pitch corrugation have recently proposed that longitudinal rail modes are responsible for corrugation initiation[5]. Therefore, investigations of rail vibrations in the vertical, longitudinal, and lateral directions are important for understanding these problems.

Rail vibrations can be seen as the superposition of a series of propagative waves[2]. Wavenumber-frequency dispersion relations and phase and group velocities provide fundamental information to understand wave propagation characteristics. In the literature, many models have been developed to model the rail, including analytical beam or plate models[6][7][8][9][10][11][12][13], the semi-analytical or 2.5D FE model (SAFE) [14][15][16][17][18], and the 3D FE model [12][19][20]. The analytical beam or plate models assume a constant cross-section of the rail, which is only valid at low frequencies [21]. The 2.5D FE model and 3D FE model can consider rail cross-section deformation, which is important to predict the dispersion relations accurately. Although the computation efficiency of the 2.5D FE model is higher because it treats the longitudinal direction analytically, the 3D FE has the advantage that it can model nonlinear wheel-rail dynamic contact, which is important when studying wheel-rail rolling noise and short pitch corrugation. Many chapters[22] [16][17][18][23] have reported the dispersion curves and phase and group velocities of rail waves in the ultrasound frequency range (i.e., 100 kHz) for long-range rail inspection. In the frequency range of rolling noise and short pitch corrugation (below 5 kHz), Thompson[10]and Gavric[14]predicted the dispersion curves, while the phase and group velocities were not presented. This chapter applies a 3D FE model to predict the dispersive waves in a free rail at 0-5 kHz and derived the phase and group velocities.

Although many models have predicted the multiple wave modes in a free rail[10][14][22], few experimental methods have been reported in the literature to distinguish different wave modes. One possible reason is that most researchers have focused only on the vertical rail vibration because the wheel-rail excitation mainly acts in this direction [6][11][19]. There is only one type of wave mode called the vertical bending mode in this direction; thus, the influence of modal coupling is insignificant. However, when studying three-dimensional rail vibrations, modal coupling of different directions may occur, making one natural frequency correspond to multiple rail modes. In this case, the widely used experimental method for the railway structure, frequency response function (FRF) measurement[24][25] [26][27], has difficulty identifying the coupled modes because it can only obtain the natural frequencies. Another experimental method named operating deflection shape (ODS) measurement can derive both the natural frequencies and the corresponding mode shapes. In the literature[27][28][29][30], this method has been successfully applied in specific engineering structures such as beams and plates. The modes were uncoupled in these studies because the beams and plates have relatively

simple cross-sections, and the research interest only focused on the vertical direction at frequencies lower than 1600 Hz. In this work, the rail has a more complicated arbitrary cross-section geometry, and our research interest is three-dimensional rail vibrations up to 5 kHz. Considerably more vibration modes (hundreds) need to be dealt with, and they may couple with each other. Coupled modes have dissimilar wavelengths that hinder the ability of sensors to capture them simultaneously. In this chapter, the ODS measurement will be used to distinguish coupled-wave modes in a free rail.

In addition to the multiple modes, dispersion is another feature of the propagative waves in rail that makes the experimental identification of waves more difficult[10][14][22]. For the experimental analysis of the propagation and dispersion of elastic waves, the wavelet transform (WT) has been proven to be an effective tool[31][32][33][16][34][35]. Lanza[36] applied this time-frequency analysis method in railway tracks and obtained group velocity dispersion curves for the vertical, longitudinal, and lateral rail vibration modes at 1-7 kHz. Only qualitative agreement was achieved with Gavric's numerical simulation results[14]. The deviations between the measurement and simulation may have been caused by the different boundary conditions of the rail. In Gavric's simulation, the rail had a free-free boundary, while in Lanza's experiment, the rail was supported by steel plates on wooden sleepers, which introduced additional stiffness and damping to the rail. In addition, the accuracy of the single-acceleration wavelet approach used in Lanza's experiment might have been reduced by the wave reflection at the rail ends. A synchronized multiple-acceleration wavelet (SMAW) approach will be developed in this chapter to improve the experimental accuracy and achieve better agreement with the simulation. The experimental setup will also improve the test boundary condition to better match the free-free boundary of the FE simulation.

This work aims to gain a better understanding of free rail vibrations and provide experimental methods to distinguish different wave modes and measure wave propagation and dispersion characteristics. The chapter is organized as follows. In Section 2.2, a 3D FE model is built to predict the multimodal dispersive waves in a free rail. The modal behavior, wavenumber-frequency dispersion relations, and phase and group velocities of these waves are derived. In Section 2.3, two methods—ODS measurement and SMAW measurement—are introduced to investigate the multimodal dispersive waves. In Section 2.4, the experimental results, including ODSs, wavenumber-frequency dispersion curves, WPSs, and group velocities, are obtained and compared with the simulations. Section 2.5 discusses the advantages and disadvantages of ODS and SMAW measurements and the effectiveness of these two methods in field tracks. The main conclusions are drawn in Section 2.6.

2.2. NUMERICAL SIMULATION OF MULTIMODAL DISPERSIVE WAVES IN FREE RAIL

This section presents a solution method based on FE modeling to predict the multimodal dispersive waves in a free rail. The method includes 1) building a 3D FE model of a free rail using ANSYS; 2) a modal analysis to derive the natural frequencies, modal shapes, and cross-section deformation; and 3) a numerical prediction of dispersion relations by postprocessing the modal results, including phase and group velocities. Figure 2.1 shows

a flowchart of this method.

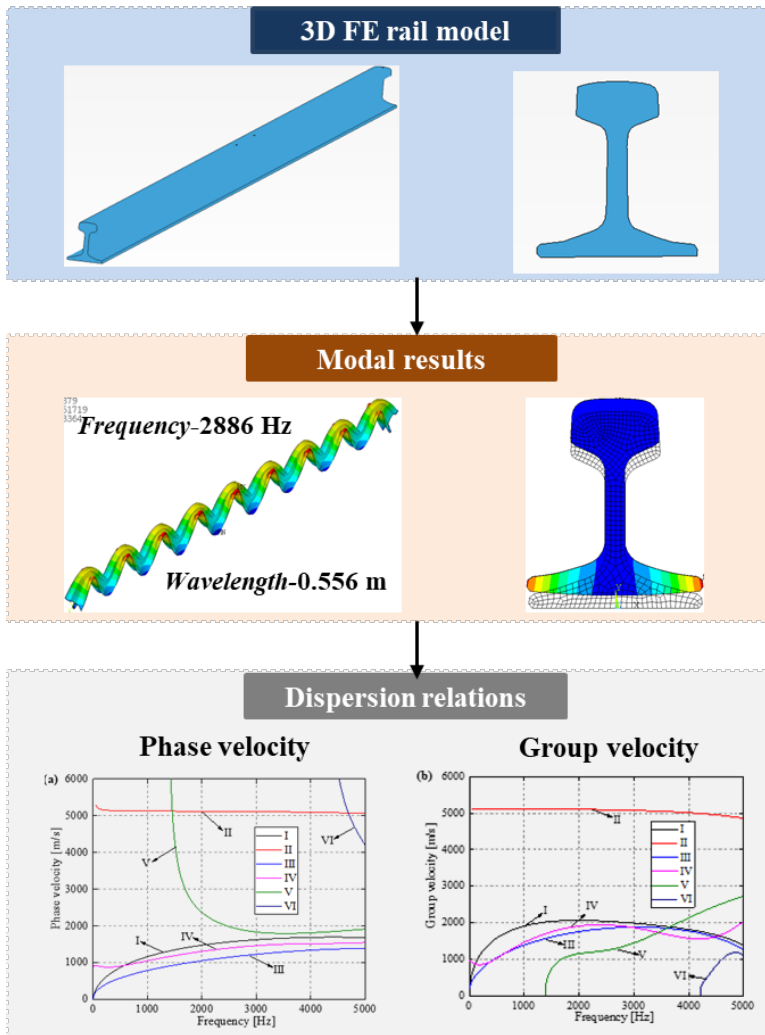


Figure 2.1: Flowchart of the solution method based on FE modeling.

2.2.1. 3D FE MODEL

A 3D FE rail model is built with ANSYS, as shown in Figure 2.2. The rail is modeled with 8-node solid elements based on the measured UIC 54E1 profile used in the experimental setup in Section 2.4. The rail length in the model is 4.97 m. Figure 2.2b shows the mesh of the rail cross-section. The rail profile is discretized with an equal element edge length of 4 mm. The longitudinal element size is 10 mm. The mesh size, model length, and rail profile are crucial parameters for FE prediction, and their details are discussed in Appendix A. The rail material is treated as elastic and isotropic with a Young's modulus of

210 GPa, a Poisson's ratio of 0.3, and a density of 7850 kg/m³. A free boundary condition is applied, and no damping effect is considered. The dynamic behaviors of the rail are studied through modal analysis. The mode extraction method used is Block Lanczos, and the analyzed frequency range is up to 5 kHz.

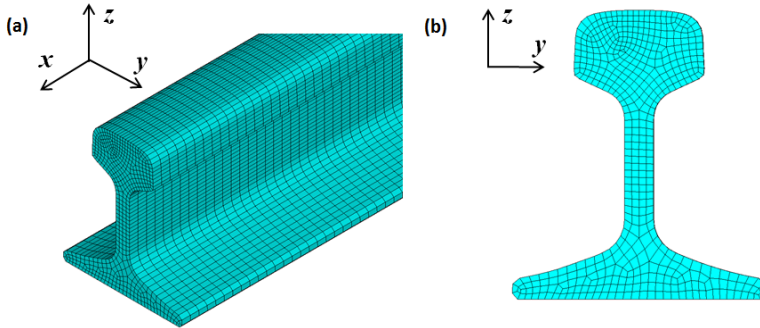


Figure 2.2: 3D FE rail model: (a) overview of rail model; (b) mesh of cross-section.

2.2.2. MODAL RESULTS

Six types of characteristic modes of the rail are extracted in the vertical, longitudinal, and lateral directions up to 5 kHz. The modes in the vertical and longitudinal directions are specifically referred to as vertical bending modes (designated 'I' in Figure 2.3) and longitudinal compression modes (II). The modes in the lateral direction include four types of cross-sectional deformation, regarded as lateral bending modes (III), lateral torsion modes (IV), web 1st bending modes (V), and web 2nd bending modes (VI). Each mode is described in terms of three features: modal frequency, mode shape, and cross-sectional deformation.

For all six types of modes, the modal shapes in the longitudinal direction (x direction) are approximately sinusoidal, and their wavelengths (λ) are derived from the FE simulation. The wavelengths of vertical bending modes (I) and lateral bending modes (II) are approximately $2L/(N+0.5)$, and wavelengths of the other four types of rail modes are approximately $2L/N$, where L is the rail length, and N is an integer.

Figure 2.3 shows the cross-sectional deformation of the six types of rail modes. The color contrast indicates the relative displacements of the elements. Blue is the minimum displacement, and red is the maximum.

For vertical bending modes (I), the rail moves vertically and has no cross-sectional deformation below around 1 kHz, at which point the rail foot begins to flap. At higher frequencies, rail foot flapping becomes increasingly dominant while the displacement of the rail head decreases. For longitudinal compression modes (II), the rail has dominant axial displacement, and the cross-section does not deform in the whole frequency range of 0-5 kHz.

With lateral bending modes (III), the rail undergoes lateral displacement and exhibits no cross-sectional deformation below around 420 Hz, at which point the rail foot starts rotating. As the frequency increases, the rail head displacement decreases, and rail foot

rotation increases, which causes the deformation of the rail web. Above around 4600 Hz, the rail head is almost stationary, and rail foot rotation dominates the rail vibration. For lateral torsion modes (IV), the rail movement can be seen as a rigid cross-section rotation at low frequency. As the frequency increases, the rotation of the rail head decreases and is replaced by horizontal displacement, while the deformation shape of the rail foot remains almost unchanged, which together results in rail web bending.

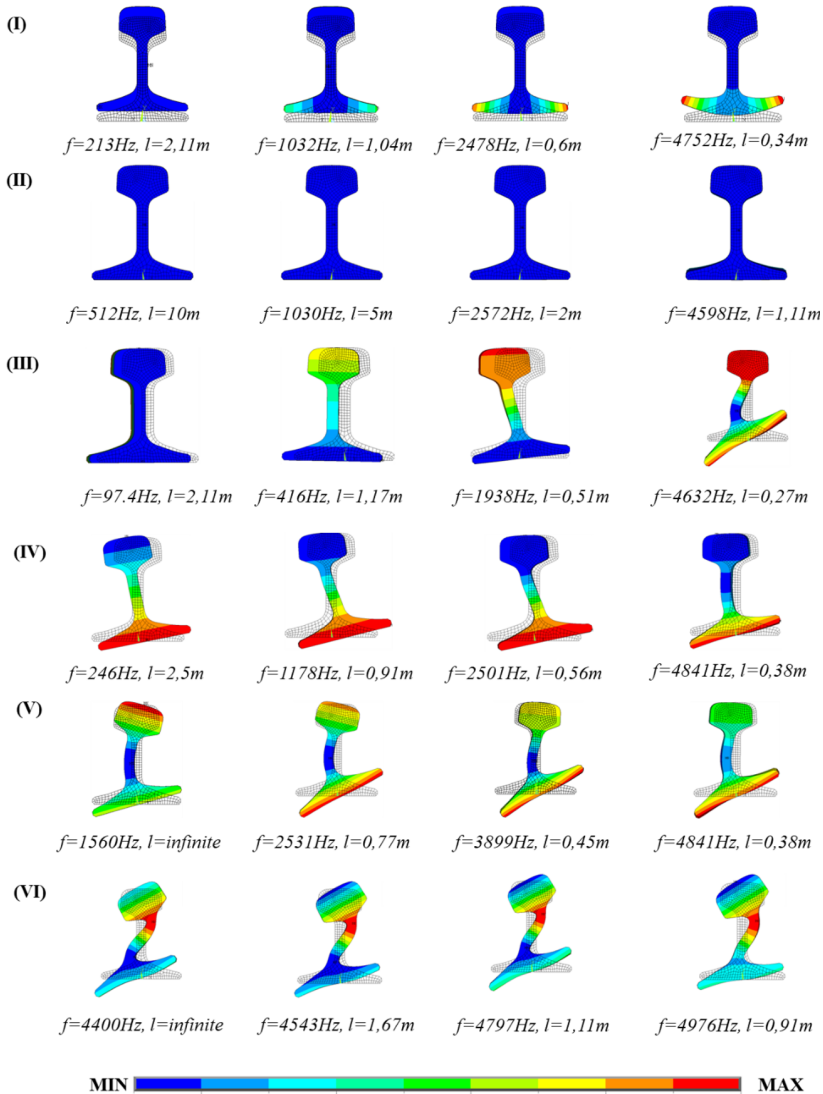


Figure 2.3: Cross-sectional deformation of vertical bending modes (I), longitudinal compression modes (II), lateral bending modes (III), lateral torsion modes (IV), web 1st bending modes (V), and web 2nd bending modes (VI).

Web 1st bending modes (V) start from 1570 Hz. For these modes, the rail head rotates out of phase with the rail foot and causes significant bending of the rail web. The largest deformation of the rail web occurs near its middle part. Web 2nd bending modes (VI) appear first at around 4400 Hz. In contrast to web 1st bending modes, the rail head rotates in phase with the rail foot for these modes, resulting in double bending of the rail web. The largest deformation of the rail web occurs at its two ends, and the middle part is nearly stationary.

2.2.3. DISPERSION RELATIONS

The characteristic modes outlined above (standing waves) are directly equivalent propagative waves of an infinite rail[10]. Each natural frequency and wavelength corresponds to a point on the wavenumber-frequency dispersion curves. The wavenumbers are calculated by $k = 2\pi/\lambda$, where λ is the wavelength, k is the wavenumber.

Figure 2.4 shows the dispersion curves of the six types of waves by connecting the discrete wavenumber-frequency points in a frequency range of 0-5 kHz. These waves are distinguished with different symbols and Roman numerals. Vertical bending waves (I), longitudinal compression waves (II), lateral bending waves (III) and lateral torsion waves (IV) all cut on at 0 Hz. Web 1st and 2nd bending waves (V, VI) propagate from 1570 Hz and 4440 Hz, respectively. Longitudinal compression waves (II) have the largest curve gradients, while web 2nd bending waves (VI) have the smallest gradients. Vertical bending waves (I) and lateral torsion waves (IV) cross at approximately 660 Hz, indicating that these two waves may exhibit mode coupling and swap their modal shapes at this frequency. Similar phenomena occur for longitudinal compression waves (II) and web 1st (V) and 2nd bending waves (VI) at 1640 Hz and 4800 Hz, respectively. When the rail is symmetrical, this mode coupling and veering between different waves are negligible[20]. The results of Figure 2.3 and Figure 2.4 agree with those in [10][11][12][14]. The small differences, such as 'cut-on' frequencies of web 1st and 2nd bending waves are likely to be caused by the different rail profiles (BR flat-bottomed rail in[10] and UIC861-3 in[14]) used for the prediction.

Two kinds of wave velocities, phase, and group velocities, are typically used to describe wave propagation characteristics in two aspects. They are calculated from the wavenumber-frequency relation as follows[37]:

$$v_p = \frac{\omega}{k} = 2\pi \frac{f}{k} \quad (2.1)$$

$$v_g = \frac{d\omega}{dk} = 2\pi \frac{df}{dk} \quad (2.2)$$

where v_p is the phase velocity, v_g is the group velocity, ω is the angular frequency, f is the ordinary frequency and k is the wavenumber. From 2.1 and 2.2, it can be seen that the phase velocity is the secant slope at a point on the wavenumber-frequency curve multiplied by 2π , and the group velocity is the corresponding tangential slope multiplied by 2π .

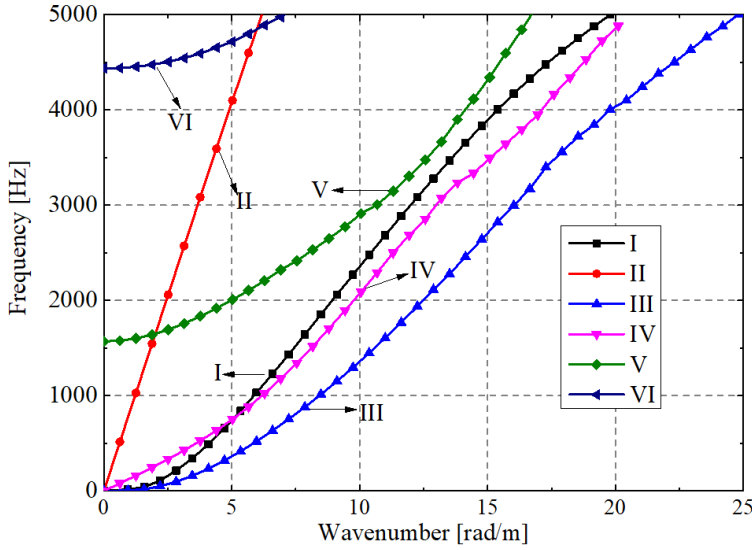


Figure 2.4: Wavenumber-frequency dispersion curves of vertical bending waves (I), longitudinal compression waves (II), lateral bending waves (III), lateral torsion waves (IV), web 1st bending waves (V), and web 2nd bending waves (VI).

Figure 2.5 shows the derived phase and group velocity dispersion curves. Vertical bending waves (I) are dispersive waves since the velocities are frequency-dependent. The phase velocity of this type of wave starts from 0 m/s at the cut-on frequency, then increases gradually to approximately 1670 m/s at 3.6 kHz, and remains almost constant at higher frequencies. The group velocity also starts from 0 m/s at 0 Hz and rises dramatically but at a decreasing rate to approximately 2000 m/s at 1 kHz. At 1–3 kHz, it is approximately frequency-independent, and at higher frequencies, a slight decrease appears.

Longitudinal compression waves (II) can be regarded as nondispersive waves in a frequency range of 0–5 kHz, although a gradually decreasing trend is found for both the phase and group velocity as the frequency increases. The average velocity of approximately 5100 m/s matches well with the propagation velocity of compression waves in solid guides, which is $\sqrt{E/\rho} = 5172$ m/s, where $E = 210$ GPa and $\rho = 7850$ m/s for the rail material.

Lateral bending waves (III) are dispersive waves, with the trends of phase and group velocities similar to those of vertical bending waves (I), but the values are approximately 300 m/s lower. Lateral torsion waves (IV) propagate at approximately 900 m/s at low frequencies. Above 500 Hz, the phase and group velocities of this type of wave follow a trend similar to those of vertical and lateral bending waves (I, III). Above 4000 Hz, there is a gradual increase in group velocity compared to the decrease in vertical and lateral bending waves (I, III).

At the cut-on frequency of web 1st bending waves (V), the wavenumber equals zero ($k = 0$), and therefore, the phase velocity becomes infinite. As the frequency increases to 3 kHz, the phase velocity drops drastically to 1830 m/s. Then, it remains almost constant

at higher frequencies. The group velocity rises significantly to 1000 m/s at 1710 Hz from 0 m/s at the cut-on frequency. At higher frequencies, it increases gradually to 2710 m/s. The phase and group velocities of web 2nd bending waves (VI) follow a trend similar to web 1st bending waves (V). Since the maximum frequency of interest is 5 kHz, only limited portions of these waves are shown in Figure 2.5b.

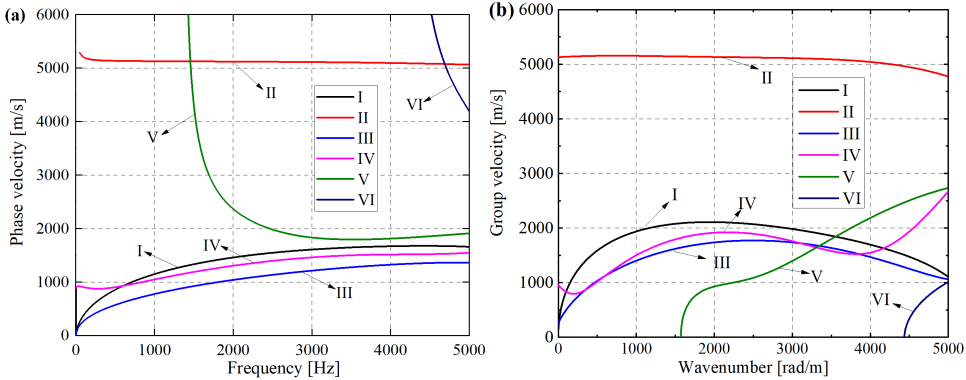


Figure 2.5: Dispersion curves of (a) phase velocity and (b) group velocity.

2.3. METHODS OF EXPERIMENTAL INVESTIGATION

This section describes two experimental methods and compares them with the numerical simulation of the multimodal dispersive waves in a free rail. One method is operating deflection shape (ODS) measurement, which distinguishes between different wave modes. Then, the wavenumber-frequency curves are derived by postprocessing the ODSs and compare with those of the simulated waves. The other method is synchronized multiple-acceleration wavelet (SMAW) measurement, which is used to measure the propagation and dispersion characteristics of the waves. The group velocities in the vertical, longitudinal, and lateral directions are estimated from the WPSs and compared with the FE simulation results.

2.3.1. SENSOR DISTRIBUTION

Lanza[36] applied a single-acceleration wavelet approach to study wave propagation in rails, as shown in Figure 2.6. This approach relied on the reflection signal from the rail ends to estimate the group velocities. Energy loss in the waves might occur during the reflection, leading to weak and less measurable signals, causing the signal-to-noise ratio to be too low, thus creating measurement error. Therefore, the SMAW approach is used in this work to avoid this potential error, as shown in Figure 2.6b. More information about the wave propagation and dispersion along the rail is also expected from the multiple accelerometer measurement.

The ODS measurement also requires the simultaneous measurement of multiple accelerometers with a multichannel acquisition system[38]. The spatially equal accelerometer distribution is typically used for the convenience of data processing. The number of accelerometers determines the largest measurable wavenumbers of the modes. More

accelerometers mean a larger wavenumber and higher wave wavenumber resolution but also a much higher cost. As a compromise, nine equally distributed accelerometers are used in this work, as shown in Figure 2.6c.

The sensor distribution in Figure 2.6c, together with a synchronized signal acquisition system, meets the demands for both the ODS measurement and the SMAW measurement and is applied in the following experimental setup.

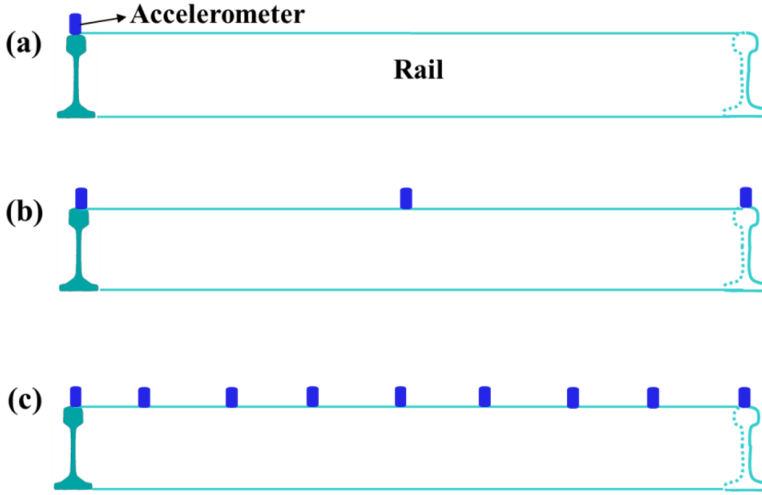


Figure 2.6: Sensor distribution. (a) Single-acceleration wavelet for group velocity estimation in[36]; (b) SMAW approach for group velocity estimation in this chapter; (c) sensor distribution for ODS measurement used in the real setup.

2.3.2. EXPERIMENTAL SETUP

Figure 2.7 shows a schematic drawing of the experimental setup. A 4.97 m long rail was suspended in the air by two nylon ropes. Because of the small stiffness and damping levels of the ropes, the rail can be considered to be in ‘free vibration’. Nine 3D accelerometers (PCB 356B21, denoted as 1-9 in Figure 2.7) were glued onto the rail head with a spacing of approximately 0.62 m. The smallest wavelength of the measurable modes by this sensor distribution is twice the sensor spacing of 1.24 m, corresponding to the largest wavenumber of approximately 5.06 rad/m. The responses of the nine accelerometers are denoted as follows:

$$a_i(t) = [a_i^x(t), a_i^y(t), a_i^z(t)]^T, \quad i = 1, 2, \dots, 9 \quad (2.3)$$

where $a_i(t)$ is the response of the i^{th} accelerometer, which includes three components $a_i^x(t)$, $a_i^y(t)$, and $a_i^z(t)$ in the longitudinal vertical and lateral directions, respectively. The experimental setup is for both the ODS measurement and SMAW measurement. For the ODS measurement, accelerometers 1-9 were used. For the SMAW measurement, accelerometers 1, 5, and 9 were used.

A small impact hammer (PCB 086C03) with a steel tip was used to excite the rail in the

high-frequency range. The excitation positions were as close to 3D accelerometer 1 as possible for the longitudinal, lateral, and vertical directions, as indicated by the red arrows in Figure 2.7, and recorded as $F_1^x(t)$, $F_1^y(t)$, and $F_1^z(t)$. The choice of the excitation positions at a rail free end is to ensure that excitation forces are not on a nodal line of any modal shape. A synchronized signal acquisition system recorded the excitation and response signals of 5 impacts in each direction with a sampling frequency of 51200 Hz. The reliable range of the impact forces and the repeatability of the signals were checked, and they were valid within 5 kHz.

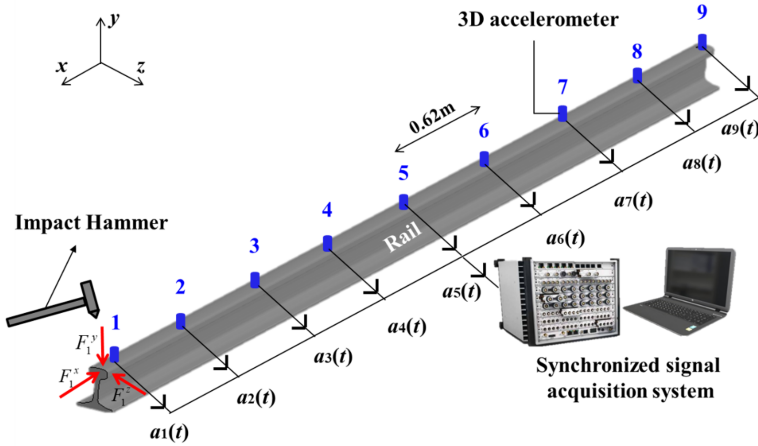


Figure 2.7: Schematic drawing of the experimental setup.

2.3.3. EXPERIMENTAL METHODS

ODS MEASUREMENT METHOD

The ODSs are measured from a set of FRFs. The FRFs in the longitudinal direction (x) can be calculated as follows[39]:

$$H_i^x(f) = \frac{S_{a_i^x F_1^x}(f)}{S_{F_1^x F_1^x}(f)(2\pi f)^2} \quad (2.4)$$

where $H_i^x(f)$ is longitudinal FRF of accelerometer i ; $S_{a_i^x F_1^x}(f)$ is the cross-spectrum between the acceleration a_i^x and force F_1^x ; and $S_{F_1^x F_1^x}$ is the auto-spectrum of the force F_1^x . The FRFs are complex-valued functions. The ODSs of rail displacement responses are taken as the spatial distribution of the imaginary parts of the FRFs, as follows[38].

$$\text{ODS}_x(f) = [\text{Im}(H_1^x(f)), \text{Im}(H_2^x(f)), \dots, \text{Im}(H_9^x(f))] \quad (2.5)$$

where $\text{ODS}_x(f)$ is the longitudinal ODS at frequency f . When the frequency is one of the rail natural frequencies, the ODS will closely approximate the mode shape[38]. The lateral and vertical FRFs and ODSs can be obtained with the same method.

Figure 2.8 shows one example to explain the procedure of the ODS measurement for

modal identification. First, a set of vertical FRFs at the nine positions are obtained with the hammer test, as shown in Figure 2.8a and 2.8b. Second, the resonance peaks at 492 Hz (indicated by red dashed circles in Figure 2.8b) are detected from the magnitude of the FRFs, which may correspond to one or more natural rail modes. Third, the imaginary parts of the FRFs at this peak frequency at the nine positions are derived, as depicted in Figure 2.8c. Last, the ODS is taken as their spatial distribution along the rail, as shown in Figure 2.8d. By comparing the measured peak frequency and ODS with the simulated natural frequency and mode shape (see Figure 2.8e), one vertical vending mode at 491 Hz in the FE simulation is identified. Other rail modes can be identified with the same procedures.

After deriving the peak frequencies and ODSs from FRFs, the wavenumber-frequency curves can be obtained and compared with the simulated curves.

SMAW MEASUREMENT METHOD

Wave propagation signals along the rail under an impulsive hammer excitation are non-stationary and contain many frequency components. The continuous wavelet transform (CWT) is applied to address this kind of signal. In the CWT, the convolutions of the analyzed signal are calculated with a group of scaled and shifted wavelet functions. The wavelet coefficients $W_n(s)$ of the analyzed signal x_n can be represented as follows[40]:

$$W_n(s) = \sum_{n'=0}^{N-1} x_{n'} \psi^* \left[\frac{(n' - n) \delta_t}{s} \right] \quad (2.6)$$

where ψ is the mother wavelet, s is the wavelet scale, N is the number of points in the time series, $n' = 0, \dots, N-1$, δ_t is the time step, n is the continuous variable for the translation, s is the wavelet scale, $*$ presents a complex conjugate and $\psi^* \left[\frac{(n' - n) \delta_t}{s} \right]$ is a family of wavelets deduced from the mother wavelet by various translation and scaling steps. Here, the Morlet function is employed as the mother wavelet[41]. The wavelet power spectrum (WPS) is calculated by $|W_n^2(s)|$. The SMAW measurement refers to the measured WPSs of synchronized accelerations at positions 1, 5, and 9.

An algorithm to estimate group velocity from the WPSs is developed, as shown in Figure 2.9a. First, WPSs of acceleration signals at the two rail ends are calculated. Then, one frequency f_j (i.e., 2500 Hz) is chosen in the WPSs, as indicated by the white solid lines in Figure 2.9b. The first peaks at time t_1 and time t_2 are detected from the WPSs at these two positions (see the red triangles), indicating the first arrival of the wave. There is a time difference dt between these two peaks, during which time the waves propagate through one rail length (L). Therefore, the group velocity at f_j is calculated as follows:

$$v_g = \frac{L}{(t_2 - t_1)} \quad (2.7)$$

Afterward, we move to the next frequency f_{j+1} and repeat the procedure above. At some frequencies, the vibration energy of the waves is small, and the obvious peaks, as in Figure 2.9b, may not be accurately detected from the WPSs. For these cases, the group velocity at these frequencies cannot be estimated accurately or measured at all.

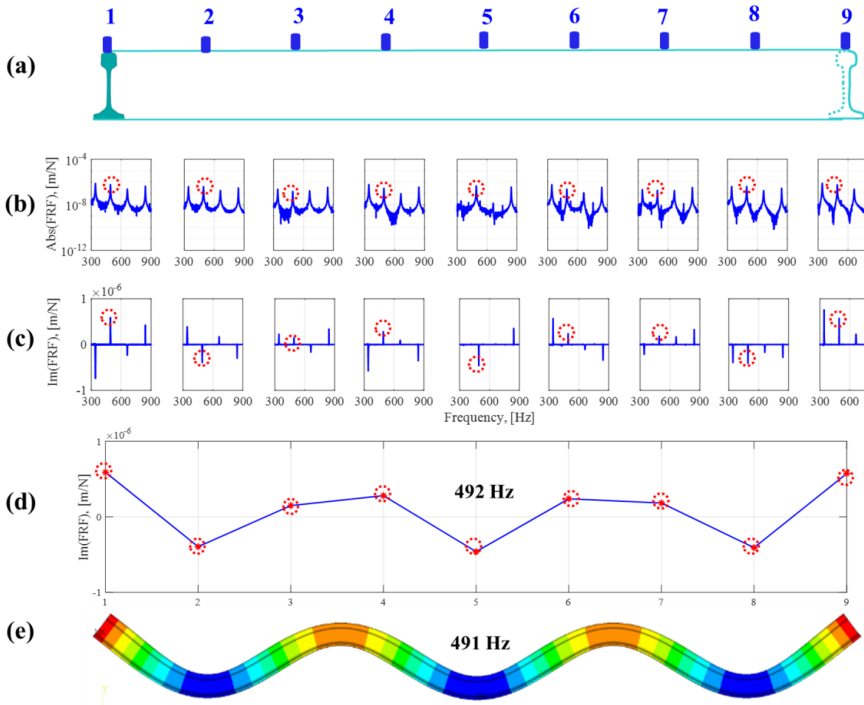


Figure 2.8: ODS measurement at 492 Hz for modal identification. (a) Sensor distribution of hammer test; (b) magnitude of FRFs at nine positions; (c) imaginary parts of FRFs at nine positions; (d) measured ODS at 492 Hz; (e) simulated mode shapes at 491 Hz. The red circles in (b) and (c) indicate the detected peaks at 492 Hz.

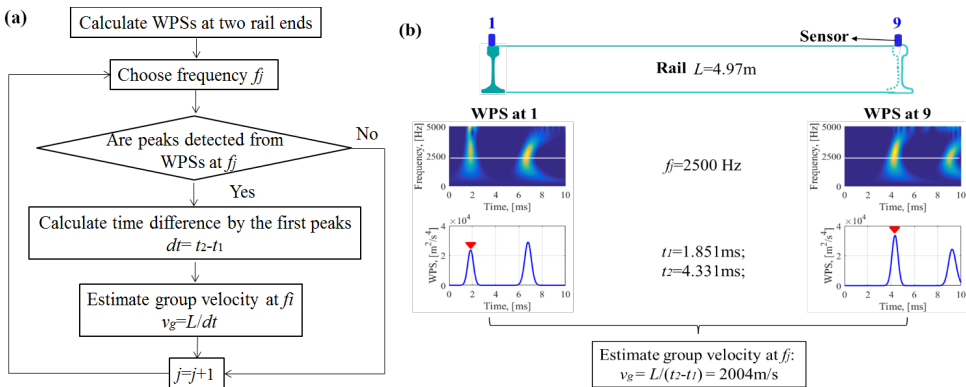


Figure 2.9: The algorithm of group velocity estimation from WPSs: (a) the flowchart of the algorithm; (b) one example of the algorithm. The white line in (b) shows WPSs at 2500 Hz. The red triangles indicate the detected first peaks from WPSs at 2500 Hz.

2.4. EXPERIMENTAL RESULTS

2.4.1. RESULTS OF ODS MEASUREMENT

Figure 2.10 shows the vertical, longitudinal, and lateral FRFs of the rail at accelerometer 1. There are many peaks of the FRF in each direction, which can be classified into ‘major peaks’ and ‘minor peaks’. Major peaks (★) of the longitudinal FRF (Figure 2.10b) refer to longitudinal compression modes, while minor peaks (◆) refer to other modes, e.g., vertical bending modes (see black dashed lines in Figure 2.10a and 2.10b for examples). The appearance of minor peaks comes from the mode coupling of the different directions. Major and minor peaks can be distinguished by peak frequencies and the corresponding ODSs. Figure 2.10c shows the coupling of four groups of major peaks, representing lateral bending, lateral torsion, web 1st bending and web 2nd bending modes. Specifically, two groups of major peaks at 0–1560 Hz correspond to lateral bending and torsion modes, and at approximately 1560 Hz and 4400 Hz, with the supplement of web 1st and 2nd bending modes (indicated by two black arrows, respectively).

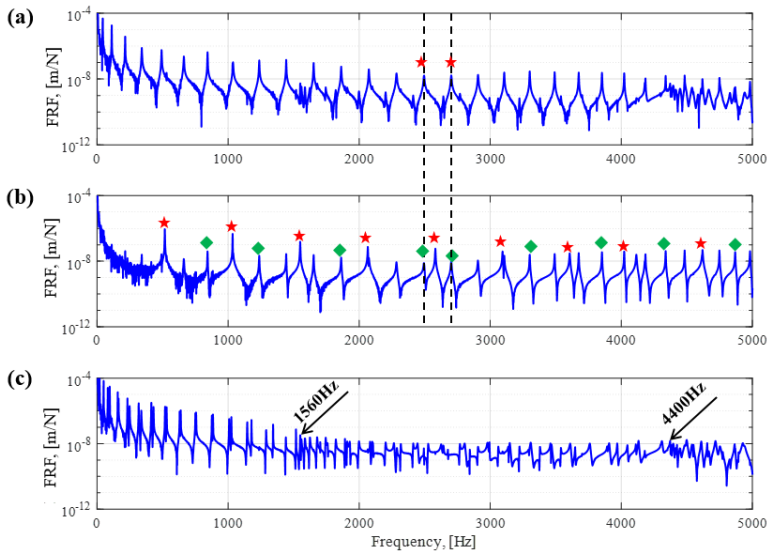


Figure 2.10: (a) Vertical, (b) longitudinal, (c) lateral FRFs of rail at accelerometer 1. (★) indicates major peaks; (◆) indicates minor peaks.

The results of the ODS measurement are derived and shown in Figure 2.11. The ODSs identify all six types of rail modes predicted from the FE model. Three examples are chosen for each type and compared to the modal results of the numerical simulation. The simulated natural frequencies and mode shapes agree well with the measured peak frequencies and the corresponding ODSs. It should be noted that the smallest wavelength that the ODSs can measure is 1.24 m, with an accelerometer spacing of 0.62 m. The modes with wavelengths smaller than 1.24 m could be measured by reducing the accelerometer spacing, not included in this chapter.

Based on the results of the ODS measurement, the dispersion curves are measured by connecting the discrete wavenumber-frequency points (see Figure 2.12). Among them, points (o) of wavenumbers below 5.06 rad/m ($2\pi/1.24$) are derived directly from the ODSs. For points (Δ) of higher wavenumbers, their natural frequencies are derived from the major peak frequencies of FRFs, and the corresponding wavenumbers are predicted with $k = N\pi/L$. The latter may require further comparison from measurements with a more dense accelerometer arrangement. Comparing the measured dispersion curves with the simulation, very good agreement was found in the frequency range of 0-5 kHz, except for a slight overestimation (1.3%) for the web 2nd bending wave (VI) of the FE model. The good agreement also verifies that the cross-section size of 4 mm and the longitudinal element size of 10 mm are accurate enough for studying rail dynamic behavior within 5 kHz, and the measured rail height can achieve a better solution than the nominal height, with the largest difference being 3.8%.

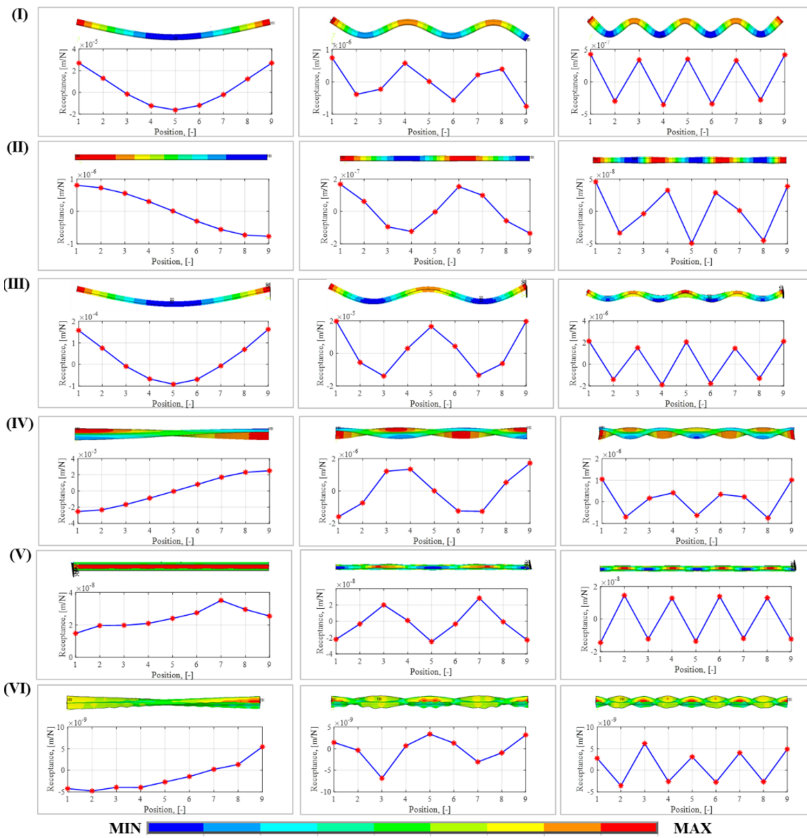


Figure 2.11: Comparison between the mode shapes from FE simulation ('Worn 1' in A. 3) and ODSs from measurement (I) vertical bending modes at 42/43 (simulation/measurement), 345/341, 845/843 Hz, (II) longitudinal compression modes at 515/517, 1545/1550, 3084/3095 Hz, (III) lateral bending modes at 18/18, 97/97, 416/414 Hz, (IV) lateral torsion modes at 81/82, 246/248, 527/530 Hz, (V) web 1st bending modes at 1570/1555, 1693/1681, 2008/2000 Hz, (VI) web 2nd bending modes at 4440/4383, 4505/4448, 4718/4666 Hz.

2.4.2. RESULTS OF SMAW MEASUREMENT

The WPSs for vertical signals at accelerometers 1, 5, and 9 are shown in Figure 2.13a, 2.13b, and 2.13c, respectively. The color contrast indicates the amount of energy concentrated in a frequency range (the vertical axis) at a particular time (the horizontal axis). The shapes of the wave envelope are captured from the WPSs. The wave envelope propagation along the rail can be seen: at time t_{1z} , the impulsive hammer is excited on the rail close to accelerometer 1; then, the energy envelope propagates to accelerometer 5 at time t_{2z} and to accelerometer 9 at time t_{3z} ; after that, the waves reflect at accelerometer 9 and return to accelerometer 5 at time t_{4z} and to accelerometer 1 at t_{5z} . From t_{1z} to t_{5z} , the wave envelope finishes a cycle, and the propagation distance is twice the rail length ($2L$).

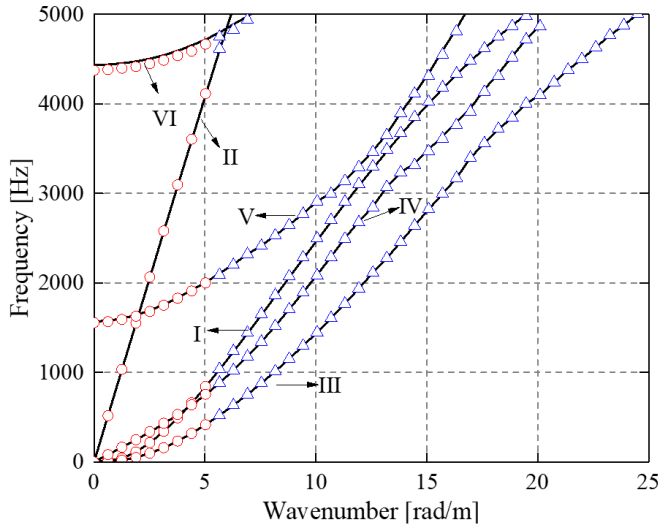


Figure 2.12: Wavenumber-frequency dispersion curves: (—) FE simulation ('Worn 1' in A. 3); (◦) wavenumber-frequency points derived from ODSs; (△) the points with measured natural frequencies and predicted wavenumbers.

During wave propagation, the shapes of the wave envelope change due to the dispersive characteristics of the rail—the dependence of velocity on frequency. With increasing time, the wave gradually takes a 'C' shape, qualitatively indicating that the vertical wave velocity (group velocity) in the middle frequency range is higher than those in the lower and higher frequency ranges, which agrees with the calculated results in Figure 2.5b. The shape at time t_{1z} at accelerometer 1 is relatively irregular because of the near-field waves. Wave energy densities at accelerometers 1 and 9 are similar and significantly larger than those at accelerometer 5, which indicates that the vibrations at the two rail ends are stronger because of the free boundaries. In addition, the wave energy at the three positions is attenuated during propagation, as observed from the increasingly dark color of the wave envelope.

The WPSs for the longitudinal and lateral signals are shown in Figure 2.14 and Figure 2.15. Waves in these two directions have propagation traces similar to the vertical ones,

but it can be seen that the longitudinal group velocity is larger than those of the vertical and lateral waves. From the numerical results in Section 2.4, it can be predicted that the shapes of the longitudinal wave envelopes should not change with propagation since the longitudinal group velocity is frequency-independent within 5 kHz. However, moderate deformation is observed in Figure 2.14, which may be caused by signal coupling from other directions, shown in Figure 2.11b. The lateral wave envelopes deform with time and have a shape similar to the vertical ones. The shapes of the lateral waves at high frequencies are quite irregular, likely caused by the superposition of the four types of lateral waves.

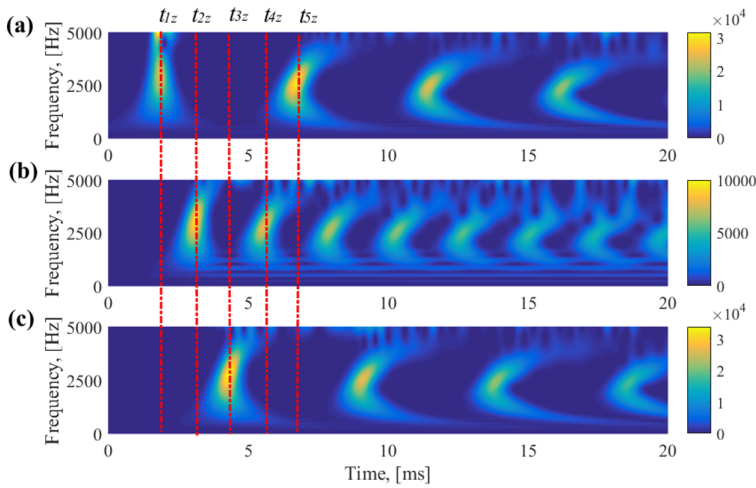


Figure 2.13: WPSs of vertical signals at (a) accelerometer 1, (b) accelerometer 5, and (c) accelerometer 9. The red dashed lines indicate the selected time.

The group velocities for the vertical, longitudinal, and lateral waves are presented in Figure 2.16. The measured vertical group velocity curve agrees well with the simulation in the frequency range of 400-3500 Hz. From 3500 to 4200 Hz, the numerical results underestimate the velocity slightly. Below 400 Hz and above 4200 Hz, the vertical vibration energy is too low (see Figure 2.13 to identify the peaks from the WPSs accurately). Good agreement of the measured and simulated longitudinal group velocity is achieved in the frequency range of 900 Hz-5 kHz. The velocity below 900 Hz cannot be obtained precisely with lower vibration energy (see Figure 2.14a). The measured lateral group velocity coincides well with the simulated lateral bending waves (III) in the frequency range of 200-3800 Hz. This means that the lateral bending waves dominate the rail head vibration in this frequency range. At frequencies above 3800 Hz, the measured group velocity curve does not follow any single type of wave but stays between web 1st bending waves (V) and the other three types. Likely, the four types of waves contribute together to the rail head vibration in this frequency range. In summary, good agreement between the simulated and measured group velocities has been achieved, indicating that the 3D FE model can accurately predict the propagation and dispersion of waves in a free rail.

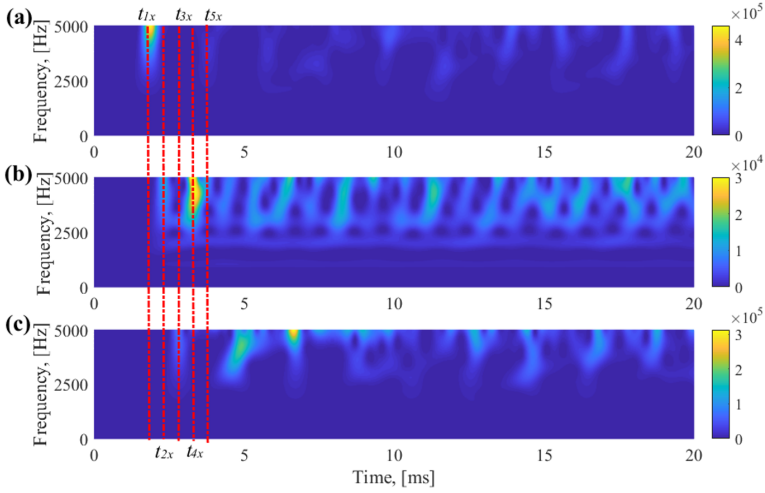


Figure 2.14: WPSs of longitudinal signals at (a) accelerometer 1, (b) accelerometer 5 and (c) accelerometer 9. The red dashed lines indicate the selected time.

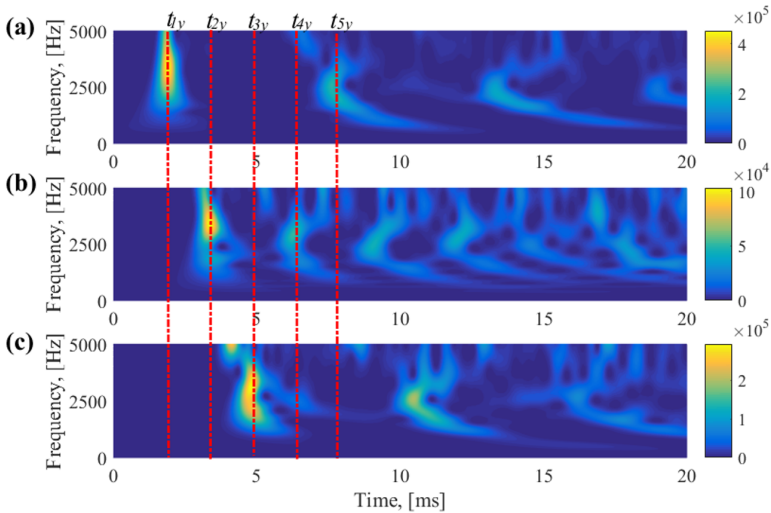


Figure 2.15: WPSs of lateral signals at (a) accelerometer 1, (b) accelerometer 5, and (c) accelerometer 9. The red dashed lines indicate the selected time.

Compared to the experimental results by the single-acceleration wavelet approach in [36], the proposed SMAW approach better presents the wave propagation and dispersion along the free rail with multiple synchronized WPSs. The valid frequencies of group velocity estimation are also extended to a broader frequency range owing to the higher signal-to-noise ratio.

2.5. DISCUSSION

This section discusses the advantages and disadvantages of ODS measurements and SMAW measurements and the effectiveness of these two methods in field tracks based on preliminary experimental results.

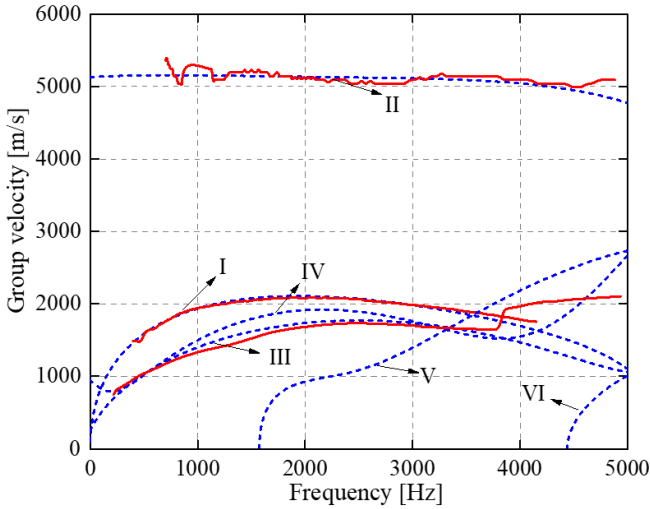


Figure 2.16: Comparison of the group velocity dispersion curve between SMAW measurement and FE simulation: (—) measurement; (---) simulation.

2.5.1. DISCUSSION OF ODS AND SMAW MEASUREMENT

The experimental results of the ODS and SMAW measurements are both in good agreement with the simulation results, which indicate these two approaches are capable of distinguishing wave modes and measuring wave propagation and dispersion characteristics. The ODS and SMAW measurement methods have their respective advantages and disadvantages. ODS measurement can identify all types of rail modes and distinguish between them easily from their wavelengths. SMAW measurements can only identify waves that have prominent vibration energy. Therefore, arrangements of the sensors at different locations of the rail cross-section (e.g., the middle part of rail web) will be helpful to identify different waves (e.g., web 1st bending waves). The advantage of SMAW measurement is its capability to obtain continuous dispersion curves, while only the discrete frequencies can be measured by ODS measurement. In addition, SMAW measurements are easier to implement since fewer 3D accelerometers are required. The sensor distribution in ODS measurement is relatively more complex, and the expected wavenumber resolution determines the number of necessary accelerometers.

2.5.2. THE EFFECTIVENESS OF ODS MEASUREMENT AND SMAW MEASUREMENT IN FIELD TRACK

The experimental and simulation results above have indicated that ODS measurement and SMAW measurement can identify the coupled vibration modes and deriving the

wave dispersion characteristics of a free rail. This section applies these two experimental methods in field railway tracks to evaluate their effectiveness on rails with real boundary conditions.

The experimental setup is shown in Figure 2.17. The track without visible defect is in Railway Testing center Faurei, Romania. The UIC60 E1 rail was constrained by Vossloh W14 fastenings on prestressed monoblock sleepers every 0.6 m. No joints, welds, and crossings are nearby. The track can thus be considered as effectively infinite. Eleven 3D accelerometers (PCB 356B21, denoted as 1-11 in Figure 2.17) were used to measure the rail vibrations under the impact of the hammer. Accelerometers 1-7 were glued onto the rail head on the field side. Among them, accelerometers 1 and 4 were above the sleeper (called on-support below); accelerometers 2 and 6 were at the mid-span of the rail; and accelerometers 3, 5 and 7 were at the quarterspan. Accelerometers 8 and 10 were glued onto the rail web, and accelerometers 9 and 11 were glued onto the rail foot.

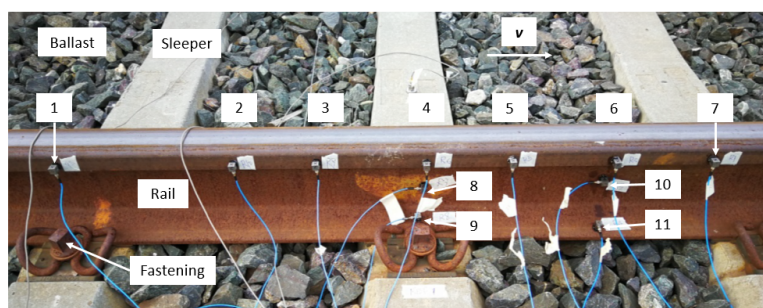


Figure 2.17: Experimental setup of ODS and SMAW measurements in the field track.

Figure 2.18 shows the measured vertical FRFs at mid-span (Position 2) and on-support (Position 4). The FRFs in front of receptance are calculated by the measured accelerations and hammer forces. From the FRF, the track appears to have quite stiff railpads [19]. A series of peaks and dips were observed in the FRFs, which correspond to the track resonance or anti-resonance modes [6][24][26]. Among them, one peak at 1240 Hz (as indicated by the dashed line) may correspond to rail vertical pinned-pinned resonance [6][26], which is the vertical banding mode with a wavelength of twice the sleeper space; see the mode shape in Figure 2.19a. The ODS at 1240 Hz from accelerometers 1-7 was derived and fitted by a sine curve to identify the rail modes corresponding to this peak, as shown in Figure 2.19b. The shape of the measured ODS agrees well with the mode shapes of the pinned-pinned resonance, indicating that the peak at 1240 Hz corresponds to the pinned-pinned resonance. From this example, ODS measurement is a possible method to identify rail vibration modes in field tracks. It is worth noting that the rail in field tracks has mostly propagating waves instead of the standing waves. Due to the track damping, the wavenumbers of the propagating waves have both real and imaginary parts. The identification of these wave modes requires considering both their real and imaginary parts from ODS measurement. These potentially make it more challenging to identify the waves by ODS measurement in the field track.

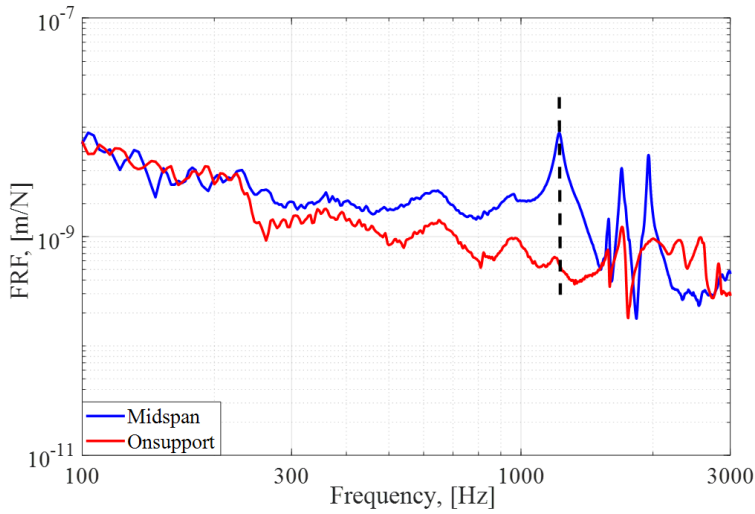


Figure 2.18: Measured vertical FRFs at mid-span and on-support. The black dashed line indicates the frequency at 1240 Hz.

The WPSs for vertical signals at accelerometers 1, 4, and 7 are shown in Figure 2.20a, 2.20b, and 2.20c, respectively. The excitation position of the hammer was as close as possible to accelerometer 1. Figure 2.20 shows that the wave envelope propagated from accelerometer 1 to accelerometer 7, and its shape changed during this process due to wave dispersion. Compared to the results of the free rail in Figure 2.13, wave reflection was not observed in the field track, which should be caused by track damping that significantly attenuates the vibrational waves. This result also shows the advantage of the SMAW approach over the single-acceleration wavelet approach, which does not depend on the reflection signal from the rail ends to measure the group velocities. In addition, the wave envelope in the field track concentrates at a higher frequency range above 2500 Hz, as indicated by the white dashed rectangle in Figure 2.20, while that of the free rail concentrates at 200 Hz-5 kHz. This may indicate that the support stiffness of the rail in the field track significantly suppresses rail vibrations at a lower frequency than 2500 Hz and leads to a higher decay rate. Using the 3D FE track model developed in [19], numerical simulation results indicated that the velocity signal is more sensitive to the rail vibration at lower frequencies than the acceleration signal. If the rail vibration at lower frequencies is of significant interest, the SMAW measurement of velocity can be better than that of acceleration.

In summary, this section presents preliminary results of ODS measurements at vertical pinned-pinned resonance peaks and SMAW measurements of vertical bending waves in field tracks. From these results, ODS measurements can be used to identify vibration modes and SWAM measurements can be applied for the wave propagation and dispersion analysis of the rail in field tracks. More experimental evidence may be needed to support the conclusions, which will be provided in future work.

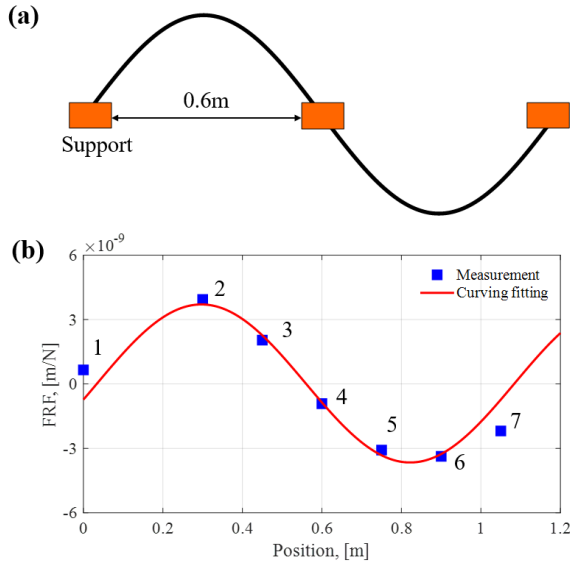


Figure 2.19: Mode shape and ODS of pinned-pinned resonance. (a) Mode shape of pinned-pinned resonance; (b) (■) Measured ODS at 1240 Hz; (—) sinusoidal curving fitting of ODS.

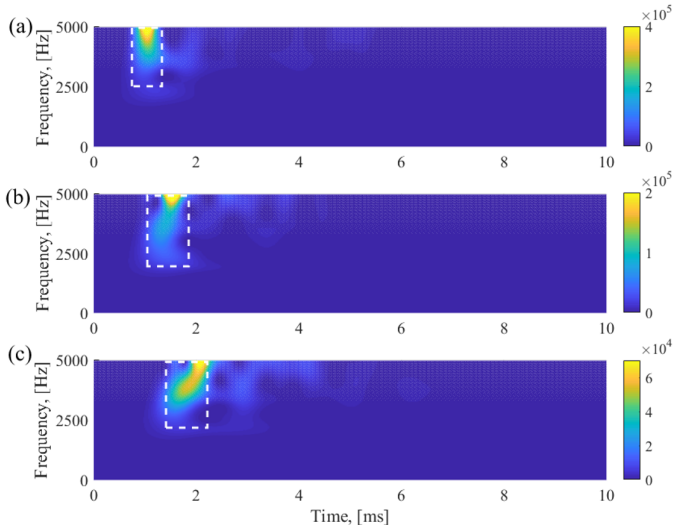


Figure 2.20: WPSs of vertical signals at (a) accelerometer 1, (b) accelerometer 4, and (c) accelerometer 7.

2.6. CONCLUSIONS AND FUTURE WORK

This chapter presents a solution method based on FE modeling to predict the multi-modal dispersive waves in a free rail at a frequency range of 0-5 kHz. Six types of waves are extracted in the vertical, longitudinal, and lateral directions. The phase and group

velocities of these waves are derived and discussed in detail and provide useful information to understand wave propagation and dispersion along the rail. Their modal behavior and wavenumber-frequency dispersion relations are also obtained and are found to be similar to the simulation results in the literature [10][14].

The ODS measurement is conducted to distinguish between different types of wave modes. Experimental results indicate that the ODS identifies all six types of wave modes. Good agreement is achieved between the simulated mode shapes and the measured ODSs. The wavenumber-frequency dispersion relations are also derived by postprocessing the ODS results and have the largest deviation of only 3.8% compared with the simulated ones.

An SMAW approach is developed and applied to study the dispersive waves in the free rail. The propagation and dispersion of the vertical, longitudinal and lateral waves are measured from the WPSs. An algorithm is also developed to estimate the group velocities from the WPSs. Good quantitative agreement is achieved between the simulated and measured results of the vertical bending waves, longitudinal compression waves and lateral bending waves, indicating that the 3D FE model can accurately predict the propagation and dispersion of waves in a free rail.

In summary, this work contributes to a better understanding of free rail vibrations and illustrates the effectiveness of the ODS measurement for rail modal identification and SMAW measurement for wave dispersion analysis. More accelerometers could be mounted in the longitudinal direction for the ODS measurement to obtain higher spatial resolution. More accelerometers could also be used on each cross-section to capture the cross-section deformation of the wave modes.

REFERENCES

- [1] P. Zhang, S. Li, A. Núñez, and Z. Li, *Multimodal dispersive waves in a free rail: Numerical modeling and experimental investigation*, Mechanical Systems and Signal Processing **150**, 107305 (2021).
- [2] D. Thompson, *Railway noise and vibration: mechanisms, modelling and means of control* (Elsevier, 2008).
- [3] K. Hempelmann and K. Knothe, *An extended linear model for the prediction of short pitch corrugation*, Wear **191**, 161 (1996).
- [4] H. Ilias, *The influence of railpad stiffness on wheelset/track interaction and corrugation growth*, Journal of Sound and Vibration **227**, 935 (1999).
- [5] S. Li, Z. Li, A. Núñez, and R. Dollevoet, *New insights into the short pitch corrugation enigma based on 3d-fe coupled dynamic vehicle-track modeling of frictional rolling contact*, Applied Sciences **7**, 807 (2017).
- [6] S. Grassie, R. Gregory, D. Harrison, and K. Johnson, *The dynamic response of railway track to high frequency vertical excitation*, Journal of Mechanical Engineering Science **24**, 77 (1982).

- [7] P. Koziol, *Experimental validation of wavelet based solution for dynamic response of railway track subjected to a moving train*, Mechanical Systems and Signal Processing **79**, 174 (2016).
- [8] L. Xu and W. Zhai, *A three-dimensional model for train-track-bridge dynamic interactions with hypothesis of wheel-rail rigid contact*, Mechanical Systems and Signal Processing **132**, 471 (2019).
- [9] W. Scholl, *Schwingungsuntersuchungen an eisenbahnschienen*, Acta Acustica united with Acustica **52**, 10 (1982).
- [10] D. Thompson, *Wheel-rail noise generation, part iii: rail vibration*, Journal of sound and vibration **161**, 421 (1993).
- [11] T. Wu and D. Thompson, *A double timoshenko beam model for vertical vibration analysis of railway track at high frequencies*, Journal of Sound and Vibration **224**, 329 (1999).
- [12] K. Knothe, Z. Strzyzakowski, and K. Willner, *Rail vibrations in the high frequency range*, Journal of Sound and Vibration **169**, 111 (1994).
- [13] L. Xu, X. Chen, X. Li, and X. He, *Development of a railway wagon-track interaction model: case studies on excited tracks*, Mechanical Systems and Signal Processing **100**, 877 (2018).
- [14] L. Gavrić, *Computation of propagative waves in free rail using a finite element technique*, Journal of Sound and Vibration **185**, 531 (1995).
- [15] R. Cettour-Janet, A. Barbarulo, F. Letourneaux, and G. Puel, *An arnoldi reduction strategy applied to the semi-analytical finite element method to model railway track vibrations*, Mechanical Systems and Signal Processing **116**, 997 (2019).
- [16] M. Sale, P. Rizzo, and A. Marzani, *Semi-analytical formulation for the guided waves-based reconstruction of elastic moduli*, Mechanical Systems and Signal Processing **25**, 2241 (2011).
- [17] I. I. Setshedi, P. W. Loveday, C. S. Long, and D. N. Wilke, *Estimation of rail properties using semi-analytical finite element models and guided wave ultrasound measurements*, Ultrasonics **96**, 240 (2019).
- [18] J. Otero, N. Galarza, B. Rubio, and E. Moreno, *Semi-analytical finite elements methods for dispersion curves using higher order elements for long range ultrasonic testing*, in *2009 IEEE International Ultrasonics Symposium* (IEEE, 2009) pp. 1966–1969.
- [19] M. Oregui, Z. Li, and R. Dollevoet, *An investigation into the vertical dynamics of tracks with monoblock sleepers with a 3d finite-element model*, Proceedings of the Institution of Mechanical Engineers, Part F: Journal of Rail and Rapid Transit **230**, 891 (2016).

- [20] J. Ryue, D. Thompson, P. White, and D. Thompson, *Investigations of propagating wave types in railway tracks at high frequencies*, Journal of Sound and Vibration **315**, 157 (2008).
- [21] D. Thompson, C. Jones, T. Wu, and A. De France, *The influence of the non-linear stiffness behaviour of rail pads on the track component of rolling noise*, Proceedings of the Institution of Mechanical Engineers, Part F: Journal of rail and rapid transit **213**, 233 (1999).
- [22] T. Hayashi, W.-J. Song, and J. L. Rose, *Guided wave dispersion curves for a bar with an arbitrary cross-section, a rod and rail example*, Ultrasonics **41**, 175 (2003).
- [23] P. W. Loveday, C. S. Long, and D. A. Ramatlo, *Mode repulsion of ultrasonic guided waves in rails*, Ultrasonics **84**, 341 (2018).
- [24] R. Lin and T. Ng, *Frequency response functions and modal analysis of general non-viscously damped dynamic systems with and without repeated modes*, Mechanical Systems and Signal Processing **120**, 744 (2019).
- [25] D. Thompson, *Experimental analysis of wave propagation in railway tracks*, Journal of sound and vibration **203**, 867 (1997).
- [26] M. Oregui, Z. Li, and R. Dollevoet, *Identification of characteristic frequencies of damaged railway tracks using field hammer test measurements*, Mechanical Systems and Signal Processing **54**, 224 (2015).
- [27] R. Sampaio, N. Maia, R. Almeida, and A. Urgueira, *A simple damage detection indicator using operational deflection shapes*, Mechanical Systems and Signal Processing **72**, 629 (2016).
- [28] S. Khoo, Z. Ismail, K. Kong, Z. Ong, S. Noroozi, W. Chong, and A. Rahman, *Impact force identification with pseudo-inverse method on a lightweight structure for under-determined, even-determined and over-determined cases*, International Journal of Impact Engineering **63**, 52 (2014).
- [29] C. Devriendt, G. Steenackers, G. De Sitter, and P. Guillaume, *From operating deflection shapes towards mode shapes using transmissibility measurements*, Mechanical Systems and Signal Processing **24**, 665 (2010).
- [30] D. Gorjup, J. Slavič, and M. Boltežar, *Frequency domain triangulation for full-field 3d operating-deflection-shape identification*, Mechanical Systems and Signal Processing **133**, 106287 (2019).
- [31] H. Inoue, K. Kishimoto, and T. Shibuya, *Experimental wavelet analysis of flexural waves in beams*, Experimental Mechanics **36**, 212 (1996).
- [32] C.-b. Xu, Z.-b. Yang, X.-f. Chen, S.-h. Tian, and Y. Xie, *A guided wave dispersion compensation method based on compressed sensing*, Mechanical Systems and Signal Processing **103**, 89 (2018).

- [33] Y. Y. Kim and E.-H. Kim, *Effectiveness of the continuous wavelet transform in the analysis of some dispersive elastic waves*, The Journal of the Acoustical Society of America **110**, 86 (2001).
- [34] A. Katunin, H. Lopes, and J. A. dos Santos, *Identification of multiple damage using modal rotation obtained with shearography and undecimated wavelet transform*, Mechanical Systems and Signal Processing **116**, 725 (2019).
- [35] H. Jia, Z. Zhang, H. Liu, F. Dai, Y. Liu, and J. Leng, *An approach based on expectation-maximization algorithm for parameter estimation of lamb wave signals*, Mechanical Systems and Signal Processing **120**, 341 (2019).
- [36] F. L. di Scalea and J. McNamara, *Measuring high-frequency wave propagation in railroad tracks by joint time-frequency analysis*, Journal of sound and vibration **273**, 637 (2004).
- [37] W. Sachse and Y.-H. Pao, *On the determination of phase and group velocities of dispersive waves in solids*, Journal of applied Physics **49**, 4320 (1978).
- [38] B. J. Schwarz and M. H. Richardson, *Introduction to operating deflection shapes*, CSI Reliability Week **10**, 121 (1999).
- [39] P. Avitabile, *Experimental modal analysis*, Sound and vibration **35**, 20 (2001).
- [40] M. Vetterli and J. Kovacevic, *Wavelets and subband coding*, BOOK (Prentice-hall, 1995).
- [41] A. Grinsted, J. C. Moore, and S. Jevrejeva, *Application of the cross wavelet transform and wavelet coherence to geophysical time series*, Nonlinear processes in geophysics **11**, 561 (2004).

3

VIBRATION MODES AND WAVE PROPAGATION OF THE RAIL UNDER FASTENING CONSTRAINT

This chapter investigates 3D rail vibrations under fastening constraint up to 5000 Hz and provides insights into rail vibration control by fastening parameters. A methodology is proposed, including experimental investigation and numerical simulations of rail vibrations. Three steps are considered: 1) experimental investigation of rail vibrations under fastening constraint; 2) validation and analysis of 3D finite element (FE) modeling of rail-fastening systems; 3) rail vibration control by fastening parameters. In Step 1, operating deflection shape (ODS) and synchronized multiple-acceleration wavelet (SMAW) measurements are applied to identify rail vibration modes and measure wave propagation characteristics under fastening constraint. In Step 2, a 3D FE model is developed to analyze rail vibrations and validated using measurements from Step 1. In Step 3, insights into the control of rail vibrations are gained by sensitivity analysis of fastening parameters using the validated 3D FE model from Step 2. The results indicate that (1) under fastening constraint, ODS measurement identifies vertical bending modes, longitudinal compression modes, and lateral bending modes of the rail with shifted frequencies and significantly reduced vibration amplitude compared to free rail. (2) Vertical wave attenuation of rail-fastening is relatively small between 1800 and 3600 Hz, and lateral wave attenuation presents a dominant peak at about 3800 Hz. (3) Compared to the vertical and lateral directions, the fastening system constrains the longitudinal rail vibrations less strongly. (4) The change of fastening stiffness and damping can control rail mode frequencies and their vibration amplitude and influence the wave propagation velocities and attenuation along the rail.

Parts of this chapter have been published in P.Zhang **150**, 107305 (2021)[1]

3.1. INTRODUCTION

Rail vibrations play an essential role in wheel-rail dynamic interaction. Problems in the field of railway systems, such as short pitch corrugation and rolling noise, are closely related to rail vibrations. Hempelmann and Knothe[2] and Grassie[3] reported that the rail vertical ‘pinned-pinned’ mode was the wavelength-fixing mechanism of short pitch corrugation. Li et al.[4] concluded that the rail longitudinal vibration modes were dominant for short pitch corrugation initiation and consistency between the longitudinal and vertical modes determines its continuous growth. Rail vibrations can also be seen as the superposition of a series of vibrational waves[5]. Thomson et al.[5][6][7] linked the decay rate of the waves along the track with noise radiation and reported that the vibrational waves in the rail were dominant for wheel-rail rolling noise in 500-1600 Hz, and generally remained important in higher frequencies up to 5000 Hz. Therefore, effective control of rail vibration modes and wave propagation may provide root-cause solutions to these vibration-related problems, for instance, by parameter optimization of fastenings[8], utilization of vibration absorber[9][10][11], and under sleeper pad[12]. This chapter aims to provide insights into rail vibration control by fastening parameter design.

Fastenings impose significant constraints on rail vibrations. Fastenings mainly consist of two components: railpads and clamps. Railpads are resilient material components placed between the rail and the sleeper to add elasticity to the track. Clamps fix the rail to the sleeper to ensure that the rail remains attached to the sleeper under train loads. Many studies have reported that the mechanical properties of railpads are nonlinear and depend on preload, excitation frequency, excitation amplitude, temperature, and aging[13][14][15][16][17]. The fastening models have been improved to consider the nonlinearity of railpads, from the simple Kelvin-Voigt (KV) model[18] to Poynting-Thomson (PT) model[19], Prony series model[17], fractional derivative model[20][21], and solid railpad model[22]. Ilias[8] and Egana et al.[23] studied the influence of railpad stiffness on corrugation development and found that the softer railpads can mitigate the corrugation growth compared to the stiffer ones. Thomson et al.[24] investigated the effect on the rolling noise of nonlinear railpad stiffness parameters, and the results indicated that stiffer railpads caused more considerable attenuation of rail vibration along the track and thus reduced the rail-radiated noise. Wei et al.[25] reported that the temperature- and frequency-dependent properties of railpads influenced the vertical accelerations of the rail above 315 Hz in high-speed vehicle-track coupled systems. Oregui et al.[26] performed a sensitivity analysis of railpad parameters on vertical track dynamics, and the derived receptance under different clamp loads and temperature could be used to monitor the fastenings in-service conditions.

Overall, most work mentioned above has explicitly or implicitly studied the vertical rail vibrations under fastening constraint because the wheel-rail excitation mainly acts in the vertical direction. Some researchers have also investigated the lateral rail vibrations under the fastening constraint for studying wheel-rail rolling noise[5][27]. However, the effect of fastening constraint on longitudinal rail vibrations have been barely reported in the literature. Therefore, this chapter proposes a methodology to comprehensively investigate rail vibrations under fastening constraint in three dimensions (3D) and provide insights into rail vibration controls by fastenings design.

When considering three-dimensional rail vibrations, multiple rail vibration modes occur, and they are coupled together[28], making the mode identification more challenging than the uncoupled modes in a single direction. The dispersion and attenuation of the vibrational waves in the rail also make the wave measurement more difficult [5][28][29]. ODS and SMAW measurements were conducted in this chapter to address these two issues. Compared to commonly-used frequency response function (FRF) measurement [27][30][31] for only deriving mode frequencies, ODS measurement has the advantage of identifying coupled vibration modes by obtaining both the mode frequencies and shapes. The SMAW approach can measure wave propagation and dispersion in the rail from the synchronized acquisition of rail accelerations in multiple positions. In this chapter, group velocities and the attenuation coefficient of the waves in the rail under fastening constraint are estimated.

When modeling high-frequency rail vibrations, analytical beam or plate models [32][33][34] are only valid up to 1500 Hz with an assumption of constant cross-section. The 2.5D FE model[35][36] and 3D FE model[37] can both consider rail cross-section deformation and thus accurately reproducing high-frequency rail vibrations. Compared to the 2.5D FE model, the 3D FE model has the advantage that it can simulate non-linear wheel-rail dynamic contact, which is important to study wheel-rail rolling noise and short pitch corrugation. Oregui et al.[37] modeled the fastenings with multiple one-dimensional spring-damper elements to reproduce vertical track dynamics within 3000 Hz. In this chapter, we extend the fastening model from one-dimensional to three-dimensional and examine its validity in three directions up to 5000 Hz, covering the frequency interest of both short pitch corrugation and rolling noise.

This chapter proposes a systematic methodology to investigate 3D rail vibration and control under fastening constraint. Through this methodology, rail vibration modes under fastening constraint can be identified by ODS measurement, and the SMAW approach can measure wave propagation characteristics. Insights into rail vibration control can be gained through sensitivity analysis of fastening dynamic parameters using a 3D FE model. The structure of this chapter is as follows. Section 3.2 describes the methodology of this chapter, including experimental investigation and numerical simulations. Section 3.3 presents the experimental results of ODS and SMAW measurements. Section 3.4 examines the validity of the proposed 3D FE rail-fastening model by comparison with measurements. Section 3.5 shows the control of rail vibration modes and wave propagation characteristics through the sensitivity analysis of fastening parameters. Section 3.6 discusses the relationship between the laboratory and in situ tests of rail vibrations under fastening constraint. The main conclusions and lines of further research are presented in Section 3.7.

3.2. METHODOLOGY

This section describes a systematic methodology for studying rail vibration modes and wave propagation under fastening constraint. This methodology includes three steps: 1) experimental investigation of rail vibrations under fastening constraint; 2) the validation and analysis of 3D FE modeling of rail-fastening; and 3) rail vibration control by fastening parameters. In Step 1, an experimental setup consisting of rail-fastening is constructed in the laboratory. ODS and SMAW measurements are conducted to iden-

tify rail vibration modes and measure wave propagation characteristics under fastening constraint. In Step 2, a 3D FE model of rail-fastening is developed and validated by the ODS and SMAW measurement results. With the simulation model, a better understanding of the rail vibrations in the experimental results is obtained. In Step 3, insights into rail vibration control are gained through sensitivity analysis of fastening dynamic parameters. The flowchart of the methodology is shown in Figure ??.

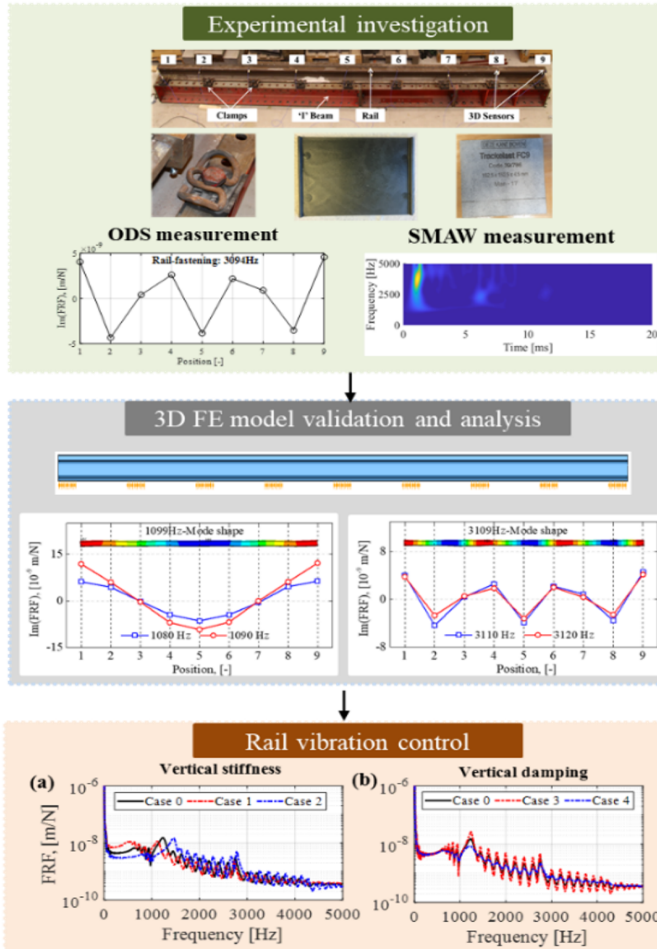


Figure 3.1: Flowchart of the methodology.

3.2.1. EXPERIMENTAL INVESTIGATION

EXPERIMENTAL SETUP

The experimental setup mainly consists of three parts: a rail, fastenings, and a standard 'I-cross section' steel beam, as shown in Figure ???. The 4.97 m long UIC 54E1 rail was

constrained on the beam by nine fastenings every 0.6 m, which is the fastening spacing in the field track. The fastening includes two components: railpads and Vossloh W-shaped tension clamps (Figure ??c). Railpads were placed between the rail and the beam to provide elasticity. The W-shaped clamps were used to fix the rail on the beam. Each clamp was tightened by a torque of 240 Nm resulting in a preload of 20 kN, which is a toe load typically applied in field track. Two types of railpads, harder Zw692-4 (Figure ??d) and softer FC9 (Figure ??e), were tested in this setup, which is commonly used in the mainline of the Dutch railway network.

The sensor distribution in this setup is the same as in [28]. Nine 3D accelerometers (PCB 356B21, denoted as 1-9 in Figure ??) were glued on the railhead surface with an approximately 0.6 m spacing. The smallest wavelength of the measurable modes by this sensor distribution is twice the sensor spacing. The responses of the nine accelerometers are denoted as follows,

$$\mathbf{a}_i(t) = [a_i^x(t), a_i^y(t), a_i^z(t)]^T, \quad i = 1, 2, \dots, 9 \quad (3.1)$$

where $a_i(t)$ is the response of the i^{th} accelerometer, which includes three components $a_i^x(t)$, $a_i^y(t)$, and $a_i^z(t)$ in the longitudinal vertical and lateral directions, respectively. The experimental setup is used to obtain both the ODS and SMAW measurements. For the ODS measurement, all accelerometers are used to get the highest wavenumber resolution. For SMAW measurement, which can identify wave propagation and dispersion in the rail, only accelerometers 1, 5, and 9 are used.

A small hammer (PCB 086C03) with a steel tip was used to excite the rail in the high-frequency range. The excitation positions were as close as possible to the 3D accelerometer 1. Accelerometer 1 is at one of the free rail ends where the mode shapes have maximum deformation, and thus the rail vibration modes can be excited with larger energy. In the real track, the rail ends are often constrained by, such as joints and welds, and the rail may have mode shapes and frequencies different from rails with free ends at the same wavelength/number. Impacts were conducted in the longitudinal, lateral, and vertical directions, recorded as $F_1^x(t)$, $F_1^y(t)$, and $F_1^z(t)$, as shown in Figure ??a. A synchronized data acquisition system recorded the excitation and the response signals. Five impacts in each direction were measured, with a sampling frequency of 51200 Hz. The reliable range of the impact forces and repeatability of the signals were checked as in [27], and they were valid up to 5000 Hz.

Compared to the field track, this setup did not include the sleepers, ballast, and other substructure components. These track components mainly contribute to the track dynamics in a lower frequency range than 400 Hz[33][38][39]. Instead, a steel beam was used as rail support in this setup, which has two advantages. Firstly, the rail support conditions were simplified compared to practice, making it easier to identify the effect of fastening constraint on rail vibrations without the influence of sleeper and ballast. Secondly, this beam support has a much larger mass and stiffness, making it possible almost completely to suppress rail vibration modes by rail constraint design. Besides, a short length of rail (4.97 m) was chosen in this setup for the laboratory test while in the field, it usually is much longer. The influence of these differences between laboratory and field measurements on rail vibration modes and wave propagation will be discussed in Section 3.6.

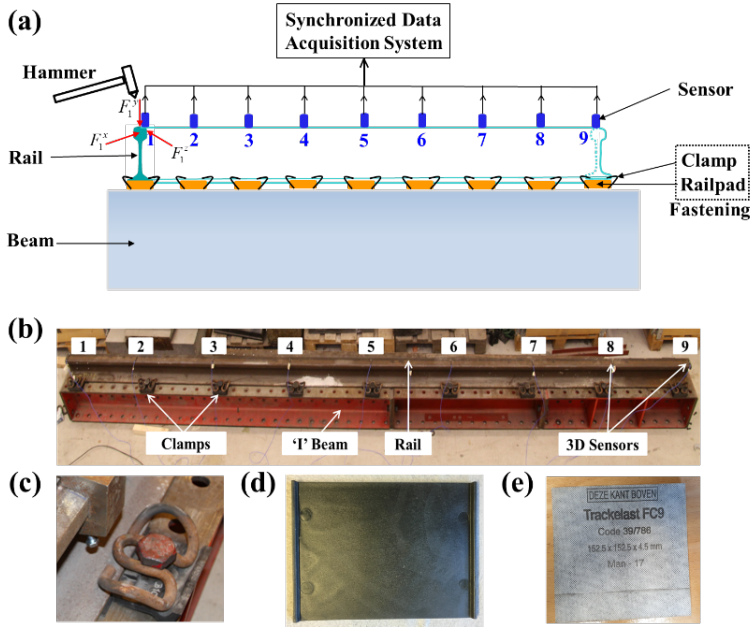


Figure 3.2: Experimental setup. (a) Schematic drawing; (b) setup in the laboratory; (c) Vossloh W-shaped tension clamps; (d) Zw692-4 railpad; (e) FC9 railpad.

ODS MEASUREMENT METHOD

ODS measurement is employed to identify different rail vibration modes. The ODSs are measured from a set of FRFs, which can be divided into two steps. The first step is to calculate the FRFs at different accelerometers by the following formula[40]:

$$FRF_i^y(f) = \frac{S_{a_i^y F_1^y}(f)}{S_{F_1^y F_1^y}(f)(2\pi f)^2} \quad (3.2)$$

where $FRF_i^y(f)$ is vertical FRF of accelerometer i ; $S_{a_i^y F_1^y}$ is the cross-spectrum between the acceleration $a_i^y(t)$, and force $F_1^y(t)$, and $S_{F_1^y F_1^y}$ is the auto-spectrum of the force $F_1^y(t)$. The FRFs are complex-valued functions. In the second step, the ODSs of rail displacement responses are taken as the spatial distribution of the imaginary parts of the FRFs, as follows[41]:

$$ODS^y(f) = [\text{Im}(FRF_1^y(f)), \text{Im}(FRF_2^y(f)), \dots, \text{Im}(FRF_9^y(f))] \quad (3.3)$$

where $ODS^y(f)$ is vertical ODS at frequency f . The ODS will closely approximate the mode shape when the frequency is one of the natural rail frequencies[41]. The longitudinal and lateral FRFs and ODSs, $FRF_i^x(f)$, $FRF_i^z(f)$, $ODS^x(f)$, $ODS^z(f)$ can be obtained with the same method. One example to explain the procedure of ODS measurement in detail can be found in[28].

SMAW MEASUREMENT METHOD

SMAW measurement is applied to study wave propagation and dispersion in the rail. Wave propagation signals along the rail under hammer excitation are non-stationary and contain many frequency components. The continuous wavelet transform (CWT) decomposes these signals, which offers a good time and frequency resolution. In the CWT, the convolutions of the analyzed signal are calculated with a group of scaled and shifted wavelet functions. The wavelet coefficients $W_n(s)$ of the analyzed signal x_n can be represented as follows[42]:

$$W_n(s) = \sum_{n'=0}^{N-1} x_n \psi^* \left[\frac{(n' - n) \delta_t}{s} \right] \quad (3.4)$$

where ψ is the mother wavelet, s is the wavelet scale, N is the number of points in the time series, $n' = 0, \dots, N-1$, δ_t is the time step, n is the continuous variable for the translation, s is the wavelet scale, \star presents a complex conjugate and $\psi^* \left[\frac{(n' - n) \delta_t}{s} \right]$ is a family of wavelets deduced from the mother wavelet by various translation and scaling steps. Here, the Morlet function is employed as the mother wavelet[43]. The wavelet power spectrum (WPS) is calculated by $|W_n^2(s)|$. In this chapter, SMAW measurement refers to the measured WPSs of synchronized accelerations at positions 1, 5, and 9 (see Figure ??). Among them, positions 1 and 9 are at the two rail ends where the wave vibration energy is stronger than the other positions because of the free boundaries. Therefore, the acceleration signals at these two positions will be used to calculate group velocities and the attenuation coefficient of the waves because of the larger signal-to-noise ratio. Position 5 is in the middle of the rail. By analyzing accelerations signals at these three positions, the wave propagation along the rail can be traced[28].

From WPSs, it is possible to estimate the group velocity and attenuation coefficient of the waves in the rail under fastening constraint, as shown in Figure 3.3. Firstly, WPSs of acceleration signals at the two rail ends are calculated. Then one frequency f_j (i.e., 2500 Hz) is chosen in the vertical WPSs, indicated by the white solid lines in Figure 3.3b. The first peaks A_1 and A_2 at time t_1 and time t_2 are detected from the WPSs (see the red triangles in Figure 3.3b), which are the first arrivals of the waves at the chosen frequency. There is a time difference dt between these two peaks, during which the waves propagate through the rail length (L). Therefore the vertical group velocity v_g^y at f_j is calculated as follows,

$$v_g^y(f_j) = \frac{L}{t_2(f_j) - t_1(f_j)}. \quad (3.5)$$

Then, wave energy attenuation in the rail is estimated from the peak amplitude A_1 relative to A_2 . A linear attenuation coefficient β_y is used to describe the wave decay per meter along the rail in the vertical direction[44], as follows,

$$\beta_y(f_j) = \frac{20 \log_{10}(A_1(f_j) / A_2(f_j))}{L} \quad (3.6)$$

Afterward, we select the next frequency to study f_{j+1} and repeat the procedure above. At some frequencies, the vibration energy of the waves is small, and peaks like in Figure 3.3b may not be accurately detected from the WPSs. For these cases, the group velocity

and attenuation coefficient are not estimated, so these are not considered in the final analysis. The longitudinal and lateral v_g^x , v_g^z and β_x , β_z can be obtained with the same method.

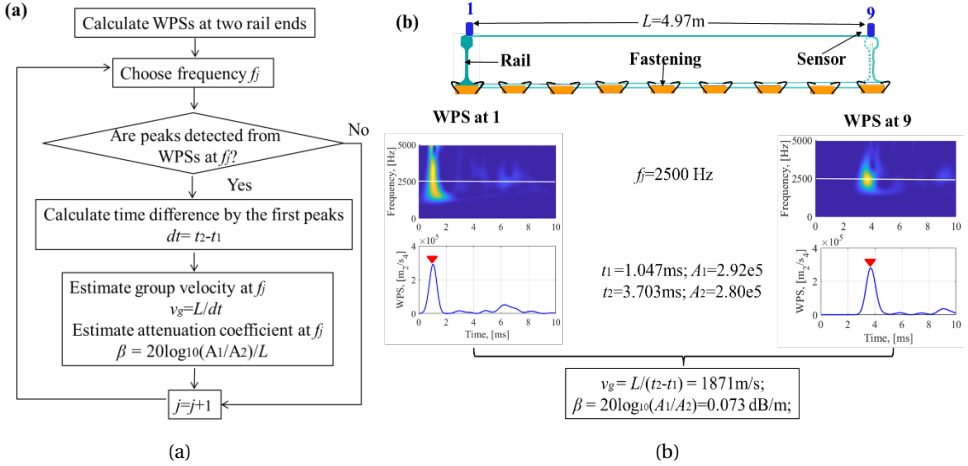


Figure 3.3: The algorithm to measure group velocity and attenuation coefficient from WPSs. (a) Flowchart of the algorithm. (b) Example of the algorithm for a selected frequency f_j . The white line in (b) shows WPSs at 2500 Hz. The red triangles indicate the detected first peaks from WPSs at 2500 Hz.

3.2.2. 3D FE MODEL

A 3D FE model of rail-fastening was developed with ANSYS, as shown in Figure 3.4. The rail was modeled with 8-node solid elements with a length of 4.97 m. The rail profile was measured by a 3D laser HandyScan with a high resolution of 30 μ m. The rail cross-section was discretized with an equal element edge length of 4 mm, as shown in the left corner of Figure 3.4. The longitudinal element size was 10 mm. This meshing method, in terms of the mesh size, was determined after a comparison of five different meshing methods in [28]. The meshing is thus a good compromise between simulation time and numerical accuracy. The rail material was treated as elastic isotropic with Young's modulus of 210 Gpa, Poisson's ratio of 0.3, and a density of 7850 kg/m^3 . Free boundary conditions were applied to the two rail ends. The fastenings were modeled with multiple linear spring-damper pairs in the vertical, longitudinal, and lateral directions, which extends the fastening model in [37]. Specifically, the fastening model consists of 72 spring-damper pairs in each direction, divided into nine rows (lateral direction of the rail in Figure 3.4b) and eight columns (longitudinal direction of the rail in Figure 3.4c). Figure 3.4d shows three spring-damper elements at one rail node (marked by R). One end of three spring-damper pairs was connected to the rail node R, and the other ends were fixed. The steel beam was not included in this model for vibration analysis because experimental results indicated that its vibration was approximately 1/10 smaller compared to that of the rail and could thus be considered stationary.

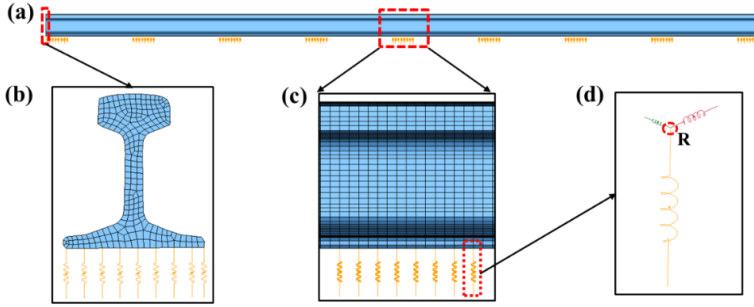


Figure 3.4: Overview of FE rail-fastening model. (a) Rail-fastening model; (b) cross-section of rail-fastening model; (c) side view of the rail-fastening model; (d) three spring-damper elements at one rail node.

The hammer tests were numerically reproduced by an implicit-explicit sequential approach [37]. First, in the implicit calculation, the rail-fastening reached an equilibrium state under gravity. Subsequently, the nodal displacement from the implicit calculation was input as the initial state of the explicit simulation. In the explicit calculation, the impact force of the small hammer was modeled by a triangular force with a zero magnitude at t_0 , a maximum magnitude at t_1 , and a vanishing magnitude at t_2 , as in [37]. The adopted time step is small enough (287 ns) to ensure the stability of the explicit integration. The stiffness and damping parameters of the fastenings were derived by best fitting the simulations to the measurement results of railpad Zw692-4, which will be shown in Section 3.4. These parameters and the nominal material properties of the rail are listed in Table 3.1.

Table 3.1: The values of parameters used in the model.

Component	Parameter	Value
Rail	Young's modulus	210 Gpa
	Poisson's value	0.3
	Density	7850 kg/m ³
	Vertical stiffness	600 kN/mm
	Vertical damping	16 kNs/m
Fastening with Zw 692 railpad	Longitudinal stiffness	160 kN/mm
	Longitudinal damping	6 kNs/m
	Lateral stiffness	160 kN/mm
	Lateral damping	20 kNs/m

3.2.3. RAIL VIBRATION CONTROL BY FASTENING PARAMETERS

Sensitivity analysis of fastening parameters is performed via the 3D FE rail-fastening model to gain insight into rail vibration control, as shown in Figure 3.5. The fastening parameters are defined as a vector u , which serves as input for the 3D FE rail-fastening model.

$$u = [k_x, d_x, k_y, d_y, k_z, d_z]^T \quad (3.7)$$

where k_x, k_y, k_z are the fastening stiffness in the longitudinal, vertical, and lateral directions, and d_x, d_y, d_z are the fastening damping in the longitudinal, vertical and lateral directions. The output y of the 3D FE rail-fastening model indicates the estimation of the set of accelerations $a_i, i = 1, \dots, 9$, FRFs, ODSs, group velocities (v_g), and attenuation coefficients (β).

$$\begin{aligned}
 y &= \{a(t), \text{FRF}(f), \text{ODS}(f), v_g(f), \beta(f)\} \\
 a(t) &= \{a_1(t), \dots, a_9(t)\} \\
 \text{FRF}_i(f) &= \{\text{FRF}_i^x(f), \text{FRF}_i^y(f), \text{FRF}_i^z(f)\} \\
 \text{FRF}(f) &= \{\text{FRF}_1(f), \dots, \text{FRF}_9(f)\} \\
 \text{ODS}(f) &= \{\text{ODS}^x(f), \text{ODS}^y(f), \text{ODS}^z(f)\} \\
 v_g(f) &= \{v_g^x(f), v_g^y(f), v_g^z(f)\} \\
 \beta(f) &= \{\beta_x(f), \beta_y(f), \beta_z(f)\}
 \end{aligned} \tag{3.8}$$

with t during the simulation time, and f in the frequency range of importance for the application (0 to 5000 Hz). The 3D FE simulation requires parameters obtained from the experimental setup (such as impact forces) and literature (such as the number of elements, rail parameters, etc.). Those parameters are included in the parameter vector θ_{FE} . Then, given the input vector of parameters of the fastening, the output of the rail-fastening model is given by:

$$Y = f_{\text{rail-fastening}}(u, \theta_{FE}) \tag{3.9}$$

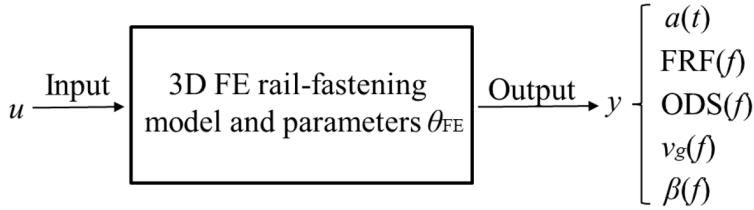


Figure 3.5: Block diagram representation of the FE rail-fastening model.

The sensitivity analysis compares changes in the output when including changes in the fastening parameters with respect to nominal parameters. Nominal fastening parameters u_{nominal} are as in Table 3.1, obtained by solving the inverse problem by fitting the output of the model to measurements from Step 1. A nominal output y_{nominal} of the rail-fastening system is obtained as follows:

$$Y_{\text{nominal}} = f_{\text{rail-fastening}}(u_{\text{nominal}}, \theta_{FE}) \tag{3.10}$$

Then, we select one fastening parameter, for example, longitudinal stiffness k_y , and define two inputs

$$\begin{aligned}
 u_A &= u_{\text{nominal}} + u_{\Delta A}^{k_y} \\
 u_B &= u_{\text{nominal}} + u_{\Delta B}^{k_y}
 \end{aligned} \tag{3.11}$$

with

$$\begin{aligned}
 u_{\Delta A}^{k_y} &= [0, 0, +\Delta A, 0, 0, 0]^T, \quad \Delta A \geq 0 \\
 u_{\Delta B}^{k_y} &= [0, 0, -\Delta B, 0, 0, 0]^T, \quad \Delta B \geq 0
 \end{aligned} \tag{3.12}$$

where ΔA and ΔB are variations of the specific parameter. The outputs y_A , y_B with parameters u_A and u_B are derived using the 3D FE model,

$$\begin{aligned} y_A &= f_{\text{rail-fastening}}(u_A, \theta_{\text{FE}}) \\ y_B &= f_{\text{rail-fastening}}(u_B, \theta_{\text{FE}}) \end{aligned} \quad (3.13)$$

Finally, y_{nominal} , y_A and y_B are compared to determine the effect of the fastening parameter (i.e., longitudinal stiffness) on rail vibrations. Thus, the effect on the rail vibration control by this parameter is determined, for instance, including the frequency shift and peak amplitude in the FRFs, wave velocities, and attenuation in the rail.

3.3. EXPERIMENTAL RESULTS

In this section, the experimental results of the rail-fastening are presented. Results are compared with those of the free rail to study the effect of fastening constraint on rail vibrations.

3.3.1. RESULTS OF ODS MEASUREMENT

Figure 3.6 shows the FRFs of rail-fastening with Zw692-4 railpads and free rail at accelerometer 1 in the vertical, longitudinal, and lateral directions up to 5000 Hz. The set of major peaks in the vertical FRF of free rail (see Figure 3.6a) correspond to the rail vertical bending modes[28]. The fluctuation amplitude of vertical FRF is much reduced with the inclusion of fastening constraint, compared to those of the free rail. The distinguishable fluctuation peaks of the rail-fastening system are only observed around 1500 and 3300 Hz. The frequencies of the fluctuation peaks are shifted, e.g., from 2283 Hz or 2495 Hz of free rail to 2398 Hz of the rail-fastening case (indicated by red arrows in Figure 3.6a). In order to identify the rail vibration modes related to these peaks, the corresponding ODSs are derived and shown in Figure 3.6a, 3.6b, and 3.6c. It can be seen that the ODS of rail-fastening at 2398 Hz shares a similar shape with the ODS of free rail at 2283 Hz, and is different from that at 2495 Hz. This indicates the peak at 2398 Hz corresponds to one vertical bending mode, and its frequency is shifted from 2283 Hz to 2398 Hz under fastening constraint. In Figure 3.7d, 3.7e, and 3.7f, another example shows that the peak frequencies are shifted from 2909 Hz of free rail to 2950 Hz of rail-fastening, confirming that fastenings increase the vertical bending mode frequencies of the rail. Besides, it is found that at frequencies higher than 1000 Hz, the overall average trends of the FRFs are similar in these two cases, but the FRF of the rail-fastening is reduced at frequencies lower than around 1000 Hz. Compared to clearly distinguished vertical bending modes of free rail in the FRF below 1000 Hz, almost no peaks were observed in that of rail-fastening system, which should be caused by the fastening damping that dissipates the vibration energy.

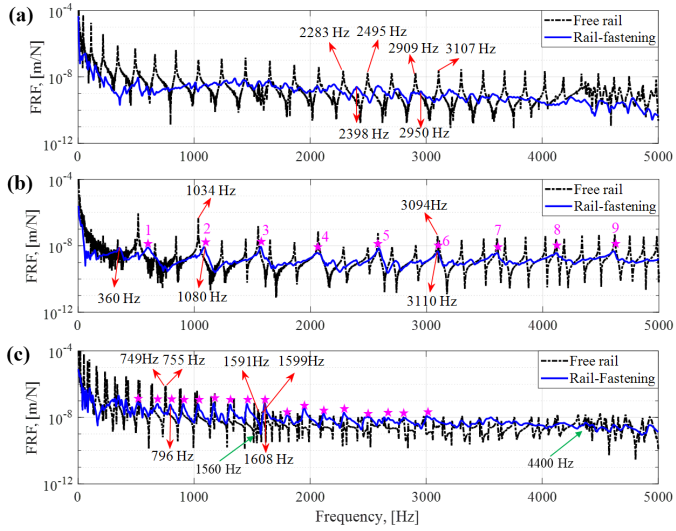


Figure 3.6: FRFs at accelerometer 1 in the (a) vertical, (b) longitudinal (c) lateral directions. The red arrows in this figure show the peak frequencies of the FRFs. The results of free rail are from [28].

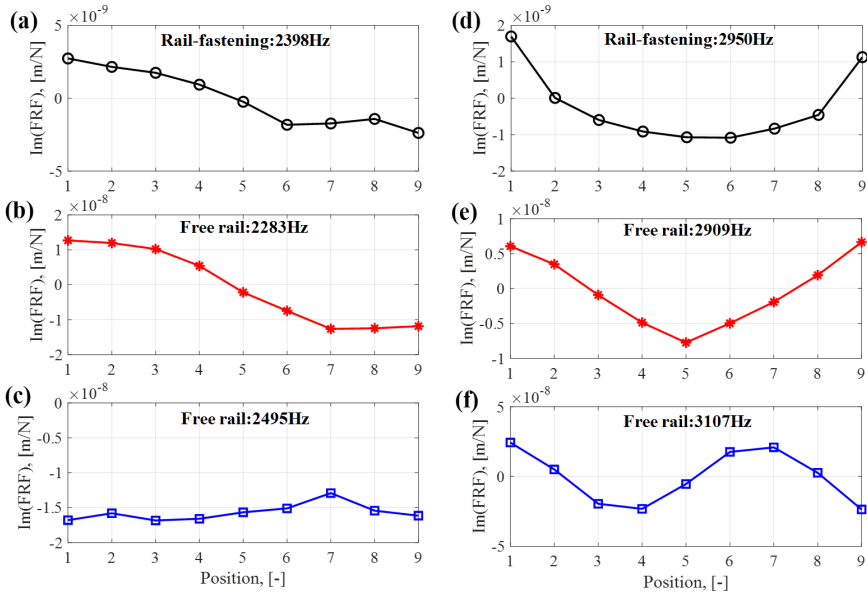


Figure 3.7: Vertical ODSs: (a) rail-fastening at 2398 Hz, (b) free rail at 2283 Hz, (c) free rail at 2495 Hz, (d) rail-fastening at 2950 Hz, (e) free rail at 2909 Hz, (f) free rail at 3107 Hz.

In Figure 3.6b, the major peaks in the longitudinal FRF of free rail correspond to longitudinal compression modes[28]. With the fastening constraint, one set of peaks (indicated

by \star and numbers) is still distinguishable in the frequency range of 0-5000 Hz, although their fluctuation amplitudes significantly decrease. It can also be observed that the frequencies of the first three peaks of free rail are shifted to the right, and the others are almost unchanged. One additional peak occurs in the longitudinal FRF of rail-fastening at around 360 Hz, corresponding to the rail resonance mode on the longitudinal fastening stiffness. Figure 3.8a and 3.8c show ODSs of rail-fastening at 1080 Hz and 3110 Hz. These have a similar shape to ODSs of free rail at 1034 Hz and 3094 Hz, respectively (see Figure 3.8b and 3.8d). These results indicate that the peaks of rail-fastening correspond to longitudinal compression modes.

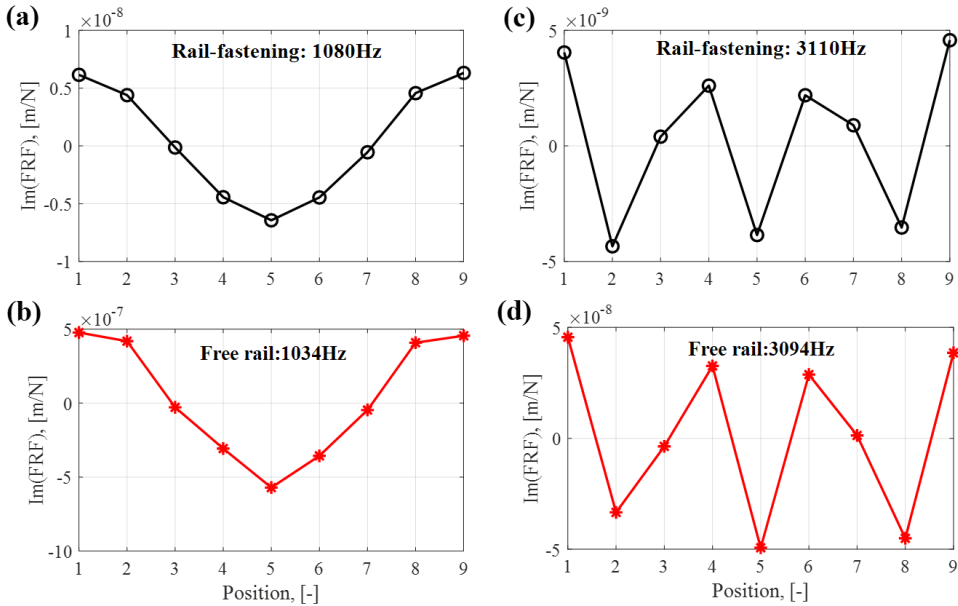


Figure 3.8: Longitudinal ODSs: (a) rail-fastening at 1080 Hz, (b) free rail at 1034 Hz, (c) rail-fastening at 3110 Hz, (d) free rail at 3094 Hz.

In Figure 3.6c, the fluctuation amplitude of the lateral FRF of rail-fastening considerably decreases compared to that of free rail. The lateral FRF of free rail in Figure 3.6c shows the coupling of four sets of major peaks, representing lateral bending, lateral torsion, web 1st bending and web 2nd bending modes, respectively[28]. Specifically, two sets of major peaks at 0-1560 Hz correspond to lateral bending and torsion modes, and at approximately 1560 Hz and 4400 Hz, with the supplement of web 1st and 2nd bending modes (indicated by two green arrows, respectively). However, with the inclusion of the fastening, only one set of major peaks (indicated by \star) can be identified between 300 Hz and 3000 Hz. Also, the frequencies of the peaks are shifted, e.g., from 749 Hz or 755 Hz of free rail to 796 Hz of rail-fastening. To identify the vibration modes of the rail-fastening, the corresponding ODSs are derived, as shown in Figure 3.9a, 3.9b, and 3.9c. It can be seen from Figure 3.9b and 3.9c that despite a marginal frequency difference of 6 Hz, the ODSs of free rail at 749 Hz and 755 Hz show a significant difference, which corresponds

to lateral bending mode and torsion mode, respectively. The ODS of rail-fastening at 796 Hz has a similar shape (Figure 3.9a) to that of free rail at 749 Hz, indicating that this peak represents a lateral bending mode. A similar result is observed in Figure 3.9d, 3.9e, 3.9f that the ODS of rail-fastening at 1608 Hz resembles the ODS of free rail at 1599 Hz (lateral bending mode) rather than that at 1591 Hz (web 1st bending mode). We also checked other peaks and their ODSs and found that the remaining set of major peaks of the rail-fastening system correspond to lateral bending modes, and the fastening constraint probably suppresses the other three types of lateral modes occurring in the FRF of free rail.

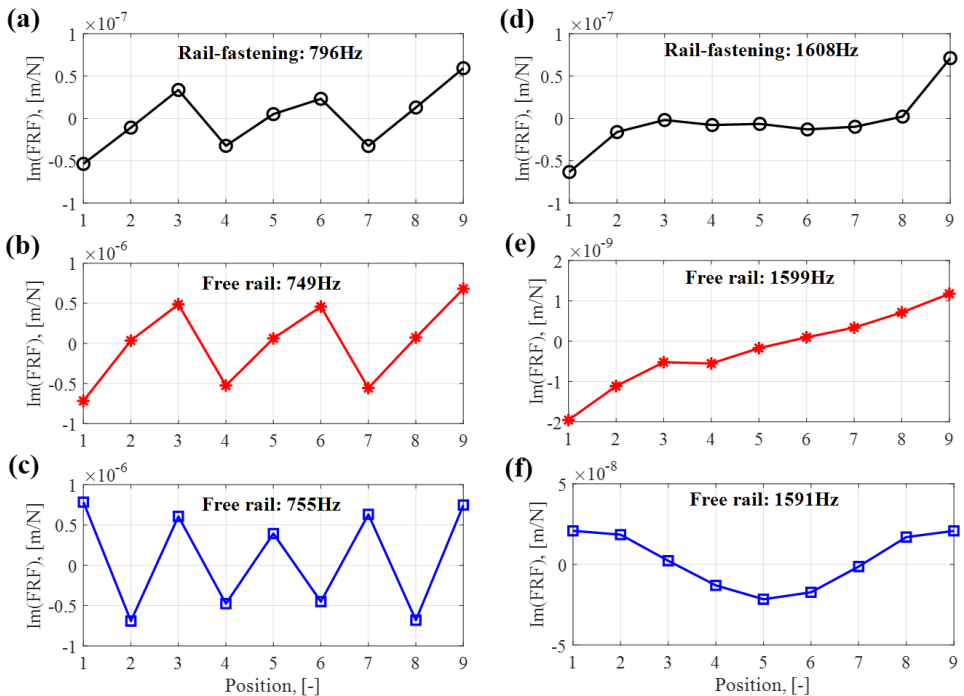


Figure 3.9: Lateral ODSs: (a) rail-fastening at 796 Hz, (b) free rail at 749 Hz, (c) free rail at 755 Hz, (d) rail-fastening at 1608 Hz, (e) free rail at 1599 Hz, (f) free rail at 1591 Hz.

Figure 3.10 compares the FRFs of the rail-fastening system with two types of railpads, harder Zw692-4, and softer FC9. Overall, the vertical and lateral FRFs in these two cases are similar below 4000 Hz, but present deviations at frequencies higher than 4000 Hz. Moderate differences are observed in the longitudinal FRFs at frequencies lower than 1500 Hz. For the softer FC9, the peak fluctuation amplitudes are larger, and the corresponding peak frequencies are smaller than those of harder Zw692-4.

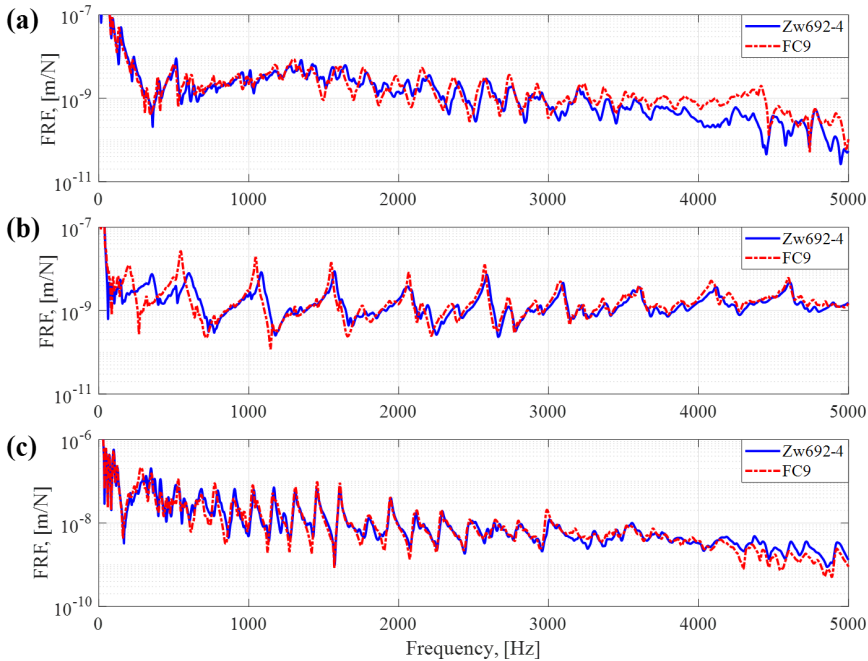


Figure 3.10: FRFs with two railpad types at accelerometer 1 in the (a) vertical, (b) longitudinal (c) lateral directions.

3.3.2. RESULTS OF SMAW MEASUREMENT

The WPSs of vertical accelerations of free rail and rail-fastening with railpads Zw692-4 and FC9 are shown in Figure 3.11. Figure 3.11a, 3.11b, and 3.11c correspond to the signals at accelerometer 1, 5, and 9, respectively. The color contrast indicates the amount of energy concentrated in a frequency range (the vertical axis) at a particular time (the horizontal axis). The wave envelope propagation along the free rail can be seen in the figures. At time t_{1z} , the hammer excites the rail near accelerometer 1. Then, the wave envelope propagates to accelerometer 5 at time t_{2z} , and to accelerometer 9 at time t_{3z} . After that, the waves reflect at accelerometer 9 and come back to accelerometer 5 at time t_{4z} , and to accelerometer 1 at t_{5z} . During propagation, the shapes of the wave envelope change to a 'C' shape due to wave dispersion. With the inclusion of fastenings, the wave envelope can be seen propagating from accelerometer 1, through accelerometer 5 and to accelerometer 9. After that, the energy of the wave envelope becomes too low to be observed. This result indicates that the wave attenuation of the rail-fastening considerably increases compared to that of free rail. Additionally, we can see that the wave envelope of the rail-fastening at accelerometer 1 concentrates on a broader frequency band in about 1200-5000 Hz, but shrinks to a narrower frequency band at accelerometer 9, as indicated by the white dashed rectangular in Figure 3.11a and 3.11c. This phenomenon qualitatively suggests that the wave attenuation in 1800-3600 Hz is less significant than that in ranges 1200-1800 Hz and 3600-5000 Hz.

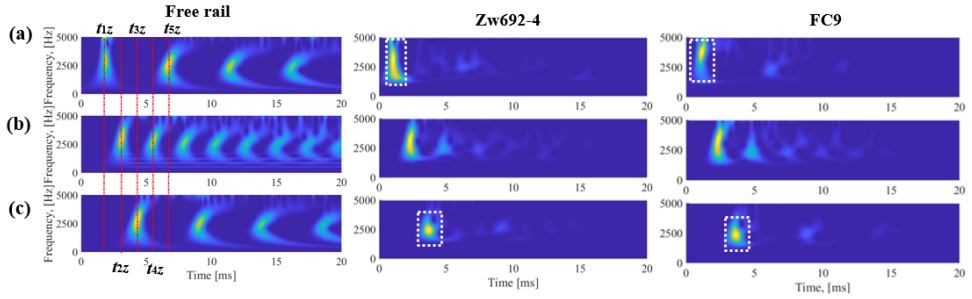


Figure 3.11: Vertical WPSs at (a) accelerometer 1; (b) accelerometer 5; (c) accelerometer 9. The left, middle, right figures refer to free rail, rail-fastening with Zw692-4 and FC9, respectively. The red dash lines are the selected time.

Figure 3.12 shows the WPSs of the longitudinal acceleration signals. Because of the group velocity (around 5100 m/s) is larger than the vertical one (maximum 2000 m/s), more wave envelopes are observed in the longitudinal WPSs of free rail than those in vertical ones. With the fastening constraint, the number of clearly observable wave envelopes is reduced, e.g., from 9 to 5 in Figure 3.12c, indicating that fastenings significantly increase the longitudinal wave attenuation.

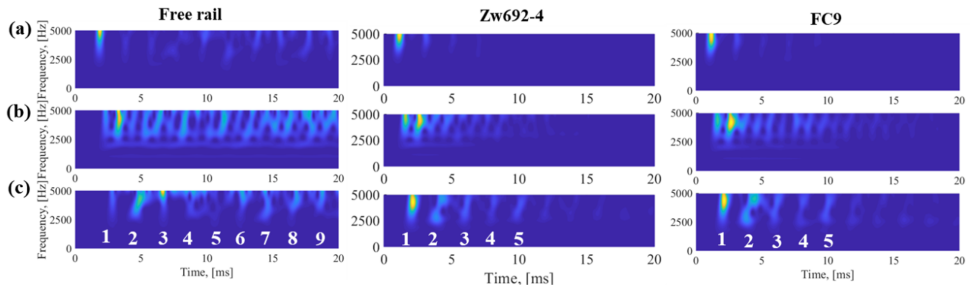


Figure 3.12: Longitudinal WPSs at (a) accelerometer 1; (b) accelerometer 5; (c) accelerometer 9. The left, middle, right figures refer to free rail, rail-fastening with Zw692-4 and FC9, respectively. The number 1-9 in Fig. 3.12 indicates the number of wave envelopes.

The WPSs of the lateral waves are shown in Figure 3.13. Similar to the vertical and longitudinal waves, the lateral waves are also considerably attenuated under fastening constraint. From the white dashed rectangular in Figure 3.13a and 3.13c, it can be seen that the wave envelopes of rail-fastening at accelerometer 1 mainly concentrate on a higher frequency band of about 2500-5000 Hz, but change to about 600-2800 Hz at accelerometer 9. This result qualitatively indicates that the lateral wave attenuation in 600-2800 Hz is smaller than that at higher frequencies. Besides, one discontinuity zone in the wave envelope of rail-fastening is found between about 3000 Hz and 4000 Hz in Figure 3.13c, suggesting that the wave attenuation is so strong that the lateral waves in this frequency range cannot propagate from position 1 to position 9.

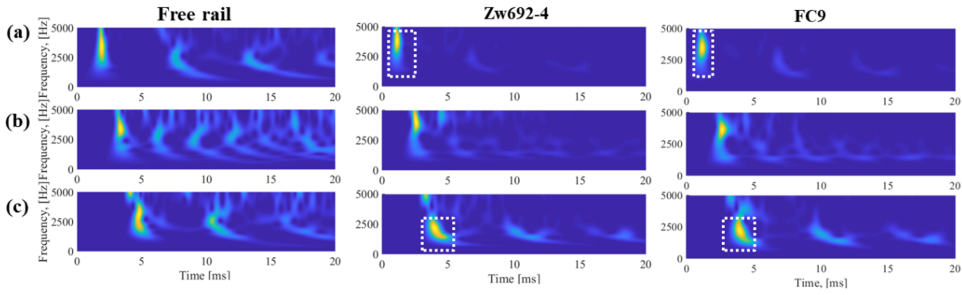


Figure 3.13: Lateral WPSs at (a) accelerometer 1; (b) accelerometer 5; (c) accelerometer 9. The left, middle, right figures refer to free rail, rail-fastening systems with Zw692-4 and FC9, respectively.

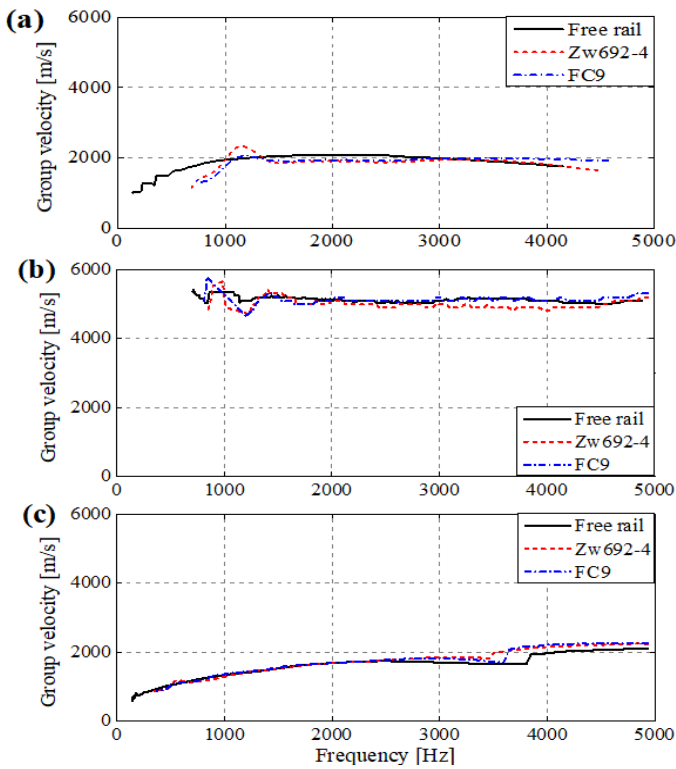


Figure 3.14: Measured group velocity dispersion curves of free rail, rail-fastening with Zw692-4, and FC9 in the (a) vertical, (b) longitudinal, and (c) lateral directions.

The group velocities of rail-fastening with Zw692-4 and FC9 are measured and compared with free rail in Figure 3.14. With the inclusion of fastenings, the vertical group velocity is significantly reduced at frequencies lower than about 1000 Hz, and one noticeable peak occurs at around 1150 Hz. This peak of harder Zw692-4 is more predominant than that of

softer FC9. The longitudinal group velocity almost does not change in these three cases with a value of around 5100 m/s, corresponding to the propagation velocity of compression waves in solid guides, which is $\sqrt{E/\rho} = 5172$ m/s, where $E = 210$ GPa, $\rho = 7850$ m/s for the rail material. The lateral group velocity curves of both railpads overlap almost entirely and are larger than that of free rail above 2500 Hz.

Figure 3.15 shows measured attenuation coefficients of the rail-fastening with Zw692-4 and FC9. The vertical attenuation coefficient firstly decreases from its lower frequency value to a minimum value (around 0 dB/m) at 2400 Hz, then increases to about 7 dB/m at 5000 Hz. These results agree with the observations in Figure 3.11a and 3.11c, where vertical wave envelope shrinks to a narrower frequency band in 1800-3600 Hz at accelerometer 9 after propagation from accelerometer 1 because of the smaller attenuation in this frequency range. The longitudinal attenuation coefficient first drops from around 200 to 800 Hz, and then gradually goes up to about 4.5 dB/m at 5000 Hz. The lateral attenuation coefficient has a valley at about 1000 Hz and a dominant peak at about 3800 Hz. This peak frequency corresponds to the discontinuity zone in the wave envelope of rail-fastening in Figure 3.13c. Compared to the harder Zw692-4, the vertical attenuation coefficient of the softer FC9 is lower before the valley at 2400 Hz and becomes higher afterward. The longitudinal attenuation coefficients show a similar level in these two cases. The lateral attenuation coefficient of harder Zw692-4 is averagely 1 dB/m larger than softer FC9.

3.4. VALIDATION AND ANALYSIS OF 3D FE MODEL

In this section, the proposed 3D FE rail-fastening model was validated by the experimental results of ODS and SMAW measurement from railpad Zw692-4. The dynamic parameters of fastenings were derived by best fitting the simulations to measurements. To better understand the experimental results, modal analysis of the FE model was performed, and the wavenumber-frequency dispersion curves were derived.

3.4.1. VALIDATION OF FRFs AND ODSS

The closest fits of the simulated and measured FRFs at accelerometer 1 in the three directions are shown in Figure 3.16. The overall tendencies and fluctuation amplitude from the simulations match the measurements well. The simulations identify almost all the peaks in the measured FRFs. Some differences are observed at lower frequencies (i.e., below 1000 Hz in the vertical direction, below 700 Hz in the lateral direction), which may be caused by the simplification of the fastenings in the simulation modeled by linear spring-damper elements. Taking the non-linear properties of fastenings (i.e., frequency-dependent) into consideration may improve the simulation results, which will be conducted in future research. Overall, good agreement has been achieved between simulations and measurements, indicating the proposed 3D FE model can accurately reproduce the dynamics behaviors of rail-fastening up to 5000 Hz.

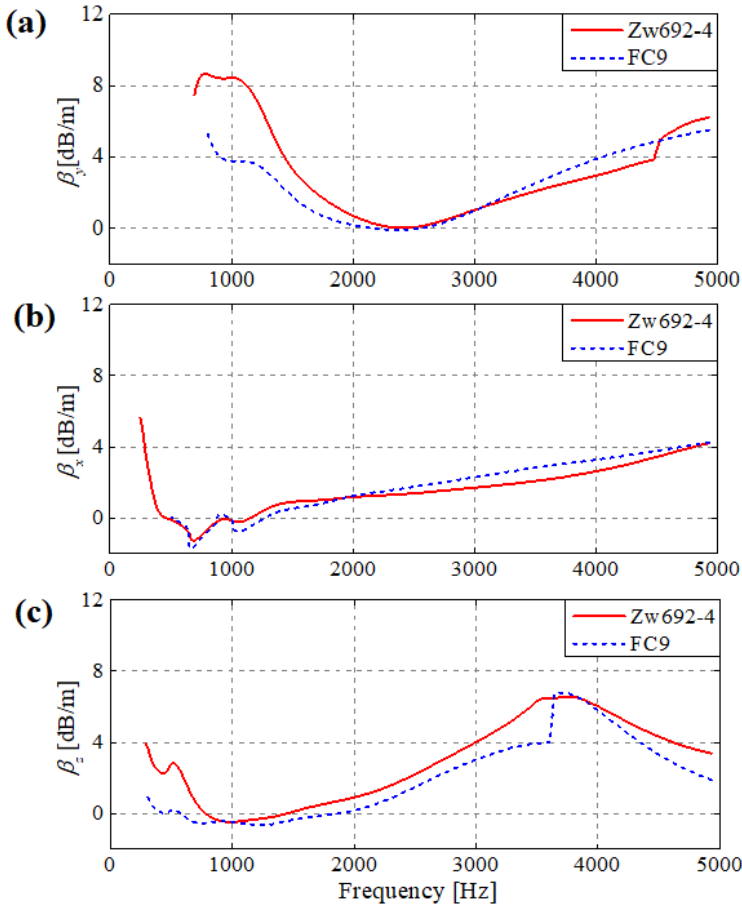


Figure 3.15: Measured attenuation coefficients of rail-fastening with Zw692-4 and FC9 in the (a) vertical, (b) longitudinal, and (c) lateral directions.

Two examples of the simulated and measured ODSs in each direction are compared in Figure 3.17. Figure 3.17a, 3.17b are the vertical ODSs, Figure 3.17c, 3.17d are the longitudinal ODSs and Figure 3.17e, 3.17f are the lateral ODSs. Overall, good agreement is achieved between simulations and measurements in terms of frequencies and the shapes of ODSs. Slight differences are found in the amplitudes of the simulated and the measured ODS, e.g., the simulation slightly underestimates the vertical ODS amplitude at around 2950 Hz in Figure 3.17b. These differences could be caused by the linear treatment of system components in the simulation, while in the real situation, they are frequency-dependent[17]. To better understand the results of the ODS measurement, the simulated mode shapes are also included in Figure 3.17. The color contrast in the mode shapes indicates the relative deformations of the elements. Blue is the minimum deformations, and red is the maximum. The numbered black dashed lines mark the nine sensor positions. It can be seen that the values of ODSs are consistent with the de-

formations of mode shapes: the larger ODS value corresponds to the larger deformation and vice versa. Additionally, it is noted that the ODSs completely capture only the mode shapes of the longitudinal modes, which have larger wavelengths. To identify the vertical and lateral modes in Figure 3.17a, 3.17b, 3.17e, 3.17f, more sensors are needed to improve the wavelength/wavenumber resolutions.

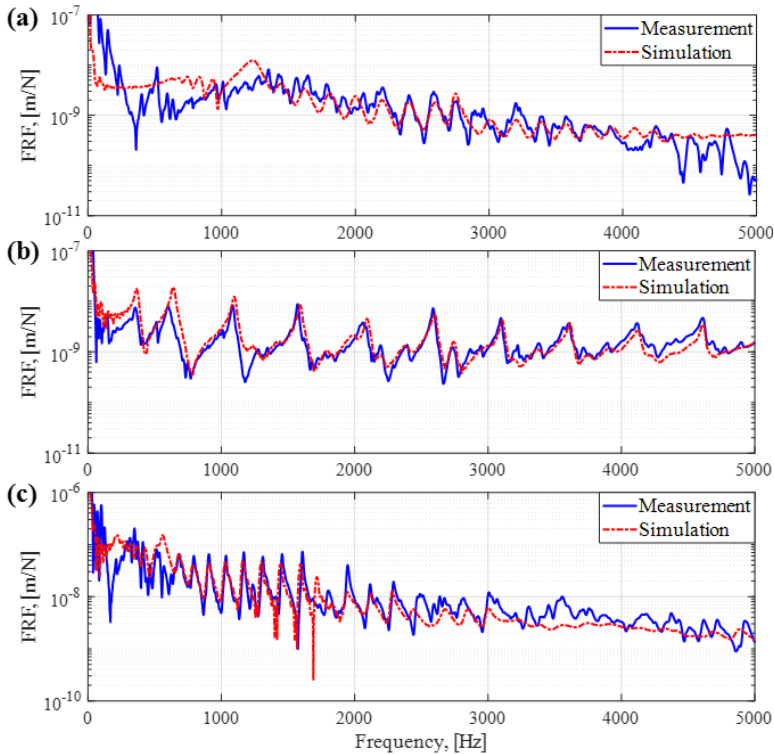


Figure 3.16: Validation of FRFs in the (a) vertical (b) longitudinal and (c) lateral directions.

3.4.2. VALIDATION OF GROUP VELOCITIES AND ATTENUATION COEFFICIENT

The simulated group velocities and attenuation coefficients are compared with the measured ones in Figure 3.18. Overall, good agreement is achieved between simulations and measurements in the three directions, indicating that the proposed model can represent the wave propagation characteristics up to 5000 Hz. Some differences are observed at frequencies lower than 1000 Hz in Figure 3.18a and 3.18c. These differences may be caused by simplifying the rail support in the simulation (the steel beam was not modeled). Slight differences above 3000 Hz in Figure 3.18a and 3.18c might be related to the rail defects in the experimental setup.

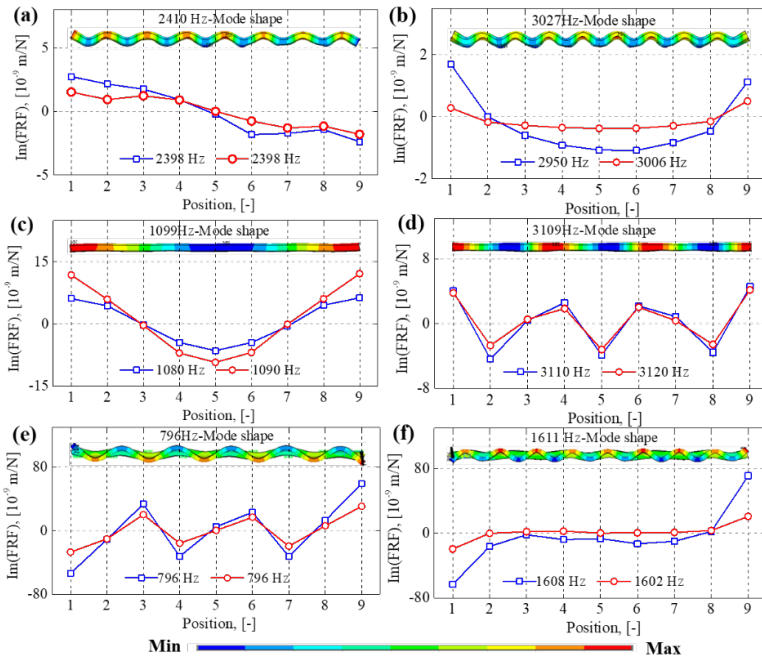


Figure 3.17: Comparison of simulated (—□—) and measured (—○—) ODSs and mode shapes. (a) (b) in vertical direction; (c) (d) in longitudinal direction; (e) (f) in lateral direction.

3.4.3. ANALYSIS OF RAIL VIBRATIONS BY WAVENUMBER-FREQUENCY DISPERSION CURVES

To better understand the rail vibration modes and wave propagation characteristics, the wavenumber-frequency dispersion curves of vibrational rail waves are derived by modal analysis, as shown in Figure 3.19. These waves include the vertical bending waves (I), longitudinal compression waves (II), and lateral bending waves (III) of free rail and rail-fastening system. The lateral torsion waves, web 1st bending, and 2nd bending waves are not included because they are not observed in the measured FRFs, see Figure 3.6c.

Firstly, the wavenumber-frequency dispersion curves explain the frequency shift of the rail vibration modes observed from FRFs. It can be seen from Figure 3.19 that fastening constraint increases the frequencies of the vertical bending waves compared to free rail, which explains that the peak frequencies of vertical FRF (Figure 3.6a) are shifted to the right in the range 1500-3300 Hz. Fastening constraint also increases the frequencies of the longitudinal compression waves at a lower wavenumber than about 1.5 rad/m, agreeing with the observation in Figure 3.6b that the frequencies of the first three longitudinal modes are shifted to the right, and the others keep almost unchanged. Besides, it can be seen that the cut-on frequencies of waves I, II, and III rise to 615 Hz, 370 Hz, and 218 Hz from 0 Hz of free rail. The cut-on frequencies correspond to the rail resonance on the fastening stiffness[5].

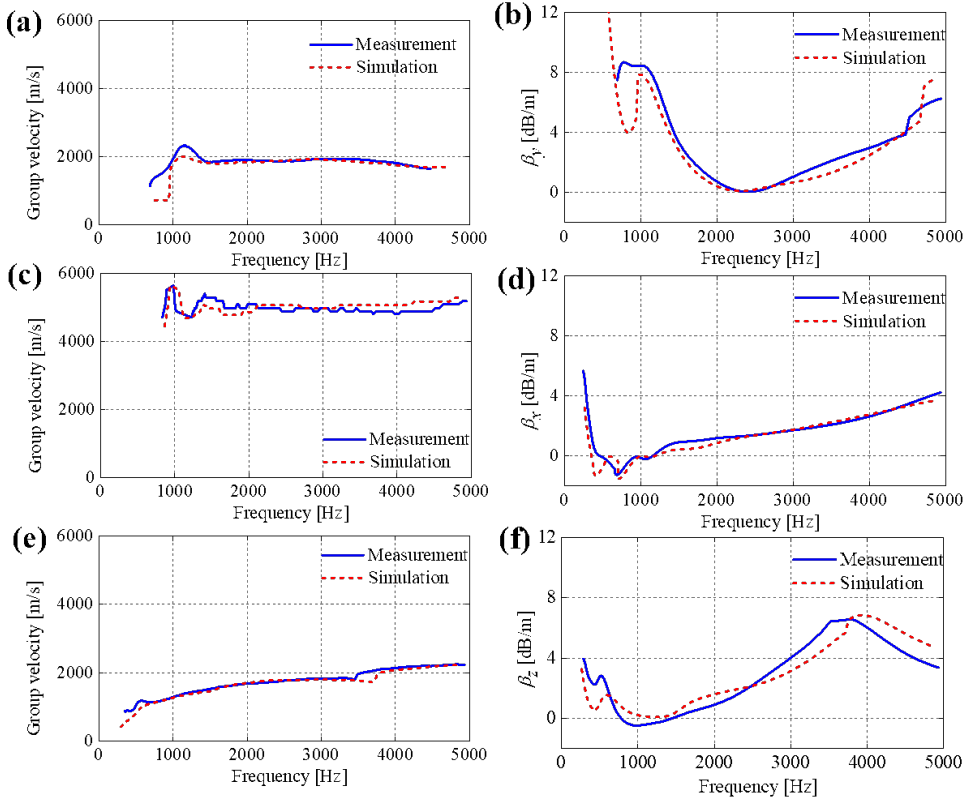


Figure 3.18: Comparison of measured and simulated group velocities and attenuation coefficient. (a) Vertical group velocity; (b) vertical attenuation coefficient; (c) longitudinal group velocity; (d) longitudinal attenuation coefficient; (e) lateral group velocity; (f) lateral attenuation coefficient.

Secondly, the wavenumber-frequency dispersion curves provide more information about the group velocities. Group velocities can be estimated from wavenumber-frequency relations as follows[45]:

$$v_g = \frac{d\omega}{dk} = 2\pi \frac{df}{dk} \quad (3.14)$$

where v_g is group velocity, ω is the angular frequency, f is the ordinary frequency, and k is the wavenumber. It can be seen that group velocity is the tangential slope at a point on the wavenumber-frequency curve multiplied by 2π . From Figure 3.19, it can be seen that at lower frequencies, close to the cut-on frequencies, the tangential slope of the wavenumber-frequency curves of the rail-fastening is smaller than those of free rail, resulting in smaller group velocities. At higher frequencies, tangential slopes of vertical (I) and longitudinal waves (II) are similar in these two cases, and therefore the group velocities change little under fastening constraint. The tangential slopes of lateral waves of rail-fastening increase at frequencies higher than 2500 Hz compared to free rail, corresponding to larger lateral group velocities. The estimations of the group velocities from the wavenumber-frequency curves provide a better understanding of the measurement

results in Figure 3.14.

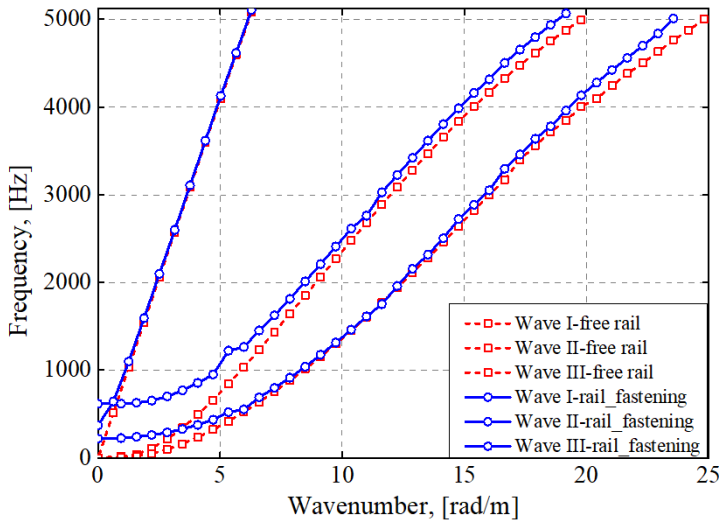


Figure 3.19: Wavenumber-frequency dispersion curves of vertical bending waves (I), longitudinal compression waves (II), lateral bending waves (III) for rail-fastening with railpad Zw692-4 (—). Curves for free rail (---) as in [28].

3.5. RAIL VIBRATION CONTROL BY FASTENING PARAMETERS

A sensitivity analysis of fastening parameters was performed to gain insight into rail vibration control. Based on the derived FRFs, rail vibration modes, wave group velocities and attenuation coefficient, a discussion over mitigation of short pitch corrugation and rolling noise by optimization of fastening parameters was included. The simulation cases are listed in Table 3.2. Case 0 is taken as a reference and applies the same fastening parameters as in Table 3.1, unominal. Other cases change one fastening parameter compared to reference Case 0, following the procedure in Section 3.2.3. For example, Case 1 reduces the vertical stiffness of Case 0 from 600 MN/m to 300 MN/m, and other parameters are kept the same.

3.5.1. RAIL VIBRATION MODES

Figure 3.20 shows the influence of fastening parameters on the FRFs. It can be seen from Figure 3.20a that with the increase of vertical stiffness, the frequencies of vertical vibration modes are shifted to higher frequencies, and meanwhile, the FRF amplitude is reduced at lower frequencies than 1000 Hz. The fluctuation amplitude of the modes does not change much in these three responses. Similar results in terms of frequency shift and FRF amplitude reduction are also observed in the longitudinal FRFs with different longitudinal stiffness (Figure 3.20b) below 2000 Hz. At higher frequencies, the influence of longitudinal stiffness on FRFs is insignificant in these three cases. With the given three

lateral stiffness, the lateral FRFs change little, indicating that the lateral vibration modes are insensitive to the fastening stiffness. In all three directions, the same trend of the influence of fastening damping is observed: larger damping leads to smaller fluctuation amplitude of the vibration modes.

Table 3.2: The simulation cases and their parameters.

Case	Vertical stiffness (MN/m)	Vertical damping (kNs/m)	Longitudinal stiffness (kNs/m)	Longitudinal damping (kNs/m)	Lateral stiffness (MN/m)	Lateral damping (kNs/m)
0	600	16	160	6	160	20
1	300	16	160	6	160	20
2	1200	16	160	6	160	20
3	600	8	160	6	160	20
4	600	32	160	6	160	20
5	600	16	80	6	160	20
6	600	16	320	6	160	20
7	600	16	160	3	160	20
8	600	16	160	12	160	20
9	600	16	160	6	80	20
10	600	16	160	6	320	20
11	600	16	160	6	160	10
12	600	16	160	6	160	40

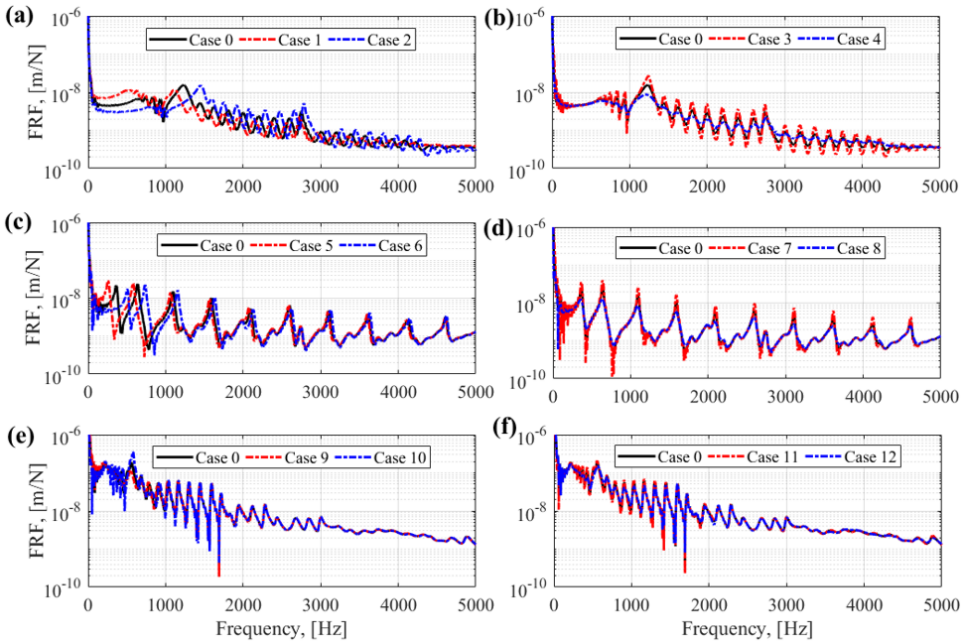


Figure 3.20: The influences of fastening parameters on FRFs. (a) Vertical stiffness on vertical FRFs. (b) Vertical damping on vertical FRFs. (c) Longitudinal stiffness on longitudinal FRFs. (d) Longitudinal damping on longitudinal FRFs. (e) Lateral stiffness on lateral FRFs. (f) Lateral damping on lateral FRFs.

The results in Figure 3.20 provide insights into the control of rail vibration modes. For instance, when wheel-rail excitation frequencies are closer to the rail mode frequencies, strong resonance vibrations happen, which accelerate the track degradation. By optimization of fastening stiffness, the rail mode frequencies could be shifted to avoid the resonance. It is reported in [4] that the consistency between the longitudinal and vertical vibration modes determines the continuous growth of corrugation. Therefore by the design of the fastening longitudinal and vertical stiffness, it is expected to control this consistency, and the corrugation growth eventually. Increasing fastening damping effectively suppresses the vibration amplitude of rail modes in three directions, which is helpful for mitigation of track vibration in practice.

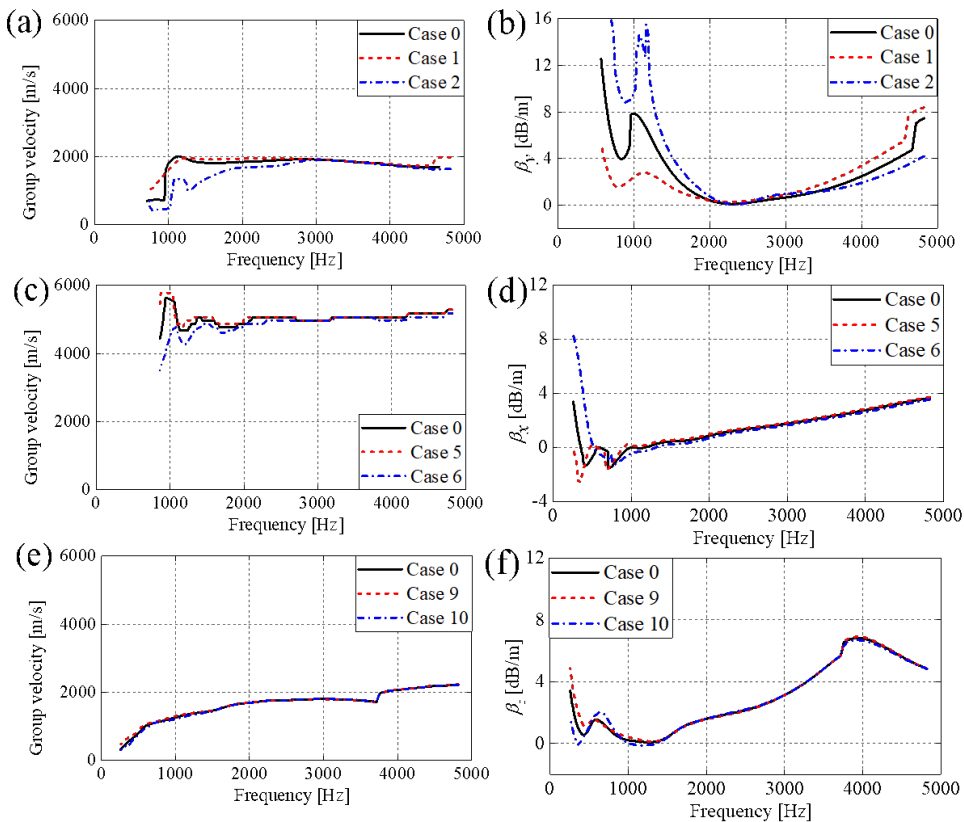


Figure 3.21: The influences of fastening stiffness on wave propagation characteristics. (a) Vertical group velocity; (b) vertical attenuation coefficient; (c) longitudinal group velocity; (d) longitudinal attenuation coefficient (e) lateral group velocity; (f) lateral attenuation coefficient.

3.5.2. WAVE PROPAGATION CHARACTERISTICS

Figure 3.21 shows the influences of fastening stiffness on rail wave propagation characteristics in the three directions. With the increase of vertical stiffness, the vertical group velocity is significantly reduced below 3000 Hz, as shown in Figure 3.21a. The vertical at-

tenuation coefficient considerably increases before the valley at 2400 Hz and decreases at higher frequencies. A similar trend in group velocity reduction and attenuation coefficient increase at low frequencies is also found in the longitudinal direction with longitudinal stiffness increase, as shown in Figure 3.21c and Figure 3.21d. Figure 3.21e and Figure 3.21f show that the lateral group velocities and attenuation coefficient are insensitive to the change of lateral stiffness.

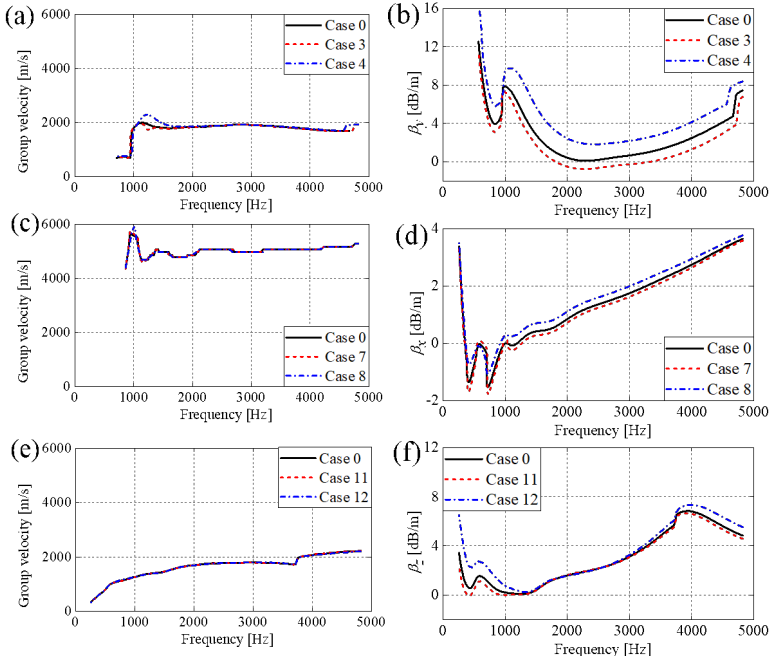


Figure 3.22: The influences of fastening damping on wave propagation characteristics. (a) Vertical group velocity; (b) vertical attenuation coefficient; (c) longitudinal group velocity; (d) longitudinal attenuation coefficient (e) lateral group velocity; (f) lateral attenuation coefficient.

Figure 3.22 shows the influence of fastening damping on rail wave propagation characteristics in the three directions. The group velocities are almost identical with different fastening damping, as shown in Figure 3.22a, 3.22c, 3.22e. The vertical and longitudinal attenuation coefficients go up overall with a damping increase in the whole frequency range. The attenuation coefficient below 1300 Hz and above 3100 Hz increases with larger damping in the lateral direction.

The results in Figure 3.21 and Figure 3.22 provide insights into the control of wave propagation to mitigate rolling noise. It was reported in [6] that the vertical and lateral waves of rail are dominant for rolling noise radiation in 500-1600 Hz. From Figure 3.21b, we can see that increasing vertical stiffness can significantly increase the wave attenuation coefficient in this frequency range and thus mitigate rolling noise. The results in Figure 3.22b and 3.22f indicate that the increased fastening damping could significantly increase the wave attenuation in a wide frequency range, which helps for rolling noise mitigation.

3.6. DISCUSSIONS

An experimental setup consisting of rail-fastening was constructed in the laboratory to investigate the effect of fastening constraint on rail vibration modes and wave propagation. Compared to the field track, this setup used a short rail length (4.97 m) and did not include the sleepers, ballasts, and other substructures. In this section, both in situ experiments and numerical simulations have been conducted to discuss the influence of these differences on rail vibration modes and wave propagation.

3.6.1. FIELD SMAW MEASUREMENT OF WAVE PROPAGATION CHARACTERISTICS

The wave propagation characteristics of the rail in the field track were measured by the SMAW approach. The experimental setup is shown in Figure 3.23. The track without visible defect is in Railway Testing center Faurei, Romania. The UIC60 E1 rail was constrained by Vossloh W14 fastenings on prestressed monoblock sleepers every 0.6 m. No joints, welds and crossings are nearby. The track can thus be considered as effectively infinite. Eleven 3D accelerometers (PCB 356B21, denoted as 1-11 in Figure 3.23) were used to measure the rail vibrations under the impact of the hammer. Accelerometers 1-7 were glued onto the railhead on the field side. Among them, accelerometers 1 and 4 were above the sleeper (called on-support below); accelerometers 2 and 6 were at the mid-span of the rail; and accelerometers 3, 5 and 7 were at the quarter-span. Accelerometers 8 and 10 were glued onto the rail web, and accelerometers 9 and 11 were glued onto the rail foot. The tests in the longitudinal directions were not performed because of the difficulty in applying longitudinal excitation on the railhead.

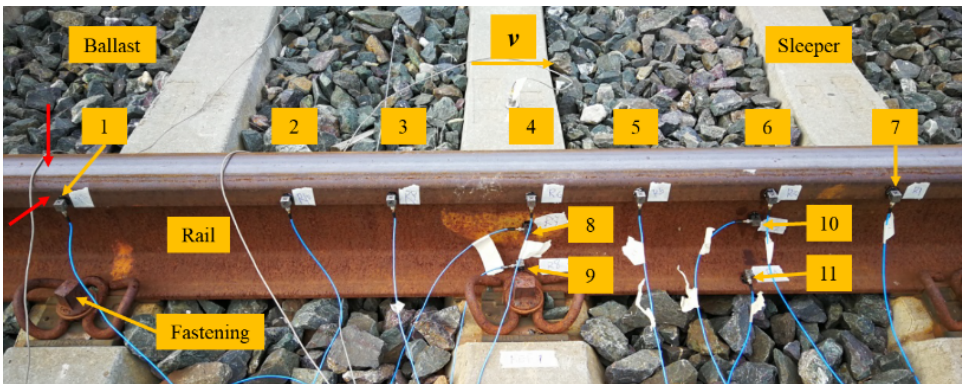


Figure 3.23: Experimental setup of ODS and SMAW measurements in the field track. The red arrows indicate the vertical and lateral hammer excitation positions.

The WPSs in Figure 3.24a, 3.24b and 3.24c show the propagation and dispersion of vertical and lateral waves of the rail in the field track. Figure 3.25 shows the measured group velocities and attenuation coefficients from the laboratory (see Section 3.3.2) and the field. Compared to the results in Section 3.3.2, reasonable agreements have been

achieved between the laboratory and field measurements. For instance, the vertical group velocities at 1000-3500 Hz in these two cases fluctuate at approximately 2000 m/s and both have a downward trend above 3500 Hz. The lateral group velocities both have an overall upward trend and rise to over 2200 m/s at 4500 Hz. The vertical wave attenuation of field measurement is relatively low in 1200-3200 Hz, which shares a similar frequency range to that of laboratory measurement in 1800-3600 Hz. The lateral wave attenuation of field measurement also has a valley at about 600 Hz and a peak at approximately 3800 Hz, similar to that of laboratory measurement. These agreements indicate that the experimental setup of rail-fastening in the laboratory is appropriate to investigate wave propagation characteristics of the rail under fastening constraint, and the experimental results can be used to understand the vibrational rail waves in the field.

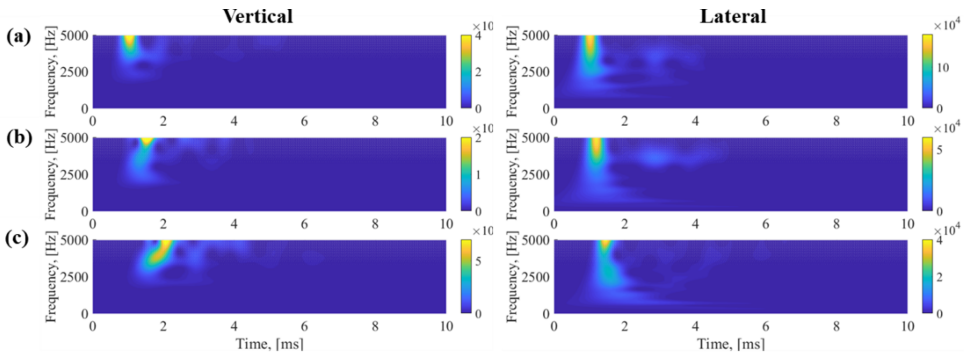


Figure 3.24: Vertical and lateral WPSs at (a) accelerometer 1; (b) accelerometer 4; (c) accelerometer 7. The results of vertical WPSs are from [28].

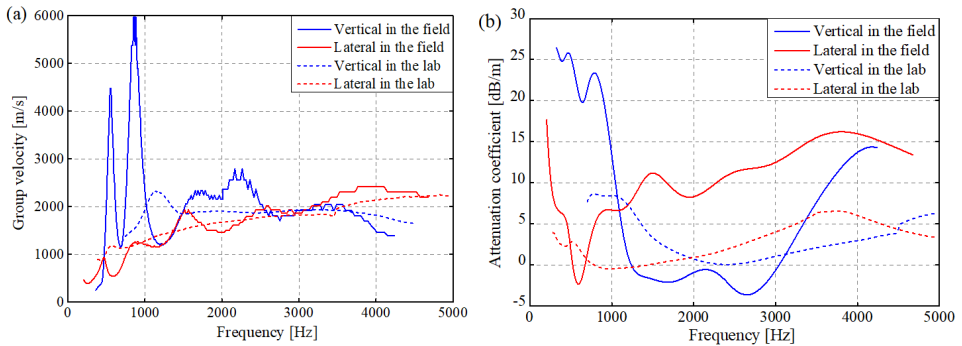


Figure 3.25: Comparison of measured group velocities and attenuation coefficients of vertical and lateral waves from the laboratory and the field. (a) Group velocities; (b) attenuation coefficient.

Some differences were also observed between the laboratory and field measurements. For example, the vertical group velocities of field measurement show strong fluctuation at lower frequencies; the values of the wave attenuation of field measurement are over three times larger than those of laboratory measurement at lower frequencies. In

the field, the dynamic behaviors of the track can be characterized into three frequency ranges depending on the contribution of the track components[30][33][38][46][47]. In the low-frequency range (0-40 Hz), the substructure layer mainly contributes to track dynamic behaviors. In the mid-frequency range (40-400 Hz), the sleeper (including sleeper pad) and ballast bed (concrete plates in ballastless track) are two key contributors to track dynamics. In the high-frequency range (400-5000 Hz), the superstructure layer including sleeper, fastener and rail, provides the major contributions. Therefore, these differences between the laboratory and field measurements at lower frequencies range may be caused by the sleepers and ballast in the field track.

3.6.2. THE INFLUENCES OF RAIL LENGTHS ON RAIL VIBRATION MODES

In the experimental setup (Figure ??), a short length of rail (4.97 m) was used for the laboratory test, while in practice, it is normally much longer. Three simulation cases were designed to study the influence of the rail lengths on rail vibration modes, as shown in Figure 3.26.

The simulated FRFs are shown in Figure 3.27a, 3.27b and 3.27c. With the increase of the rail length, the number of peaks in the FRFs considerably increases, and the fluctuation amplitudes of most peaks are reduced. That is because these peaks correspond to different types of rail vibration modes, e.g., longitudinal compression modes, vertical bending modes and lateral bending modes, respectively (as indicated by arrows in Figure 3.27). With the increase of rail length, the number of rail vibration modes increases and their frequencies are also different in the same frequency range[28]. When the rail length is up to 20 m, the fluctuation amplitudes of the vertical and lateral FRFs are so small that the FRF curves become almost smooth. Nevertheless, the fluctuation amplitude of the longitudinal FRF is still relatively strong, indicating longer rail is needed to suppress the longitudinal compression modes.

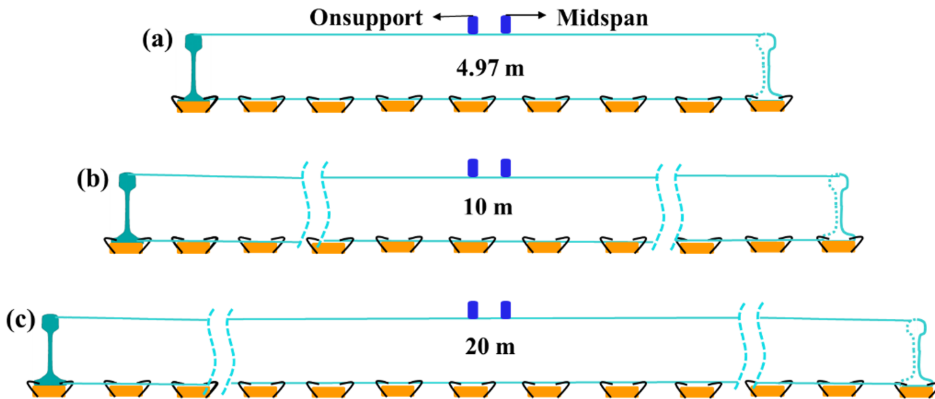


Figure 3.26: Different rail lengths in the FE simulations. (a) 4.97 m; (b) 10 m; (c) 20 m.

In the field, the nominal rail length is long, and the track dynamics are closer to the vibration responses of the 20-m rail, as shown in Figure 3.27d. Rail resonances and pinned-pinned resonances are the dominant vibration modes[33][38][46]. In some conditions,

rails may have welds and joints or defects like cracks, which cause energy reflections at these locations.

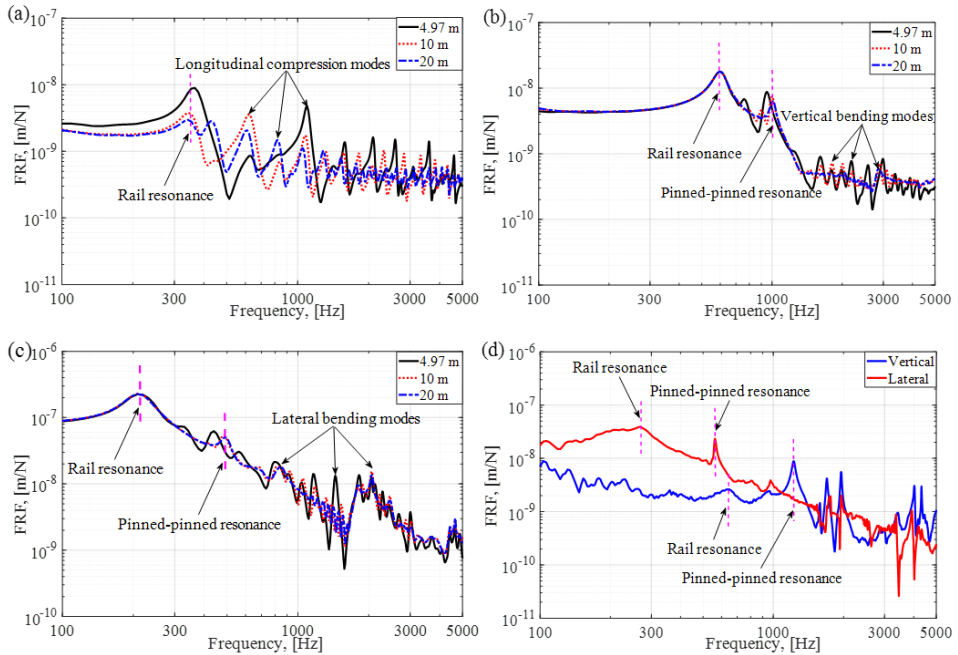


Figure 3.27: Simulated FRFs at mid-span with different rail lengths and measured FRFs at mid-span. (a) Simulated longitudinal FRFs; (b) simulated vertical FRFs; (c) simulated lateral FRFs; (d) measured vertical and lateral FRFs.

3.7. CONCLUSIONS

This chapter presents a systematic methodology to study rail vibration modes and wave propagation under fastening constraint in three directions up to 5000 Hz. This method includes three steps: 1) experimental investigation of rail vibrations under fastening constraint; 2) the validation and analysis of 3D FE modeling of rail-fastening; and 3) rail vibration control by fastening parameters. In Step 1, an experimental setup consisting of rail-fastening was constructed in the laboratory. Two types of railpads, the harder Zw692-4, and the softer FC9, were tested in this setup. ODS and SMAW measurements were conducted to identify rail vibration modes and measure wave propagation characteristics under fastening constraint. In Step 2, the 3D FE model of rail-fastening was developed and validated with the ODS and SMAW measurement results. The wavenumber-frequency dispersion curves of vibrational rail waves were derived from analyzing the experimental results. In Step 3, insights into rail vibration control were gained through sensitivity analysis of fastening dynamic parameters. Finally, the measured rail vibrations under fastening constraint in the laboratory and field tests are compared, and reasonable agreement has been found. This agreement indicates that the experimental setup of rail-fastening in the laboratory is appropriate for investigating wave propaga-

tion characteristics of the rail under fastening constraint, and the experimental results can be used to understand the vibrational rail waves in the field. The main conclusions are summarized as follows.

Vertical bending modes, longitudinal compression modes, and lateral bending modes of the rail under fastening constraint are identified from the ODS measurement but with shifted frequencies and significantly reduced vibration amplitude compared to that of free rail. The lateral torsion modes, web 1st bending modes and web 2nd bending modes of rail-fastening are not identifiable, which are possibly suppressed by the fastening constraint.

Wave propagation characteristics in terms of group velocities and attenuation coefficients were measured from WPSs of rail-fastening by SMAW measurement. Fastening constraint considerably increases the wave attenuation along the rail in all three directions. One noticeable peak occurs at around 1150 Hz in the vertical group velocity of rail-fastening. The longitudinal group velocity almost does not change under fastening constraint at a value of around 5100 m/s. Vertical wave attenuation of rail-fastening is relatively small between 1800 and 3600 Hz. Lateral wave attenuation of rail-fastening shows a dominant peak at about 3800 Hz.

Compared to the vertical and lateral directions, the fastenings constrain the longitudinal rail vibrations less strongly, which could be seen from the following facts: (1) all the longitudinal compression modes are distinguishable in FRFs up to 5000 Hz, while the vertical and lateral modes can only be observed in a narrower frequency band; (2) the fluctuation amplitude of the longitudinal modes is larger than those in the vertical and lateral directions; (3) the attenuation coefficient of a longitudinal wave is generally lower than those in the vertical and lateral directions.

The sensitivity analysis results indicate that the change of fastening stiffness and damping can control rail mode frequencies and their vibration amplitude and influence the wave propagation velocities and attenuation along the rail. Therefore, the optimization of fastening parameters could be helpful for the mitigation of short pitch corrugation and wheel-rolling noise in the relevant frequency range, which needs further research in future work.

In summary, this work contributes to a better understanding of 3D rail vibrations under fastening constraint and provides insights into rail vibration control by fastening dynamic parameters. In future work, the optimization design of rail constraint will be performed to suppress rail vibrations better. More accelerometers should be mounted on the rail to obtain better spatial resolution and to more accurately identify the rail vibration modes at higher frequencies by ODS measurement. The fastening model could be improved by, e.g., a more complex Prony series model to consider the nonlinear properties of the railpads in order to further narrow the gap between measurements and simulations.

REFERENCES

- [1] P. Zhang, S. Li, A. Núñez, and Z. Li, *Vibration modes and wave propagation of the rail under fastening constraint*, *Mechanical Systems and Signal Processing* **160**, 107933 (2021).

- [2] K. Hempelmann and K. Knothe, *An extended linear model for the prediction of short pitch corrugation*, *Wear* **191**, 161 (1996).
- [3] S. Grassie, *Rail corrugation: characteristics, causes, and treatments*, Proceedings of the Institution of Mechanical Engineers, Part F: Journal of Rail and Rapid Transit **223**, 581 (2009).
- [4] S. Li, Z. Li, A. Núñez, and R. Dollevoet, *New insights into the short pitch corrugation enigma based on 3d-fe coupled dynamic vehicle-track modeling of frictional rolling contact*, *Applied Sciences* **7**, 807 (2017).
- [5] D. Thompson, *Wheel-rail noise generation, part iii: rail vibration*, *Journal of sound and vibration* **161**, 421 (1993).
- [6] D. Thompson, B. Hemsworth, and N. Vincent, *Experimental validation of the twins prediction program for rolling noise, part 1: description of the model and method*, *Journal of sound and vibration* **193**, 123 (1996).
- [7] D. Thompson, P. Fodiman, and H. Mahé, *Experimental validation of the twins prediction program for rolling noise, part 2: results*, *Journal of sound and vibration* **193**, 137 (1996).
- [8] H. Ilias, *The influence of railpad stiffness on wheelset/track interaction and corrugation growth*, *Journal of Sound and Vibration* **227**, 935 (1999).
- [9] Y. Shen, Z. Xing, S. Yang, and J. Sun, *Parameters optimization for a novel dynamic vibration absorber*, *Mechanical Systems and Signal Processing* **133**, 106282 (2019).
- [10] D. Thompson, C. Jones, T. Waters, and D. Farrington, *A tuned damping device for reducing noise from railway track*, *Applied acoustics* **68**, 43 (2007).
- [11] X. Wang and B. Yang, *Transient vibration control using nonlinear convergence active vibration absorber for impulse excitation*, *Mechanical Systems and Signal Processing* **117**, 425 (2019).
- [12] A. Johansson, J. C. Nielsen, R. Bolmsvik, A. Karlström, and R. Lundén, *Under sleeper pads—influence on dynamic train–track interaction*, *Wear* **265**, 1479 (2008).
- [13] K. Wei, Q. Yang, Y. Dou, F. Wang, and P. Wang, *Experimental investigation into temperature- and frequency-dependent dynamic properties of high-speed rail pads*, *Construction and Building Materials* **151**, 848 (2017).
- [14] Å. Fenander, *Frequency dependent stiffness and damping of railpads*, Proceedings of the Institution of Mechanical Engineers, Part F: Journal of rail and rapid transit **211**, 51 (1997).
- [15] D. Thompson, W. Van Vliet, and J. Verheij, *Developments of the indirect method for measuring the high frequency dynamic stiffness of resilient elements*, *Journal of Sound and Vibration* **213**, 169 (1998).

- [16] J. Maes, H. Sol, and P. Guillaume, *Measurements of the dynamic railpad properties*, Journal of Sound and Vibration **293**, 557 (2006).
- [17] M. Oregui, A. De Man, M. Woldekidan, Z. Li, and R. Dollevoet, *Obtaining railpad properties via dynamic mechanical analysis*, Journal of Sound and Vibration **363**, 460 (2016).
- [18] L. B. Eldred, W. P. Baker, and A. N. Palazotto, *Kelvin-voigt versus fractional derivative model as constitutive relations for viscoelastic materials*, AIAA journal **33**, 547 (1995).
- [19] B. Ripke, *Hochfrequente Gleismodellierung und Simulation der Fahrzeug-Gleis-Dynamik unter Verwendung einer nichtlinearen Kontaktmechanik* (VDI-Verlag, 1995).
- [20] Å. Fenander, *A fractional derivative railpad model included in a railway track model*, Journal of Sound and Vibration **212**, 889 (1998).
- [21] J. Xu and J. Li, *Stochastic dynamic response and reliability assessment of controlled structures with fractional derivative model of viscoelastic dampers*, Mechanical Systems and Signal Processing **72**, 865 (2016).
- [22] M. Oregui, Z. Li, and R. Dollevoet, *An investigation into the modeling of railway fastening*, International Journal of Mechanical Sciences **92**, 1 (2015).
- [23] J. Egana, J. Vinolas, and M. Seco, *Investigation of the influence of rail pad stiffness on rail corrugation on a transit system*, Wear **261**, 216 (2006).
- [24] D. Thompson, C. Jones, T. Wu, and A. De France, *The influence of the non-linear stiffness behaviour of rail pads on the track component of rolling noise*, Proceedings of the Institution of Mechanical Engineers, Part F: Journal of rail and rapid transit **213**, 233 (1999).
- [25] K. Wei, F. Wang, P. Wang, Z.-x. Liu, and P. Zhang, *Effect of temperature-and frequency-dependent dynamic properties of rail pads on high-speed vehicle-track coupled vibrations*, Vehicle System Dynamics **55**, 351 (2017).
- [26] M. Oregui, A. Núñez, R. Dollevoet, and Z. Li, *Sensitivity analysis of railpad parameters on vertical railway track dynamics*, Journal of Engineering Mechanics **143**, 04017011 (2017).
- [27] Z. Yang, A. Boogaard, R. Chen, R. Dollevoet, and Z. Li, *Numerical and experimental study of wheel-rail impact vibration and noise generated at an insulated rail joint*, International Journal of Impact Engineering **113**, 29 (2018).
- [28] P. Zhang, S. Li, A. Núñez, and Z. Li, *Multimodal dispersive waves in a free rail: Numerical modeling and experimental investigation*, Mechanical Systems and Signal Processing **150**, 107305 (2021).
- [29] T. Hayashi, W.-J. Song, and J. L. Rose, *Guided wave dispersion curves for a bar with an arbitrary cross-section, a rod and rail example*, Ultrasonics **41**, 175 (2003).

- [30] A. Man, *Dynatrack: A survey of dynamic railway track properties and their quality*. (2004).
- [31] M. Oregui, Z. Li, and R. Dollevoet, *Identification of characteristic frequencies of damaged railway tracks using field hammer test measurements*, *Mechanical Systems and Signal Processing* **54**, 224 (2015).
- [32] K. Giannakos, *Modeling the influence of short wavelength defects in a railway track on the dynamic behavior of the non-suspended masses*, *Mechanical Systems and Signal Processing* **68**, 68 (2016).
- [33] S. Grassie, R. Gregory, D. Harrison, and K. Johnson, *The dynamic response of railway track to high frequency vertical excitation*, *Journal of Mechanical Engineering Science* **24**, 77 (1982).
- [34] L. Xu and W. Zhai, *A three-dimensional model for train-track-bridge dynamic interactions with hypothesis of wheel-rail rigid contact*, *Mechanical Systems and Signal Processing* **132**, 471 (2019).
- [35] R. Cettour-Janet, A. Barbarulo, F. Letourneaux, and G. Puel, *An arnoldi reduction strategy applied to the semi-analytical finite element method to model railway track vibrations*, *Mechanical Systems and Signal Processing* **116**, 997 (2019).
- [36] I. I. Setshedi, P. W. Loveday, C. S. Long, and D. N. Wilke, *Estimation of rail properties using semi-analytical finite element models and guided wave ultrasound measurements*, *Ultrasonics* **96**, 240 (2019).
- [37] M. Oregui, Z. Li, and R. Dollevoet, *An investigation into the vertical dynamics of tracks with monoblock sleepers with a 3d finite-element model*, *Proceedings of the Institution of Mechanical Engineers, Part F: Journal of Rail and Rapid Transit* **230**, 891 (2016).
- [38] S. Grassie, R. Gregory, and K. Johnson, *The dynamic response of railway track to high frequency lateral excitation*, *Journal of Mechanical Engineering Science* **24**, 91 (1982).
- [39] S. Grassie, R. Gregory, and K. Johnson, *The dynamic response of railway track to high frequency longitudinal excitation*, *Journal of Mechanical Engineering Science* **24**, 97 (1982).
- [40] N. M. M. Maia and J. M. M. e Silva, *Theoretical and experimental modal analysis* (Research Studies Press, 1997).
- [41] B. J. Schwarz and M. H. Richardson, *Introduction to operating deflection shapes*, *CSI Reliability Week* **10**, 121 (1999).
- [42] M. Vetterli and J. Kovacevic, *Wavelets and subband coding*, BOOK (Prentice-hall, 1995).

- [43] A. Grinsted, J. C. Moore, and S. Jevrejeva, *Application of the cross wavelet transform and wavelet coherence to geophysical time series*, *Nonlinear processes in geophysics* **11**, 561 (2004).
- [44] F. L. di Scalea and J. McNamara, *Measuring high-frequency wave propagation in railroad tracks by joint time–frequency analysis*, *Journal of sound and vibration* **273**, 637 (2004).
- [45] W. Sachse and Y.-H. Pao, *On the determination of phase and group velocities of dispersive waves in solids*, *Journal of applied Physics* **49**, 4320 (1978).
- [46] S. Grassie, R. Gregory, and K. Johnson, *The dynamic response of railway track to high frequency longitudinal excitation*, *Journal of Mechanical Engineering Science* **24**, 97 (1982).
- [47] C. Shen, R. Dollevoet, and Z. Li, *Fast and robust identification of railway track stiffness from simple field measurement*, *Mechanical Systems and Signal Processing* **152**, 107431 (2021).

4

PARAMETRIC INVESTIGATION OF RAILWAY FASTENINGS INTO THE DEVELOPMENT AND MITIGATION OF SHORT PITCH CORRUGATION

This chapter conducts a parametric investigation of fastenings to understand the corrugation development mechanism and gain insight into corrugation mitigation. A three-dimensional finite element vehicle-track dynamic interaction model was employed, which considers the coupling between the structural dynamics and the contact mechanics, and the damage mechanism is assumed to be differential wear. Various fastening models with different configurations, boundary conditions, and stiffness and damping parameters were built up and analyzed. These models may represent different service stages of fastenings in the field. Besides, the effect of modeled track length on corrugation features was studied. The results indicate that (1) fastening parameters and modeling play an important role in corrugation development. To better understand the corrugation features in the field and reliably predict corrugation in the numerical simulation, it is suggested to carefully examine the service stages of fastenings to determine appropriate parameters. (2) The fastening longitudinal constraint to the rail is the major factor determining corrugation development. The fastening vertical and lateral constraints influence corrugation features in terms of spatial distribution and wavelength components. (3) The increase of fastening constraint in the longitudinal dimension helps to mitigate corrugation. Meanwhile, the inner fastening constraint in the lateral dimension is necessary for corrugation alleviation. (4) The increase of fastening longitudinal stiffness and damping can reduce the vibration amplitudes of longitudinal compression modes and thus reduces the track corrugation propensity.

Parts of this chapter is based on the paper in P.Zhang [1]

4.1. INTRODUCTION

Short pitch corrugation (refers to corrugation hereinafter) is a periodic rail head defect recognized by shining peaks and dark troughs (see Figure 4.1). Corrugation typically falls in the wavelength range of 20-80 mm with amplitude up to 100 μm , and mainly occurs in straight tracks or gentle curves[2][3]. Corrugation excites large wheel-rail impact forces, accelerating the deterioration of track components and inducing other rail defects, such as squats[4], as shown in Figure 4.1. Besides, a high level of ‘roaring’ noise generated by corrugation is a nuisance to passengers and residents near railway lines. Although corrugation has been a problem to railway managers worldwide for over a century, there has been no ultimate countermeasure against it so far, and the most efficient and reliable solution is grinding. However, grinding increases the maintenance cost and also reduces the railway network availability. Therefore, it is essential to understand the corrugation formation mechanism and find effective solutions.

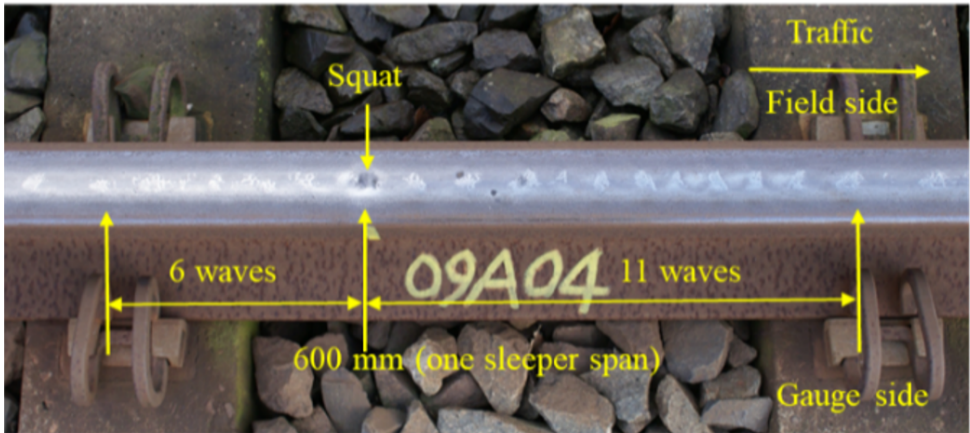


Figure 4.1: Short pitch corrugation with a wavelength of about 35 mm. The squat was induced by corrugation and occurred at around 1/3 sleeper span. The photo was taken near Steenwijk, the Netherlands.

The mechanism of corrugation formation is generally considered to consist of two features: the wavelength-fixing mechanism and the damage mechanism[3]. The damage mechanism of short pitch corrugation is commonly assumed to be wear[3][5][6][7][8]. The wavelength-fixing mechanism is mostly explained by the interplays of the structural dynamics and the contact mechanics. The structural dynamics determine possible corrugation wavelengths while the contact mechanics creates a contact filtering effect which suppresses very short and long wavelength corrugations from growing[6][7][9] and only corrugation in the short pitch range (i.e., 20-80 mm) can develop. Pinned-pinned resonance, where rail vibrates with the wavelength of two sleeper spans, is usually attributed to be the corrugation wavelength-fixing mechanism[6][7][10]. It is therefore also defined in[2] as pinned-pinned resonance corrugation. Nevertheless, one difficulty with this mechanism is that it cannot easily explain the relatively small variation of corrugation wavelength with train speed, as observed in the field. Additionally, ac-

According to this mechanism, corrugation may occur everywhere above the sleeper support after a certain amount of train passages, and the embedded rail system that eliminates pinned-pinned modes should be corrugation-free, which are both not the case in practice[3][11].

Therefore, corrugation formation mechanism seems more complex than the current understanding. Further research efforts into this problem are necessary. New insights [8] were gained into the corrugation development enigma employing a three-dimensional (3D) finite element (FE) vehicle-track dynamic interaction model. The main insights include: (1) the rail longitudinal vibration modes are considered dominant for corrugation initiation; (2) the consistency in the longitudinal and vertical contact forces, the resulting differential wear and the existing corrugation should determine the continuous growth of corrugation. Based on these insights, together with an "initial excitation" governed by the fastening model, consistent corrugation initiation and growth have been successfully reproduced from a smooth rail[12]. The simulated corrugation shares features similar to the corrugation observed and measured in the field in terms of spatial distribution and major wavelength components, indicating the validity of the hypothesis for the corrugation development process proposed in[12].

It is worth emphasizing that in[12] the fastening models, identified as the initial excitation to the vehicle-track system, play a significant role in corrugation initiation. In those situations, the fastening models cannot effectively suppress the rail longitudinal compression modes, and thus dynamic longitudinal contact force arises, resulting in initial differential wear. Corrugation can hence continuously initiate and grow if the consistency condition is satisfied[12]. Field experiments also indicate that corrugation formation is sensitive to the types of fastenings[13][14]. It is reported that in[15] fastening modeling significantly influences the high-frequency vehicle-track interaction at singular rail surface defects, such as, squats. It was suggested that the service stages of fastenings, mainly of the railpads, need to be carefully examined to determine an appropriate fastening model for reliable predictions of squat development. Considering the close relationship between rail squats and corrugation observed in the field[16] and their similarity in nature in terms of impact loadings, and in light of[8] and [12], in this chapter, we perform a systematically parametric investigation of fastenings employing a 3D FE vehicle-track interaction model. The purpose of this work is twofold: (1) to further understand the corrugation development mechanism with various fastening constraint that correspond to different service stages of fastenings; (2) to gain insights into the corrugation mitigation by new fastening design.

The structure of this chapter is as follows. Section 4.2 describes the methodology of this chapter, including the modeling methods of vehicle-track dynamic interaction, fastenings and wear, and the simulation procedure for corrugation development. Section 4.3 analyses the influence of fastening configurations and boundary conditions on corrugation formation. Section 4.4 studies the effect of fastening parameters (i.e., stiffness and damping) on corrugation development. Section 4.5 discuss the effects of different track lengths. Section 4.6 discusses the corrugation formation mechanism under different fastening constraint, and some possible corrugation mitigation approaches. Finally, the main conclusions and lines of further research are presented in Section 4.7.

4.2. METHODOLOGY

4.2.1. 3D FE VEHICLE-TRACK INTERACTION MODEL

Figure 4.2 shows the 3D transient FE vehicle-track interaction model built with Ansys/LS-dyna. A Cartesian coordinate system was adopted, where the axes x, y and z are in the longitudinal (rolling), lateral and vertical directions. The model considered a straight track and the vehicle-track system was assumed to be symmetric about the central and vertical plane of the track. Therefore, a half-track and a half wheelset were included. The structures above the primary suspension of the vehicle were simplified as mass elements as their vibration frequency is usually not high than 10 Hz[17]. The wheel has a nominal radius of 0.46 m with a conicity of 1/40. The rail profile is UIC 54E1 with 1/40 inclination. The wheelset, rail, and sleeper were all modeled with 3D solid elements according to their nominal geometry and material properties. The finest element size of the rail is 0.8 mm in the solution zone. The sleeper was connected to the rail through the fastenings and supported by the ballast. The primary suspension and the ballast were modeled as multiple spring-damper elements. Several fastening models corresponding to different service stages of fastenings in the field track were built up and described in Section 4.2.2. The track length is 20.54 m, including 34 sleeper spans. Besides, the half (10.27 m) and twice (41.08 m) length of this track have also been considered to study their influences on corrugation features in Section 4.5. The parameters of the vehicle-track system are listed in Table 4.1, which are commonly used to study the Dutch railway system[8][10][18].

Table 4.1: Vehicle and track parameters[8] .

Parameter		Values	Parameters		Values
Sprung mass		7200kg	Wheel and rail material	Young's modulus	210 GPa
Primary suspension	Stiffness	1.15 MN/m		Poisson's ratio	0.3
	Damping	2.5 kNs/m	Density	7,800 kg/m ³	
Railpad	Stiffness	1,300 MN/m	Sleeper	Young's modulus	38.4 GPa
	Damping	45 kNs/m		Poisson's ratio	0.2
Ballast	Stiffness	45 MN/m		Mass density	2520 kg/m ³
	Damping	32 kNs/m	Spacing(L)	0.6 m	

The contact between the wheel and rail was modeled with a surface-to-surface contact algorithm based on a penalty approach[19]. The mechanical contact filtering effect is inherently included in the numerical calculations[15]. Coulomb's frictional law was applied with a friction coefficient of 0.4. The traction coefficient is 0.15. The time step for the explicit mechanical solver was 4.67×10^{-8} s, which is small enough to meet the Courant stability condition[20]. The model simulates a Dutch passenger vehicle with a speed of 140 km/h.

This vehicle-track interaction model has been extensively validated in terms of frictional rolling contact solutions[20][21], wheel dynamics [22], and track dynamics[23][24]. The model also explained the dynamic contact problems such as rail squats and the corrugation-like waves after squats [4][16][25]. Hence, it is concluded in [26] that "the model provides a good explanation for the development of corrugation initiated from isolated rail-head irregularities". In addition, this model has been used to gain new insights into corrugation development mechanism in[8] and further successfully reproduce the con-

sistent initiation and growth of corrugation in[12]. This chapter extends its application for parametric investigation of fastenings to better understand the corrugation development mechanism and gain insights into corrugation mitigation by the fastening design.

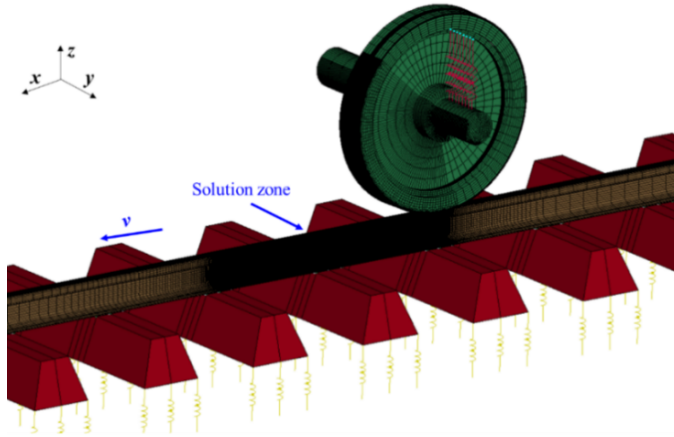


Figure 4.2: 3D FE vehicle-track interaction model.



Figure 4.3: Worn railpads from Dutch railway. (a) Example one of worn railpad; (b) Example two of worn railpad.

4.2.2. FASTENING MODELS

The railway fastenings, mainly consisting of railpads and clamps, are used to constrain the rail to the sleepers in the vertical, longitudinal and lateral directions, and filter out the high-frequency vibrations from the rail. Due to the dynamic train loads during long-term service, fastenings become gradually degraded. Figure 4.4 shows two examples of worn railpads observed on the Dutch railway. Due to the irregular wear, railpads lose

their original geometry, and the rail may not necessarily be in uniform contact with the railpads and hence not be uniformly constrained. Different configurations of fastenings with various boundary conditions and parameters are designed (see Table 4.2) to consider these constraining conditions and analyze their influences on corrugation development.

Table 4.2: Variation of fastening models..

Fastening model(RPM)	Description	Purposes
1	Corresponding to Figure 4.4a Configuration: 3x4 Vertical: spring-damper pairs Longitudinal: rigid constraint Lateral: rigid constraint	To model a nominal track situation.
2 3 4 5	Corresponding to Figure 4.4b 1x4 in the 2 nd column 2x4 in the 1 st and 3 rd columns 3x2 in the 2 nd and 3 rd rows(inner) 3x2 in the 1 st and 4 th rows(outer)	To investigate the influence of fastening configurations on corrugation development.
6 7 8 9	Corresponding to Figure 4.5 Releases the longitudinal fastening constraint of RPM1 in the 1 st and 3 rd columns Releases the longitudinal fastening constraint of RPM1 in the 2 nd column Releases the longitudinal fastening constraint of RPM1 in the 1 st and 4 th rows Releases the longitudinal fastening constraint of RPM1 in the 2 nd and 3 rd rows	To investigate the influence of fastening boundary conditions on corrugation development.
10 11 12	Corresponding to Figure 4.6 Configuration: 3x4 Vertical and Lateral: the same as RPM1 Longitudinal springs with stiffness of 150 MN/m Longitudinal springs with stiffness of 300 MN/m Longitudinal springs with stiffness of 900 MN/m	To investigate the influence of fastening longitudinal stiffness on corrugation development.
13 14	Add longitudinal damping of 6 kNs/m to RPM11 Add longitudinal damping of 24 kNs/m to RPM11	To investigate the influence of fastening longitudinal damping on corrugation development.

FASTENING MODELS WITH DIFFERENT CONFIGURATIONS

Figure 4.4a shows a fastening model applied in the FE vehicle-track interaction model, designated as RPM1. In the vertical direction, the fastening was represented by 3x4 spring-damper elements (i.e., 3 columns in the longitudinal dimension and 4 rows in the lateral), connecting the rail bottom nodes (marked by R) and sleeper nodes (marked by S). Each of the 12 elements has the same parameters, equal to 1/12 of the nominal values. The longitudinal and lateral restrictions of the fastening were considered as rigid constraint to the rail nodes. Although this simplifies the nominal track situation, it has been proved to be appropriate for representing track dynamics[24] and wheel-rail dynamic interaction[15][18][27]. The schematic drawing of RPM1 is shown in Figure 4.4b. The red and yellow triangles represent rigid constraints to the rail nodes from fastenings in the longitudinal and lateral directions, respectively. To consider non-uniform constraints of fastenings due to, i.e., railpad degradation, other four types of configurations are designed, 1x4 in the 2nd column (RPM2), 2x4 in the 1st and 3rd columns (RPM3), 3x2 in the 2nd and 3rd rows (RPM4), 3x2 in the 1st and 4th rows (RPM5), respectively, as shown in Figure 4.4b. RPM4 constrains the inner rail nodes under the rail web along the lateral dimension while RPM5 the outer.

FASTENING MODELS WITH DIFFERENT BOUNDARY CONDITIONS

It is reported in[8][12] that differential wear that causes initial corrugation is dominated by rail longitudinal compression modes and sensitive to the longitudinal boundary conditions of fastenings. Therefore in this chapter, the longitudinal boundary conditions of fastenings are varied to investigate their influences on corrugation development and also attempt to gain insight for corrugation mitigation. Figure 4.5 shows schematic drawings of four fastening models with different boundary conditions, RPM6 RPM9. Compared to RPM1, RPM6 and RPM7 vary the column number of the fastening longitudinal boundary conditions in the longitudinal dimension, while RPM8 and RPM9 vary the row number of in the lateral dimension. Specifically, RPM6 releases the fastening longitudinal constraint of RPM1 in the 1st and 3rd columns, while RPM7 in the second column. RPM8 keeps the fastening longitudinal constraint of RPM1 in the 2nd and 3rd rows (inner), while RPM9 in the 1st and 4th rows (outer). The lateral boundary conditions of the RPM6 RPM9 are the same as those of RPM1.

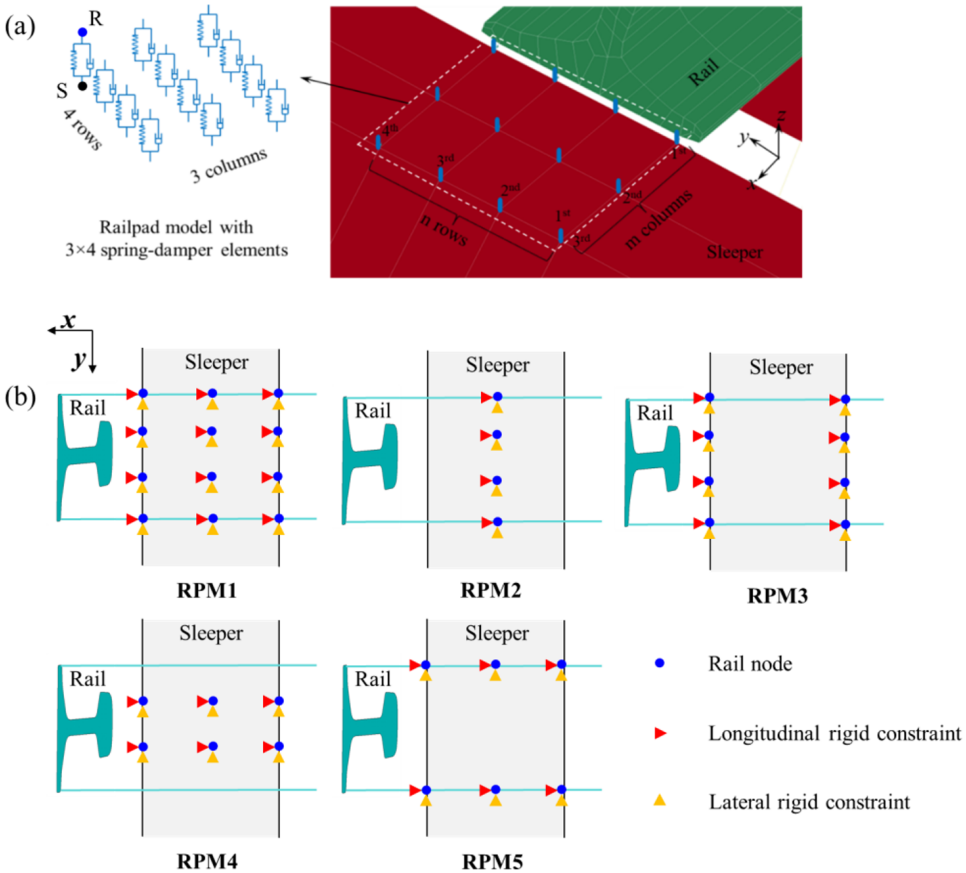


Figure 4.4: Fastening models with different configurations. (a) Fastening model RPM1 in the FE vehicle-track interaction model; (b) schematic drawings of fastening models RPM1 RPM5 with different configurations.

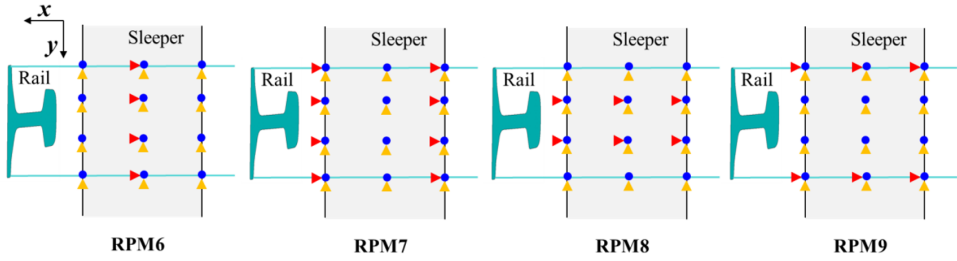


Figure 4.5: Schematic drawings of fastening models RPM6 RPM9 with different longitudinal boundary conditions.

4

FASTENING MODELS CONSIDERING LONGITUDINAL STIFFNESS AND DAMPING

The fastening models defined in Section 4.2.2.2 simplified the fastening longitudinal restriction as rigid constraint to the rail nodes. In reality, the rail has certain flexibility on the elasticity of railpads in the longitudinal direction, similar to that in the vertical direction. Therefore, a more realistic representation of fastening longitudinal constraint should consider the longitudinal stiffness and damping by, such as multiple spring-damper elements, as shown in Figure 4.6.

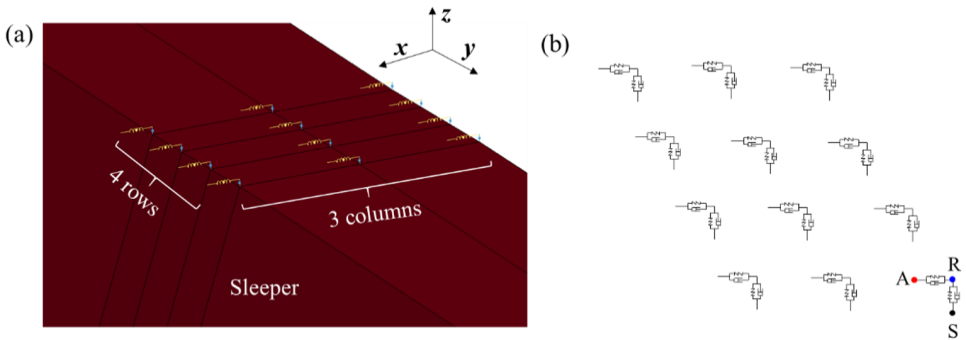


Figure 4.6: The fastening model considering longitudinal stiffness and damping. (a) Fastening model in the FE vehicle-track interaction model; (b) schematic drawings of the fastening model. 'R' refers to rail nodes, 'S' refers to sleeper nodes, and 'A' refers to end nodes of the longitudinal spring-damper pairs.

Unlike the vertical ones, the fastening longitudinal parameters have been barely reported in the literature. Zhang et al.[28] studied the 3D rail vibrations under fastening constraint, and calibrated 3D fastening parameters with ZW 692 railpads by best fitting to the hammer test measurements. The derived longitudinal stiffness and damping of fastenings are around 160 MN/m and 6 kNs/m. Oregui et al.[29] compared the master curves of new and worn railpads and found that the damping behavior of the worn railpads is nearly non-existent and thereby becomes purely elastic. Besides, the stiffness of worn railpads is significantly reduced due to aging and degradation. Five fastening models with different longitudinal stiffness and damping values are designed considering different types of railpads and the aging effect. RPM10-12 modeled fastenings by 3×4 spring

elements with the stiffness values of 150 MN/m, 300 MN/m, and 900 MN/m, respectively. Damping is not considered in these three models to simulate the severely worn railpads. RPM13-14 simulated fastenings by 3×4 spring-damper pairs with the damping of 6 kNs/m and 24 kNs/m, respectively. The stiffness of these two models is 300 MN/m, the same as RPM11.

4.2.3. WEAR MODEL

The damage by wear at a point in the rail surface is assumed to be proportional to the accumulated frictional work done during wheel passages[9][17][30]. When a surface element represents such a point, the frictional work is calculated for each wheel passage, i.e., from the element entering until leaving the contact patch, as follows:

$$w(x, y) = kW_f(x, y) = k \sum_{i=1}^N \tau_i(x, y) v_i(x, y) \Delta t \quad (4.1)$$

where k is the wear coefficient, $W_f(x, y)$ is the frictional work, $\tau_i(x, y)$ and $v_i(x, y)$ the local tangential stress and micro-slip, respectively, N the number of time steps Δt during which a node passes the contact patch.

4.2.4. SIMULATION PROCEDURE FOR CORRUGATION DEVELOPMENT WITH DIFFERENT FASTENING MODELS

The simulation procedure for corrugation development includes four steps[12], as shown in Figure 4.7.

In Step 1, one of the fastening models from Table 4.1 is applied in the 3D FE vehicle-track interaction model. The rail is smooth in the beginning, i.e., without corrugation. Let the wheel roll over the track and calculate the rail wear.

In Step 2, if this wear has negligible fluctuation amplitude, corrugation will not develop with the current fastening model, which will then be dropped. Otherwise, it means this fastening model can serve as the initial excitation to the vehicle-track system. Rail longitudinal compression modes are excited, causing dynamic longitudinal contact force and initial differential wear. This differential wear will result in the very initial corrugation whose severity is quantified with a maximal peak to trough distance $(2A_{max})_0$.

In Step 3, the obtained initial corrugation of $(2A_{max})_0$ is applied to the rail surface. It is proportional to and in anti-phase with the initial differential wear. Anti-phase means a wear peak causes a corrugation trough. Similarly, additional wear from Step 4 is added to the corrugation in the subsequent wheel passages. The rail is thus with corrugation, which can be in its initial form of $(2A_{max})_0$ as from Step 1 or in a more advanced form of $(2A_{max})_i$ ($i = 1, 2, 3, \dots$) as from Step 4.

In Step 4, let the wheel roll over the corrugated rail, calculate the differential wear caused by the joint excitation from the fastening model and the corrugation. Subsequently, check if the consistency condition is satisfied, i.e., if the differential wear is in phase with the initial differential wear and in anti-phase with the existing corrugation: If the condition is satisfied, it means that corrugation can continuously grow, and then repeat Steps 2, 3 and 4 with increased $(2A_{max})_i$ until a limiting amplitude $(2A_{max})_c$, with which the condition is not satisfied anymore. When the condition is not satisfied, the simulation

will stop and another fastening model will be analyzed, repeating Step 1 to 4. More details about the simulation procedure can be found in [12].

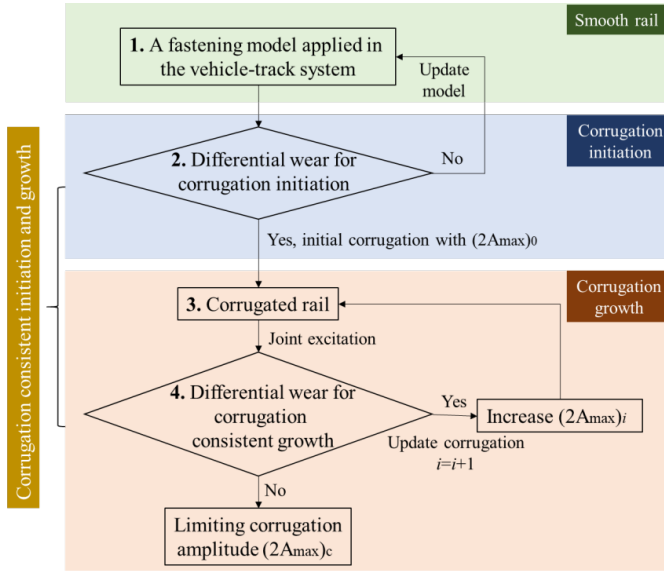


Figure 4.7: The simulation procedure for corrugation development with different fastening models [12]

4.3. THE INFLUENCE OF FASTENING CONFIGURATIONS AND BOUNDARY CONDITIONS ON CORRUGATION DEVELOPMENT

4.3.1. FASTENING CONFIGURATIONS

Figure 4.8 shows the spatial distributions of differential wear under increasing corrugation amplitude with two fastening configurations RPM1 and RPM2. The fluctuation amplitude of the initial differential wear with RPM2 is considerably larger than that with RPM1. With RPM 1, after applying corrugation amplitude $2A_{max} = 10 \mu\text{m}$, the differential wear due to the joint excitations of the initial excitation and the corrugation tends to vary from initial differential wear and the consistency condition for corrugation growth can barely hold. When further increasing the corrugation amplitude up to $2A_{max} = 40 \mu\text{m}$, the differential wear tends to be in anti-phase with the initial differential wear and in-phase with the existing corrugation, as shown in Figure 4.8a. In this case, the existing corrugation will be leveled out. In contrast, with RPM 2, the consistency condition between differential wear and corrugation is still satisfied when amplitude $2A_{max} = 40 \mu\text{m}$, as shown in Figure 4.8b, indicating corrugation can at least continuously grow up to $40 \mu\text{m}$. With a relatively large trial amplitude $2A_{max} = 160 \mu\text{m}$, the differential wear becomes anti-phase with the initial differential wear, and the existing corrugation will be erased, indicating the corrugation with RPM2 cannot infinitely grow, e.g., limiting $2A_{max}$ not exceeding $160 \mu\text{m}$. There should be an intermediate stage of corrugation amplitude, limiting amplitude in Figure 4.7, between $40 \mu\text{m}$ and $160 \mu\text{m}$, in which the

corrugation development reaches a saturation state without further accumulation of differential wear.

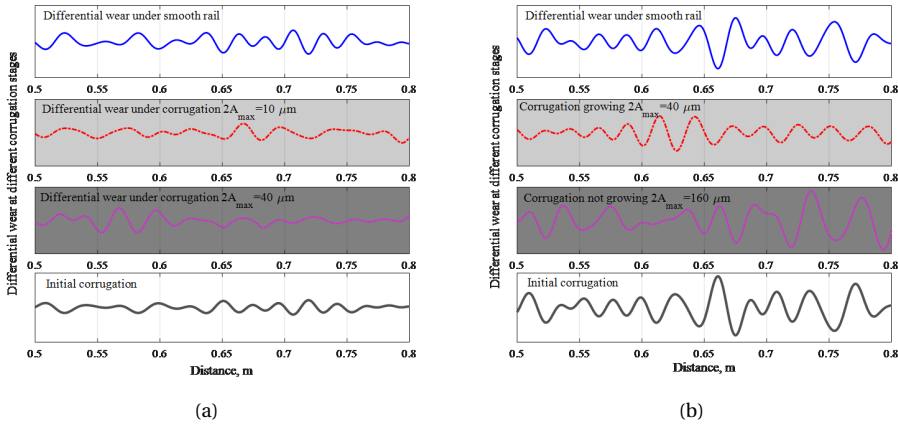


Figure 4.8: Differential wear in the spatial domain with fastening configurations RPM1 and RPM2. (a) Differential wear at different corrugation stages with RPM1; (b) differential wear at different corrugation stages with RPM2.

Overall, with fastening configuration RPM1, corrugation can barely grow up to $10 \mu\text{m}$, while with RPM2, it can at least grow up to $40 \mu\text{m}$. Compared to RPM2 (1×4 configuration), RPM1 (3×4 configuration) provides a much stronger longitudinal constraint to the rail, as shown in Figure 4.4b. Hence rail longitudinal compression modes with RPM1 are more severely suppressed, leading to considerably smaller fluctuation amplitudes of the dynamic longitudinal contact forces and the resulting initial differential wear. From these two cases, we can conclude that the limiting corrugation amplitude is dependent on the intensity of the initial excitation determined by the fastening model and the resulting dynamic longitudinal contact force and initial differential wear. Higher fluctuation amplitude of initial differential wear tends to grow into severer corrugation with larger limiting amplitude. Initial differential wear rate can hence be considered as an indicator of the possible severity of the maximum mature corrugation. In addition, according to the consistency condition, corrugation has the same features as initial differential wear in terms of spatial distribution and major wavelength components. Therefore, we mainly analyze the influence of fastening models on initial differential wear hereinafter. Figure 4.9 shows the features of initial differential wear under the various fastening configurations of RPM1 RPM5. Comparing the results of RPM1 RPM3 in Figure 4.9a and 4.9c, it is found that the variation of column number of fastening constraint significantly influences the spatial distribution and wavelength components of initial differential wear. Specifically, the result of the RPM1 model shows the lowest level of initial differential wear. In the latter two configurations, i.e., RPM 2 and RPM 3, initial differential wear has relatively larger fluctuation amplitudes and contains major wavelength components between 20 mm and 50 mm (corresponding to about 800–2000 Hz with a speed of 140 km/h). One difference between the two latter configurations is that there

are three major wavelength components at 22.0 mm, 28.6 mm, and 37.7 mm with RPM2, while there contains only one major wavelength component at 25.6 mm with RPM3. Besides, the fluctuation amplitude of initial differential wear with RPM2 is larger than that with RPM3. That is because RPM3 (2×4 configuration) provides a stronger fastening constraint to the rail than RPM2 (1×4 configuration), and thus more longitudinal compression modes are suppressed with reduced vibration amplitudes.

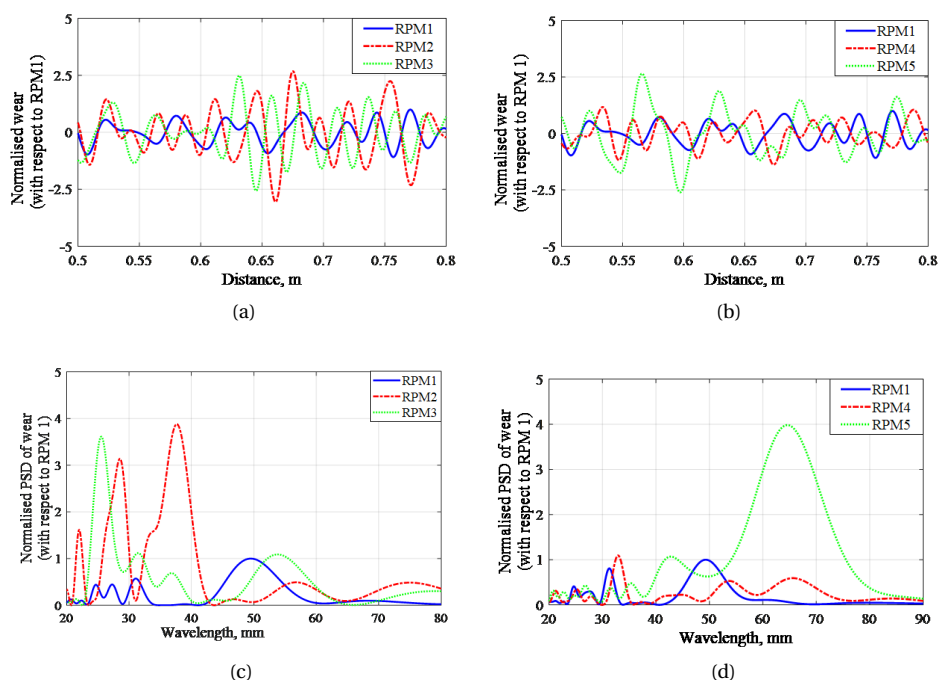


Figure 4.9: Initial differential wear in spatial and wavelength domains with different fastening configurations RPM1 RMP5. (a) Initial differential wear in the spatial domain under RPM1 RPM3; (b) initial differential wear in the spatial domain under RPM1, RPM4 and RPM5; (c) initial differential wear in the wavelength domain under RPM1 RPM3; (d) initial differential wear in the wavelength domain under RPM1, RPM4 and RPM5.

Comparing the results of RPM4 (3×2 configuration, inner, see Figure 4.4b) and RPM1 (3×4 configuration) in Figure 4.9b and 4.9d, it is found that initial differential wear with RPM4 has a low level similar to that of RPM1. In comparison to RPM1, RPM4 removes the fastening constraint in the 1st and 4th rows. Corrugation can barely grow in this condition, as shown in Figure 4.8a. This result indicates that the inner fastening constraint in the 2nd and 3rd rows can effectively suppress rail longitudinal compression modes and mitigate corrugation. When we removed the fastening constraint of RPM1 in the 2nd and 3rd rows (corresponding to RPM5, 3×2 configuration, outer, see Figure 4.4b), a dominant wavelength component at about 64.7 mm (about 600 Hz with a speed of 140 km/h) with larger fluctuation amplitude was observed in Figure 4.9b and 4.9d. The

fluctuation amplitude of wavelength components between 20 mm and 50 mm remains small. These results indicate that the outer fastening constraint in the 1st and 4th rows can only mitigate corrugation with relatively shorter wavelengths (i.e., 20–50 mm), while the relatively longer-wavelength corrugation (i.e., 64.7 mm) can still develop.

In summary, fastening configurations significantly influence the spatial distribution and wavelength components of corrugation. Specifically, initial differential wear and corrugation are sensitive to the fastening configurations in the longitudinal dimension, i.e., the column number of spring-damper elements. When increasing the column number from one (RPM2) to two (RPM3), the major wavelength components of initial differential wear decrease from three to one, and the fluctuation amplitude also reduces. When further increasing the column number to three (RPM1), initial differential wear has the lowest level and corrugation barely grows. These results point out a direction for corrugation mitigation by increasing the column number or the fastening constraint in the longitudinal dimension. With the same column number as RPM1, it is shown that the variation of row number (RPM4 and RPM5) can effectively change the major corrugation wavelength components. Specifically, the removal of the inner fastening constraint in the 2nd and 3rd rows (RPM5) leads to the development of the relatively longer-wavelength corrugation. Therefore, for corrugation mitigation, inner fastening constraint in the 2nd and 3rd rows are necessary.

4.3.2. FASTENING LONGITUDINAL BOUNDARY CONDITIONS

Figure 4.10 shows the features of initial differential wear with fastening models under different longitudinal boundary conditions (RPM1 and RPM6–RPM9, see Figure 4.5). Comparing the results of RPM1, RPM6, and RPM7 in Figure 4.10a and 4.10c, it is found that the variation of column number of longitudinal rigid constraints considerably affects the spatial distribution and wavelength components of initial differential wear. Specifically, initial differential wear with RPM6 has the highest power intensity with four major wavelength components. Corrugation can consistently initiate and grow up to 80 μm in this condition[12]. Compared to RPM6, the fluctuation amplitude of initial differential wear with RPM7 is smaller, and the number of major wavelength components decreases from four to two, which is caused by the relatively stronger longitudinal constraints to the rail, as shown in Figure 4.5. Initial differential wear with RPM1 has the lowest fluctuation level and corrugation can barely grow.

Comparing the results of RPM1, RPM8 and RPM9 in Figure 4.10b, it can be seen that the variation of row number of longitudinal rigid constraints has little influence on the spatial distribution and fluctuation amplitude of initial differential wear. However, Figure 4.10d shows that the PSD magnitude at 48.6 mm with RPM9, which releases the longitudinal rigid constraint of RPM1 in the 2nd and 3rd rows, increases about twice of those with RPM1 and RPM8. Initial differential wear with RPM5, which has the same longitudinal fastening constraint as RPM9, also shows a dominant peak at 64.7 mm. These results indicate that the absence of inner longitudinal constraint in the 2nd and 3rd rows seems a preferred condition for developing relatively longer-wavelength corrugation. Meanwhile, it should be noted that the initial differential wear of RPM5 and RPM9 is different from each other, indicating that fastening vertical and lateral constraints also influence

the rail longitudinal compression modes and the corrugation features.

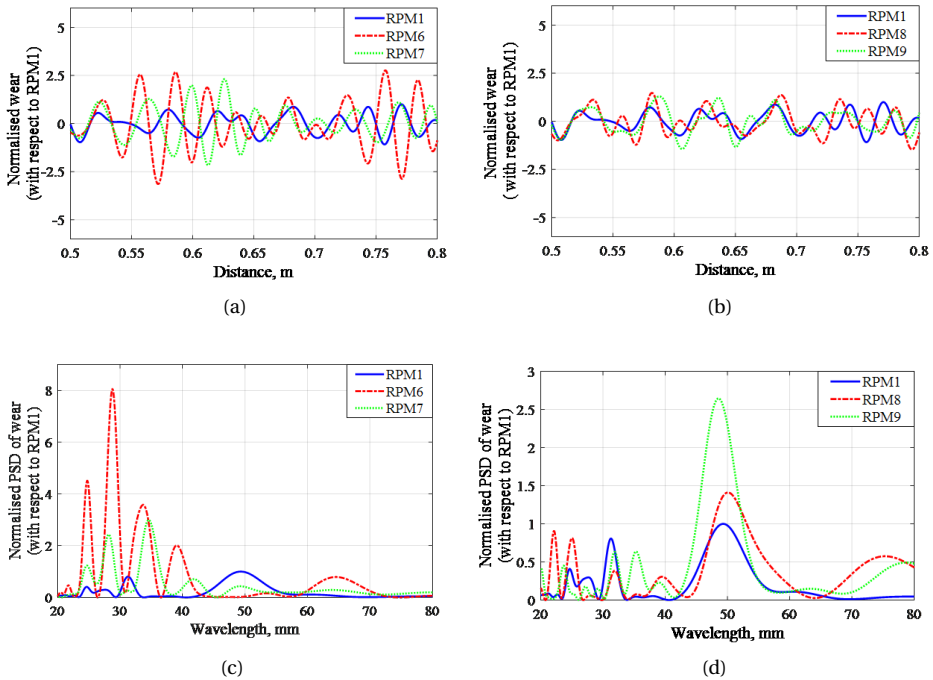


Figure 4.10: Initial differential wear in spatial and wavelength domains with different fastening boundary conditions RPM1 and RPM6 RMP9. (a) Initial differential wear in the spatial domain under RPM1, RPM6, and RPM7; (b) initial differential wear in the spatial domain under RPM1, RPM8 and RPM9; (c) initial differential wear in the wavelength domain under RPM1, RPM6, and RPM7; (d) initial differential wear in the wavelength domain under RPM1, RPM8 and RPM9.

In summary, initial differential wear and corrugation are sensitive to the column number of fastening longitudinal boundary conditions. When gradually reducing the column number from three (RPM1) to two (RPM7) and further to one (RPM6), the fluctuation amplitude of initial differential wear significantly increases, as well as the number of major wavelength components. This result, in turn, suggests that the increase of column number or rail constraint in the longitudinal dimension contributes to corrugation mitigation. With the same number of columns as RPM1, initial differential wear and corrugation seem insensitive to the variation of the number of rows of the fastening longitudinal boundary conditions (RPM8 and RPM9), except for a relatively longer-wavelength corrugation at 48.6 mm. Further, a common feature is found between the fastening longitudinal boundary conditions and the fastening configurations that corrugation is more sensitive to the variation of column number (in the longitudinal dimension) than the row number (in the lateral dimension). That is because the rail longitudinal modes, which are responsible for corrugation initiation, are a type of compression/rarefaction

vibration in the longitudinal direction. This result also indicates that the fastening longitudinal constraint to the rail is the major factor determining corrugation development.

4.4. INFLUENCE OF FASTENING LONGITUDINAL STIFFNESS AND DAMPING

Figure 4.11 shows the spatial distribution of differential wear under different corrugation severities with RPM10 (see Figure 4.6). The longitudinal fastening stiffness of RPM10 is 150 MN/m, and the longitudinal fastening damping is not considered to simulate severely worn railpads without damping capacity[29]. It can be seen that when amplitude $2A_{max} = 40 \mu\text{m}$, differential wear is in-phase with the initial differential wear and anti-phase with corrugation, indicating that corrugation can consistently grow up to $40 \mu\text{m}$ with RPM10. This result also suggests that the introduction of the fastening longitudinal stiffness can reproduce the consistent corrugation initiation and growth. The consistency condition between differential wear and corrugation is not satisfied with a trial amplitude $2A_{max} = 160 \mu\text{m}$, indicating the limiting corrugation amplitude is below $160 \mu\text{m}$ with RPM10. The following sections will further vary fastening longitudinal parameters (i.e., stiffness and damping) and analyze their effects on corrugation development.

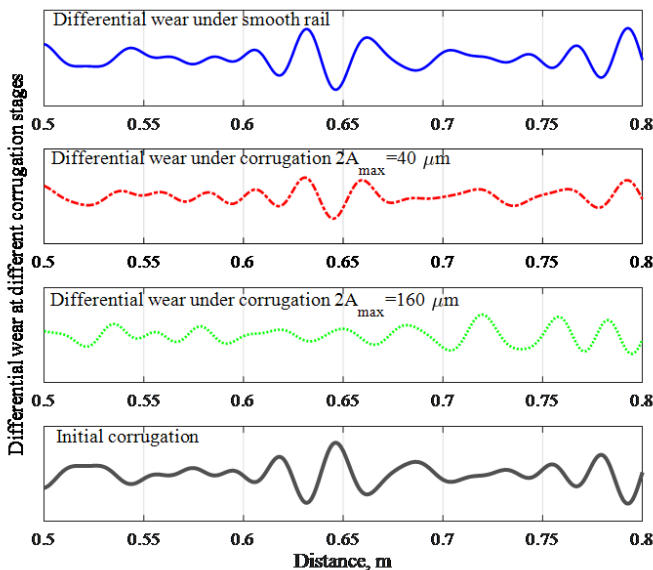


Figure 4.11: Differential wear in the spatial domain with RPM10.

4.4.1. INFLUENCE OF FASTENING LONGITUDINAL STIFFNESS

Figure 4.12 shows the spatial distribution and wavelength components of initial differential wear with different fastening longitudinal stiffness of 150 MN/m (RPM10), 300 MN/m (RPM11), and 900 MN/m (RPM12), as listed in Table 4.2. The fastening longitudinal damping is not considered. When the stiffness is small (RPM10), initial differential wear shows larger fluctuation amplitude, but the wave patterns with high amplitude mainly occur in the local positions between 0.6 m and 0.7 m and after 0.75 m, as shown in Figure 4.12a. With the increase of longitudinal stiffness (RPM11 and RPM12), the fluctuation amplitudes of initial differential wear decrease, but the wave patterns become more continuously and evenly distributed along the rail between 0.5 m and 0.8 m. Figure 4.12b shows initial differential wear in the wavelength domain. It can be seen that the increase of fastening longitudinal stiffness shifts the major wavelength components to the shorter ones with significantly reduced magnitude. That is because that larger longitudinal stiffness increases the frequencies of longitudinal compression modes and reduces the corresponding vibration amplitudes[28]. These results indicate that increasing fastening longitudinal stiffness is helpful to mitigate corrugation.

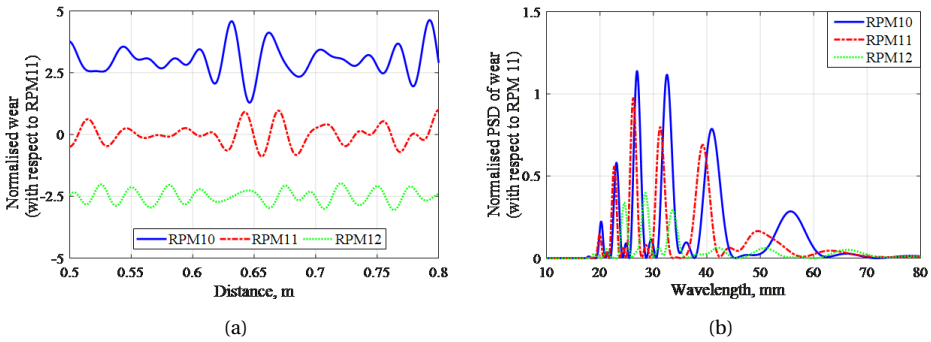


Figure 4.12: Initial differential wear in spatial and wavelength domains with different fastening longitudinal stiffness (a) Initial differential wear in the spatial domain under RPM10, RPM11, and RPM12; (b) initial differential wear in the spatial domain under RPM10, RPM11 and RPM12.

4.4.2. INFLUENCE OF FASTENING LONGITUDINAL DAMPING

Figure 4.13 shows the spatial distribution and wavelength components of initial differential wear with different fastening longitudinal damping of 0 (RPM11), 6 kNs/m (RPM13) and 24 kNs/m (RPM14), as listed in Table 4.2. The fastening longitudinal stiffness in these three cases is 300 MN/m. When damping increases from 0 to 6 kNs/m, the fluctuation amplitude of initial differential wear is significantly attenuated while the major wavelength components do not change. That is because larger longitudinal damping leads to smaller fluctuation amplitude of longitudinal compression modes without frequency shifts[28]. When further increasing the damping to 24 kNs/m, initial differential wear has nearly negligible fluctuation amplitude and corrugation cannot grow in this case. These results suggest that increasing fastening longitudinal damping can effectively attenuate the initial excitation and reduce the track corrugation propensity.

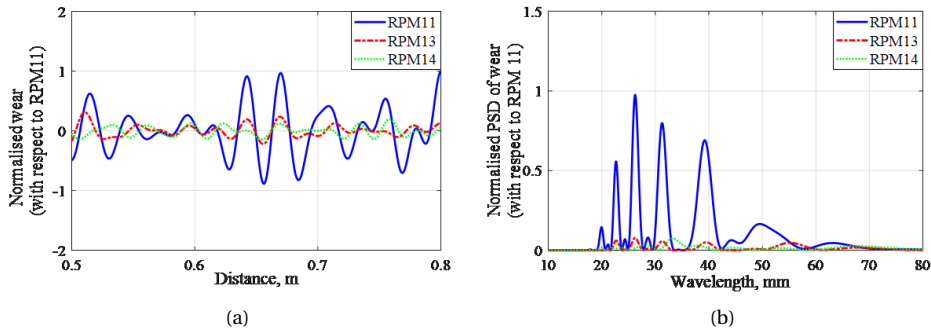


Figure 4.13: Initial differential wear in spatial and wavelength domains with different fastening longitudinal damping (a) Initial differential wear in the spatial domain under RPM11, RPM13, and RPM14; (b) initial differential wear in the spatial domain under RPM11, RPM13, and RPM14.

4.5. INFLUENCE OF TRACK LENGTH ON CORRUGATION FEATURES

It is reported that rail length influences the frequencies and fluctuation amplitude of rail vibration modes[28][31]. Since rail longitudinal compression modes are dominant for corrugation initiation, the track length is varied in this section to provide a comparative evaluation of corrugation features. The fastening model is RPM 11. The length of the track model is halved (10.27 m) and doubled (41.08 m), respectively. Figure 4.14 shows the spatial and wavelength domain distributions of initial differential wear. The wear of the shortest track model (10.27 m) has a relatively even spatial distribution with a dominant wavelength component at 29.0 mm, corresponding to 1341 Hz with a speed of 140 km/h. With the doubled track length, the spatial distribution of initial differential wear becomes uneven in amplitude. The uneven amplitude can be explained by the amplitude modulation of multiple major wavelength components, as shown in Figure 4.14b. In addition, a governing wavelength component of 29.0 mm for the shortest length model (10.27 m) provides a better explanation to the field measured corrugation with a major wavelength at 28.6 mm[12].

In summary, the track length significantly influences the spatial distribution and wavelength components of initial differential wear and corrugation. This explains various corrugation features observed in the field, which may be related to the effective track length that participates in the vehicle-track dynamic interaction. In a nominal condition, the track can be approximately considered as an "infinite" structure, and its dynamic behavior is typically characterized by the superposition of a series of 'propagative waves' instead of 'vibration modes'[32]. In this case, corrugation should not develop because of the absence of rail longitudinal compression modes that are dominant for corrugation initiation. However, because of the long-term dynamic train loads during the service, track conditions deteriorate with, for instance, damaged fastenings and bad joints. The propagative waves of the rail may reflect at these positions and interfere with themselves, resulting in the 'standing waves', or vibration modes in a finite rail. Rail lon-

itudinal compression modes are thus excited, and dynamic longitudinal contact force arises, which causes corrugation. Field observations show that corrugation usually occurs at certain locations, accompanying squats, joints, and welds, but not necessarily after them[10][25]. Except for track defects, some researchers also reported that the rail modes or standing waves due to the wave reflection between multiple wheels are responsible for corrugation formation[33][34].

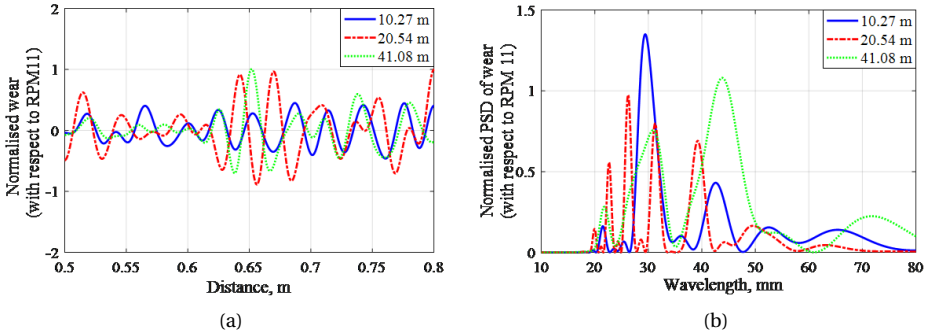


Figure 4.14: Initial differential wear with different track lengths under RPM 11. (a) Initial differential wear in the spatial domain; (b) initial differential wear in the wavelength domain.

4.6. DISCUSSION

In this work, fourteen fastening models were employed to investigate their influences on corrugation formation. These fastening models correspond to different service stages of fastenings in the field track, from nominal (i.e., RPM1) to severely worn conditions (i.e., RPM2). With some models, corrugation can consistently initiate and grow, while some cannot. Based on these results, we can better understand the corrugation development mechanism and gain insights into corrugation mitigation.

Rail longitudinal compression modes are responsible for corrugation initiation, and hence the suppression of these modes is helpful to mitigate corrugation. Figure 4.15 shows one example of a longitudinal compression mode at 1545 Hz of a free 5 m long rail. The term 'node' in the mode shape refers to a place where the rail does not move, and 'antinode' is used to describe a place with maximum displacement. The natural frequencies of longitudinal compression modes of a free rail can be predicted as follows[31]:

$$f = Nv_p/2L, \quad N = 1, 2, 3, \dots \quad (4.2)$$

where L is the length of the rail, v_p is the phase velocity. The longitudinal compression wave is non-dispersive within 5000 Hz, with a constant phase velocity of around 5170 m/s[31]. It can be seen from this equation that rail length influences longitudinal compression mode frequencies, which explains the effect of track length on corrugation features in Section 4.5.

In the field track, the rail is restricted by fastening systems. Figure 4.16 shows experimental results of rail longitudinal compression modes (indicated by ★ and numbers)

with and without fastenings by operating deflection shape (ODS) measurement[28]. We tested two types of railpads, harder Zw692-4 and softer FC9 were tested. They are commonly applied in the mainline of the Dutch railways. Compared to free rail, the longitudinal compression mode frequencies shift to larger values, and the corresponding vibration amplitude is significantly reduced under fastening constraint. For the softer FC9, the frequency shift and amplitude reduction are smaller than harder Zw692-4. These results explain the effect of longitudinal stiffness and damping on corrugation development in Section 4.4. Despite the considerable attenuation by fastening constraint, longitudinal compression modes still have large vibration amplitude and show distinguishable peaks in Figure 4.16.

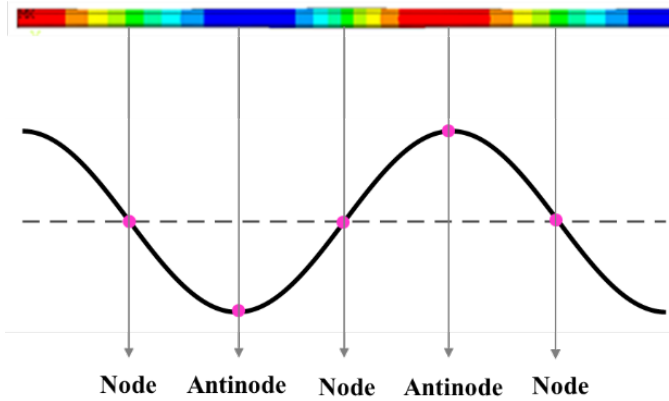


Figure 4.15: A longitudinal compression mode at 1545 Hz of a 5 m long free rail.

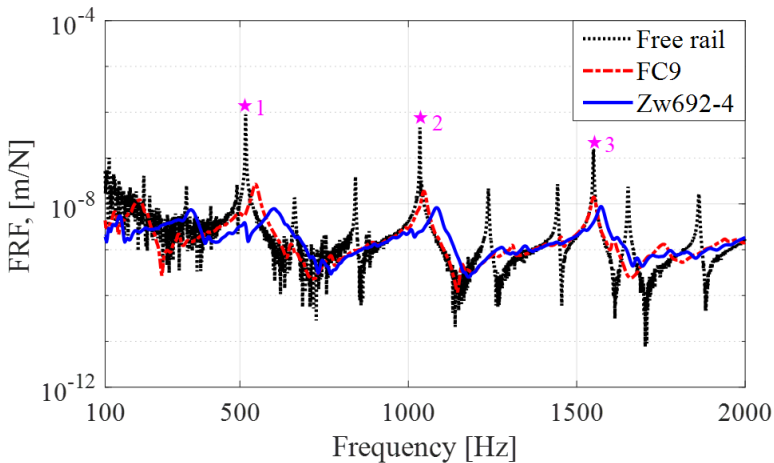


Figure 4.16: Rail longitudinal compression modes in the free condition and under fastening constraint with two railpad types. The results are from[28]

To further suppress these modes, there are two possible approaches. One is to increase the fastening longitudinal damping. When the damping is sufficient to attenuate the longitudinal modes, corrugation cannot develop, as with RPM14 in Figure 4.13. However, it should be noted that the damping capacity of railpads becomes weaker and even non-existent after long-term aging and degradation, and corrugation can develop afterward. A rail vibration absorber/damper might be a solution[34], but its application requires information about the characteristic frequencies of corrugation. According to the analysis above, corrugation characteristic wavelengths/frequencies depend on the fastening parameters and effective track length, covering a wide range (i.e., 600-2000 Hz) and making the vibration absorber/damper difficult to design and apply in the field.

4

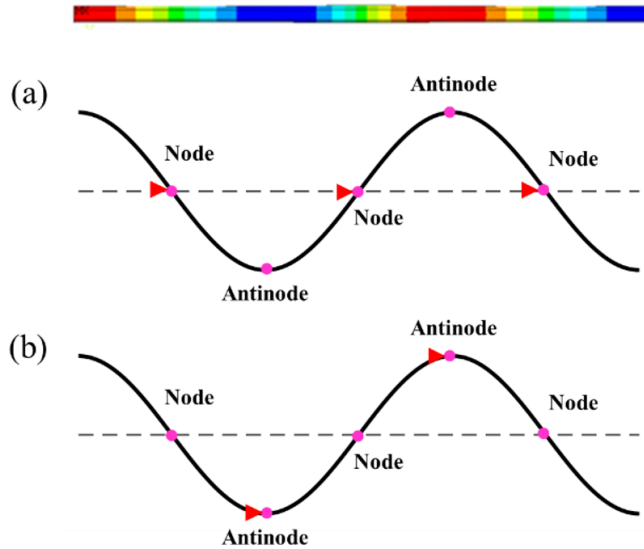


Figure 4.17: Schematic drawing of two types of rigid constraint to the longitudinal compression mode. (a) Rigid constraint to 'nodes'; (b) rigid constraint to 'antinode'.

Another approach is to increase the fastening longitudinal stiffness. One extreme condition of larger stiffness is the rigid constraint, as the fastening model RPM1. With RPM1, rail longitudinal compression modes are effectively suppressed, and corrugation can barely grow, as shown in Figure 4.8a. Nevertheless, despite the longitudinal rigid constraint to the rail with RPM2 and RPM6, corrugation can still grow, indicating that longitudinal compression modes are not completely constrained. To explain these phenomena, Figure 4.17 shows the schematic drawing of two types of rigid constraints to the longitudinal compression mode. When the rigid constraint is applied in the proximity of the 'nodes' of the mode shape, it has negligible influence on longitudinal compression modes, which could be the case of RPM2 and RPM6. When the rigid constraint is applied in the vicinity of the 'antinodes' of the mode shape, longitudinal compression nodes can be effectively suppressed, which could be the case of RPM1. This result provides an insight for the new fastening design for corrugation mitigation in future work.

4.7. CONCLUSIONS AND FUTURE WORK

Employing a 3D FE vehicle-track interaction model, a parametric investigation of fastenings was performed in this chapter to better understand the corrugation development mechanism and gain insight into its mitigation by fastening design. Fastening models with different configurations, boundary conditions, and parameters, representing different service stages of fastenings in the field were built up and analyzed. In addition, the influence of track length on corrugation features was studied.

The understanding of the corrugation development mechanism is summarised as follows.

1. Fastening parameters and modeling play an important role in corrugation development. To better understand the corrugation features in the field and reliably predict corrugation in the simulation, it is suggested to carefully examine the service stages of fastenings to determine appropriate parameters.
2. The variation of fastening constraint in the longitudinal dimension (i.e., the number of columns) significantly influences the corrugation development and features. The absence of inner fastening constraint in the lateral dimension (i.e., 2nd and 3rd rows) seems a preferred condition for developing relatively longer-wavelength corrugation.
3. The fastening longitudinal constraint to the rail is the major factor determining the corrugation development because the rail longitudinal modes responsible for corrugation initiation are a type of compression/rarefaction vibration in the longitudinal direction. The fastening vertical and lateral constraints influence the spatial distribution and wavelength components of corrugation.
4. Larger longitudinal stiffness of fastenings shifts the major wavelength components of corrugation to the shorter ones with significantly reduced amplitude. Larger longitudinal damping reduces the corrugation amplitude without changing the wavelength components.
5. Limiting corrugation amplitude is dependent on the intensity of the initial excitation and the resulting fluctuation amplitude of longitudinal dynamic contact force and initial differential wear.
6. Effective track length that participates in the vehicle-track dynamic interaction influences the spatial distribution and wavelength components of corrugation.

Insights are gained for the corrugation mitigation by fastening design and summarised as follows.

1. The increase of fastening constraint in the longitudinal dimension helps to mitigate corrugation. Meanwhile, the inner fastening constraint in the lateral dimension is necessary for corrugation mitigation.

2. The increase of fastening longitudinal stiffness and damping can reduce the vibration amplitudes of longitudinal compression modes and thus reduces the track corrugation propensity.
3. To effectively mitigate corrugation, fastening constraint should be applied in the proximity of the 'antinodes' of the longitudinal compression mode shape instead of the 'nodes'.

Future work will focus on the new design of fastening systems, which can effectively suppress rail longitudinal compression modes and mitigate or even eliminate corrugation in the track.

REFERENCES

- [1] P. Zhang, S. Li, R. Dollevoet, and Z. Li, *Parametric investigation of railway fastenings into the development and mitigation of short pitch corrugation*, Submitted to a journal.
- [2] S. Grassie, *Rail corrugation: characteristics, causes, and treatments*, Proceedings of the Institution of Mechanical Engineers, Part F: Journal of Rail and Rapid Transit **223**, 581 (2009).
- [3] S. Grassie and J. Kalousek, *Rail corrugation: characteristics, causes and treatments*, Proceedings of the Institution of Mechanical Engineers, Part F: Journal of Rail and Rapid Transit **207**, 57 (1993).
- [4] X. Deng, Z. Qian, Z. Li, and R. Dollevoet, *Investigation of the formation of corrugation-induced rail squats based on extensive field monitoring*, International Journal of Fatigue **112**, 94 (2018).
- [5] S. Grassie and K. Johnson, *Periodic microslip between a rolling wheel and a corrugated rail*, Wear **101**, 291 (1985).
- [6] K. Hempelmann and K. Knothe, *An extended linear model for the prediction of short pitch corrugation*, Wear **191**, 161 (1996).
- [7] S. Muller, *A linear wheel-track model to predict instability and short pitch corrugation*, Journal of Sound and Vibration **227**, 899 (1999).
- [8] S. Li, Z. Li, A. Núñez, and R. Dollevoet, *New insights into the short pitch corrugation enigma based on 3d-fe coupled dynamic vehicle-track modeling of frictional rolling contact*, Applied Sciences **7**, 807 (2017).
- [9] J. Neilsen, *Evolution of rail corrugation predicted with a non-linear wear model*, Journal of Sound and Vibration **227**, 915 (1999).
- [10] M. Hiensch, J. C. Nielsen, and E. Verheijen, *Rail corrugation in the netherlands—measurements and simulations*, Wear **253**, 140 (2002).
- [11] K. Oostermeijer, *Review on short pitch rail corrugation studies*, Wear **265**, 1231 (2008).

- [12] Z. Li, S. Li, P. Zhang, A. Nunez, and R. Dollevoet, *Mechanism of short pitch corrugation: Initial excitation and wavelength selection for consistent initiation and growth*, Submitted (2021).
- [13] H. Zhang, W. Liu, W. Liu, and Z. Wu, *Study on the cause and treatment of rail corrugation for beijing metro*, *Wear* **317**, 120 (2014).
- [14] W. Liu, H. Zhang, W. Liu, and D. J. Thompson, *Experimental study of the treatment measures for rail corrugation on tracks with egg fasteners in the beijing metro*, *Proceedings of the Institution of Mechanical Engineers, Part F: Journal of Rail and Rapid Transit* **232**, 1360 (2018).
- [15] X. Zhao, Z. Li, and R. Dollevoet, *Influence of the fastening modeling on the vehicle-track interaction at singular rail surface defects*, *Journal of Computational and Non-linear Dynamics* **9** (2014).
- [16] Z. Li, X. Zhao, C. Esveld, R. Dollevoet, and M. Molodova, *An investigation into the causes of squats—correlation analysis and numerical modeling*, *Wear* **265**, 1349 (2008).
- [17] K. Knothe and S. Grassie, *Modelling of railway track and vehicle/track interaction at high frequencies*, *Vehicle system dynamics* **22**, 209 (1993).
- [18] M. Molodova, Z. Li, A. Núñez, and R. Dollevoet, *Validation of a finite element model for axle box acceleration at squats in the high frequency range*, *Computers & Structures* **141**, 84 (2014).
- [19] D. J. Benson and J. O. Hallquist, *A single surface contact algorithm for the post-buckling analysis of shell structures*, *Computer methods in applied mechanics and engineering* **78**, 141 (1990).
- [20] X. Zhao and Z. Li, *The solution of frictional wheel–rail rolling contact with a 3d transient finite element model: Validation and error analysis*, *Wear* **271**, 444 (2011).
- [21] Z. Yang, X. Deng, and Z. Li, *Numerical modeling of dynamic frictional rolling contact with an explicit finite element method*, *Tribology international* **129**, 214 (2019).
- [22] Z. Yang, A. Boogaard, R. Chen, R. Dollevoet, and Z. Li, *Numerical and experimental study of wheel-rail impact vibration and noise generated at an insulated rail joint*, *International Journal of Impact Engineering* **113**, 29 (2018).
- [23] M. Oregui, Z. Li, and R. Dollevoet, *An investigation into the modeling of railway fastening*, *International Journal of Mechanical Sciences* **92**, 1 (2015).
- [24] M. Oregui, Z. Li, and R. Dollevoet, *An investigation into the vertical dynamics of tracks with monoblock sleepers with a 3d finite-element model*, *Proceedings of the Institution of Mechanical Engineers, Part F: Journal of Rail and Rapid Transit* **230**, 891 (2016).

- [25] Z. Li, R. Dollevoet, M. Molodova, and X. Zhao, *Squat growth—some observations and the validation of numerical predictions*, *Wear* **271**, 148 (2011).
- [26] S. Grassie, *Squats and squat-type defects in rails: the understanding to date*, Proceedings of the Institution of Mechanical Engineers, Part F: Journal of Rail and Rapid Transit **226**, 235 (2012).
- [27] X. Deng, Z. Li, Z. Qian, W. Zhai, Q. Xiao, and R. Dollevoet, *Pre-cracking development of weld-induced squats due to plastic deformation: Five-year field monitoring and numerical analysis*, *International Journal of Fatigue* **127**, 431 (2019).
- [28] P. Zhang, S. Li, A. Núñez, and Z. Li, *Vibration modes and wave propagation of the rail under fastening constraint*, *Mechanical Systems and Signal Processing* **160**, 107933 (2021).
- [29] M. Oregui, A. De Man, M. Woldekidan, Z. Li, and R. Dollevoet, *Obtaining railpad properties via dynamic mechanical analysis*, *Journal of Sound and Vibration* **363**, 460 (2016).
- [30] J. Kalousek and K. Johnson, *An investigation of short pitch wheel and rail corrugations on the vancouver mass transit system*, Proceedings of the Institution of Mechanical Engineers, Part F: Journal of Rail and Rapid Transit **206**, 127 (1992).
- [31] P. Zhang, S. Li, A. Núñez, and Z. Li, *Multimodal dispersive waves in a free rail: Numerical modeling and experimental investigation*, *Mechanical Systems and Signal Processing* **150**, 107305 (2021).
- [32] D. Thompson, *Wheel-rail noise generation, part iii: rail vibration*, *Journal of sound and vibration* **161**, 421 (1993).
- [33] T. Wu and D. Thompson, *An investigation into rail corrugation due to micro-slip under multiple wheel/rail interactions*, *Wear* **258**, 1115 (2005).
- [34] T. Wu, *Effects on short pitch rail corrugation growth of a rail vibration absorber/damper*, *Wear* **271**, 339 (2011).

5

SHORT PITCH CORRUGATION MITIGATION BY RAIL CONSTRAINT DESIGN

Short pitch corrugation is a quasi-periodic rail defect that induces a high level of noise and accelerates track degradation. This chapter proposes a methodology to mitigate short pitch corrugation by rail constraint design, including four steps. In Step 1, corrugation is numerically reproduced by employing a three-dimensional (3D) finite element (FE) model which couples the structural dynamics, wheel-rail contact mechanics and damage mechanism of the vehicle-track system. In Step 2, the corrugation initiation mechanism is identified by the operating deflection shapes (ODSs) approach. In Step 3, different types of rail constraints are designed and their effects on rail vibration modes are analysed. Then FE models of these rail constraints are built up and validated. In Step 4, rail constraint models from Step 3 are applied to the 3D FE vehicle-track interaction model and their effectiveness on corrugation mitigation is evaluated. The results indicate rail longitudinal compression modes and the induced longitudinal dynamic contact force dominate the initial differential wear and corrugation initiation. Based on this mechanism, a new rail constraint is designed in this chapter that can completely suppress longitudinal compression modes and significantly reduce the fluctuation amplitude of the longitudinal contact force so that corrugation can hardly initiate. This chapter points out a direction for field corrugation mitigation by strengthening the rail longitudinal constraint.

5.1. INTRODUCTION

Short pitch corrugation (hereinafter corrugation) has been reported as a type of wary rail defect for over 100 years and remains a severe problem for railway administrations worldwide. Rail corrugation is mainly observed on tangent tracks or gentle curves with a typical wavelength of 20-80 mm [1][2], and it can be identified by shiny crests and dark valleys in the running band. One example of rail corrugation in the Dutch Railway is shown in Figure 5.1, with a wavelength of about 40 mm. Corrugation can excite high-frequency wheel-rail contact forces[3][4] and generate a high level of noise[5][6][7], for which it is often referred to as ‘roaring rails’ [1]. In addition, the resulting dynamic contact forces will accelerate the degradation of the track component[8], such as fastenings, sleepers and ballast, and lead to other types of rail defects, e.g., squats[9]. In practice, rail grinding has been widely applied to treat corrugation[10][11][12]. For the guidance of field grinding maintenance, some novel inspection approaches of corrugation have been proposed, for instance, based on the self-contained electromagnetic energy harvesting system[13], carriage interior noise[14], or one-dimensional convolution neural network and data-driven method[15]. However, grinding considerably increases the maintenance cost and meanwhile reduces the service life of the rail. Therefore, it is of great significance to identify the corrugation formation mechanism and develop effective root-cause solutions to prevent corrugation.

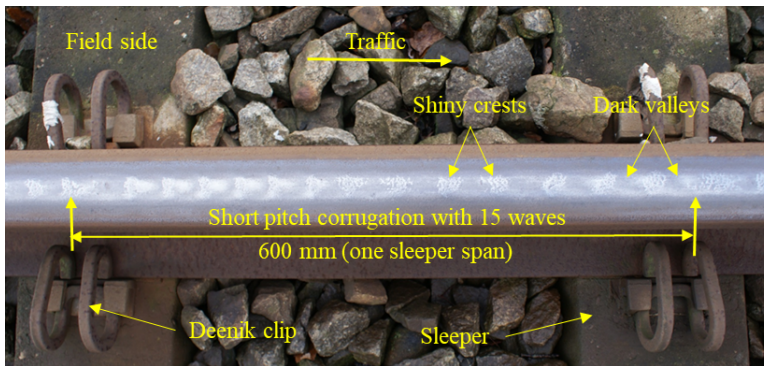


Figure 5.1: Short pitch corrugation with a wavelength of about 40 mm in the Dutch railway network. Corrugation wavelength refers to the distance between two adjacent shiny crests. This corrugation is developed on a straight ballasted track with duo-block sleepers and fastenings with the Deenik clip.

The corrugation formation mechanism is generally considered to consist of two features: the wavelength-fixing mechanism and the damage mechanism[1][2]. Corrugation damage mechanism has been commonly considered as wear[11][16][17][18][19][20][21]. A well-validated wavelength-fixing mechanism has not yet been demonstrated, although many hypotheses have been proposed in the literature. K. Hempelmann and K. Knothe [22] and S. Muller[23] employed the linear wheel-track model to predict the corrugation formation and found that the track pinned-pinned resonance together with the contact filter effect are the wavelength-fixing mechanisms. L. Afferrante and M. Ciavarella[24] reported that the influence of pinned-pinned resonance has been possibly overestimated

and first proposed the longitudinal creepage may be the most important mechanism without corresponding to any resonance of the vehicle-track system. A. Johansson and J.C. Nielsen[25] numerically studied the influence of powered wheelsets with wheel corrugation on the rail corrugation growth and found that the local rail bending modes between the two wheelsets in a bogie determine the corrugation wavelength. T. Wu and D. Thompson[26] and C. Ma et al.[27] also reported that the dynamic resonance between multiple wheelset-rail interactions can induce vertical wheel-rail dynamic force and be responsible for corrugation formation. P. Meehan et al.[16][28][29][30] performed numerical simulations and field and laboratory tests of rail corrugation, and concluded that train speed variation can significantly reduce the corrugation rate. G. Chen [31] and X. Cui [32][33] employed the finite element wheelset-track model to investigate the corrugation development mechanism and proposed that the frictional self-excited vibration of the wheelset-track system is responsible for the wavelength-fixing mechanism. W. Li et al.[34] conducted field measurement and numerical calculations to study corrugation formation on tracks with resilient fastenings and found corrugation arises by a wavelength-fixing mechanism of rail vertical resonance on the elasticity of resilient fastenings.

Despite the different or even contradictory theories in the literature, it is commonly accepted that the wavelength-fixing mechanism is mainly determined by the interplays of the structural dynamics and the contact mechanics. Therefore, the accurate modelling of high-frequency dynamics and wheel-rail contact of the vehicle-track system is essential to understand corrugation formation. With the development of computational power, the finite element model (FEM) has been extensively applied in simulating vehicle-track dynamic interaction. Compared to the multibody models[35][36] or beam models[37][38][39], the FEM has the advantage in dealing with nonlinear material properties and arbitrary contact geometry and inherently include continuum dynamics[40][41]. It thus has been used to investigate, e.g., wheel-rail impact contact[42][43], contact-induced waves[44], rail ratchetting [45][46], and railway curve squeal[47][48].

Employing a novel modelling approach based on the three-dimensional (3D) FE simulation of vehicle-track dynamic interaction, S. Li et al.[3] obtained new insights into the corrugation development mechanism. It was inferred that rail longitudinal vibration modes are probably dominant for corrugation initiation. Further, continuous corrugation initiation and growth require a consistency condition between the vertical and longitudinal vibration modes, dynamical responses and the resulting wear. According to these insights, together with a necessary initial excitation determined by fastening constraint, consistent corrugation initiation and growth have been successfully reproduced. The simulated corrugation achieved good agreement with the field corrugation in terms of the spatial distribution and major wavelength components[49]. These results point out a promising direction that rail corrugation can be mitigated or even eliminated by completely constraining longitudinal compression modes[50][51] to suppress corrugation initiation.

In railway tracks, fastenings impose major constraints on rail vibrations. Fastenings mainly consist of two components: railpads and clips. Railpads are made of resilient materials placed between the rail and the sleeper to reduce vibration and noise, and its dynamic properties are highly nonlinear[52][53][54][55]. Clips fix the rail to the sleeper to

ensure that the rail remains attached to the sleeper under train loads. Railpads and clips together constrain the displacement of the rail in the vertical, longitudinal and lateral directions[56]. Many experimental and numerical studies indicate that fastenings play an important role in the corrugation formation[23][57][58][59][60]. P. Zhang et al.[61][62] systematically investigated rail vibration modes in three directions using the operating deflection shape (ODS) approach and reported that the fastenings constrain the longitudinal rail compression modes less strongly compared to those in the vertical and lateral directions. Therefore, it is necessary to design new rail constraint instead of the current fastenings to better suppress longitudinal compression modes to mitigate corrugation. This chapter proposes a methodology to mitigate corrugation by rail constraint design. Through this methodology, corrugation is numerically reproduced using a 3D FE vehicle-track interaction model and its initiation mechanism is identified by the ODS approach. Different types of rail constraints are designed and their effects on rail vibrations and corrugation mitigation are investigated. The structure of this paper is as follows. Section 2 describes the methodology of this paper, including numerical simulations and experimental investigation. Section 3 presents the simulated corrugation and identifies the corrugation initiation mechanism by the ODS approach. Section 4 investigates different rail constraint designs and their modelling methods. Section 5 evaluates the effectiveness of rail constraints on corrugation mitigation. The main conclusions are presented in Section 6.

5

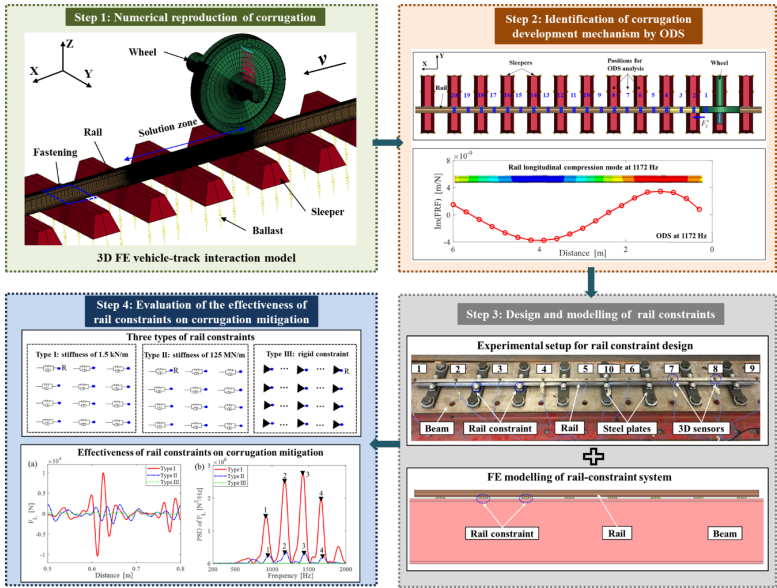


Figure 5.2: Flowchart of the methodology for corrugation mitigation by rail constraint design. In Step 1, corrugation is numerically reproduced by employing a 3D FE vehicle-track interaction model. In Step 2, the corrugation development mechanism is identified by the ODS approach. In Step 3, different types of rail constraints are designed and modelled. In Step 4, the effectiveness of the designed rail constraints on corrugation mitigation is evaluated.

5.2. METHODOLOGY

In this section, we describe a methodology for corrugation mitigation by rail constraint design, as shown in Figure 5.2. This methodology includes four steps: 1) corrugation reproduction; 2) identification of corrugation initiation mechanism; 3) design and modelling of rail constraints; 4) evaluation of the designed rail constraints on corrugation mitigation. In Step 1, a 3D FE vehicle-track interaction model is employed to numerically reproduce corrugation. In Step 2, the ODS approach is applied to identify the corrugation development mechanism. In Step 3, different rail constraints are designed and their influences on rail vibration modes are analysed. Afterwards, models of these rail constraints are established and validated. In Step 4, the rail constraint models from Step 3 are applied to the FE vehicle-track model and their effectiveness on corrugation mitigation is evaluated.

5.2.1. 3D FE VEHICLE-TRACK INTERACTION MODEL FOR CORRUGATION REPRODUCTION

In this subsection, we introduce the 3D FE vehicle-track interaction model in detail in Section 2.1.1, which can comprehensively simulate the wheel-rail contact and high-frequency dynamics of the vehicle-track system. This model is used to reproduce corrugation by introducing an initial excitation from the fastening model. The damage mechanism is assumed as wear, which is calculated by the approach provided in Section 2.1.2.

3D FE VEHICLE-TRACK INTERACTION MODEL

A 3D FE vehicle-track interaction model was built up for corrugation reproduction, as shown in Figure 5.3. A Cartesian coordinate system was adopted in the model, where the axes X, Y, and Z were in the longitudinal (rolling), lateral and vertical directions. The vehicle was modelled by a wheel with the sprung mass of the car body and bogie supported by the primary suspension. The secondary suspension was not included because the vibration of the sprung mass on the secondary suspension mainly influences vehicle-track vibration at lower frequencies (usually below 10 Hz[63]), which is beyond the frequency range of corrugation. The wheel, rail and sleeper were modelled by 8-node solid elements based on their nominal geometry and material. The radius of the wheel was 0.46 m with a conicity of 1/40. The rail profile was UIC 54 E1 with an inclination of 1/40. The primary suspension and ballast were modelled by vertical spring-damper elements. Figure 5.3c shows a close-up of the fastening model. Fastenings were modelled by vertical 3×4 spring-damper elements (i.e. 3 columns in the longitudinal dimension and 4 rows in the lateral). The lateral fastening constraint was modelled by rigidly fixing the rail nodes in all three columns, while the longitudinal one only rigidly constrained the rail in the central column to simulate the fastening degradation for corrugation initiation. The track length was 20.54 m, including 34 sleeper spans. The vehicle and track parameters were taken primarily from[3][64]. The wheel-rail contact model (see Figure 5.3d) applied an automatic surface-to-surface contact scheme with a penalty contact algorithm[65]. The wheel-rail friction coefficient was 0.4. No geometric irregularities were applied to the wheel-rail contact surface. The solution zone had a meshing size of 0.8 mm×0.8 mm. The initial wheel position was at position O, as shown in Figure 5.3d (0 m). The running

speed is 140 km/h.

An implicit-explicit sequential approach was employed in the simulation to minimize the solution time and the dynamic effects during the initialization of wheel-rail interaction [47] [66]. In the implicit calculation, the vehicle-track system reached an equilibrium state under gravity. The calculated nodal displacement was subsequently input as an initial condition of the explicit calculation of the vehicle-track dynamic interaction. In the explicit calculation, initial forward translation and rotation velocities were prescribed to the wheel model to generate rolling motion. The same initial translation velocity was applied to the car body and bogie. A driving torque was applied to the wheel axle as a load boundary condition to generate a traction coefficient of 0.15. The adopted integration time step was sufficiently small (79 ns) to ensure the stability of the integration and the contact.

This vehicle-track interaction model has been extensively validated in terms of frictional rolling contact solutions[47][41][66], wheel dynamics[67] and track dynamics[56]. The simulated dynamic responses of the vehicle-track system, such as axle box accelerations [68] and rail accelerations[67], have also achieved good agreement with measurements. Besides, this model has been employed to successfully identify the development mechanism of squats[43][69], and predict the contact-induced waves[44].

5

WEAR MODEL

The wear of the rail surface is assumed to be proportional to the accumulated frictional work during wheel passages[70] [71]. In the FE simulation, the frictional work at each node is calculated for a wheel passage, i.e., from the node entering until leaving the contact patch as follows:

$$w(x, y) = k W_f(x, y) = k \sum_{i=1}^N \tau_i(x, y) V_i(x, y) \Delta t \quad (5.1)$$

where k is the wear coefficient, $W_f(x, y)$ is the frictional work, $\tau_i(x, y)$ and $v_i(x, y)$ are the local tangential stress and micro-slip, respectively, N the number of time steps Δt during which a node passes the contact patch.

5.2.2. ODS APPROACH TO IDENTIFY CORRUGATION INITIATION MECHANISM

In this work, the ODS approach is applied to identify rail vibration modes to understand the corrugation development mechanism. Compared to the widely-used frequency response function (FRF) approach[72][73], the ODS approach has the advantage in distinguishing coupled rail vibration modes[61]. ODS is calculated from a set of frequency response functions (FRFs), which can be divided into three steps. First, a longitudinal impact signal (denoted as $F2x(t)$) is applied at position 2 (see Figure 5.3e), which is 0.6 m away from the origin position (O) and in the middle of the solution zone of corrugation. The vibration signals at 20 positions (see Figure 5.3e) are captured and denoted as $aix(t)$. Second, the FRFs at these positions are calculated by the following formula:

$$FRF_i^x(f) = \frac{S_{a_i^x F_2^x}(f)}{S_{F_2^x F_2^x}(f)(2\pi f)^2} \quad (5.2)$$

where $FRF_i^x(f)$ is the longitudinal FRF at position i , $S_{a_i^x F_2^x}(f)$ is the cross-spectrum between the acceleration $a_i^x(t)$, and force $F_2^x(t)$, and $S_{F_2^x F_2^x}$ is the auto-spectrum of the force $F_2^x(t)$. Third, the ODSs of rail displacement responses are taken as the spatial distribution of the imaginary parts of the FRFs, as follows:

$$ODS^x(f) = [\text{Im}(FRF_1^x(f)), \text{Im}(FRF_2^x(f)), \dots, \text{Im}(FRF_{20}^x(f))] \quad (5.3)$$

where $ODS^x(f)$ is the longitudinal ODS at frequency f . When the frequency is one of the natural rail frequencies, the ODS will closely approximate the mode shape. More detailed introduction of the ODS approach can be found in [62][61].

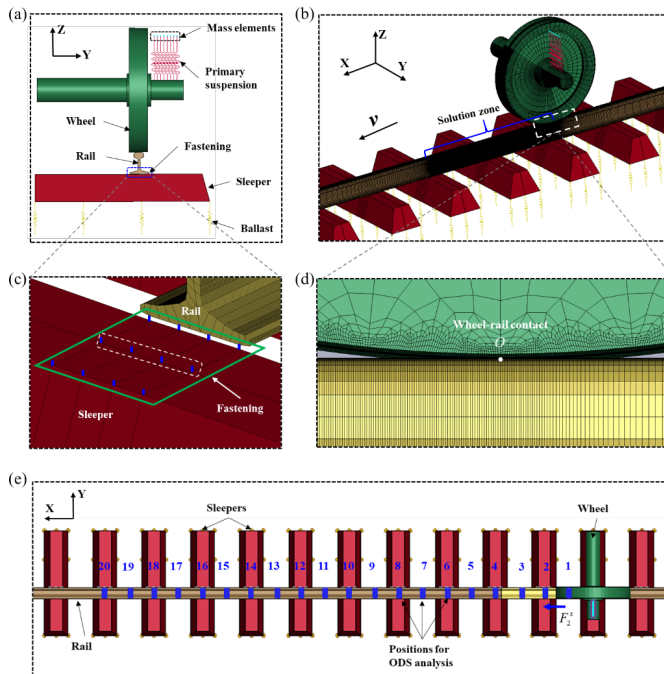


Figure 5.3: 3D FE vehicle-track interaction model. (a) Front view; The car body and bogie were modelled as mass elements, the wheel, the rail and sleepers were modelled by 8-node solid elements, and the primary suspension, fastenings and the ballast were modelled by spring-damper elements. (b) detailed mesh of the FE model; The rail in the solution zone has the element size of $0.8 \text{ mm} \times 0.8 \text{ mm}$. (c) close-up of the fastening model; Fastenings were modelled by vertical 3×4 spring-damper elements (i.e. 3 columns in the longitudinal dimension and 4 rows in the lateral). The fastening longitudinal constraint was only applied in the central column of rail nodes, as indicated by the white dashed box. (d) close-up of the wheel-rail contact; The initial wheel position was at position O (0 m). (f) top view; The vibration signal acquisition positions for ODS analysis are shown with numbers $1, 2, \dots, 20$.

5.2.3. DESIGN AND MODELLING OF RAIL CONSTRAINTS FOR CORRUGATION MITIGATION

In this subsection, experimental setups with different types of rail constraints are introduced. Afterwards, FE models of these rail constraints are developed.

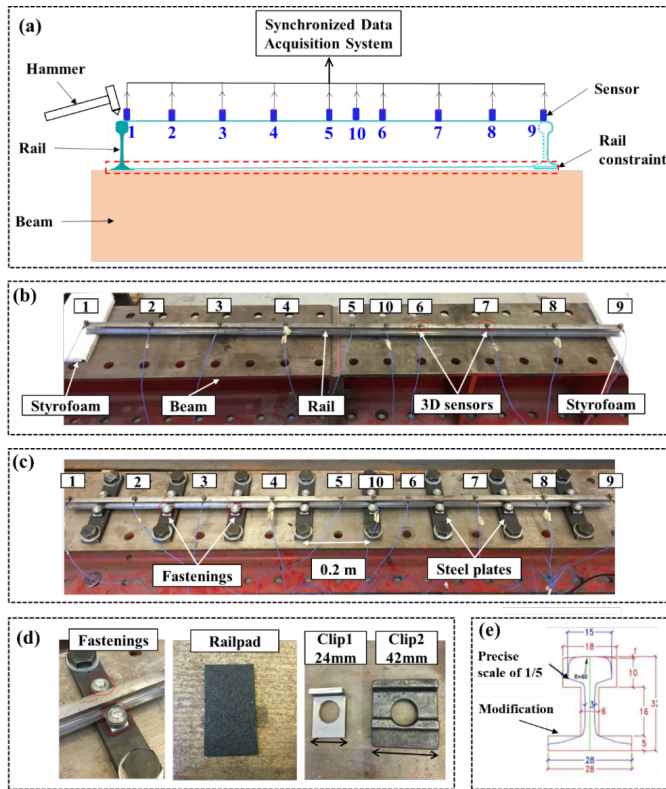


Figure 5.4: Experimental setups for rail constraint design. (a) Schematic drawing; The experimental setup mainly consists of a scaled rail and a steel beam. The rail is supported on the beam by different types of rail constraints. A hammer test is performed to analyse the rail vibration characteristics by the ODS approach[61]. (b) setup for the free rail; the rail is supported on the beam by two soft styrofoam blocks at two ends. In this condition, the rail can be approximately considered to be in 'free vibrations'. (c) setup for the constrained rail; The rail is fixed on eight steel plates by different types of rail constraints. (d) fastenings consisting of the railpads and two types of clips; (e) scaled rail profile used on the setup.

EXPERIMENTAL SETUPS FOR RAIL CONSTRAINT DESIGN

Figure 5.4 shows the experimental setups for rail constraint design to mitigate corrugation. The experimental setups mainly consist of three parts (see Figure 5.4a): a rail, a standard 'I-cross section' steel beam, and different types of rail constraints. The rail is 1.6 m long and its profile is approximately 1/5 scale of the UIC 54 E1 rail but with some modifications for ease of fabrication, as shown in Figure 5.4e. According to the similarity law[74][75], the vibration modes of a scaled rail are equivalent to those of the full-scale rail by considering a corresponding scale factor. Compared to the full-scale one, the downscaled rail is easier to control by rail constraints in the laboratory because of its much smaller mass and stiffness. Besides, it is possible to experimentally examine the effectiveness of the designed rail constraint for corrugation mitigation in an innovative downscale test rig[75][76] in future work. The steel beam has a considerably larger mass and stiffness than the scaled rail, provides an approximately rigid support to the rail, and

makes it possible to completely suppress rail vibration modes by rail constraints. To control longitudinal compression modes, five types of rail constraints were designed, as shown in Figure 5.4 and listed in Table 5.1. For the first type of rail constraint (type 1), the rail was supported on the steel beam by two soft styrofoam blocks at the two rail ends, as shown in Figure 5.4b. In this condition, the rail can be approximately considered to be in ‘free vibrations’. For the second type (type 2), eight steel plates were rigidly fixed on the beam by bolts every 0.2 m, and the rail was constrained on the steel plates by eight fastenings, as shown in Figure 5.4c and 5.4d. Each fastening consists of a railpad and a pair of clips (clip1 in Figure 5.4d). The clip toe loads were applied through preload springs and the value was controllable by adjusting the spring compression displacement. In this case (type 2), the toe load from each pair of clips was around 0.4 kN, which is equivalent to 10 kN of the full-scale rail, half the nominal value in the field track. This case was thus called half-tight clip1 to simulate the fastening constraint with insufficient toe load. For the third type (type 3), the clip load increased to 0.8 kN (called full-tight clip1) to simulate the nominal toe load of the fastening constraint in the field track. For the fourth type (type 4), the resilient railpads were removed and the rail was directly restricted on the steel plates by the full-tight clip1. In this condition, the rail was approximately regarded as ‘rigidly’ constrained on the steel beam. The last type (type 5) is the same as type 4, except that the narrower and thinner clip1 was replaced with the wider and thicker clip2, which was expected to provide a stronger constraint to the rail and more completely suppress the longitudinal compression modes. Overall, from type 1 to type 5, we designed to gradually strengthen the rail constraint to examine whether rail longitudinal compression modes can be effectively suppressed for corrugation mitigation.

Table 5.1: Five types of rail constraints in the experimental setups.

Types of rail constrains	Description	Purposes
1	Soft styrofoam blocks	To simulate the free boundary of the rail.
2	Railpads with half-tight clip 1	To simulate the fastening constraint with insufficient toe loads.
3	Railpads with full-tight clip 1	To simulate the nominal fastening constraint.
4	Steel plates with full-tight clip 1	To simulate the relatively rigid rail constraint.
5	Steel plates with full-tight clip 2	To simulate the relatively rigid rail constraint.

A hammer test is performed to analyse the rail vibration characteristics by the ODS approach[61]. The sensor distribution of the hammer test in the setups is shown in Figure 5.4a. In total, ten 3D accelerometers (PCB 356B21, denoted as 1-10 in Figure 5.4a) were used. The first nine sensors were glued on the railhead surface with a spacing of 0.2 m. The tenth sensor was glued in the middle of sensor 5 and sensor 6. The responses of the ten accelerometers are denoted as follows,

$$a_i(t) = [a_{ix}(t), a_{iy}(t), a_{iz}(t)]^T, \quad i = 1, 2, \dots, 10 \quad (5.4)$$

where $a_i(t)$ is the vector with the responses of the i_{th} accelerometer, which includes three components $a_{ix}(t)$, $a_{iy}(t)$, $a_{iz}(t)$ in the longitudinal, lateral, and vertical directions, respectively.

A small hammer (PCB 086C03) with a steel tip was used to excite the rail in the high-

frequency range. The excitation positions were as close as possible to the sensor 1. Sensor 1 is at one of the free rail ends where the mode shapes have maximum deformation and thus the rail vibration modes can be excited with largest energy. Impacts were conducted in the longitudinal, lateral, and vertical directions, recorded as $F_{1x}(t)$, $F_{1y}(t)$, $F_{1z}(t)$. A synchronized data acquisition system recorded the excitation and the response signals. Five impacts in each direction were measured for each test with a sampling frequency of 51200 Hz to reduce the random errors. The FRFs and corresponding ODSs can be obtained using Equations (2) and (3).

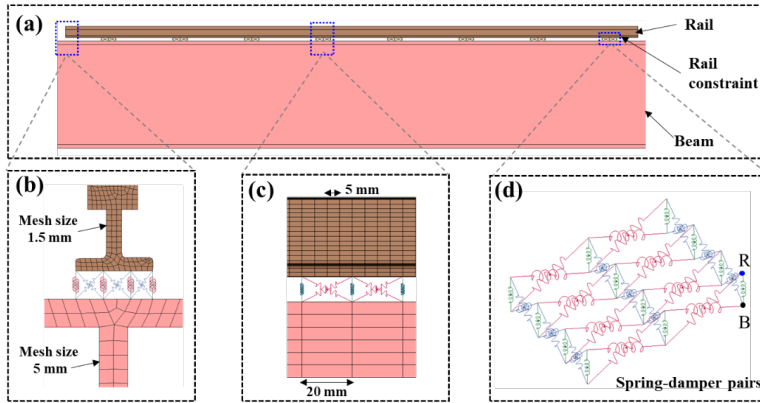


Figure 5.5: 3D FE model of the rail-constraint system. (a) Front view; The rail and beam were modelled by 8-node solid elements, and rail constraint was modelled by multiple spring-damper elements. (b) cross-section mesh of the FE model; The element sizes of the rail and beam were 1.5 mm and 5 mm, respectively. (c) longitudinal mesh of the FE model; The longitudinal element size of the rail and the beam were 5 mm and 20 mm, respectively. (d) spring-damper elements of the rail constraint. 'R' designates the rail node of the spring-damper elements, and 'B' beam node.

FE MODELLING OF RAIL CONSTRAINTS

A 3D FE model of the rail-constraint system in Figure 5.4 was developed, as shown in Figure 5.5. The rail and the steel beam were modelled by 8-node solid elements with their nominal geometry and material. The cross-sections of the rail and the beam were discretized with an equal element edge length of 1.5 mm and 5 mm, respectively, as shown in Figure 5.5b. The longitudinal element size of the rail was 5 mm, and that of the beam was 20 mm, as shown in Figure 5.5c. The rail and beam material were treated as elastic isotropic with Young's modulus of 210 GPa, Poisson's ratio of 0.3, and density of 7850 kg/m^3 . Free boundary conditions were applied to the two rail ends and the beam. The bottom nodes of the beams are fixed in three directions to simulate the foundation support.

The rail constraints of type 1, type 3 and type 5 in Table 5.1 were modelled by multiple spring-damper elements with various parameters and boundary conditions, as shown in Figure 5.5d. One end of the spring-damper elements was connected to the rail bottom node (marked by R), and the other end to the beam node (marked by B). For type 1, a vanishingly small longitudinal stiffness of 0.3 kN/m of the spring-damper elements was

used to simulate the styrofoam-block support. For type 3, the stiffness and damping of the spring-damper elements were identified by best fitting the simulations to the measurement results[77], which are 25 MN/s and 0.2 kNs/m, respectively. For type 5, the rail bottom nodes were fixed to simulate the rigid constraint.

5.2.4. EVALUATION OF RAIL CONSTRAINTS FOR CORRUGATION MITIGATION

Based on the modelling and identified parameters of rail constraints in Section 2.3, three rail constraint models (called type I, II, III) were built up and applied in the 3D FE vehicle-track interaction model (see Figure 5.3) to examine their effects on corrugation mitigation, see a schematic drawing in Figure 5.6. These three models in the vertical and lateral directions remained the same as the fastening model in Figure 5.3c, while the rail longitudinal constraints were varied. In these models, rail longitudinal constraint was represented by multiple spring-damper elements as in Figure 5.5d with various parameters and boundary conditions. Type I intends to simulate the longitudinal free boundary of the rail constraint type 1 in Table 5.1 with a small longitudinal stiffness of 1.5 kN/m equivalent to the parameters of type 1 by considering a scale factor of 1/5[75]. Type II was built up to simulate the fastening longitudinal constraint of type 3 in Table 1 with the longitudinal stiffness and damping values of 125 MN/m and 5 kNs/m, respectively. The type III model fixed the rail bottom nodes above the sleeper in the longitudinal direction to simulate the rigid longitudinal constraint of type 5 in Table 5.1. The longitudinal wheel-rail dynamic contact force, which causes the differential wear and corrugation initiation (discussed in Section 3), will be evaluated with these three rail constraint models.

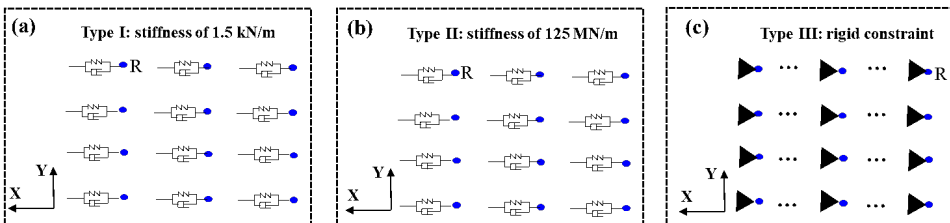


Figure 5.6: Three rail constraint models in the FE vehicle-track interaction model. R' designates the constrained rail node. (a) Type I: rail constraint with a small longitudinal stiffness of 1.5 kN/m; (b) type II: rail constraint with the longitudinal stiffness and damping values of 125 MN/m and 5 kNs/m; (c) type III: rigid rail constraint in the longitudinal direction.

5.3. CORRUGATION REPRODUCTION AND THE INITIATION MECHANISM

With the initial excitation introduced by the fastening model in Figure 5.3c, the longitudinal wheel-rail contact force (F_L) with strong fluctuation is induced, as shown in Figure 5.7a. It has four main wavelength components in the range of 20-80 mm, which are 24.9 mm, 28.6 mm, 33.3 mm and 39.4 mm respectively, as shown in Fig. 7b. Among them, the wavelength of 28.6 mm has the highest PSD magnitude and is thus dominant. Figure

5.7 also presents the calculated initial differential wear in the spatial and wavelength domains. Compared with F_L , it is found that initial differential wear and F_L have approximately the same trend and phase of the fluctuation amplitude in the spatial domain (see Figure 5.7a) and four almost identical wavelength components (see Figure 5.7b). It is hence concluded that longitudinal contact force F_L dominates initial differential wear. This initial differential wear causes corrugation initiation, and with the continuous accumulation of differential wear after multiple wheel passages, corrugation can consistently grow up to 80 μm [49]. Therefore, to mitigate or even eliminate corrugation, the fluctuation amplitude of the longitudinal contact force should be suppressed.

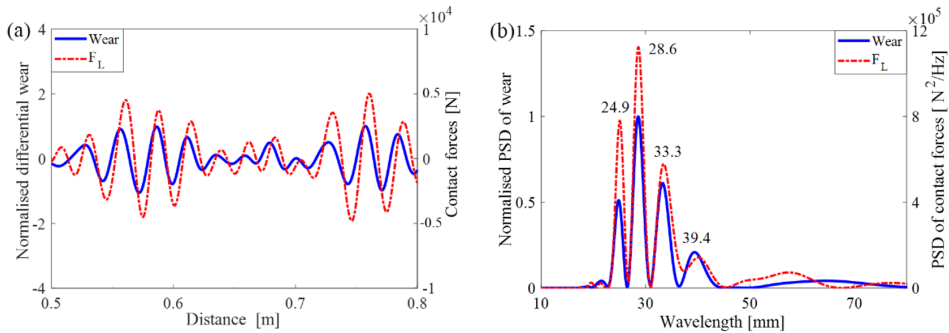


Figure 5.7: The simulated longitudinal contact force and initial differential wear from the 3D FE vehicle-track interaction model (see Figure 5.3) in spatial and wavelength domains. The results are band-pass filtered in the range of 20 – 80 mm. (a) Spatial domain; Initial differential wear and longitudinal contact force have approximately the same trend and phase of the fluctuation amplitude. (b) wavelength domain. Initial differential wear and longitudinal contact force have four almost identical wavelength components of 24.9 mm, 28.6 mm, 33.3 mm and 39.4 mm, respectively.

To better understand the fluctuation of the longitudinal contact force, its characteristic frequency f is calculated as follows.

$$f = v/\lambda \quad (5.5)$$

where v is the running speed 140 km/h, and λ is a characteristic wavelength, corresponding to the four major wavelength components of 39.4 mm, 33.3 mm, 28.6 mm and 24.9 mm, the characteristic frequencies of the longitudinal contact force are calculated as 977 Hz, 1161 Hz, 1360 Hz and 1556 Hz, respectively, as shown in Figure 5.8a and Table 5.2. These frequencies should be determined by the eigenmodes of the vehicle-track system. Figure 5.8b shows the track longitudinal dynamics characterized by FRF at position 2 (see Figure 5.3e). It is found from Figure 5.8b and Table 5.2 that characteristic frequencies of the longitudinal force correspond well to the peak frequencies of the FRF, indicating that rail vibration modes related to these peaks induce the fluctuation of longitudinal contact force and dominate the corrugation initiation. In order to identify these modes, the corresponding ODSs at these peak frequencies were derived and compared with rail longitudinal compression modes from modal analysis, as shown in Figure 5.9. The colour contrast in the mode shapes indicates the relative deformations of the elements. Blue is the minimum deformation, and red is the maximum. It can be

seen from Figure 5.9 that the ODSs at 977 Hz, 1161 Hz, 1360 Hz and 1556 Hz are consistent with the deformations of rail longitudinal compression modes at 923 Hz, 1172 Hz, 1420 Hz and 1671 Hz, respectively, indicating that the peaks in Figure 5.8b correspond to longitudinal compression modes. It should be noted that the fastening longitudinal rigid constraint in Figure 5.3c was replaced by the approximately equivalent longitudinal springs with a stiffness of 100 MN/m for the modal analysis. It is thus inferred that the longitudinal compression modes are responsible for the corrugation initiation.

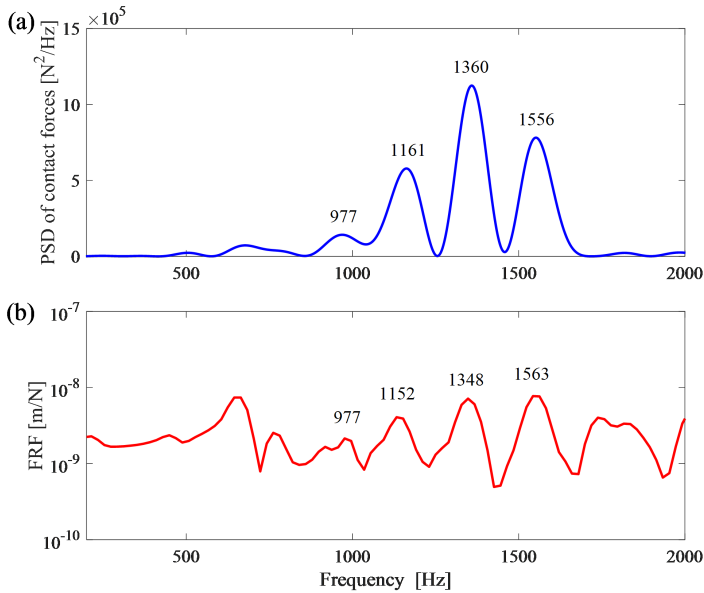


Figure 5.8: Comparison of characteristic frequencies of the longitudinal contact force and the longitudinal FRF at position 2. (a) PSD of the longitudinal contact force; it has four characteristic frequencies of 977 Hz, 1161 Hz, 1360 Hz and 1556 Hz. (b) the longitudinal FRF at position 2. It has corresponding four peak frequencies of 977 Hz, 1152 Hz, 1338 Hz and 1563 Hz.

Table 5.2: The values of parameters used in the model.

Longitudinal contact force frequency	977 Hz	1161 Hz	1360 Hz	1556 Hz
Longitudinal compression mode frequency with the fastening constraint in Figure 5.3c	977 Hz	1152 Hz	1348 Hz	1563 Hz
Longitudinal compression mode frequency with the fastening longitudinal stiffness of 100 MN/m	923 Hz	1172 Hz	1420 Hz	1671 Hz

Based on the results of Figure 5.7, Figure 5.8 and Figure 5.9, the corrugation initiation mechanism is further understood. With the fastening constraint in Figure 5.3c, rail longitudinal compression modes are released, as shown in Figure 5.8b. When the wheel

rolls over the rail, some of them are excited, and induce the fluctuation of the longitudinal wheel-rail contact force with the corresponding frequencies, resulting in initial differential wear and corrugation. Based on this insight, an approach to mitigate or even eliminate corrugation is proposed. That is to design a new rail constraint that can effectively suppress rail longitudinal compression modes so that longitudinal contact force fluctuates little, differential wear can barely accumulate, and corrugation can hardly initiate.

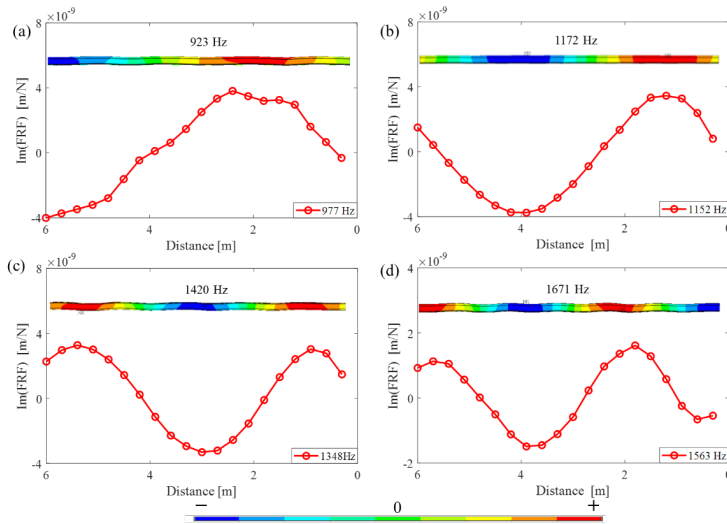


Figure 5.9: Comparison of ODSs at the four peak frequencies of the longitudinal FRF and rail longitudinal compression modes. (a) ODS at 977 Hz and longitudinal compression mode at 923 Hz; (b) ODS at 1152 Hz and longitudinal compression mode at 1172 Hz; (c) ODS at 1348 Hz and longitudinal compression mode at 1420 Hz; ODS at 1563 Hz and longitudinal compression mode at 1671 Hz. The colour contrast in the mode shapes indicates the relative deformations of the elements. Blue is the minimum deformation, and red is the maximum.

5.4. EXPERIMENTAL RESULTS AND MODELLING OF RAIL CONSTRAINTS FOR CORRUGATION MITIGATION

In this section, the influences of five types of rail constraints (see Table 5.1) on rail vibration modes, especially longitudinal compression modes, are analysed. Rail constraints type 1, type 3 and type 5 in Table 5.1 are modelled and validated against the measurement results.

5.4.1. EXPERIMENTAL RESULTS AND DISCUSSION

In this subsection, the experimental results of free rail vibrations (Section 4.1.1), rail vibrations under fastening constraints (Section 4.1.2) and rigid rail constraints (Section 4.1.3) are present. These results are further discussed in Section 4.1.4.

FREE RAIL VIBRATIONS

Figure 5.10 shows the FRFs with the rail constraint type 1 at accelerometer 1 in the vertical, longitudinal, and lateral directions up to 10 kHz. The rail with this constraint can be approximately considered to be in ‘free vibrations’, as described in Figure 5.4b and Table 5.1. The set of major peaks in the vertical FRF (★ in Figure 5.11 a) correspond to the rail vertical bending modes, and those in the longitudinal FRF (★ in Figure 5.11) correspond to longitudinal compression modes. Two sets of major peaks in the lateral FRF are coupled together (★ in Figure 5.11c), representing lateral bending and lateral torsion modes, respectively. A detailed description of these rail vibration modes can be found in[61].

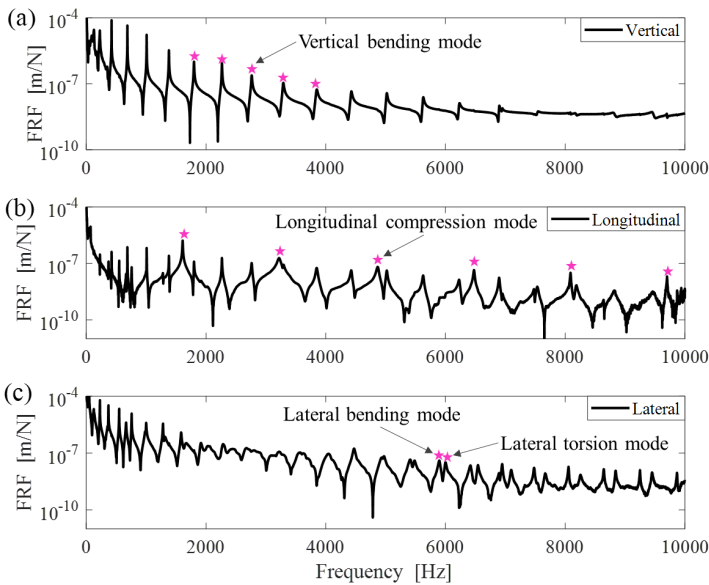


Figure 5.10: FRFs with the rail constraint type 1 at accelerometer 1 in the (a) vertical, (b) longitudinal and (c) lateral directions. In this figure, (★) show some examples of vertical bending modes, longitudinal compression modes, lateral bending and torsion modes.

Based on the FRF measurement results, the wavenumber-frequency dispersion curves of the 1/5 scaled rail were derived by connecting the discrete wavenumber-frequency points, as shown in Fig. 11a. The natural frequencies were derived from the major peak frequencies of FRFs in Figure 5.10, and the corresponding wavenumbers are calculated with $k = N\pi/L$, where λ is the wavelength, k is the wavenumber, N is an integer. Four types of waves, vertical bending waves (I), longitudinal compression waves (II), lateral bending waves (III) and lateral torsion waves (IV), were identified. Figure 5.11b compares the dispersion curves of the 1/5 scaled rail with those of full-scale rail. It should be noted that the frequency and wavenumber of the scaled rail have been modified by a

scaling factor of 1/5 for comparison based on the similarity law[75]. It can be seen that the dispersion curves of longitudinal compression waves (II) overlap almost completely with each other in these two cases. Differences were observed for vertical bending waves (I) above 1500 Hz, where significant cross-section deformations start to occur[61]. The dispersion curves of two lateral waves of the 1/5 scaled rail are considerably different from those of full-scale rail. The difference in these two cases is caused by the modification of the scaled rail profile, as shown in Figure 5.4e, which influences the rail vibration modes involving cross-section deformation. This also explains the absence of the web 1st bending waves (V) of the scaled rail in Figure 5.11b, whose cut-on frequency is beyond 2000 Hz because of the wider rail web, compared to the precisely 1/5 scaled one. In summary, longitudinal compression modes/waves of the scaled rail are equivalent to those of full-scale rail, which provides a basis for rail constraint design on the scaled rail instead of the full-scale rail. Despite the slight deviation, the vertical bending modes/waves of the scaled rail can be approximately regarded as the same as those of the full-scale rail. However, the lateral modes/waves show a significant difference in these two cases because of the imperfectly scaled rail profile.

5

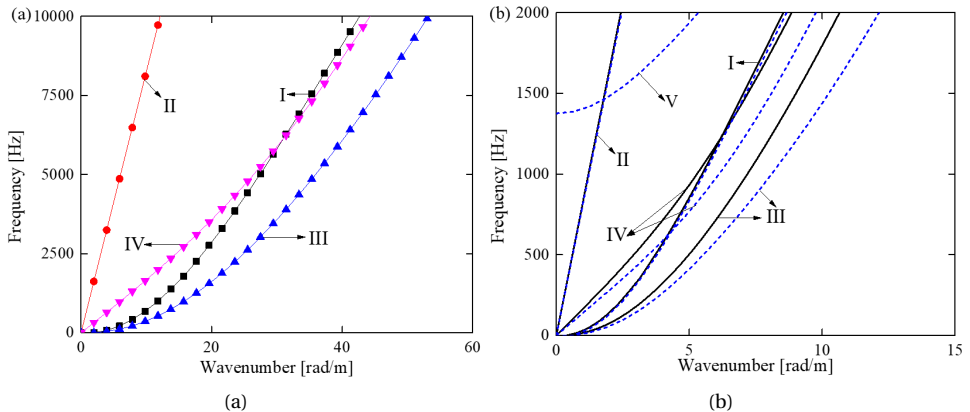


Figure 5.11: Wavenumber-frequency dispersion curves of the 1/5 scaled and full-scale free rails. (a) 1/5 scaled rail; (b) comparison between 1/5 scaled rail (—after modification) and full-scale rail (---). The result of the full-scale rail is from[61]. In this figure, 'I' refers to vertical bending waves, 'II' longitudinal compression waves, 'III' lateral bending waves, 'IV' lateral torsion waves, 'V' web 1st bending waves.

RAIL VIBRATIONS UNDER FASTENING CONSTRAINTS

Figure 5.12 shows the FRFs with rail constraints type 1, 2 and 3 at accelerometer 1 in the vertical, longitudinal, and lateral directions up to 10 kHz. Type 2 and type 3 correspond to railpads with half-tight and full-tight clip 1, respectively, as listed in Table 5.1, which are used to simulate field fastening constraints. Compared to type 1, vertical bending modes with type 2 and type 3 were significantly suppressed and could barely be distinguished in the vertical FRFs, as shown in Figure 5.12a. Only one dominant peak was observed at around 1050 Hz, corresponding to the rail resonance mode on the fastening vertical stiffness. The tightness (half- or full-tight) of clip 1 has an insignificant influence on the vertical FRFs. Different from the vertical bending modes, the longitudi-

nal compression modes were still identifiable under the fastening constraint, although their fluctuation amplitudes were considerably reduced. When the tightness of clip 1 increased from type 2 to type 3, the overall fluctuation amplitudes of longitudinal compression modes became slightly smaller, and the rail longitudinal resonance mode was shifted from about 845 Hz to 965 Hz. Figure 5.13 shows that the ODSs of type 3 at 1742 Hz and 4840 Hz have shapes similar to the ODSs of type 1 at 1610 Hz and 4870 Hz and are consistent with the deformations of longitudinal compression modes of the free rail at 1620 Hz and 4880 Hz. This result confirms that the major peaks in Figure 5.11b and Figure 5.12b correspond to longitudinal compression modes, which share features similar to those of the full-scale rail in Figure 5.9. Similar to vertical bending modes, rail lateral bending and torsion modes were also significantly suppressed by the fastening constraint with half-tight clip 1, and became almost invisible from the lateral FRF with full-tight clip 1, as shown in Figure 5.12c.

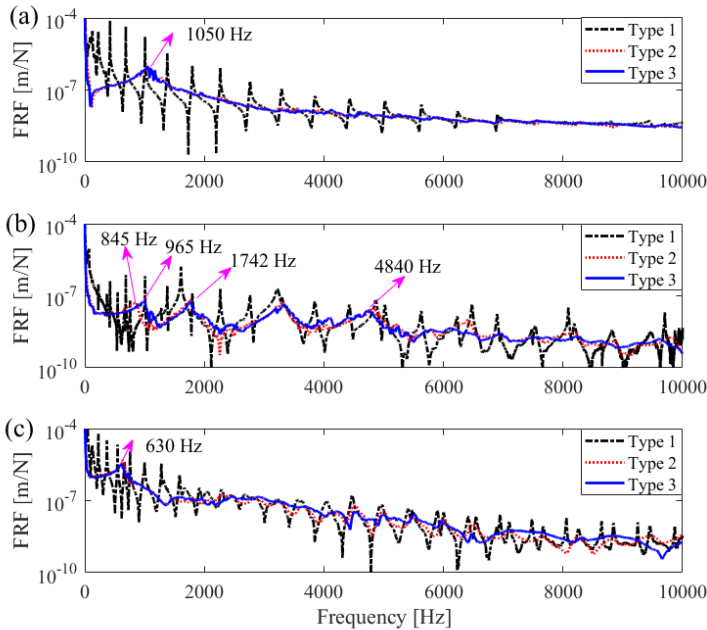


Figure 5.12: FRFs with rail constraints type 1, 2 and 3 at accelerometer 1 in the (a) vertical, (b) longitudinal and (c) lateral directions. The pink arrow in (a) shows the vertical resonance mode at 1050 Hz, the arrows in (b) indicate the longitudinal resonance modes at 845 Hz for type 2 and 965 Hz for type 3, and the arrow in (c) shows the lateral resonance mode at 630 Hz.

Overall, vertical bending modes and lateral bending and torsion modes are effectively suppressed by the fastening constraint with full-tight clip 1, while longitudinal compression modes still have relatively strong fluctuation amplitude. This result agrees with the findings in[61] that, the fastenings constrain the longitudinal rail vibrations less strongly

compared to the vertical and lateral directions.

RAIL VIBRATIONS UNDER RIGID RAIL CONSTRAINTS

Figure 5.14 shows the FRFs with rail constraints types 3, 4 and 5 at accelerometer 1 in the vertical, longitudinal, and lateral directions. Type 4 and type 5 correspond to steel plates with full-tight clip 1 and clip 2, respectively, as listed in Table 5.1, which are used to simulate relatively rigid rail constraints. Compared to clip 1, clip 2 is wider and thicker, which is expected to provide a stronger constraint to the rail and more completely suppress the longitudinal compression modes. It can be seen from Figure 5.14a and Figure 5.14c that the vertical bending modes and lateral bending and torsion modes are effectively suppressed by the two types of rigid rail constraints. Despite the significant mitigation, longitudinal compression modes are still identifiable at about 4935 Hz and 6230 Hz (indicated by pink arrows in Figure 5.14b) with type 4. By replacing clip 1 with clip 2, longitudinal compression modes are almost invisible in the longitudinal FRE, indicating the type 5 is capable of completely suppressing them. In addition, compared to type 3, the rail resonance modes in the vertical, longitudinal and lateral directions have been shifted to 1500 Hz, 1495 Hz and 1025 Hz, respectively, with reduced amplitude, as shown in Figure 5.14. That is because the support stiffness of steel pads of type 4 and 5 are larger than the resilient railpads of type 3.

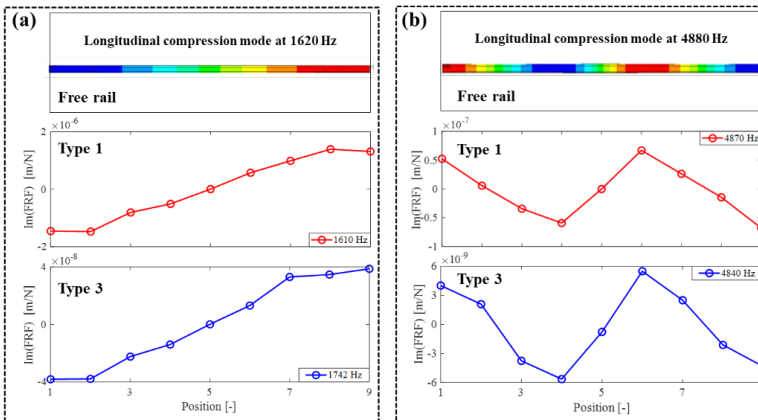


Figure 5.13: Comparison of longitudinal ODSs with rail constraints type 1 and type 3 and longitudinal compression modes of free rail. (a) Comparison of ODS with type 1 at 1610 Hz, ODS with type 3 at 1742 Hz, and longitudinal compression mode at 1620 Hz; (b) comparison of ODS with type 1 at 4870 Hz, ODS with type 3 at 4840 Hz and longitudinal compression mode at 4880 Hz.

DISCUSSION OF EXPERIMENTAL RESULTS

In this chapter, five types of rail constraints were designed and their influences on rail vibration modes were analysed. Overall, these five types of rail constraints can be characterized into three categories, 'zero stiffness' of free rail (type 1), 'finite stiffness' of fastening constraint (type 2 and 3), 'infinite stiffness' of rigid constraint (type 4 and 5). The experimental results indicate that longitudinal compression modes/waves of the scaled free rail are equivalent to those of full-scale rail within 2 kHz with a scaling factor of 1/5.

That is because the dispersion relation of longitudinal waves of free rail is only determined by the rail material, i.e., young's modulus and density. However, the rail vibration modes involving cross-section deformation, such as lateral torsion modes, web 1st bending modes, are significantly influenced by the imperfectly scaled rail profile. The fastening constraint with finite stiffness (type 3) can effectively suppress vertical bending modes and lateral modes with appropriate parameter design, but cannot completely restrict longitudinal compression modes. Therefore, we further strengthened the rail constraints with 'infinite stiffness' (type 5). Experimental results indicated this constraint can effectively suppress longitudinal compression modes and thus be supposed to mitigate or even eliminate corrugation.

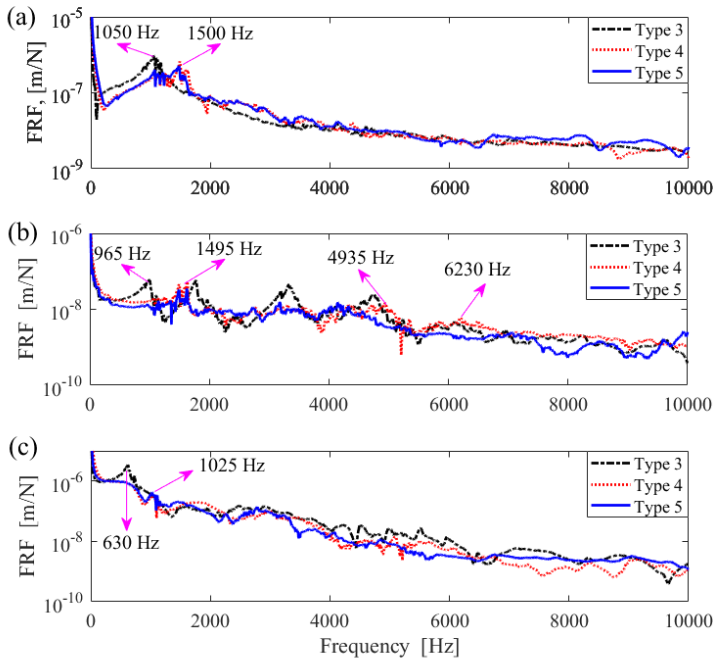


Figure 5.14: FRFs with rail constraints types 3, 4 and 5 at accelerometer 1 in the (a) vertical, (b) longitudinal and (c) lateral directions. The pink arrows in (a) show the vertical resonance mode shifts from 1050 Hz with type 3 to 1500 Hz with type 5, arrows in (b) show the longitudinal resonance mode shifts from 965 Hz with type 3 to 1495 Hz with type 5, and arrows in (c) show the lateral resonance mode shifts from 630 Hz with type 3 to 1025 Hz with type 5.

5.4.2. VALIDATION OF FE MODELLING OF RAIL CONSTRAINTS

Figure 5.15 shows the simulated and measured longitudinal FRFs with rail constraints type 1, type 3 and type 5 to consider the cases of 'zero stiffness', 'finite stiffness' and 'infinite stiffness', respectively. The overall tendencies and fluctuation amplitude from the simulations match the measurements well. The simulations identify almost all the peaks in the measured FRFs, as shown in Figure 5.16a and 5.16b. In these three cases, it is ob-

served that the simulations seem to overestimate the FRFs at higher frequencies above 7 kHz. The reason is that the excitation energy of the small hammer in the test has considerably dropped over 7 kHz [67] and thus the rail-constraint system cannot be sufficiently excited at higher frequencies, leading to the smaller FRFs of the measurements. Overall, good agreement has been achieved between the simulations and the measurements, indicating the modelling of the rail constraints can accurately reproduce the dynamic behaviours of the rail-constraint system.

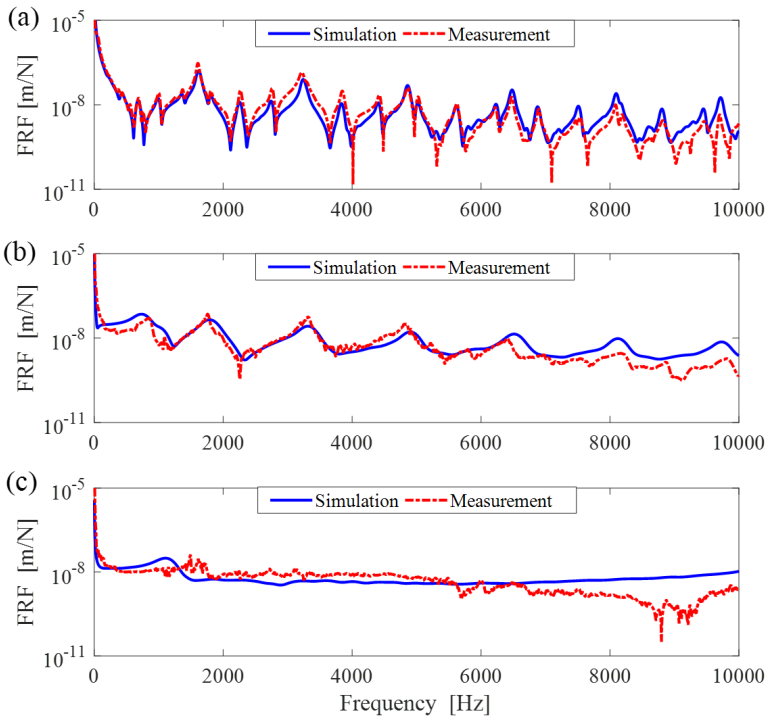


Figure 5.15: Validation of longitudinal FRFs with rail constraints type 1, type 3 and type 5. (a) Type 1, free rail; (b) type 3, rail under the fastening constraint; (c) type 5, rail under the rigid constraint.

5.5. EVALUATION OF RAIL CONSTRAINTS FOR CORRUGATION MITIGATION

Three rail constraint models (type I, II, III in Figure 5.6) were applied in the 3D FE vehicle-track interaction model to examine their effectiveness on corrugation mitigation. Figure 5.16 shows the longitudinal wheel-rail contact forces with these constraint models. It can be seen that the fluctuation amplitude of longitudinal contact force with type III is significantly smaller than those with type I and II. Therefore the resulting initial differential wear is much smaller, and corrugation can hardly initiate. This result indicates the rail constraint model type III, corresponding to the rigid constraint of type 5 in the ex-

perimental setup (see Table 5.1), can effectively suppress rail longitudinal compression mode, reduce the fluctuation of longitudinal contact force, and mitigate corrugation.

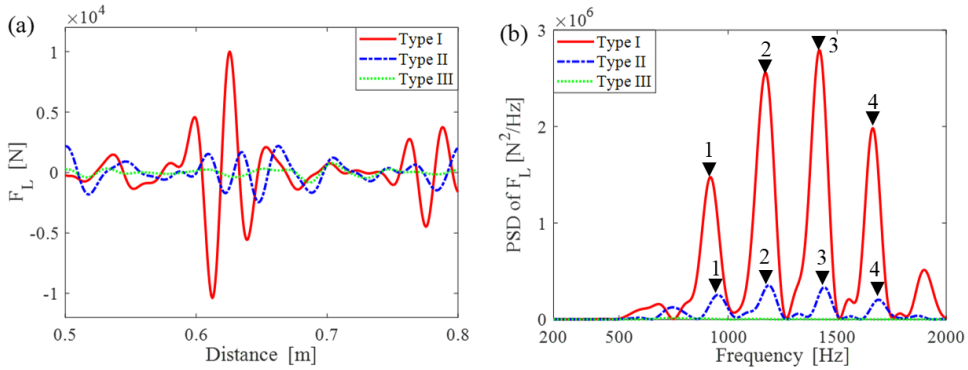


Figure 5.16: Longitudinal wheel-rail contact forces with rail constraint models type I, II, III in the spatial and frequency domains. (a) Spatial domain; The fluctuation amplitude of longitudinal contact force with type III is significantly smaller than those with type I and II. (b) frequency domain. The marks (\blacktriangledown) indicate the characteristic frequencies of the contact forces with type I and type II.

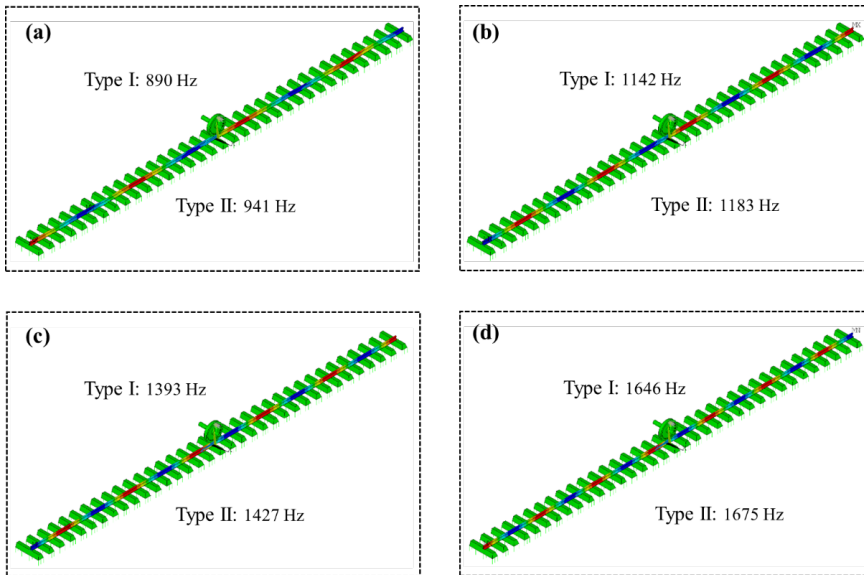


Figure 5.17: Rail longitudinal compression modes with rail constraint models type I and II. (a) 890 Hz for type I and 941 Hz for type II with the same mode shape; (b) 1142 Hz for type I and 1183 Hz for type II; (c) 1393 Hz for type I and 1427 Hz for type II; (d) 1646 Hz for type I and 1675 Hz for type II.

In addition, it is observed that type II considerably reduces the fluctuation amplitude of longitudinal force, compared to that of type I. Figure 5.16b also shows that the major frequency components (marked by \blacktriangledown and number) of longitudinal force with types I and

II are different from each other. That is because of the different fastening parameters in these two cases, which influence the eigen frequencies of the vehicle-track system and thus characteristic frequencies of longitudinal force and corrugation. To gain insight into the dynamic behaviour of the vehicle-track system with type I and type II, a modal analysis was performed and their longitudinal compression modes were compared in Figure 5.17 and Table 5.3. It is found that characteristic frequencies of the longitudinal force correspond well to the eigen frequencies of longitudinal compression modes, confirming that longitudinal compression modes are responsible for corrugation initiation. Besides, the mode frequencies with type I are shifted to larger values with type II because of the larger fastening longitudinal stiffness.

Table 5.3: Comparison of characteristic frequencies of longitudinal force and longitudinal compression modes with rail constraint models type I and type II.

Number in Figure 5.16b	Longitudinal force peak frequency with type I in Figure 5.16b	Mode frequency with type I in Figure 5.17	Longitudinal force peak frequency with type II in Figure 5.16b	Mode frequency with type II in Figure 5.17
1	915 Hz	890 Hz	958 Hz	941 Hz
2	1170 Hz	1142 Hz	1184 Hz	1183 Hz
3	1418 Hz	1393 Hz	1440 Hz	1427 Hz
4	1663 Hz	1646 Hz	1691 Hz	1675 Hz

5.6. CONCLUSIONS

This paper proposes a methodology to mitigate short pitch corrugation by rail constraint design. This methodology includes four steps. In Step 1, short pitch corrugation were numerically reproduced by employing a 3D FE vehicle-track interaction model. In Step 2, the corrugation initiation mechanism was identified by comparing the ODSs with rail longitudinal compression modes. In Step 3, five types of rail constraints were designed and their influences on rail vibration modes were analyzed. Models of rail constraints types 1, 3 and 5 were built up and validated. In Step 4, the rail constraint models from Step 3 were applied in the FE vehicle-track interaction model, and their effectiveness on corrugation mitigation was evaluated. The main findings are summarized as follows.

The corrugation initiation mechanism is identified from the analysis of ODSs. With a particular fastening constraint, rail longitudinal compression modes may not be effectively suppressed. When the wheel rolls over the rail, some of them are excited, and induce longitudinal wheel-rail dynamic contact force with corresponding frequencies, resulting in the initial differential wear and corrugation. Based on this corrugation initiation mechanism, an approach is proposed to mitigate or even eliminate corrugation. That is to design a new rail constraint that can effectively suppress rail longitudinal compression modes so that the induced longitudinal contact force fluctuates little, differential wear can barely accumulate, and corrugation can hardly initiate.

Five type of rail constraints are designed and evaluated, and among them, a relatively rigid constraint (type 5) can completely suppress rail longitudinal compression modes. Afterwards, this rail constraint model is applied in the FE vehicle-track model and the simulated longitudinal contact force has a significantly small fluctuation amplitude so that corrugation can hardly initiate. Besides, it is found that fastening longitudinal parameters influence the frequencies of longitudinal compression modes and thus the characteristic wavelengths/frequencies and spatial distribution of short pitch corruga-

tion.

Overall, this paper points out a direction for short pitch corrugation mitigation in the field by strengthening the rail longitudinal constraint. In future work, we will perform the experimental validation of corrugation initiation mechanism and the designed new rail constraint for corrugation mitigation by employing an innovative V-Track test rig[75].

REFERENCES

- [1] S. Grassie and J. Kalousek, *Rail corrugation: characteristics, causes and treatments*, Proceedings of the Institution of Mechanical Engineers, Part F: Journal of Rail and Rapid Transit **207**, 57 (1993).
- [2] S. Grassie, *Rail corrugation: characteristics, causes, and treatments*, Proceedings of the Institution of Mechanical Engineers, Part F: Journal of Rail and Rapid Transit **223**, 581 (2009).
- [3] S. Li, Z. Li, A. Núñez, and R. Dollevoet, *New insights into the short pitch corrugation enigma based on 3d-fe coupled dynamic vehicle-track modeling of frictional rolling contact*, Applied Sciences **7**, 807 (2017).
- [4] J. Xu, K. Wang, X. Liang, Y. Gao, Z. Liu, R. Chen, P. Wang, F. Xu, and K. Wei, *Influence of viscoelastic mechanical properties of rail pads on wheel and corrugated rail rolling contact at high speeds*, Tribology International **151**, 106523 (2020).
- [5] J. Sadeghi and A. Hasheminezhad, *Correlation between rolling noise generation and rail roughness of tangent tracks and curves in time and frequency domains*, Applied Acoustics **107**, 10 (2016).
- [6] J. Han, X. Xiao, Y. Wu, Z. Wen, and G. Zhao, *Effect of rail corrugation on metro interior noise and its control*, Applied Acoustics **130**, 63 (2018).
- [7] T. Xin, S. Wang, L. Gao, H. Huo, Y. Ding, P. Wang, P. Chen, and P. Liu, *Field measurement of rail corrugation influence on environmental noise and vibration: A case study in china*, Measurement **164**, 108084 (2020).
- [8] R. Clark, P. Dean, J. Elkins, and S. Newton, *An investigation into the dynamic effects of railway vehicles running on corrugated rails*, Journal of Mechanical Engineering Science **24**, 65 (1982).
- [9] X. Deng, Z. Qian, Z. Li, and R. Dollevoet, *Investigation of the formation of corrugation-induced rail squats based on extensive field monitoring*, International Journal of Fatigue **112**, 94 (2018).
- [10] S. Grassie, M. Saxon, and J. Smith, *Measurement of longitudinal rail irregularities and criteria for acceptable grinding*, Journal of Sound and Vibration **227**, 949 (1999).
- [11] P. Cuervo, J. Santa, and A. Toro, *Correlations between wear mechanisms and rail grinding operations in a commercial railroad*, Tribology International **82**, 265 (2015).

- [12] Y. M. Liu, T. Y. Yang, Z. He, and J. Y. Li, *Analytical modeling of grinding process in rail profile correction considering grinding pattern*, Archives of Civil and Mechanical Engineering **18**, 669 (2018).
- [13] Y. Sun, P. Wang, J. Lu, J. Xu, P. Wang, S. Xie, Y. Li, J. Dai, B. Wang, and M. Gao, *Rail corrugation inspection by a self-contained triple-repellent electromagnetic energy harvesting system*, Applied Energy **286**, 116512 (2021).
- [14] Z. Wei, X. Sun, F. Yang, Z. Ke, T. Lu, P. Zhang, and C. Shen, *Carriage interior noise-based inspection for rail corrugation on high-speed railway track*, Applied Acoustics **196**, 108881 (2022).
- [15] Q. Xie, G. Tao, B. He, and Z. Wen, *Rail corrugation detection using one-dimensional convolution neural network and data-driven method*, Measurement, 111624 (2022).
- [16] P. Meehan, P. Bellette, R. Batten, W. Daniel, and R. Horwood, *A case study of wear-type rail corrugation prediction and control using speed variation*, Journal of Sound and Vibration **325**, 85 (2009).
- [17] P. Bellette, P. Meehan, and W. Daniel, *Contact induced wear filtering and its influence on corrugation growth*, Wear **268**, 1320 (2010).
- [18] T. Vuong, P. Meehan, D. Eadie, K. Oldknow, D. Elvidge, P. Bellette, and W. Daniel, *Investigation of a transitional wear model for wear and wear-type rail corrugation prediction*, Wear **271**, 287 (2011).
- [19] N. Correa, E. Vadillo, J. Santamaria, and J. Herreros, *A versatile method in the space domain to study short-wave rail undulatory wear caused by rail surface defects*, Wear **352**, 196 (2016).
- [20] J. Santa, A. Toro, and R. Lewis, *Correlations between rail wear rates and operating conditions in a commercial railroad*, Tribology International **95**, 5 (2016).
- [21] X. Zhao, P. Zhang, and Z. Wen, *On the coupling of the vertical, lateral and longitudinal wheel-rail interactions at high frequencies and the resulting irregular wear*, Wear **430**, 317 (2019).
- [22] K. Hempelmann and K. Knothe, *An extended linear model for the prediction of short pitch corrugation*, Wear **191**, 161 (1996).
- [23] S. Muller, *A linear wheel-track model to predict instability and short pitch corrugation*, Journal of Sound and Vibration **227**, 899 (1999).
- [24] L. Afferrante and M. Ciavarella, *Short-pitch rail corrugation: A possible resonance-free regime as a step forward to explain the “enigma”?* Wear **266**, 934 (2009).
- [25] A. Johansson and J. C. Nielsen, *Rail corrugation growth—influence of powered wheelsets with wheel tread irregularities*, Wear **262**, 1296 (2007).
- [26] T. Wu and D. Thompson, *An investigation into rail corrugation due to micro-slip under multiple wheel/rail interactions*, Wear **258**, 1115 (2005).

- [27] C. Ma, L. Gao, T. Xin, X. Cai, M. M. Nadakatti, and P. Wang, *The dynamic resonance under multiple flexible wheelset-rail interactions and its influence on rail corrugation for high-speed railway*, Journal of Sound and Vibration **498**, 115968 (2021).
- [28] R. Batten, P. Bellette, P. Meehan, R. Horwood, and W. Daniel, *Field and theoretical investigation of the mechanism of corrugation wavelength fixation under speed variation*, Wear **271**, 278 (2011).
- [29] P. Bellette, P. Meehan, and W. Daniel, *Validation of a tangent track corrugation model with a two disk test rig*, Wear **271**, 268 (2011).
- [30] P. Meehan, R. Batten, and P. Bellette, *The effect of non-uniform train speed distribution on rail corrugation growth in curves/corners*, Wear **366**, 27 (2016).
- [31] G. Chen, Z. Zhou, H.-j. Ouyang, X. Jin, M. Zhu, and Q. Liu, *A finite element study on rail corrugation based on saturated creep force-induced self-excited vibration of a wheelset-track system*, Journal of sound and Vibration **329**, 4643 (2010).
- [32] X. Cui, G. Chen, J. Zhao, W. Yan, H. Ouyang, and M. Zhu, *Field investigation and numerical study of the rail corrugation caused by frictional self-excited vibration*, Wear **376**, 1919 (2017).
- [33] X. Cui, Z. He, B. Huang, Y. Chen, Z. Du, and W. Qi, *Study on the effects of wheel-rail friction self-excited vibration and feedback vibration of corrugated irregularity on rail corrugation*, Wear **477**, 203854 (2021).
- [34] W. Li, Z. Zhou, X. Zhao, Z. Wen, and X. Jin, *Formation mechanism of short-pitch rail corrugation on metro tangent tracks with resilient fasteners*, Vehicle System Dynamics, 1 (2022).
- [35] J. L. Escalona and J. F. Aceituno, *Multibody simulation of railway vehicles with contact lookup tables*, International Journal of Mechanical Sciences **155**, 571 (2019).
- [36] X. Yu, J. F. Aceituno, E. Kurvinen, M. K. Matikainen, P. Korkealaakso, A. Rouvinen, D. Jiang, J. L. Escalona, and A. Mikkola, *Comparison of numerical and computational aspects between two constraint-based contact methods in the description of wheel/rail contacts*, Multibody System Dynamics **54**, 303 (2022).
- [37] C. Shen, X. Deng, Z. Wei, R. Dollevoet, A. Zoeteman, and Z. Li, *Comparisons between beam and continuum models for modelling wheel-rail impact at a singular rail surface defect*, International Journal of Mechanical Sciences **198**, 106400 (2021).
- [38] Z. Dimitrovová, *Two-layer model of the railway track: Analysis of the critical velocity and instability of two moving proximate masses*, International Journal of Mechanical Sciences **217**, 107042 (2022).
- [39] L. Xu, X. Chen, X. Li, and X. He, *Development of a railway wagon-track interaction model: case studies on excited tracks*, Mechanical Systems and Signal Processing **100**, 877 (2018).

- [40] Z. Yang, X. Deng, and Z. Li, *Numerical modeling of dynamic frictional rolling contact with an explicit finite element method*, Tribology international **129**, 214 (2019).
- [41] X. Deng, Z. Qian, Z. Li, and R. Dollevoet, *Applicability of half-space-based methods to non-conforming elastic normal contact problems*, International Journal of Mechanical Sciences **126**, 229 (2017).
- [42] Z. Yang, A. Boogaard, Z. Wei, J. Liu, R. Dollevoet, and Z. Li, *Numerical study of wheel-rail impact contact solutions at an insulated rail joint*, International Journal of Mechanical Sciences **138**, 310 (2018).
- [43] X. Deng, Z. Li, Z. Qian, W. Zhai, Q. Xiao, and R. Dollevoet, *Pre-cracking development of weld-induced squats due to plastic deformation: Five-year field monitoring and numerical analysis*, International Journal of Fatigue **127**, 431 (2019).
- [44] Z. Yang and Z. Li, *A numerical study on waves induced by wheel-rail contact*, International Journal of Mechanical Sciences **161**, 105069 (2019).
- [45] N. K. Mandal and M. Dhanasekar, *Sub-modelling for the ratchetting failure of insulated rail joints*, International Journal of Mechanical Sciences **75**, 110 (2013).
- [46] H. Su, C. L. Pun, P. Mutton, Q. Kan, G. Kang, and W. Yan, *Numerical study on the ratcheting performance of rail flash butt welds in heavy haul operations*, International Journal of Mechanical Sciences **199**, 106434 (2021).
- [47] Z. Yang and Z. Li, *Numerical modeling of wheel-rail squeal-exciting contact*, International Journal of Mechanical Sciences **153**, 490 (2019).
- [48] V.-V. Lai, O. Chiello, J.-F. Brunel, and P. Dufrenoy, *The critical effect of rail vertical phase response in railway curve squeal generation*, International Journal of Mechanical Sciences **167**, 105281 (2020).
- [49] S. Li, *Mechanisms of short pitch rail corrugation*, Delft University of Technology (2022).
- [50] K. Knothe, Z. Strzyzakowski, and K. Willner, *Rail vibrations in the high frequency range*, Journal of Sound and Vibration **169**, 111 (1994).
- [51] D. Thompson, *Wheel-rail noise generation, part iii: rail vibration*, Journal of sound and vibration **161**, 421 (1993).
- [52] D. Thompson and J. Verheij, *The dynamic behaviour of rail fasteners at high frequencies*, Applied Acoustics **52**, 1 (1997).
- [53] M. Oregui, A. De Man, M. Woldekidan, Z. Li, and R. Dollevoet, *Obtaining railpad properties via dynamic mechanical analysis*, Journal of Sound and Vibration **363**, 460 (2016).
- [54] K. Wei, F. Wang, P. Wang, Z.-x. Liu, and P. Zhang, *Effect of temperature-and frequency-dependent dynamic properties of rail pads on high-speed vehicle-track coupled vibrations*, Vehicle System Dynamics **55**, 351 (2017).

- [55] Y. Luo, Y. Liu, and H. Yin, *Numerical investigation of nonlinear properties of a rubber absorber in rail fastening systems*, *International Journal of Mechanical Sciences* **69**, 107 (2013).
- [56] M. Oregui, Z. Li, and R. Dollevoet, *An investigation into the modeling of railway fastening*, *International Journal of Mechanical Sciences* **92**, 1 (2015).
- [57] J. Egana, J. Vinolas, and M. Seco, *Investigation of the influence of rail pad stiffness on rail corrugation on a transit system*, *Wear* **261**, 216 (2006).
- [58] O. Oyarzabal, J. Gomez, J. Santamaria, and E. Vadillo, *Dynamic optimization of track components to minimize rail corrugation*, *Journal of sound and vibration* **319**, 904 (2009).
- [59] X. Cui, G. Chen, H. Yang, Q. Zhang, H. Ouyang, and M. Zhu, *Study on rail corrugation of a metro tangential track with cologne-egg type fasteners*, *Vehicle System Dynamics* **54**, 353 (2016).
- [60] W. Liu, H. Zhang, W. Liu, and D. J. Thompson, *Experimental study of the treatment measures for rail corrugation on tracks with egg fasteners in the beijing metro*, *Proceedings of the Institution of Mechanical Engineers, Part F: Journal of Rail and Rapid Transit* **232**, 1360 (2018).
- [61] P. Zhang, S. Li, A. Núñez, and Z. Li, *Multimodal dispersive waves in a free rail: Numerical modeling and experimental investigation*, *Mechanical Systems and Signal Processing* **150**, 107305 (2021).
- [62] P. Zhang, S. Li, A. Núñez, and Z. Li, *Vibration modes and wave propagation of the rail under fastening constraint*, *Mechanical Systems and Signal Processing* **160**, 107933 (2021).
- [63] K. Knothe and S. Grassie, *Modelling of railway track and vehicle/rail interaction at high frequencies*, *Vehicle system dynamics* **22**, 209 (1993).
- [64] M. Hiensch, J. C. Nielsen, and E. Verheijen, *Rail corrugation in the netherlands—measurements and simulations*, *Wear* **253**, 140 (2002).
- [65] D. J. Benson and J. O. Hallquist, *A single surface contact algorithm for the post-buckling analysis of shell structures*, *Computer methods in applied mechanics and engineering* **78**, 141 (1990).
- [66] X. Zhao and Z. Li, *The solution of frictional wheel–rail rolling contact with a 3d transient finite element model: Validation and error analysis*, *Wear* **271**, 444 (2011).
- [67] Z. Yang, A. Boogaard, R. Chen, R. Dollevoet, and Z. Li, *Numerical and experimental study of wheel-rail impact vibration and noise generated at an insulated rail joint*, *International Journal of Impact Engineering* **113**, 29 (2018).
- [68] M. Molodova, Z. Li, A. Núñez, and R. Dollevoet, *Validation of a finite element model for axle box acceleration at squats in the high frequency range*, *Computers & Structures* **141**, 84 (2014).

- [69] Z. Li, X. Zhao, R. Dollevoet, and M. Molodova, *Differential wear and plastic deformation as causes of squat at track local stiffness change combined with other track short defects*, *Vehicle System Dynamics* **46**, 237 (2008).
- [70] J. Kalousek and K. Johnson, *An investigation of short pitch wheel and rail corrugations on the vancouver mass transit system*, *Proceedings of the Institution of Mechanical Engineers, Part F: Journal of Rail and Rapid Transit* **206**, 127 (1992).
- [71] J. Neilsen, *Evolution of rail corrugation predicted with a non-linear wear model*, *Journal of Sound and Vibration* **227**, 915 (1999).
- [72] M. Oregui, Z. Li, and R. Dollevoet, *Identification of characteristic frequencies of damaged railway tracks using field hammer test measurements*, *Mechanical Systems and Signal Processing* **54**, 224 (2015).
- [73] D. Thompson, *Experimental analysis of wave propagation in railway tracks*, *Journal of sound and vibration* **203**, 867 (1997).
- [74] C. Heliot, *Small-scale test method for railway dynamics*, *Vehicle System Dynamics* **15**, 197 (1986).
- [75] M. Naeimi, Z. Li, R. H. Petrov, J. Sietsma, and R. Dollevoet, *Development of a new downscale setup for wheel-rail contact experiments under impact loading conditions*, *Experimental Techniques* **42**, 1 (2018).
- [76] P. Zhang, J. Moraal, and Z. Li, *Design, calibration and validation of a wheel-rail contact force measurement system in v-track*, *Measurement* **175**, 109105 (2021).
- [77] M. Oregui, Z. Li, and R. Dollevoet, *An investigation into the vertical dynamics of tracks with monoblock sleepers with a 3d finite-element model*, *Proceedings of the Institution of Mechanical Engineers, Part F: Journal of Rail and Rapid Transit* **230**, 891 (2016).

6

DESIGN, CALIBRATION AND VALIDATION OF A WHEEL-RAIL CONTACT FORCE MEASUREMENT SYSTEM IN V-TRACK

An innovative downscale test rig called V-Track has been constructed for wheel-rail contact experiments under impact loading conditions. In this chapter, a force measurement system termed a dynamometer was developed in V-Track to measure the wheel-rail contact forces. The dynamometer consists of four 3-component piezoelectric force sensors and was mounted between the wheel assembly and the steel frame of V-Track, enabling it to measure the forces transmitted from the wheel-rail interface to the frame. Static tests were first carried out to calibrate the dynamometer in three directions. Then, several tests were performed in V-Track to examine the reliability and validity of the dynamometer for measuring the wheel-rail contact forces under running conditions. Experimental results show that the dynamometer is capable of reliably and accurately measuring these forces. Utilizing the measurement results from the dynamometer, the control of the wheel-rail contact forces in V-Track has also been achieved.

6.1. INTRODUCTION

Railway transport is a major means of transportation worldwide and has become increasingly popular because it is economic, safe and environmentally friendly. In recent years, with increasing train speed and axle loads, more defects have arisen in the wheels and rails, such as rail squats, head checks, corrugation, and wheel polygonization, which considerably increase the maintenance cost. To pinpoint the formation mechanisms of these defects and develop the corresponding countermeasures, an innovative downscale test rig called ‘V-Track’ has been developed in the laboratory[2] to simulate vehicle-track interactions, as shown in Figure 6.1. Compared to other existing test facilities[3][4][5][6], V-Track can simulate not only the wheel-rail contact but also the high-frequency dynamics of the vehicle-track system, enabling wheel-rail contact experiments under impact loading in this system. In[2], a potential corrugation after the rail joint in the V-track has been reproduced, which shares similar features with an actual corrugation after the rail joint in the Dutch railway network. Wheel-rail contact force measurement is funda-

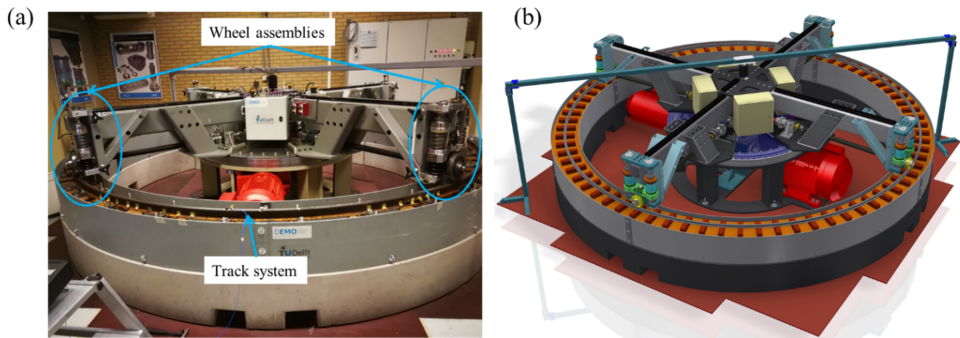


Figure 6.1: Downscale V-Track for wheel-rail contact experiments. (a) V-Track developed in the laboratory; (b) schematic CAD drawing of V-Track.

mental to understanding wheel-rail interaction. The forces are responsible for the wear, deformation, and fatigue of the wheels and rails. Train derailment criteria are based on the amplitudes of the contact forces[7]. For laboratory test facilities, accurate measurement of wheel-rail contact forces is a prerequisite for force control to simulate different loading conditions from engineering practice, for instance, traction, braking, and curve negotiation.

Several measurement approaches for wheel-rail contact forces have been reported in the literature, and they can be classified into two categories, i.e., direct methods and indirect methods. Direct methods typically use an instrumented wheelset equipped with dynamometric sensors to directly measure the forces. For example, Gullers et al.[8] employed strain gauges on a wheel disc to measure vertical wheel-rail contact forces at up to 2 kHz in the field, and four different classes of rail irregularities were identified when evaluating the measured forces. Gomez et al.[9] analyzed two distribution methods of strain gauges based on axle instrumentation and wheel web instrumentation and found that the method based on the axle presented dynamic errors because of the inertia of the wheel mass. Matsumoto et al.[10] proposed a new method in which noncontact

gap sensors were mounted on a bogie frame to measure the lateral wheel-rail contact force from the lateral distortion of the wheel. Urda et al.[11] equipped a 1/10 scaled dynamometric wheelset with two technologies: strain gauges and noncontact gap sensors. The results indicated that the technology using strain gauges is a favorable choice for measuring lateral wheel-rail contact forces with high accuracy. Nevertheless, strain gauges are much more expensive than gap sensors because the former require expensive telemetry system(s) to transfer data from the rotating wheelset to the data acquisition system. Another type of direct method utilized strain gauges[12][13][14] or piezoelectric sensors[15] on the rail web to measure the wheel-rail contact forces. This rail instrumentation method has an advantage over the wheel instrumentation method in that the former does not need an expensive telemetry system for data transmission, but the disadvantage is that the measurement can be performed only at some discrete points of the track.

Indirect methods combine the measurement of vehicle dynamic responses (i.e., acceleration) with a vehicle-track interaction model to derive the wheel-rail contact forces. An example is the work of Xia et al.[16][17], who developed an inverted wagon model to estimate these forces based only on the measurements of the car body responses. Wei et al.[18] applied the indirect method to derive the wheel-rail contact forces by measuring the accelerations of the bearing box and the relative displacements of the primary suspension. Compared to direct methods, indirect methods are less expensive because the instrumentation on the vehicles is less complicated. One of the limitations is that these methods require a highly accurate vehicle-track computation model to minimize the measurement errors.

The goal of this work is to develop a wheel-rail contact force measurement system on the downscale V-Track. A direct method is preferable because it can directly derive the contact forces and avoid potential errors from the modeling in the indirect method. A continuous measurement is needed when the wheels run on the track, and hence, the measurement system should be developed on the wheel instead of the rail. The instrumented wheel equipped with strain gauges is too expensive and complicated for data transmission with the requirement of a telemetry system. The method using noncontact gap sensors is more cost-efficient, but its accuracy is influenced by the position of wheel-rail contact points, and errors are hard to accommodate in practice[10]. In addition to these approaches, Meymand and Ahmadian[19] designed a novel force measurement system using the concept of a dynamometer [20] to measure the wheel-rail contact force. The static calibration of the dynamometer was conducted on a 1/4 scaled roller rig. However, no experimental results were presented to evaluate the validity of the dynamometer for contact force measurements under a real running scenario.

This chapter describes the development of a force measurement system in the dynamometer category in a downscale V-Track apparatus for measuring the wheel-rail contact forces in running conditions. Utilizing the measurement results from the dynamometer, the control of these forces was also achieved in V-Track. The chapter is organized as follows. Section 6.2 introduces the structure of V-Track and the design of the dynamometer for the wheel assembly. Section 6.3 describes the static calibration of the dynamometer. Section 6.4 measures the wheel-rail contact forces in V-Track under running conditions and examines the reliability and validity of the measurements. Section 6.5 analyses the

influences of wheel torques and running speeds on the measured contact forces. Section 6.6 presents the control methods of wheel-rail contact forces in V-Track. The main conclusions are drawn in Section 6.7.

6.2. DESIGN OF THE DYNAMOMETER IN V-TRACK

6.2.1. STRUCTURE OF V-TRACK

V-Track consists of four wheel assemblies running over a ring track system, as shown in Figure 6.1. Figure 6.1 shows the structure of one of the four wheel assemblies. A wheel (1) with a diameter of 200 mm is fixed on a guiding block (3) through an axle box (2). The position of the wheel along the wheel axle is adjustable. The wheel, axle box, and guiding block move vertically along two parallel guiding shafts (9) under the preloads of two springs (4). The combined stiffness of the two springs is 230 N/mm, which is 1/5 the scale of the primary suspension stiffness of the ICM-type Dutch intercity passenger train. The two springs are loaded at their upper ends by two nuts (6) through load cells (5). By changing the position of the nuts along the threaded part of the guiding shafts, the spring preload can be adjusted between 0 and 7500 N. The wheel angle of attack is also adjustable between -2° and $+2^\circ$ [21]. By adjustment of the angle of attack and the wheel position along the wheel axle, we can simulate various wheel-rail contact conditions of different curvatures in real tracks using the V-Track.

6

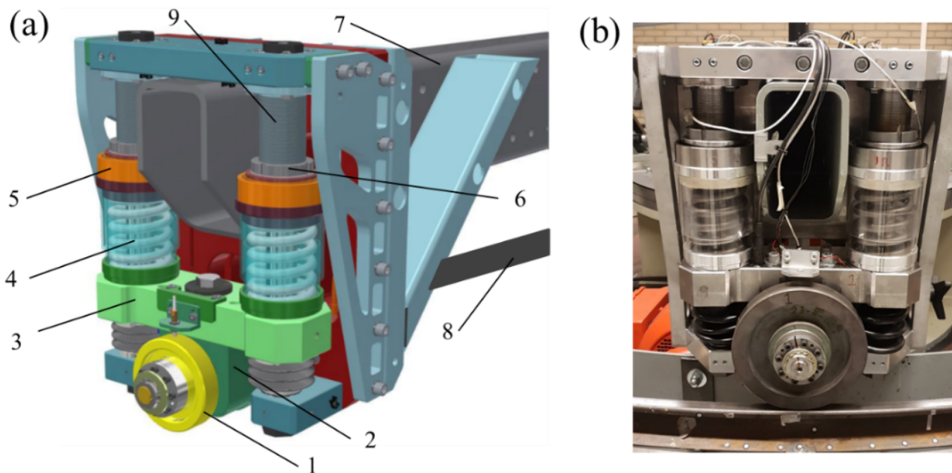


Figure 6.2: Structure of one wheel assembly of V-Track. (a) Schematic drawing in CAD: 1) wheel, 2) axle box, 3) guiding block, 4) suspension springs, 5) load cells, 6) preload nut, 7) steel frame, 8) braking shaft, and 9) guiding shaft; (b) single wheel assembly in V-Track.

Each of the four wheel assemblies is mounted on an arm of a steel frame (7), shown also in Figure 6.1. One motor (the driving motor) drives the steel frame so that wheel assemblies are pulled to move along the ring track. The speed range of the wheel assemblies is between 0 and 40 km/h. Another motor (the braking motor) is connected to the wheels

through the braking shafts (8). This motor generates a torque in the opposite direction of the driving torque so that a braking force arises at the wheel-rail contact. The braking torque applied by the braking motor can be measured by torque sensors in each of the four braking shafts and can be controlled. Thus, each wheel works like a wheel in an unpowered vehicle: it is pulled by the vehicle (the steel frame on V-Track) and rolls almost freely forward. It should roll almost freely because (ideally) there should be no frictional tangential contact force at the wheel-rail interface. In reality, resistance in the load path of the wheel, e.g., in bearings, causes a (usually small) tangential contact force. A large tangential contact force has to be intentionally applied by, e.g., a braking system. In V-Track, this is the braking torque from the braking motor applied via the braking shaft. A more detailed description can be found in [2].

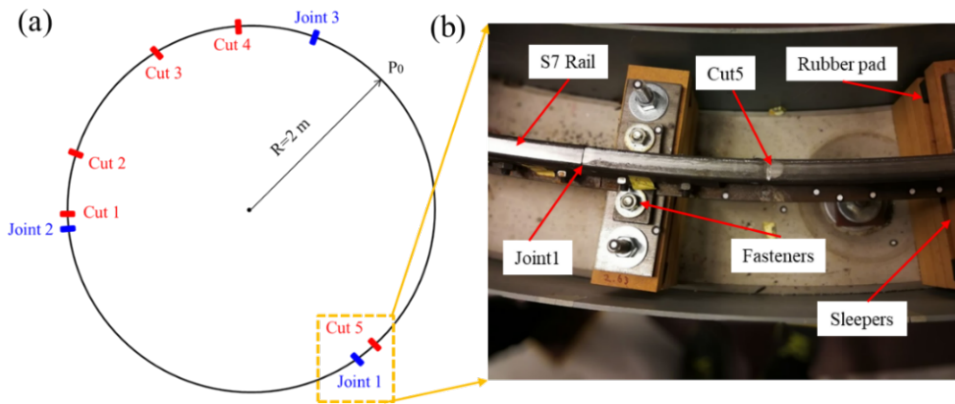


Figure 6.3: The track structure of V-Track. (a) Cuts and joints on the ring track; (b) main track components.

The ring track, which has a radius of 2 m, consists of three pieces of rails connected by three fishplate rail joints, as shown in Figure 6.3a. The choice of the V-Track's radius (2 m) was mainly driven by its bulkiness. This radius is geometrically not representative of the typical curvatures encountered in real tracks. Yet the physical vehicle-track lateral interaction, especially wheel-rail lateral interaction, can be simulated in V-Track. For instance, V-Track cannot generate the centrifugal force of trains experienced in curved track, but the effects of such a lateral force on wheel-rail contact and vehicle-track interaction can be generated and investigated in V-Track by properly setting (1) the angle of attack, (2) the rail inclination and (3) the wheel conicity. The ring rail, which has a standard S7 profile is supported on steel plates. The standard S7 rail is defined in German norm DIN 5901. It has a mass of 6.75 kg per meter and is thus called "S7". The rail and plates are fixed on wooden sleepers by fasteners, as shown in Figure 6.3b. The sleeper spacing is 0.4 m. Different numbers of steel plates are placed between the rail and the steel plates to adjust the track vertical irregularity. Underneath the sleepers are rubber pads, which are used to simulate the elasticity and damping of ballast layers in the real-life track. Five artificial cuts with different widths and depths were made on the rail surface to excite high-frequency wheel-rail forces, which may induce rail squats or short pitch corrugation. The positions of the five cuts and three rail joints are shown in

Figure 6.3a. The position P_0 in Figure 6.3a is the origin position to start data recording. Figure 6.4 presents the schematic drawing of the wheel-rail contact system in V-Track. The cross-section of the wheel-rail contact system is shown in Figure 6.4a. Figure 6.4b shows the side view of the wheel-rail system. The upper arrow indicates the positive direction of braking torque, which generates a traction force at the wheel-rail interface. On the contrary, a negative braking torque will generate a braking force at the wheel-rail interface. Figure 6.4c shows the top view of the wheel-rail contact system with a positive angle of attack.

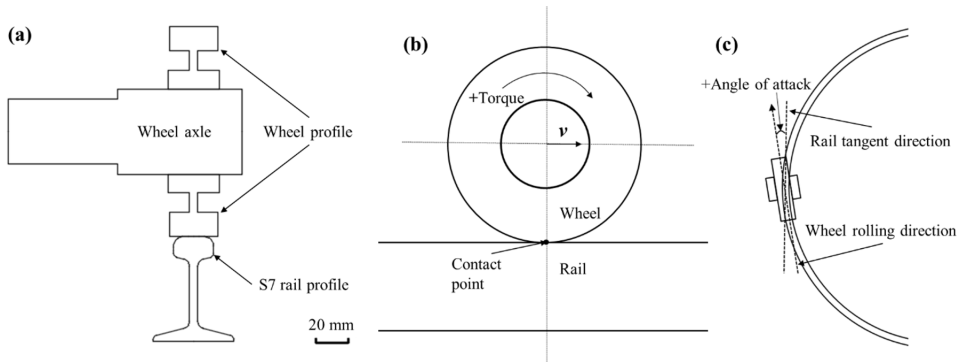


Figure 6.4: The schematic drawing of the wheel-rail contact system in V-Track. (a) Cross-section of wheel-rail contact; (b) side view of the wheel-rail system; (c) top view of the wheel-rail system with a positive angle of attack.

The designed maximum vertical load is 7500 N per wheel, equivalent to a static axle load of approximately 380 kN, considering a scale factor of 1/5. The maximum allowed longitudinal and lateral forces are both 3750 N with a friction coefficient of 0.5.

6.2.2. DESIGN OF THE DYNAMOMETER

The dynamometer consists mainly of four 3-component piezoelectric force sensors (Kistler, type 9067C) mounted between 2 steel plates, as shown in Figure 6.5a. A set of high-strength preloading bolts connects the two plates and provides the force sensors with the necessary preload. The shear forces are transmitted through static friction from one plate to the other. Each force sensor contains three pairs of quartz plates to measure the three orthogonal components of the applied static and dynamic forces. The technical data of the Kistler force sensor type 9067C are shown in Table 6.1[22].

After assembly (see Figure 6.5a), the dynamometer was installed in V-Track, as shown in Figure 6.5b, 6.5c, 6.5d, and 6.5e. The directions of the dynamometer are aligned with the kinematic coordinate system of the wheel assembly, with the axes x , y , and z oriented in the longitudinal (rolling), lateral and vertical directions, respectively. The dynamometer forces in the three directions are calculated by the summation of the output from the four force sensors as follows:

$$F_x = F_{1x} + F_{2x} + F_{3x} + F_{4x} \quad (6.1)$$

$$F_y = F_{1y} + F_{2y} + F_{3y} + F_{4y} \quad (6.2)$$

$$F_z = F_{1z} + F_{2z} + F_{3z} + F_{4z} \quad (6.3)$$

where F_x , F_y , and F_z are the dynamometer forces in the longitudinal, lateral and vertical directions and F_{ix} , F_{iy} , and F_{iz} ($i=1,2,3,4$) are the i^{th} sensor forces in the longitudinal, lateral and vertical directions, respectively.

Table 6.1: The technical data of the Kistler force sensor type 9067C.

Range	F_x, F_z	kN	-30...-30
	F_y	kN	-60...-60
Calibration range	F_x, F_z	kN	0...30
	F_y	kN	0...30
Sensitivity	F_x, F_z	pC/N	≈ -8.1
	F_y	pC/N	≈ -3.9
Linearity, each axis		%FSO	$\leq \pm 0.25$
Hysteresis, each axis		%FSO	≤ 0.25
Crosstalk	$F_y \rightarrow F_x, F_z$	%	$\leq \pm 0.5$
	$F_x \leftrightarrow F_z$	%	$\leq \pm 2$
	$F_x, F_z \rightarrow F_y$	%	$\leq \pm 3$
Operating temperature range		°C	-40...120

According to the equilibrium of the wheel assembly, the longitudinal wheel-rail contact force can be calculated as follows:

$$F_{conx} = F_x + \sum m_j a_{jx} \quad (6.4)$$

where F_{conx} is the wheel-rail contact force in the longitudinal direction, F_x is the measured dynamometer force in the longitudinal direction, m_j is the mass of the j^{th} component of the wheel assembly, which is indicated by blue dashed lines in Figure 6.5b and Figure 6.5c, and is the total inertia force of the wheel assembly in the longitudinal direction, $j=1,2,3, \dots$, denoting components like the wheel, axle box, guiding block, guiding axis. Equation 6.4 indicates that the wheel-rail contact forces comprise two components: one is the inertia force of the wheel assembly, and the other is the force transmitted to the frame through the dynamometer. If we reduce the loading condition to a (quasi)static state in which the accelerations of the system are zero, the dynamometer forces can be regarded as equal to the wheel-rail contact forces, as follows:

$$F_{conx} = F_x \quad (6.5)$$

In the measurements described in the following sections, the inertia force of the wheel assembly is not considered. This arrangement applies to most situations except at the cuts and joints where large impact vibrations occur so that the inertia forces are large. Further research is needed on the compensation of the wheel inertia forces to more accurately measure the dynamic contact forces.

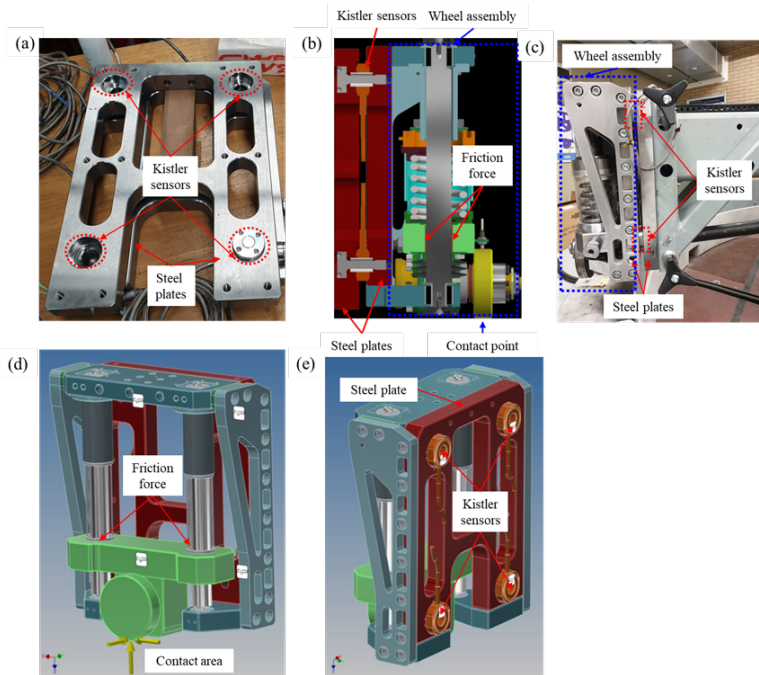


Figure 6.5: The designed dynamometer in V-Track. (a) Kistler force sensors between two steel plates; (b) the cross-section of the dynamometer in the V-Track schematic drawing; (c) the dynamometer in V-Track; (d) Contact forces acting in the contact area; (e) the position of the dynamometer in V-Track.

6.3. STATIC CALIBRATION

Before running tests on V-Track, a static calibration of the dynamometer is needed to check whether the force sensors can work satisfactorily and whether the sensitivity parameters given by the manufacturer in Table 6.1 are precise. This section describes the static calibration setups in three single directions (x, y, z), as shown in Figure 6.6. In addition, the accuracies and crosstalk errors of the dynamometer are evaluated. The static calibration with loads in arbitrary directions was not conducted to avoid errors from the force decomposition.

6.3.1. SETUP FOR STATIC CALIBRATION

The setup for the vertical calibration is shown in Figure 6.6a. A crane was used to apply a vertical force to the wheel axle by a sling. A load sensor was mounted between the crane and the sling to record the crane force. The sling was configured to be as vertical as possible to avoid force components in the other two directions. The crane force was increased step by step up to 9000 N, larger than the designed maximum vertical preload (7500 N). The data of the dynamometer were recorded with a sampling frequency of 1 Hz.

The longitudinal and lateral calibration cannot be conducted directly on V-Track as the vertical calibration is because the crane can apply a vertical force only. Therefore, the

dynamometer, together with the wheel assembly, was detached from V-Track. For the longitudinal calibration, the dynamometer and wheel assembly were rotated 90 degrees and mounted on a vertical rigid I beam to ensure that the longitudinal direction became vertical, as shown in Figure 6.6b. A crane and sling were used to apply a nominally longitudinal wheel-rail contact force. The crane force was increased step by step up to 4000 N, larger than the designed maximum longitudinal force (3750 N).

For the lateral calibration, the dynamometer and wheel assembly were rotated 90 degrees and mounted horizontally on a rigid frame to ensure that the lateral direction of the system became vertical, as shown in Figure 6.6c. A crane and sling were used to simulate lateral force applied to the system. The crane force was increased step by step up to 8000 N.

Before the calibration of the dynamometer, the accuracy of the crane load sensor was first examined to ensure a good reference. Weight blocks in approximately 13.2 kg intervals were applied to the crane up to 532.2 kg. The largest error of the crane load sensor compared to the block weight was less than 0.6%, which is acceptable for calibration.

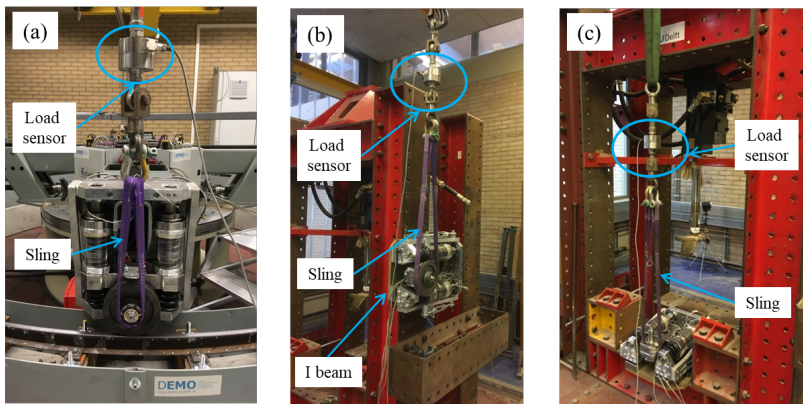


Figure 6.6: Setups for static calibration of the dynamometer. (a) Vertical setup; (b) longitudinal setup; (c) lateral setup.

6.3.2. RESULTS FOR STATIC CALIBRATION

Three repeated measurements were performed in each direction, and similar values were obtained, which verified the consistency of the measurement. Figure 6.7a, 6.7b and 6.7c show one of the measured results in the vertical, longitudinal and lateral directions, respectively.

In the longitudinal direction, the dynamometer measured the crane force with a high accuracy of 99.05%. The crosstalk errors in the vertical and lateral directions were 0.28% and 1.79%, respectively. The adjusted R-Squares of these three linear fittings in Figure 6.7a are 99.99%, 99.93%, 98.40%. In the vertical direction, the accuracy of the dynamometer was 99.04%. The crosstalk errors in the longitudinal and lateral directions were 1.04% and 1.03%, respectively. The adjusted R-Squares of these three linear fittings in Figure 6.7b are 99.48%, 99.99%, 99.94%. In the lateral direction, the accuracy of the dynamometer was 95.62%, slightly lower than those in the other two directions.

The crosstalk errors in the longitudinal and vertical directions were 0.30% and 0.87%, respectively. The adjusted R-Squares of these three linear fittings in Figure 6.7c are 94.60%, 99.53%, 99.99%.

Overall, a high accuracy of the dynamometer was achieved in measuring the static forces in the three directions, indicating that the force sensors worked properly and that the given sensitivity parameters in Table 6.1 were precise. Compared to the longitudinal and vertical directions, the accuracy in the lateral direction was lower (95.62%), and the crosstalk errors from the other two directions were higher (1.79%, 1.04%). The reason may be that the lateral force is measured based on the compression pressure of the quartz plates and is less sensitive than the shearing in the longitudinal and lateral directions, as shown in Table 6.1. Nevertheless, the maximum crosstalk error of 1.79% was considered acceptable in the current work. Future research will be performed to further reduce it.

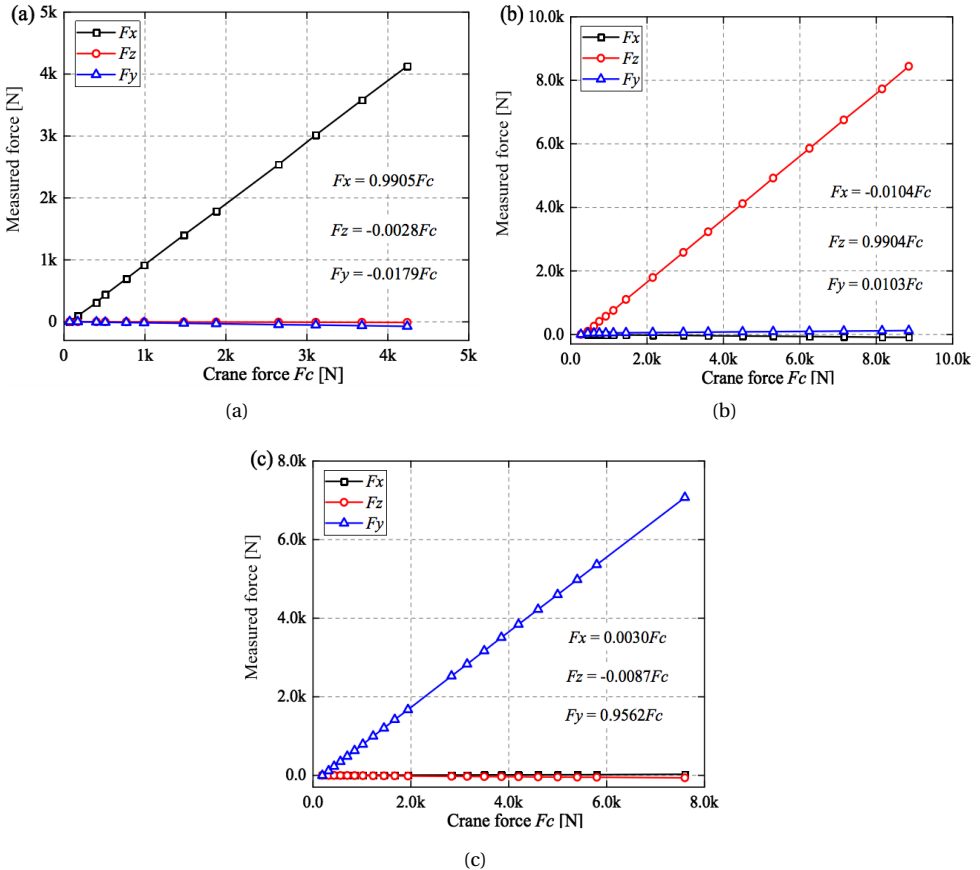


Figure 6.7: Results of static calibration in the (a) longitudinal direction, (b) vertical direction, and (c) lateral direction. F_c denotes the crane force.

6.4. VALIDATION OF RUNNING TESTS

After the static calibration, the wheel assembly and dynamometer were mounted to V-Track. In this section, we examined the repeatability and validity of the dynamometer to measure the wheel-rail contact forces under running conditions.

6.4.1. THE REPEATABILITY OF MEASUREMENTS IN RUNNING CONDITIONS

The running speed of the wheel assemblies on the ring track was 4 km/h. The wheel preload was 4500 N. No braking torque was applied on the wheel by the braking motor. The angle of attack was not measured. The wheel-rail contact forces in the three directions were measured by the dynamometer with a sampling frequency of 16.67 kHz. In each direction, the data were recorded for three rounds of the wheel rolling along the ring to examine the repeatability of the measurements, as shown in Figure 6.8. The starting (0 m) and ending positions (12.56 m) in Figure 6.8 correspond to the same position P_0 in Figure 6.3a.

Figure 6.8a, 6.8b and 6.8c show very good repeatability of the measurements in the three directions, indicating that the dynamometer can reliably measure the wheel-rail contact forces under running conditions.

Figure 6.8a shows that the measured longitudinal force along the track is not constant but changes significantly at different positions. It first increases from 407 N at P_0 to a maximum value of 933 N at 5.44 m and then gradually decreases. Considering that no braking torque was applied, the longitudinal force is unexpectedly large. The reasons are discussed in Section 6.4.3.1.

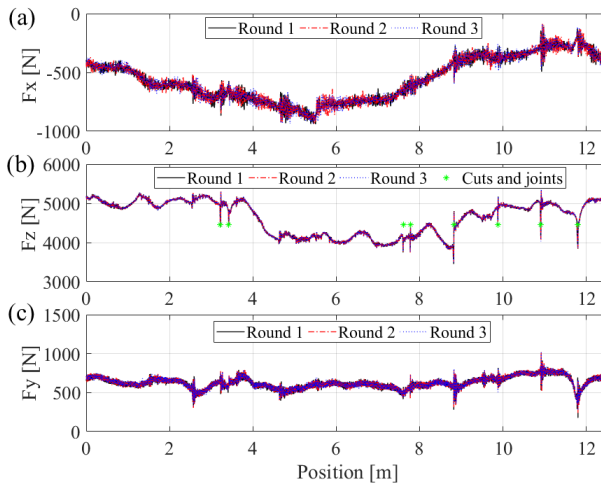


Figure 6.8: Measured wheel-rail contact forces under running conditions in three directions. (a) Longitudinal force, (b) vertical force, (c) lateral force. The green stars in Figure 6.8b indicate the positions of cuts and rail joints. The running speed was 4 km/h, and the wheel preload was 4500 N.

The measured vertical force in Figure 6.8b shows strong fluctuation between approx-

imately 4 kN and 5 kN, which is expected to arise from the vertical track irregularity. When the wheel runs over the track, the length of the suspension springs varies because the upper ends of the springs are fixed on the frame while the lower ends go up and down, following the vertical track irregularity, leading to the fluctuation of the vertical force. Eight sharp peaks are observed in this figure, and their positions correspond to those of the three rail joints and five artificial cuts, indicated by the green stars in Figure 6.8b. This demonstrates that the dynamometer can capture the dynamic features of the wheel-rail impact vibrations, although it may not be currently capable of quantitatively measuring the impact forces without considering the inertia forces of the wheel assembly.

Compared to the measured longitudinal and vertical forces, the overall lateral force response is relatively flat, varying in the range of approximately 500 N-750 N, as shown in Figure 6.8c. This indicates that an angle of attack exists between the wheel and the rail, which must be constant along the track.

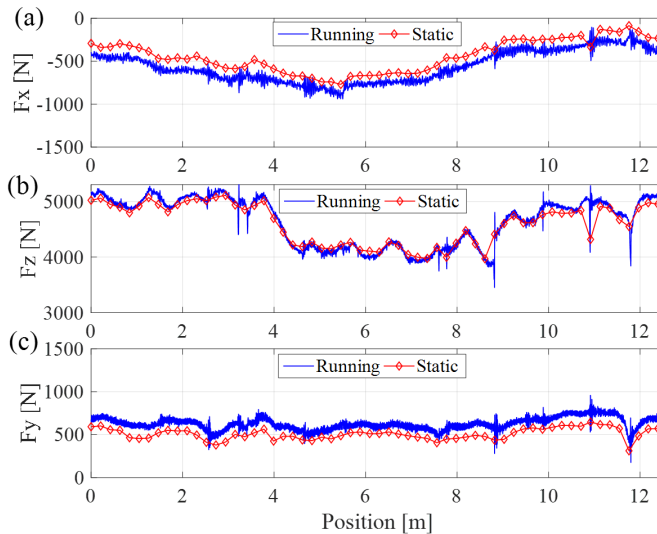


Figure 6.9: Measured wheel-rail contact forces by the dynamometer under static and running conditions. (a) Longitudinal force, (b) vertical force and (c) lateral force.

6.4.2. VALIDATION BY A STATIC MEASUREMENT

The static force measurement calibration of the dynamometer is described in Section 6.3. Therefore, in this section, we describe using the dynamometer to measure the static wheel-rail contact forces in V-Track and compare them with those in the running condition. The wheel preloads, braking torques, and angle of attack in this static measurement are the same as in Section 6.4.1. The only difference is that the wheel assemblies are manually pushed forward along the ring track in the static tests and stopped every 0.2 m instead of continuously running as driven by the driving motor in the running tests. The stopping positions are either above the track supports ('on-support') or at the middle of two supports ('at midspan') to consider the influences of different track

support stiffnesses on the contact forces. The measured forces by the dynamometer are recorded when the wheel assemblies stand still, corresponding to the static wheel-rail contact forces.

The measured static wheel-rail contact forces are compared with those in the running test in Figure 6.9. Overall, good agreement between these two cases is achieved in the three directions, indicating that the dynamometer can accurately measure the wheel-rail contact forces under running conditions. The results also reveal that the loading of V-Track is approximately quasistatic under these conditions, indicating that our arrangement—which does not consider the inertia forces of the wheel assembly—is appropriate in these cases. At the rail joints and cuts, the static measurement does not capture the impact forces, which can be observed from the running tests.

Figure 6.9 shows that the longitudinal and lateral forces are reduced by approximately 110 N in the static measurement. This amplitude difference is probably caused by frictional interlocking in the load chains in V-Track. Additionally, in the lateral direction, the centrifugal force of the wheel assembly is another source of this reduction, which is approximately 55 N, considering the wheel assembly mass of approximately 90 kg.

6.4.3. VALIDATION BY WHEEL TORQUE AND SPRING LOAD MEASUREMENT

In addition to the dynamometer, the torque sensors in the braking shafts and load cells ((5) in Figure 6.2a) along the guiding shafts can be used to estimate the longitudinal and vertical wheel-rail contact forces. In this section, we compare the measurement results from the dynamometer with those from the torque sensors and the load cells.

VALIDATION OF LONGITUDINAL FORCE BY WHEEL TORQUE MEASUREMENT

In Section 6.4.1, it was found that the measured longitudinal wheel-rail contact force was unexpectedly large, although no braking torque was applied on the wheel by the braking motor. In this section, the measured torque from the torque sensor is as depicted in Figure 6.10a. The torque is not zero but changes considerably along the track with a maximum value of approximately 88 N.m. The negative torque generates a braking force at the wheel-rail interface, which can be calculated as follows:

$$F_{xc} = M_x / r_w \quad (6.6)$$

where F_{xc} is the calculated longitudinal force, M_x is the measured torque from the torque sensor, and r_w is the radius of the wheel, which is 0.1 m.

Figure 6.10b compares the longitudinal force calculated from the measured torque and the longitudinal force measured by the dynamometer. The good agreement confirms that the dynamometer can accurately measure the longitudinal wheel-rail contact force. The negative torque is expected to arise from the resistance in the load chain of V-Track, including the gearbox and the braking motor. This resistant torque can be compensated by applying a positive torque to the wheel by the braking motor.

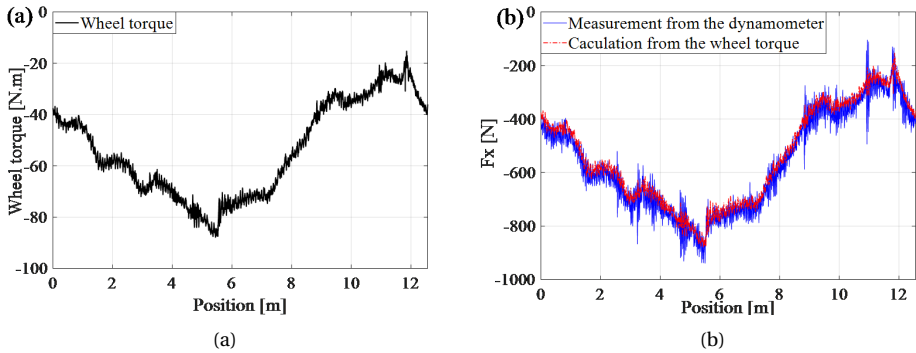


Figure 6.10: Validation of the measured longitudinal wheel-rail contact force by wheel torque measurement: (a) measured wheel torque; (b) comparison of the calculation from wheel torque and the measurement from the dynamometer.

VALIDATION OF VERTICAL FORCE BY SPRING LOAD MEASUREMENT

The vertical spring loads can be measured by the load cells ((5) in Figure 6.2a). Figure 6.11 compares the vertical wheel-rail contact force measured from the dynamometer and the spring loads from the load cells. Both measurements fluctuate by approximately 4500 N and have a similar tendency: first, they are relatively flat between 0 m and 3.8 m, then go down from 3.8 m to 8.8 m, and gradually rise after 8.8 m. However, the dynamometer results show much stronger fluctuation.

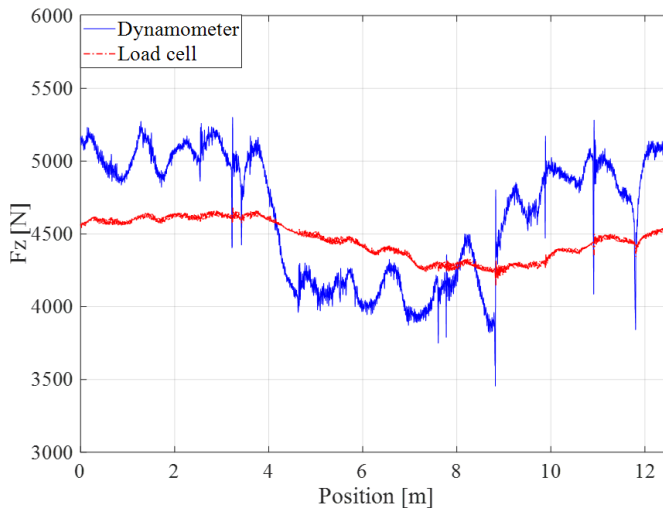


Figure 6.11: Comparison of vertical contact force from the dynamometer and the spring load from the load cells.

To understand the difference in these two cases, the static spring deformation was mea-

sured along the track by a digital dial indicator, as shown in Figure 6.12a. The dial indicator was mounted firmly to the frame by an adjustable magnetic base. The needle of the dial indicator vertically contacted the guiding block. Therefore, the dial indicator measured the relative displacement between the guiding block and the frame, which was also the spring deformation. We manually pushed the wheel assemblies running along the track, stopped every 0.2 m, and recorded the readout of the dial indicator when stopping. This process was similar to the static measurement in Section 6.4.1. The resolution of the dial indicator was 0.01 mm.

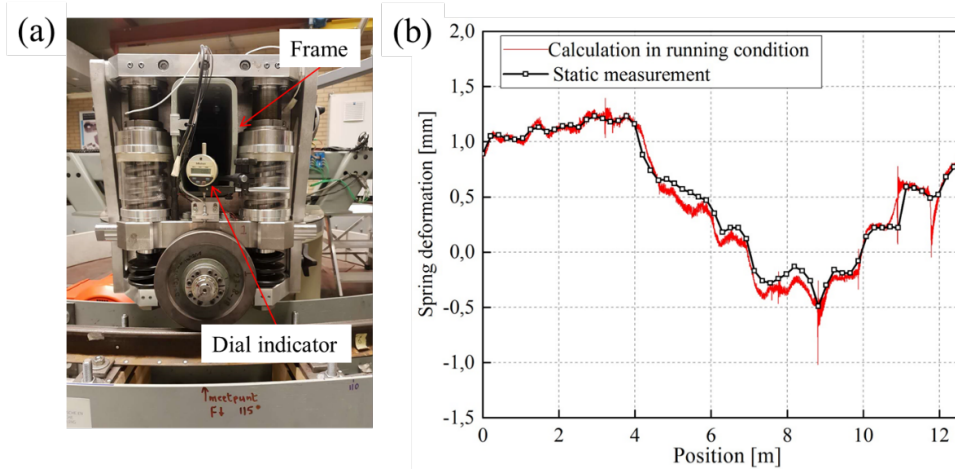


Figure 6.12: Comparison of the spring deformation along the track under static and running conditions. (a) Setup for static measurement; (b) comparison of the spring deformation under static and running conditions.

The measured static spring deformation along the track is shown in Figure 6.12b. The spring deformation in the running tests can be estimated as follows:

$$d_s = F_l / k_s \quad (6.7)$$

where d_s is the calculated spring deformation in the running condition, F_l is the measured spring load from the load cells, and k_s is the stiffness of the springs. The calculated spring deformation under running conditions is compared with the deformation measured under static conditions in Figure 6.12b. The good agreement between them shows that the load measured from the load cells is quasistatic under the running conditions, except for the impacts at the rail joints and cuts.

Figure 6.9 shows that the vertical force measured by the dynamometer is also quasistatic under running conditions. Therefore, the difference between the dynamometer and the load cells should also be caused by a (quasi)static force. To identify the source of this force, static tests were performed at three positions on the track: 0 m, 1.6 m, and 4 m. In these tests, the wheel-rail contact was first loaded by tightening and then unloaded by loosening the preload nuts step by step. The vertical force measured by the dynamometer and the spring load measured by the load cells are shown in Figure 6.13. The hysteresis relationships between them in these three positions are similar and illustrate a

friction force in the load path between the wheel-rail interface and the dynamometer. The structure of the wheel assembly in Figure 6.2 indicates that such friction force can exist only between the guiding block and the guiding shafts. The wheel plane is out of the plane formed by the two guiding shafts, causing normal contact forces between the guiding block and guiding shafts. The friction force occurs when the guiding block slides along the guiding shafts.

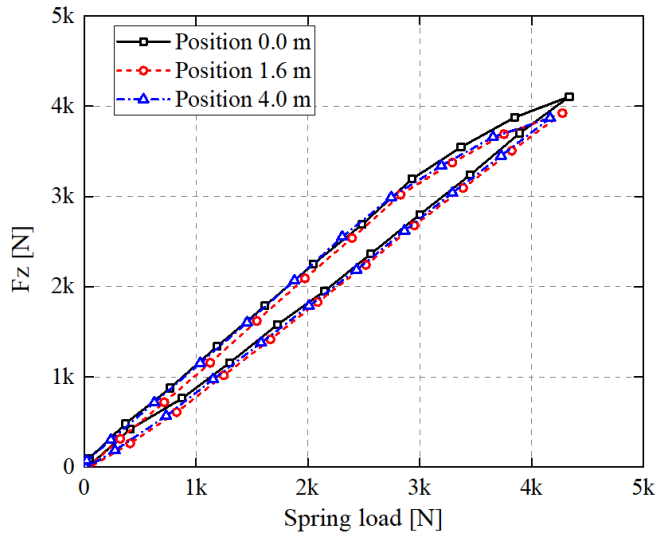


Figure 6.13: The relationship between the spring load from the load cells and the vertical contact force from the dynamometer.

Therefore, the difference between the vertical contact force measured by the dynamometer and the spring loads by the load cells can be explained as follows: the vertical wheel-rail contact force transmits to the dynamometer through two load paths. One is through the suspension springs and load cells, and the other is via the friction between the guiding block and guiding shafts. The contact between the guiding block and guiding shafts has a higher stiffness than the suspension springs, and the high-frequency dynamic force can be transferred to the dynamometer without the buffering of the springs, enabling the dynamometer to capture the dynamic features of the wheel-rail impact vibrations.

6.5. INFLUENCING FACTORS

6.5.1. THE INFLUENCE OF BRAKING TORQUES ON CONTACT FORCES

In the experiments described in Section 6.4, no braking torque was applied on the wheels by the braking motor in the running tests. This section describes how nine braking torques were used to analyze their influence on the measured wheel-rail contact forces. The torques were 0, -50, -100, -150, -200, -250, -275, -285, and -300 N.m. The braking torque was applied through one gearbox, which distributes the torque onto the four

wheels. When the braking torque was increased to slightly larger than -300 N.m, wheel skidding occurred with sparks at the wheel-rail interface, which indicated that the tangential creep force reached the saturation value. In this condition, the coefficient of friction f between the wheel and the rail is determined with the Coulomb friction law (8).

$$f \leq \sqrt{F_x^2 + F_y^2} / F_z \quad (6.8)$$

Figure 6.14 shows the measured wheel-rail contact forces under different torques. The longitudinal force increases with increasing braking torque. The increment between 4 m and 8 m is smaller than at the other positions because (1) the original longitudinal force without braking torque is larger in this position (see Figure 6.9(a)) and is thus closer to the saturation value and (2) the saturated longitudinal force between 4 m and 8 m (with -300 N.m) is also smaller than other positions because the corresponding vertical force in 4-8 m is small and the saturated longitudinal force cannot exceed the limit of vertical force times friction coefficient, according to the Coulomb friction law (8). The vertical contact force remains almost the same under the different braking torques, as expected. The lateral contact force shows a decreasing trend with increasing braking torque, as at each point in the wheel-rail contact patch, the longitudinal component of the tangential contact stress increases, whereas the maximum tangential stress is bounded by the Coulomb friction law (8). The friction coefficient is approximately 0.25, calculated with (8) under a torque of -300 N.m.

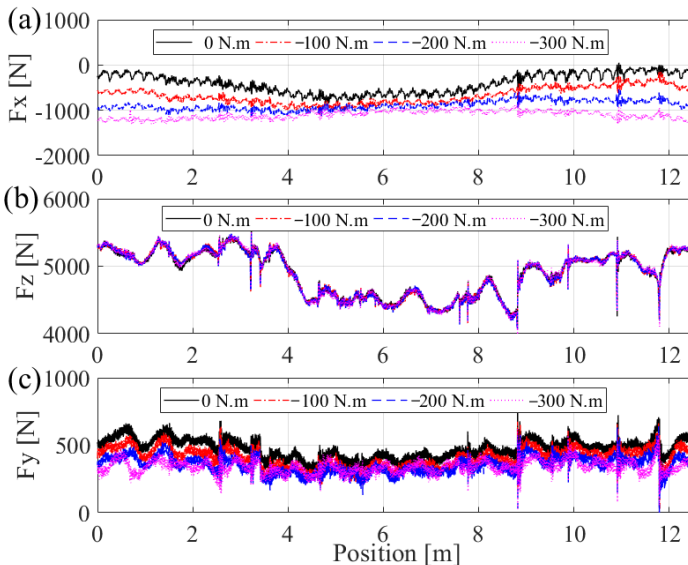


Figure 6.14: Measured wheel-rail contact forces under different braking torques from the braking motor. (a) Longitudinal force, (b) vertical force and (c) lateral force.

To better understand the experimental results, the theoretical creep force-creepage curves were calculated using Kalker's CONTACT[23]. The longitudinal and lateral creepage were calculated as follows,

$$v_x = (|v| - |c|)/v \quad (6.9)$$

$$v_y = a \quad (6.10)$$

Where v_x and v_y are the longitudinal and lateral creepage, v is actual forward velocity, c is pure rolling forward velocity, v is forward velocity, a is the angle of attack. The longitudinal and lateral forces were solved based on Kalker's exact three-dimensional rolling contact theory, where the linear elastic half-space assumption was applied. To consider nonlinear material properties (i.e., elasto-plastic) and wheel-rail dynamic effects, the explicit FEM has been proven suitable[24][25], which will be used in future work. The calculated creep force-creepage curves were shown in Figure 6.14a. In this calculation, the normal load is 5250 N, which is the vertical contact force at the track position of 0.5 m. The friction coefficient is 0.25. The angle of attack is assumed to be constant at this position with the different braking torques, and its value is taken as 0.8 mrad in the calculation, which is estimated by CONTACT based on the measured contact forces. The longitudinal creepage is varied from 0 to 1% to simulate the different braking torque conditions in the tests.

6

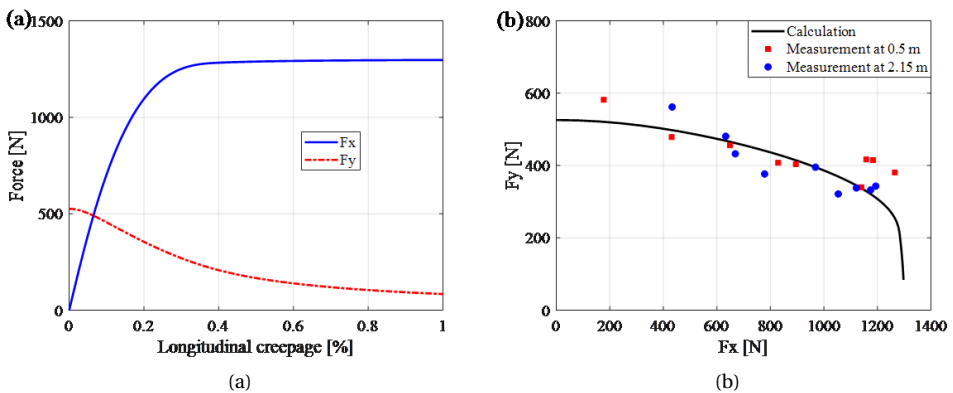


Figure 6.15: The relationship between the longitudinal and lateral forces. (a) Calculated creep force/creepage curves; (b) the calculated and measured relationship between the longitudinal and lateral creep forces.

Figure 6.15a shows that the longitudinal creep force increases with increasing longitudinal creepage before reaching the saturation point, while the lateral creep force decreases. This explains the measurement results in Figure 6.14 that the longitudinal contact force increases while the lateral contact force decreases when the braking torque increases. According to the curves in Figure 6.15a, the relationship between the longitudinal and lateral forces can also be obtained, as shown in Figure 6.15b. The lateral creep force first gradually decreases with increasing longitudinal creep force and then drops dramatically when the total tangential force reaches the saturation value. The measured longitudinal and lateral contact forces at positions 0.5 m and 2.15 m under the nine braking torque

conditions are compared with the calculated curve in Figure 6.15b. The agreement between the calculation and measurement confirms the validity of the dynamometer for contact force measurement in the longitudinal and lateral directions.

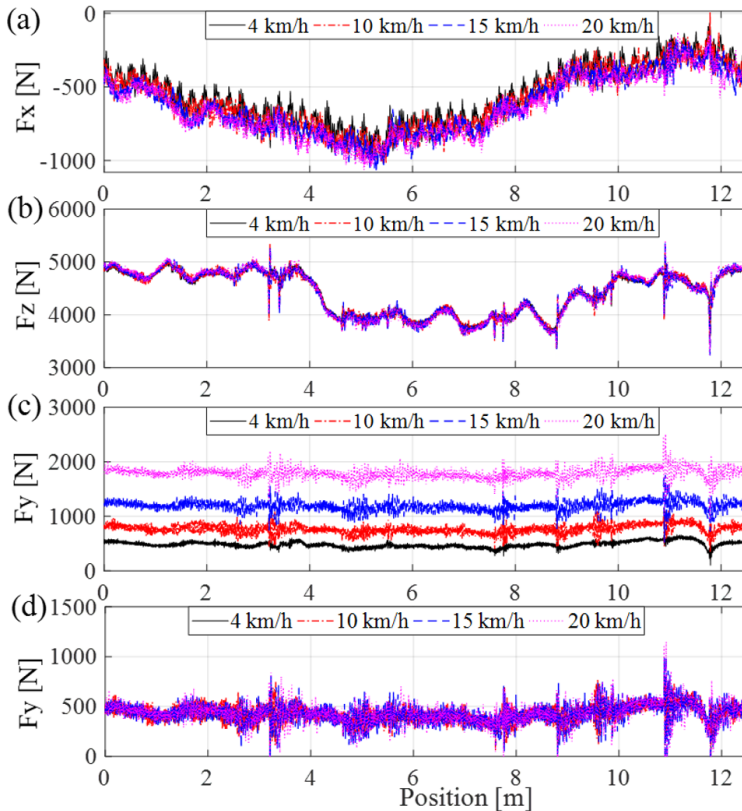


Figure 6.16: Measured wheel-rail contact forces with different running speeds: (a) longitudinal force, (b) vertical force and (c) lateral force before compensation, (d) lateral force after compensation.

6.5.2. THE INFLUENCE OF RUNNING SPEEDS

In the experiments described in Section 6.4, the running speed of the wheel assemblies on the ring track was 4 km/h. In the work described in this section, the running speed was increased to 10, 15, and 20 km/h; the measured forces from the dynamometer are shown in Figure 6.16.

Figure 6.16a and 6.16b show that the longitudinal and vertical contact forces change little with increasing speed, which confirms that the loading condition of V-Track is approximately quasistatic. The measured lateral force significantly increases with increasing speed, and the increment is almost uniform along the whole track, as shown in Figure 6.16c. These increments are caused by the increasing centrifugal force of the wheel assembly at higher running speeds. According to Equation 6.4, the dynamometer needs to compensate for the centrifugal force to accurately measure the lateral wheel-rail contact

force. After compensation, it is found that the lateral contact force is almost constant with the different running speeds, as shown in Figure 6.16d.

6.6. MEASUREMENT AND CONTROL OF CONTACT FORCES IN A 1/7 SCALED V-TRACK

The discussion of the preceding sections is based on the configuration of V-Track shown in Figure 6.1 (wheel diameter 200 mm and the standard rail profile S7), which is one of the different possible configurations of V-Track. In this section, the measurement and control of the wheel-rail contact forces are discussed with another configuration: the 1/7 scaled configuration, as shown in Figure 6.17. In this configuration, the dimensions of the wheels and rails are 1/7 of the sizes of real-life wheels and rails. This is the maximum scale at which both the scaled wheels and the rails can be made from the corresponding real materials. The scaled wheels then have a diameter of 130 mm. In Figure 6.17, the ring rail is 1/7 the size of UIC54E1, consisting of four sections of rails with different materials connected by rail joints. The parameters of the sleepers, fastenings, and slab layer are chosen based on the similarity law[2][26] to make the track dynamic behaviors equivalent to those of the real systems. Only two wheel assemblies (W1, W3) equipped with the dynamometers were installed in V-Track.

6

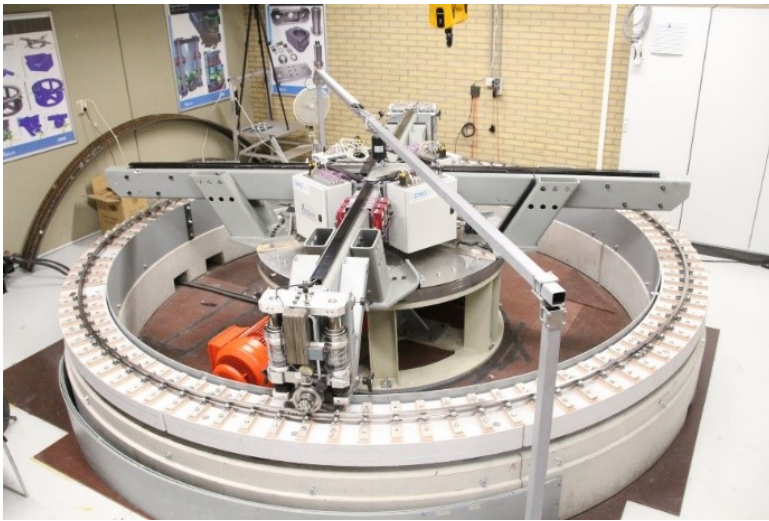


Figure 6.17: The 1/7 configuration of V-Track.

In reality, the wheel-rail contact forces are influenced by many factors, such as axle loads, traction/braking, curve negotiation, and track and rail irregularities. The formation of rail defects is related to different wheel-rail contact conditions. For example, short pitch corrugation appears primarily in tangential tracks with relatively low axle loads and with no contact between the wheel flange and the rail gauge corner[27]. Head checks occur mainly on the outer rails of curves with radii of 500-3000 m, where a large lateral force

arises at the rail gauge corner or shoulder[28][29]. Squats are usually caused by short-wavelength rail defects [30][31]. To simulate different wheel-rail contact conditions in real life, the control of wheel-rail contact forces in three directions is achieved in the 1/7 scaled V-Track, as shown in Figure 6.18.

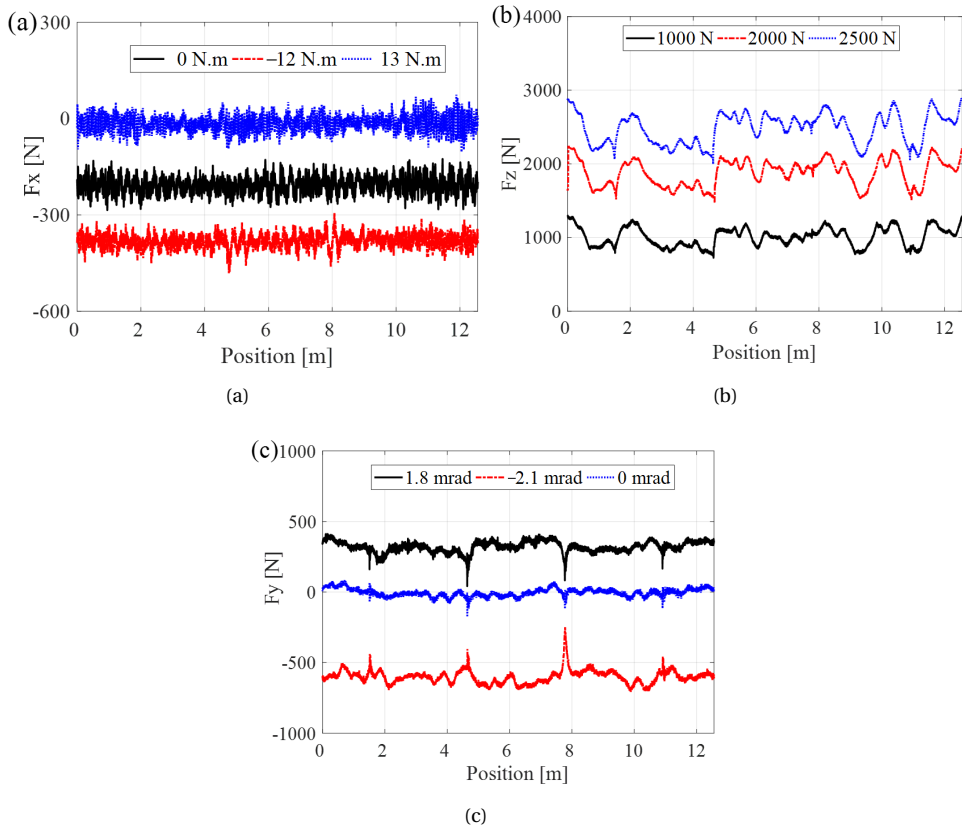


Figure 6.18: Measurement and control of wheel-rail contact forces of W1 in the three directions. (a) Longitudinal force with different braking torques; (b) vertical force with different preloads; (c) lateral force with different angles of attack.

Figure 6.18a shows that the longitudinal force is controlled by applying different braking torques from the braking motor. When the braking torque is zero, the torque on the wheel is negative and generates a braking force of approximately 200 N at the wheel-rail interface. The negative wheel torque arises from the resistance of the gearbox and the bearings of the braking motor. When the braking torque is -12 N.m, the braking force increases to approximately 380 N. When the braking torque is 13 N.m, the negative wheel torque is compensated, and the longitudinal force slightly fluctuates around zero. Figure 6.18b shows that the vertical force is controlled by wheel preloads, adjusted through the preload nuts. Different axle loads can thus be simulated in V-Track. The fluctuation of

the vertical forces, which arises from vertical track irregularity, under different preloads has similar trends. Figure 6.18c shows that the lateral force is controlled by adjusting the angle of attack. The impacts of the lateral forces at the four joints are much stronger than those of the longitudinal and vertical forces, probably caused by the sudden change of the angle of attack at the joints where fishplates were absent.

6.7. CONCLUSIONS AND FUTURE WORK

In this study, a force measurement system termed a dynamometer was developed to measure the wheel-rail contact forces in V-Track. The dynamometer consists of four 3-component piezoelectric force sensors and is mounted between the wheel assembly and the steel frame, which is in the load path from the wheel-rail interface to the frame on which V-Track is mounted. Static calibration of the dynamometer was first conducted, and high accuracy was achieved in measuring the static forces in three directions. Running tests were also carried out in V-Track.

The results showed that the designed dynamometer is capable of reliably and accurately measuring the wheel-rail contact forces. Utilizing the measurement results from the dynamometer, the control of these forces in the longitudinal, vertical and lateral directions was achieved by adjusting the braking torque, wheel preload and angle of attack, respectively.

In addition, the following observations were made.

- Compared to the longitudinal and vertical directions, the accuracy of the dynamometer in the lateral direction was lower, and the crosstalk errors from the other two directions were higher, probably because the lateral force was measured by compression of the piezo sensing elements instead of by shearing in the other two directions.
- Without braking torque from the braking motor, a negative torque due to resistance from the load path was measured on the wheel; this resistant torque generates a braking force at the wheel-rail interface. The torque can be compensated by applying an equal torque from the braking motor in the opposite direction.
- The offset of the wheel plane from the plane of guiding shafts was found to cause considerably large normal contact forces and friction forces between the guiding block and guiding shafts, which might potentially lead to relatively fast wear of the elements there, but it also enables the dynamometer to capture the high-frequency vibrations at the wheel-rail interface.
- Although the dynamometer can capture the dynamic features of the wheel-rail impact vibrations, a compensation method should be derived by considering the inertia of the wheel assembly to quantitatively measure the impact forces.

In summary, the wheel-rail contact forces of V-Track can be accurately measured and well-controlled. In the future, we plan to use the 1/7 scaled V-Track to reproduce wheel and rail defects, such as rail corrugation, wheel polygonization, head checks, and squats,

to understand their formation mechanisms and develop the corresponding countermeasures. Further research on the compensation of the wheel inertia forces to more accurately measure the dynamic contact forces is also needed in future work. Since the dynamometer uses piezoelectric force sensors, signals inevitably drift over long-term measurement, which is a limitation of this system.

REFERENCES

- [1] P. Zhang, J. Moraal, and Z. Li, *Design, calibration and validation of a wheel-rail contact force measurement system in v-track*, *Measurement* **175**, 109105 (2021).
- [2] M. Naeimi, Z. Li, R. H. Petrov, J. Sietsma, and R. Dollevoet, *Development of a new downscale setup for wheel-rail contact experiments under impact loading conditions*, *Experimental Techniques* **42**, 1 (2018).
- [3] W. Zhang, J. Chen, X. Wu, and X. Jin, *Wheel/rail adhesion and analysis by using full scale roller rig*, *Wear* **253**, 82 (2002).
- [4] A. Matsumoto, Y. Sato, H. Ono, Y. Wang, M. Yamamoto, M. Tanimoto, and Y. Oka, *Creep force characteristics between rail and wheel on scaled model*, *Wear* **253**, 199 (2002).
- [5] J. Brouzoulis, P. T. Torstensson, R. Stock, and M. Ekh, *Prediction of wear and plastic flow in rails—test rig results, model calibration and numerical prediction*, *Wear* **271**, 92 (2011).
- [6] J. Koch, N. Vincent, H. Chollet, and O. Chiello, *Curve squeal of urban rolling stock—part 2: Parametric study on a 1/4 scale test rig*, *Journal of sound and vibration* **293**, 701 (2006).
- [7] V. Garg, *Dynamics of railway vehicle systems* (Elsevier, 2012).
- [8] P. Gullers, L. Andersson, and R. Lundén, *High-frequency vertical wheel–rail contact forces—field measurements and influence of track irregularities*, *Wear* **265**, 1472 (2008).
- [9] E. Gomez, J. Giménez, and A. Alonso, *Method for the reduction of measurement errors associated to the wheel rotation in railway dynamometric wheelsets*, *Mechanical systems and signal processing* **25**, 3062 (2011).
- [10] A. Matsumoto, Y. Sato, H. Ohno, M. Tomeoka, K. Matsumoto, J. Kurihara, T. Ogino, M. Tanimoto, Y. Kishimoto, Y. Sato, *et al.*, *A new measuring method of wheel–rail contact forces and related considerations*, *Wear* **265**, 1518 (2008).
- [11] P. Urda, S. Muñoz, J. F. Aceituno, and J. L. Escalona, *Wheel-rail contact force measurement using strain gauges and distance lasers on a scaled railway vehicle*, *Mechanical Systems and Signal Processing* **138**, 106555 (2020).

- [12] A. Johansson and J. C. Nielsen, *Out-of-round railway wheels—wheel-rail contact forces and track response derived from field tests and numerical simulations*, Proceedings of the Institution of Mechanical Engineers, Part F: Journal of Rail and Rapid Transit **217**, 135 (2003).
- [13] D. Milković, G. Simić, Ž. Jakovljević, J. Tanasković, and V. Lučanin, *Wayside system for wheel–rail contact forces measurements*, Measurement **46**, 3308 (2013).
- [14] D. Cortis, M. Bruner, G. Malavasi, S. Rossi, M. Catena, and M. Testa, *Estimation of the wheel-rail lateral contact force through the analysis of the rail web bending strains*, Measurement **99**, 23 (2017).
- [15] K. Sekuła and P. Kołakowski, *Piezo-based weigh-in-motion system for the railway transport*, Structural Control and Health Monitoring **19**, 199 (2012).
- [16] F. Xia, C. Cole, and P. Wolfs, *An inverse railway wagon model and its applications*, Vehicle system dynamics **45**, 583 (2007).
- [17] F. Xia, C. Cole, and P. Wolfs, *Grey box-based inverse wagon model to predict wheel–rail contact forces from measured wagon body responses*, Vehicle System Dynamics **46**, 469 (2008).
- [18] L. Wei, J. Zeng, P. Wu, and H. Gao, *Indirect method for wheel–rail force measurement and derailment evaluation*, Vehicle System Dynamics **52**, 1622 (2014).
- [19] S. Meymand and M. Ahmadian, *Design, development, and calibration of a force-moment measurement system for wheel–rail contact mechanics in roller rigs*, Measurement **81**, 113 (2016).
- [20] S. Yaldız and F. Ünsaçar, *A dynamometer design for measurement the cutting forces on turning*, Measurement **39**, 80 (2006).
- [21] Z. Yang, Z. Li, and R. Dollevoet, *Modelling of non-steady-state transition from single-point to two-point rolling contact*, Tribology International **101**, 152 (2016).
- [22] Kistler, *Instruction manual: 3-component force sensor type 9067c, 9068c,9066c4*, Winterthur .
- [23] J. J. Kalker, *Three-dimensional elastic bodies in rolling contact*, Vol. 2 (Springer Science & Business Media, 2013).
- [24] Z. Yang, X. Deng, and Z. Li, *Numerical modeling of dynamic frictional rolling contact with an explicit finite element method*, Tribology international **129**, 214 (2019).
- [25] X. Zhao and Z. Li, *The solution of frictional wheel–rail rolling contact with a 3d transient finite element model: Validation and error analysis*, Wear **271**, 444 (2011).
- [26] A. Jaschinski, H. Chollet, S. Iwnicki, A. Wickens, and J. Würzen, *The application of roller rigs to railway vehicle dynamics*, Vehicle System Dynamics **31**, 345 (1999).

- [27] S. Grassie and J. Kalousek, *Rail corrugation: characteristics, causes and treatments*, Proceedings of the Institution of Mechanical Engineers, Part F: Journal of Rail and Rapid Transit **207**, 57 (1993).
- [28] R. Dollevoet, Z. Li, and O. Arias-Cuevas, *A method for the prediction of head checking initiation location and orientation under operational loading conditions*, Proceedings of the institution of mechanical engineers, Part F: Journal of Rail and Rapid Transit **224**, 369 (2010).
- [29] A. Zoeteman, R. Dollevoet, and Z. Li, *Dutch research results on wheel/rail interface management: 2001–2013 and beyond*, Proceedings of the Institution of Mechanical Engineers, Part F: Journal of Rail and Rapid Transit **228**, 642 (2014).
- [30] Z. Li, X. Zhao, C. Esveld, R. Dollevoet, and M. Molodova, *An investigation into the causes of squats—correlation analysis and numerical modeling*, Wear **265**, 1349 (2008).
- [31] X. Deng, Z. Qian, Z. Li, and R. Dollevoet, *Investigation of the formation of corrugation-induced rail squats based on extensive field monitoring*, International Journal of Fatigue **112**, 94 (2018).

7

EXPERIMENTAL STUDY ON THE DEVELOPMENT MECHANISM OF SHORT PITCH CORRUGATION USING A DOWNSCALE V-TRACK TEST RIG

This chapter presents an experimental study on the development mechanism of short pitch corrugation using an innovative downscale V-Track test rig. The loading conditions of the V-Track were designed to simulate the vehicle-track interaction where short pitch corrugation mainly occurs in the field. Short pitch corrugation is successfully reproduced in the V-Track with two major wavelength components of 6.4 mm and 8.9 mm, approximately equivalent to the field corrugation with 32 mm and 45 mm wavelengths. Based on the measured wheel-rail dynamic contact forces, track dynamic behaviors, and observations, a general process for the consistent development of the reproduced corrugation is proposed. The specific wavelength-fixing mechanisms of the wheel-track systems with two wheel assemblies (W1 and W3) are also identified. For the W1-track system, the rail lateral vibration mode at 572 Hz, vertical mode at 570 Hz, and the induced vertical and lateral contact forces at 564 Hz contribute to the corrugation development at 6.4 mm. For the W3-track system, the longitudinal mode at 574 Hz and the induced longitudinal force at 564 Hz are responsible for the corrugation wavelength of 6.4 mm, together with the vertical mode at 570 Hz and the vertical force at 540 Hz. For both wheel-track systems, the lateral and vertical modes at 400 Hz and the induced lateral and vertical contact forces determine the corrugation development at 8.9 mm. This chapter provides the first experimental evidence indicating that rail longitudinal vibration modes contribute to the consistent development of short pitch corrugation, to the best knowledge of the authors.

Parts of this chapter have been based on the paper [1]

7.1. INTRODUCTION

Short pitch corrugation (hereinafter corrugation) is recognized as the periodic undulation of rail running surfaces on the tangent track with a wavelength range of 20-80 mm[2]. Figure 7.1a shows a typical example of corrugation in the Dutch railway. Rail corrugation excites large wheel-rail impact forces, causes excessive vibration and noise, and accelerates the deterioration of the vehicle-track system, which considerably increases maintenance costs. Therefore, it is of great significance to identify the corrugation formation mechanism and develop effective root-cause solutions.

Many theoretical and numerical studies[3][4][5][6][7][8][9][10][11] have been performed to understand the corrugation development mechanism. S. L. Grassie and J. Kalousek[2] presented a feedback loop for a general corrugation mechanism, which comprises two features: the wavelength-fixing mechanism and the damage mechanism. The damage mechanism of short pitch corrugation has been commonly considered as wear[2][12][13], while different hypotheses have been proposed for the wavelength-fixing mechanism. The vertical pinned-pinned resonance was reported as the wavelength-fixing mechanism in[4][5][13], which is a rail vertical bending mode with a wavelength of two sleeper spans. S. Muller[8] introduced a geometrical filter function that allows corrugation development within a fixed wavelength band (i.e., 20-100 mm) and showed that both the vertical and lateral track dynamics in this band dominate corrugation development. T. X. Wu and D. J. Thompson[10] considered multiple wheel/rail interactions and found that wavelengths of short pitch corrugation are associated with several vertical vibration frequencies due to the wave reflections between the wheels, rather than the only pinned-pinned frequency in the case of a single wheel/rail interaction. Employing a three-dimensional (3D) finite element (FE) vehicle-track interaction model to study corrugation, S. Li et al.[7][14] indicated that rail longitudinal vibration modes are probably dominant for the corrugation initiation and that a consistency condition between the longitudinal and vertical vibration modes is likely to determine the corrugation growth. Experimental studies have been conducted in the laboratory to validate and better understand the corrugation formation mechanism[15][16][17][18][19]. P.A. Bellette et al.[15] validated a tangent track corrugation model in terms of corrugation growth rate with a downscale two disk test rig. They also analyzed the effect of the speed variation and the friction modifier on corrugation growth and found that these two factors can considerably reduce the corrugation growth rate. X. Jin and Z. Wen[17] reproduced rail corrugation with different wavelengths using a full-scale test rig. It was found that the high-frequency vibration of the test rig can initiate a corrugation on the smooth contact surfaces of the wheel under specific test conditions, including the non-zero steady creepage of the wheelset/rollers and the circumference of the wheel rolling circle approximately equal to a multiple of the corrugation wavelength. The majority of test facilities mainly concentrate on the simulation of the wheel-rail contact of the vehicle-track interaction. Little consideration has been taken into reproducing the dynamic behaviors of the vehicle-track system, especially in the high-frequency range, which is crucial to the wavelength-fixing of corrugation in the field[2]. Therefore, although the natural vibration modes of these test facilities can well explain the wavelengths of the reproduced corrugation [17][19], they may not be comparable to those of the real vehicle-track system because of the dynamic dissimilarity, and thus cannot be used to understand the

wavelength-fixing mechanism of short pitch corrugation in the field.

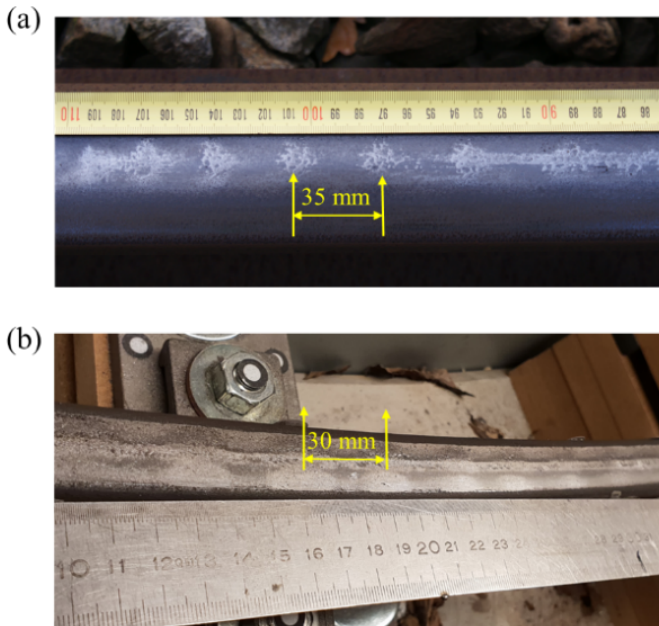


Figure 7.1: Corrugation observed in the Dutch railway and reproduced in the V-Track test rig. (a) Corrugation with a wavelength of approximately 35 mm, Steenwijk, the Netherlands. (b) Corrugation with a wavelength of approximately 30 mm reproduced in the V-Track test rig after about 8000 rotations.

To remedy the lack of dynamic similarity between the laboratory facilities and the real-life railways, M. Naeimi et al.[20] have developed an innovative downscale test rig called ‘V-Track’ to simulate vehicle-track dynamic interactions. The V-Track can comprehensively simulate both the wheel-rail contact and the high-frequency dynamic behaviors of the real vehicle-track system by the detailed treatment of wheel/rail material and geometry and the inclusion of important track structural components, such as fastenings, sleepers, and ballast layer. Therefore, it is suitable to perform wheel-rail contact experiments under highly dynamic loadings, such as short pitch corrugation, squats, and wheel polygonization. Figure 7.1b shows an example of a reproduced corrugation in one of the configurations of the V-Track. Controlling the loading conditions, are essential to reproduce and understand the corrugation formation mechanism experimentally. P. Zhang et al.[21] developed a force measurement system called “dynamometer” in the V-Track, which can measure the wheel-rail contact forces in the vertical, longitudinal, and lateral directions.

This chapter uses the innovative V-Track to reproduce rail corrugation and provide experimental evidence regarding wheel-rail contact forces, track dynamic behaviors, and hardness to understand its formation mechanism. This chapter is organized as follows. Section 7.2 introduces the structure of the V-Track and the procedures to reproduce the

rail corrugation. Section 7.3 presents the features of the reproduced corrugation in the V-Track in terms of spatial distribution, wavelength components, and hardness variation. Section 7.4 identifies the corrugation formation mechanism by analyzing the measured wheel-rail dynamic contact forces and track dynamic behaviors. Section 7.5 further discusses the experimental results and simulation results from the literature. The conclusions are drawn in Section 7.6.

7.2. CORRUGATION EXPERIMENT IN THE V-TRACK

7.2.1. EXPERIMENTAL SETUP

The V-Track test rig consists of a maximum of four-wheel assemblies running over a ring track system[21]. Two-wheel assemblies, wheel 1 (W1) and wheel 3 (W3), were utilized in the current configuration (see Figure 7.2a). Figure 7.2b and 7.2c show the structure and main components of W3. Cylindrical wheels (see “1” in Figure 7.2c) with a radius of 65 mm were used. The wheels were obtained from an actual wheel rim to ensure the identical material as in the real field. W3 was connected to a guiding block (“3” in Figure 7.2c) through an axle box (“2” in Figure 7.2c). The wheel position is adjustable along the wheel axle. The guiding block, axle box, and wheel can move along two parallel guiding shafts (“9” in Figure 7.2c) vertically under the preloads of two primary suspension springs (“4” in Figure 7.2c). The stiffness of each spring is 115 N/mm. The upper ends of these two springs were loaded by two nuts (“6” in Figure 7.2c) through load cells (“5” in Figure 7.2c). The spring load is adjustable in the range of 0-7500 N by screwing the nuts upward or downward along the threaded part of the guiding shafts. The angle of attack (AoA) of the wheel is adjustable between -2° and $+2^\circ$ by rotating the axle box around its vertical axis. The two-wheel assemblies were mounted on the arms of a steel frame (“7” in Figure 7.2c), as shown in Figure 7.2a. The steel frame was driven by a motor called ‘driving motor’ so that the wheel assemblies were pulled to run along the ring track. The maximum running speed is 40 km/h. Another motor, called ‘braking motor,’ was directly connected to the wheels through the braking shafts (“8” in Figure 7.2c), which can apply a controllable negative/positive torque to the wheels to generate desired braking/traction forces. The ring track has a radius of 2 m. This radius is not geometrically representative of any typical curvatures in real tracks. The lateral vehicle-track interaction, especially the lateral wheel-rail contact of different curvatures, can be simulated and investigated in the V-Track by adequately adjusting the AoA, the wheel conicity, and rail inclination. The ring track comprised four sections of S7 rails[21] with a head curvature radius of 120 mm, connected through four rail joints. The rails were supported by railpads and were fixed on steel sleepers by clamps, as shown in Figure 7.2d. In total, 100 sleepers were used, and the sleeper spacing was approximately 0.125 m. All sleepers were numbered from 1 to 100 for positioning; for instance, SL1 designates sleeper 1. Clamps were installed every three or four sleepers to simulate the fastening degradation, which may provide a preferred condition for corrugation initiation and growth[7][14]. Underneath the sleepers were rubber pads used to reproduce the elasticity and damping of ballast layers in real tracks. Plywood layers simulated the subgrade. The rail inclination is adjustable between 0 and 1/10 by mounting wedges on plywood layers. In the exper-

imental setup considered in this chapter, the rail inclination was approximately zero to achieve the wheel-rail head contact. Overall, the inclusion of main track components in the V-Track makes it a suitable laboratory representation of the real-life vehicle-track system in high-frequency dynamic behaviors[20], which affects the corrugation wavelength.

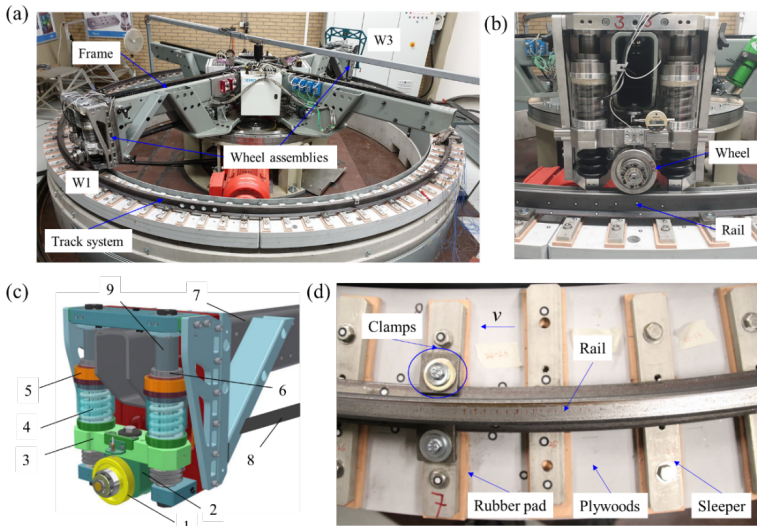


Figure 7.2: The V-Track test rig for corrugation experiments. (a) The V-Track test rig in two-wheels assemblies configuration in the laboratory; (b) wheel 3 of the V-track; (c) schematic drawing of components of W3 in CAD, 1) wheel, 2) axle box, 3) guiding block, 4) primary suspension springs, 5) load cells, 6) preload nut, 7) steel frame, 8) braking shaft, and 9) guiding shaft; (d) main components of the track system.

The parameters of the V-Track test rig are designed to be approximately 1/5 scale of the real vehicle-track system based on the similarity law[20][22], as listed in Table 7.1. A more detailed description of the V-Track can be found in[21][20].

7.2.2. CORRUGATION EXPERIMENT

Before the corrugation experiment, the loading conditions of the V-Track need first to be designed and adjusted to simulate the vehicle-track interaction on the field tangent track where corrugation mainly occurs. The vertical (normal) load was adjusted to be around 4500 N to achieve maximum contact pressure of approximately 1.15 Gpa, similar to that in the field. The AoA was as small as possible to simulate the wheel-rail lateral interaction on tangent tracks. The braking motor adjusted the wheel torque to achieve a relatively small adhesion coefficient between 0.05 and 0.15 because corrugation seems more reliably formed in low creep conditions[15]. The coefficient of friction was 0.42 after cleaning and drying the rail and the wheel surfaces. The running speed was 13 km/h. During the corrugation experiment, the wheel-rail contact forces were continuously measured and recorded by the dynamometer. Every 500 rotations, the V-Track was stopped for a

Table 7.1: Values of parameters of the V-Track test rig.

Components	Parameters	Values
Wheel, rail, sleeper material	Young's modulus	210GPa
	Poisson's ratio	0.3
	Density	7800kg/ m^3
Wheel	Radius	65mm
	Conicity	0
	Hardness	250HB
Rail	Head curvature radius	120mm
	Inclination	0
	Hardness	210 HB
Sleeper	Dimensions	255x40x15 mm
	Distance	125 mm
Primary suspension	Stiffness	230 kN/m
	Damping	100 N.s/m
Railpads	Stiffness	200 MN/m
	Damping	1.9 kN.s/m
Rubber pads to simulate ballast	Stiffness	10 MN/m
	Damping	0.86 kN.s/m

visual inspection of the rail and wheel surfaces to check whether corrugation occurred or not. After the corrugation in the V-Track was reproduced, a 3D HandyScan test was performed to measure the spatial distribution of corrugation. A hardness test was then conducted to identify the hardness variation along the corrugation. Additionally, the hammer test was performed to obtain the dynamic behavior of the track, which is related to the corrugation characteristic frequencies and wavelengths. The detailed introduction of the wheel-rail contact force measurement, the 3D HandyScan test, the hardness test, and the hammer test is provided in the following sections.

WHEEL-RAIL CONTACT FORCE MEASUREMENT

A dynamometer has been developed in the V-Track to measure the wheel-rail contact forces in the vertical (z), longitudinal (rolling, x), and lateral directions (y) [21]. It consists of four 3-component piezoelectric force sensors mounted between the wheel assembly and the steel frame. The sampling frequency is 16.67 kHz. Figure 7.3 shows the measured wheel-rail contact forces of W1 and W3 in three directions after adjusting the spring preload, the wheel torque, and the AoA based on the designed loading conditions. The starting (0 m) and ending positions (12.56 m) referred to the same position at SL1 of the ring track. The adhesion coefficient was calculated by dividing the tangential force by the vertical (normal) force:

$$\mu = \sqrt{F_x^2 + F_y^2} / F_z \quad (7.1)$$

where is adhesion coefficient, and F_x , F_y , and F_z are the contact forces in the longitudinal, lateral, and vertical directions, respectively.

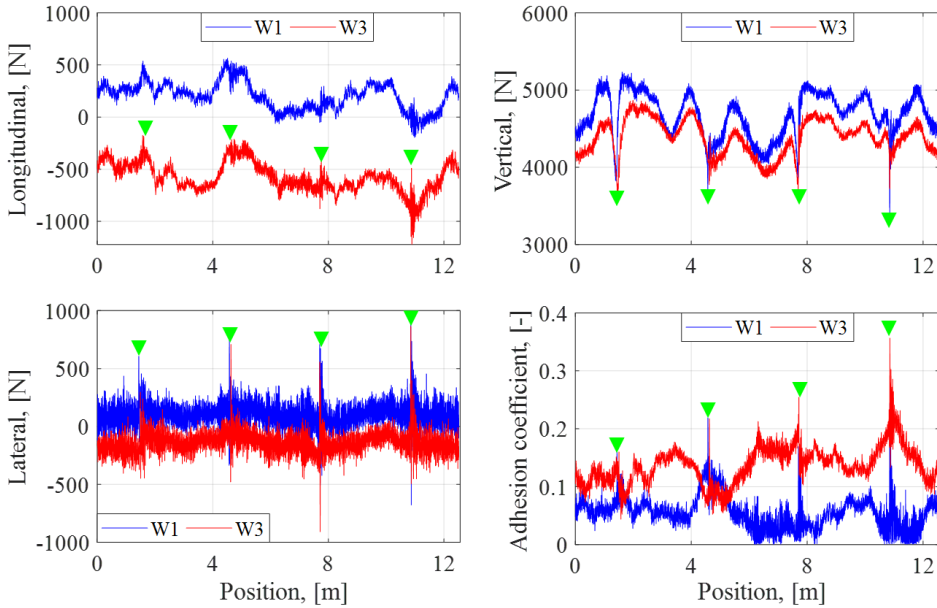


Figure 7.3: Measured wheel-rail contact forces and adhesion coefficient of W1 and W3. (a) Longitudinal forces; (b) vertical forces; (c) lateral forces; (d) adhesion coefficient. The joint positions are marked by (▼).

Figure 7.3a shows that the longitudinal force of W1 fluctuates around 200 N, and that of W3 changes between -220 N and -1200 N with an average value of -575 N. W1 was in traction in most positions, while W3 was in braking conditions. The longitudinal forces were determined by the torques on W1 and W3 applied through a coupled gearbox[21]. We can only control the overall torque applied to the gearbox in the current setup but cannot control how the gearbox distributes the torque to the two wheels. The difference in the longitudinal force of W1 and W3 was caused by the uneven distribution of the wheel torque by the gearbox. It can be seen from Figure 7.3b that the measured vertical forces of W1 and W3 change mostly in the range of 4 kN and 5 kN. The vertical track irregularity causes this strong long-wavelength (i.e., 1-2 m) fluctuation. In future work, more efforts will be made to adjust the irregularity to achieve more even vertical force along the track. The average vertical load of W1 is approximately 4650 N, slightly larger than of W3, which is 4400 N. Compared to the longitudinal and vertical forces, the overall lateral forces of both wheels are small, with average values of 100 N and -140 N for W1 and W3, respectively, as shown in Figure 7.3c. Besides, the impacts of the lateral forces at rail joints, corresponding to four dominant peaks in Figure 7.3c (indicated by ▼), are significantly strong, possibly resulting from the sudden change of the AoA at the joints fishplates were absent. Figure 7.3d depicts the adhesion coefficient of the two wheels. Neglecting the proximity to the joints, the adhesion coefficients of W1 and W3 are in the range of 0.1 and 0.1-0.2, respectively. Overall, the contact forces of the two wheels roughly satisfy the designed loading conditions to simulate the vehicle-track interaction

on the field tangent track. In addition, the fluctuation of the wheel-rail contact forces allows us to study the influences of different axle loads, adhesion coefficients, and AoAs on corrugation formation.

CORRUGATION MEASUREMENT BY THE 3D HANDYSCAN TEST

After reproducing corrugation, the rail profile with corrugation was measured with a laser-based HandyScan, as shown in Figure 7.4. In this measurement, the laser strips projected a reference on the rail surface, and two cameras captured the reflection signals and transmitted them to a data acquisition system (see Figure 7.4a). When moving along the rail, the HandyScan positioned itself to a unique dynamic referencing system which ensured high measurement repeatability and accuracy. Figure 7.4b shows an example of the measured corrugation in the V-Track in Figure 7.1b. The longitudinal-vertical profile in the central of the running band was derived, and 15-point smooth was used to reduce the measurement errors. It can be seen that the corrugation wavelength is approximately 30 mm, agreeing well with the observation in Figure 7.1b.

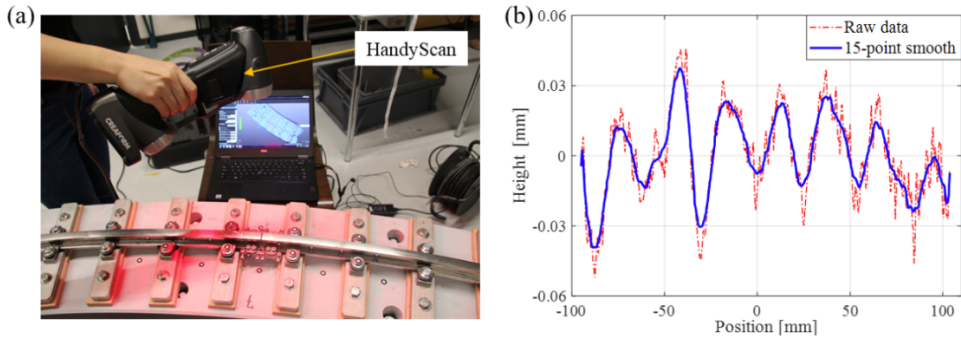


Figure 7.4: Corrugation measurement by the 3D HandyScan test. (a) 3D HandyScan test; (b) measured corrugation in the V-Track in Figure 7.1b.

HARDNESS TEST

It has been reported in the literature that the rail hardness is varied along the corrugation because of the different microstructures at the peaks and troughs [23][24]. The hardness test was performed on the running band of the rail to capture the hardness variation along the corrugation, as shown in Figure 7.5. A hardness tester (DynMIC34248) was used together with a self-developed ruler guide. The interval between two adjacent test points was 2 mm.

The hardness values of the rails and the wheels were measured before the experiments to define their initial conditions. The hardness value of the original S7 rail is about 170 HB. After some trial running tests, the rail hardness has increased to about 210 HB. The wheel hardness increased from about 200 HB to 250 HB, which is harder than the rail.

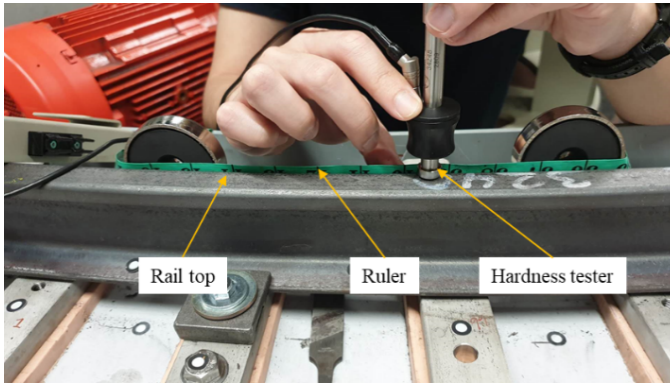


Figure 7.5: Experimental setup for the hardness test in the V-Track.

HAMMER TEST

Track dynamics is important to understand the wavelength-fixing mechanism of corrugation. Hammer test is a widespread testing technique to obtain the dynamic behavior of the railway tracks [25][26][27]. Figure 7.6 shows the experimental setup for the hammer test in the V-Track. Two 3D accelerometers (PCB 356B21) were glued on the rail gauge face to capture the rail vibration signals. They were not placed on the rail head to avoid the glue contamination on the wheel-rail contact surfaces. One was on a rail section above a sleeper (named 'on-support' in Figure 7.6a), the other was in the middle of two sleeper (named 'mid-span' in Figure 7.6a). A small hammer (PCB 086C03) with a metal tip was used to excite the rail in the high-frequency range. The excitation positions were as close as possible to the accelerometers in three directions. The vertical and lateral hammer impacts were conducted on the rail head and gauge face, respectively. The longitudinal impacts were applied through a self-made clamp, as shown in Figure 7.6b. The frequency response function (FRF) is calculated as follows[28].

$$FRF(f) = \frac{S_{aF}(f)}{S_{FF}(f)(2\pi f)^2} \quad (7.2)$$

where S_{aF} is the cross-spectrum between the acceleration and force, and S_{FF} is the auto-spectrum of the force, and f is frequency.

7.3. THE REPRODUCED CORRUGATION IN THE V-TRACK

After 4500 rotations, corrugation was first observed from SL80 to SL85 of the V-Track. Figure 7.7 shows the corrugation between SL84 and SL85, with the shiny parts marked by red lines on the rail surfaces. The corrugation wavelength observed from this figure is 6-7 mm. The running band was close to the inner edge of the rail head because of the rail tilt during the installation process. Its width was about 4 mm, larger than the 3.2 mm calculated based on the Hertz theory due to the plastic deformation[29]. There is a rail joint between SL85 and SL86. Because of the insufficient length of the two adjacent rails, a small piece of rail was included in this joint. This imperfect joint was just after the cor-

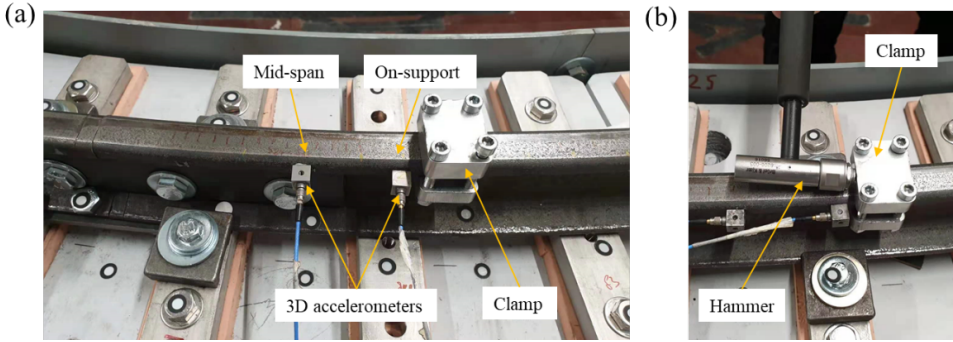


Figure 7.6: Experimental setup for the hammer test in the V-Track. (a) Experimental setup; (b) longitudinal hammer excitation by a self-made clamp.

rugation in the space and thus not the direct initiators of corrugation. Fastening clamps were used only at SL80 and SL85, and it was observed that one of the fastening bolts at SL85 was loose during the corrugation experiment, as shown in Figure 7.7a. Overall, the imperfect joint, the absent fastening clamps at SL81- SL84, and the loose fastening bolt at SL85 lead to relatively weak constraint to the rail and serve as the initial excitation to the wheel-rail system for corrugation formation.

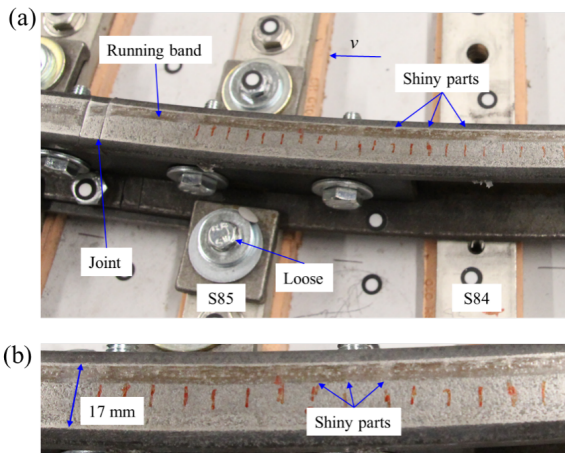


Figure 7.7: The reproduced corrugation between SL84 and SL85 in the V-Track. (a) Corrugation with a wavelength of approximately 6-7 mm in the V-Track; (b) close-up of the corrugation.

After observing the corrugation, we further run another 6000 rotations to grow the corrugation. Figure 7.8 shows the measured corrugation in the spatial and wavelength domains after the 10500 rotations from the 3D HandyScan test. The corrugation was between 10.72 m and 10.83 m, just before the rail joint (at 10.83 m), which served as a reference point for the ease of comparison with the measurement results of the hardness

and contact forces. It is observed from Figure 7.8a that the corrugation amplitude (maximum peak to trough distance) is approximately 60 μm , indicating a relatively severely developed corrugation. Figure 7.8b shows that the corrugation has two major wavelength components of 6.4 mm and 8.9 mm, respectively, and the wavelength of 6.4 mm has the highest PSD magnitude, which agrees with the observation in Figure 7.7, where the wavelength is 6-7 mm. There are also some minor wavelength components, i.e., at 7.7 mm and 10.8 mm. According to the similarity law[20][22], the major corrugation wavelengths of 6.4 mm and 8.9 mm are approximately equivalent to 32 mm and 45 mm of corrugation wavelengths in the field considering a scale factor of 1/5. Therefore, the reproduced rail corrugation in the V-Track falls in the typical wavelength range of short pitch corrugation, and the analysis of its formation mechanism can be applied to understand the formation of corrugation in the field.

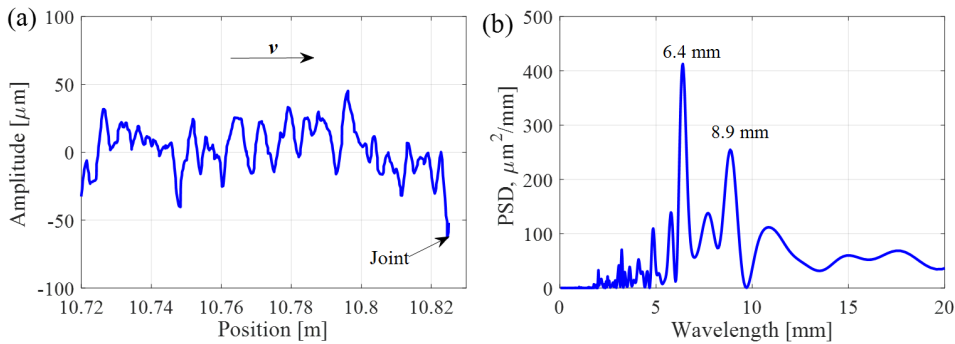


Figure 7.8: The reproduced corrugation in the spatial and wavelength domains. (a) In the spatial domain, the corrugation just before the joint (at position 10.83 m) was selected for analysis; (b) in the wavelength domain.

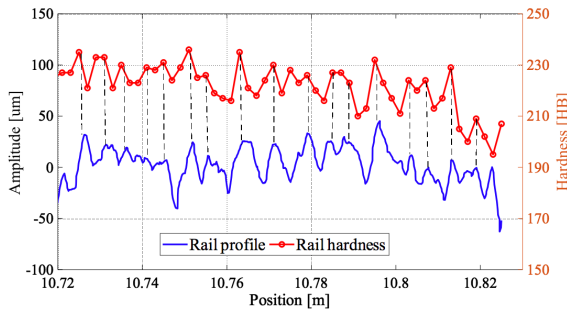


Figure 7.9: Measured rail hardness along the corrugation compared with the rail profile.

Figure 7.9 shows measured rail hardness along the corrugation together with the rail profile. It can be seen that the rail hardness fluctuates between 195 HB and 235 HB and has a wave pattern similar to that of the rail profile. The hardness peaks correspond well to the corrugation peaks, as indicated by the dashed lines in Figure 7.9, which agrees with

the findings in [24], possibly resulting from different microstructures in the corrugation peaks and troughs due to the dynamic loads.

7.4. CORRUGATION DEVELOPMENT MECHANISM

In this section, the corrugation development mechanism is identified based on the measured wheel-rail contact forces, track dynamic behaviors, and observations.

7.4.1. CORRUGATION WAVELENGTHS

The corrugation formation requires the continuous accumulation of differential wear or plastic deformation at certain locations, which means that wear or plastic deformation caused by one-wheel passage should repeat the same wavelength and phase as the previous wheel passages. The wheel-rail dynamic contact forces cause the wear and plastic deformation of the rails. It is thus inferred that the corrugation formation should depend on the repeatable wavelength and phase of the contact forces under multiple wheel passages. Figure 7.10 and Figure 7.11 show the measured contact forces with W1 and W3 at rotations 1 (beginning of the experiment), 5000 (middle), and 10500 (end) in the spatial and wavelength domains, respectively.

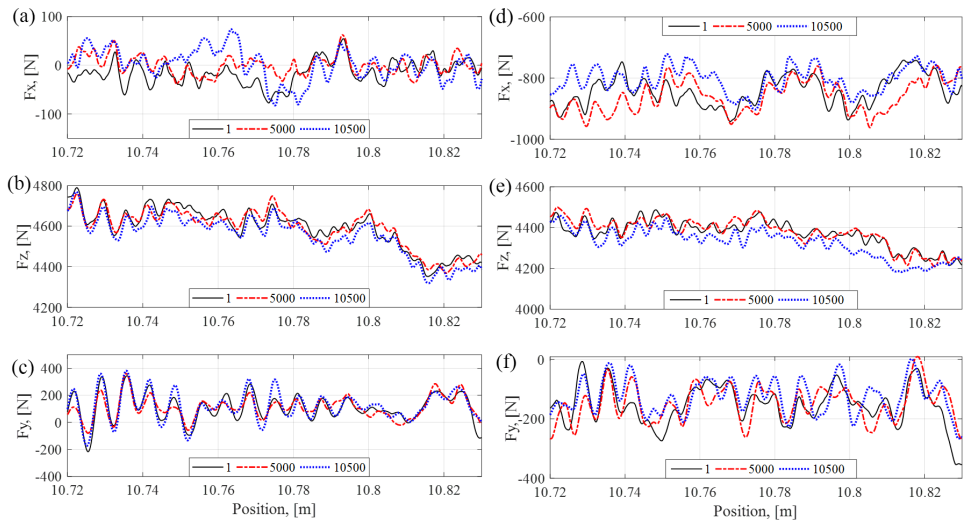


Figure 7.10: Measured wheel-rail dynamic contact forces of W1 and W3 in the spatial domain at rotations 1, 5000 and 10500. (a) Longitudinal force of W1; (b) vertical force of W1; (c) lateral force of W1; (d) longitudinal force of W3; (e) vertical force of W3; (f) lateral force of W3.

Figure 7.10a and Figure 7.11a show that the overall longitudinal force with W1 is small (below 100 N) with a wavelength of 7.7 mm, which may be related to a minor corrugation wavelength of 7.7 mm (see Figure 7.8b). The vertical and lateral forces with W1 repeat the wavelength and phase for all the rotations, as shown in Figure 7.10b and 7.10c. They both have a dominant wavelength component of 6.4 mm (see Figure 7.11b, 7.11c), which

should contribute to corrugation formation at 6.4 mm. It is found that the magnitude of the lateral force with W1 at 6.4 mm is considerably larger than that of the vertical force, indicating that the lateral force is dominant for the corrugation wavelength of 6.4 mm. It is also observed from Figure 7.11c that the lateral force has another major wavelength component of 9.5 mm, which may be responsible for corrugation development at 8.9 mm. Figure 7.11b shows that the vertical force with W1 has multiple wavelength components in 7-20 mm, and the one at 9.3 mm is the closest to the corrugation wavelength of 8.9 mm.

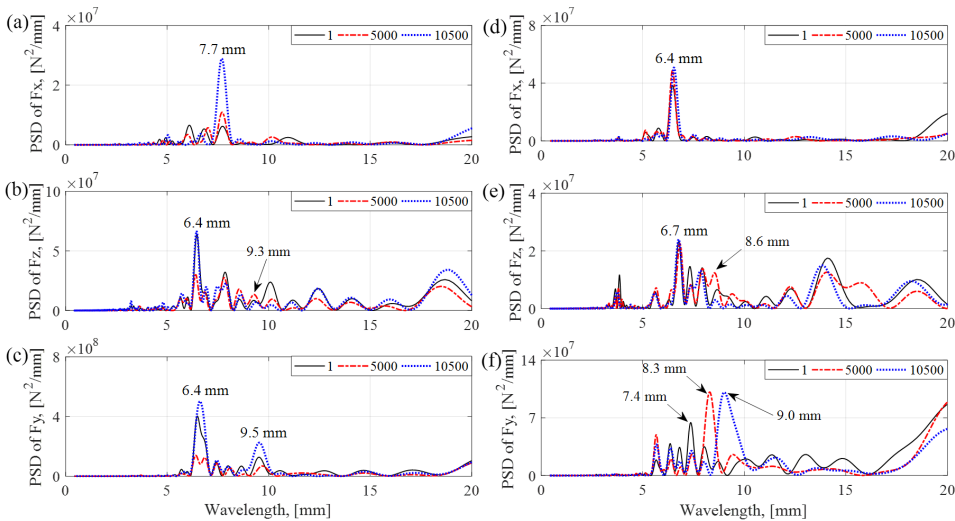


Figure 7.11: Measured wheel-rail dynamic contact forces of W1 and in the wavelength domain at rotations 1, 5000 and 10500. (a) Longitudinal force of W1; (b) vertical force of W1; (c) lateral force of W1; (d) longitudinal force of W3; (e) vertical force of W3; (f) lateral force of W3.

Figure 7.10d shows that the longitudinal force with W3 fluctuates around -850 N and repeats the wavelength and phase for all the rotations. It has a dominant wavelength component of 6.4 mm, as shown in Figure 7.11d, which should be responsible for corrugation development at 6.4 mm. Figure 7.10e and Figure 7.11e depicts that the vertical force with W3 also has repeatable wavelength and phase for all rotations with a major wavelength component of 6.7 mm, which is closely related to the corrugation wavelength of 6.4 mm. Due to the larger magnitude and closer to corrugation wavelength, the longitudinal force with W3 seems more decisive on corrugation development at 6.4 mm than the vertical force. Like W1, the vertical force with W3 also has multiple wavelength components in 7-20 mm, which may be relevant to some minor corrugation wavelengths. Among them, the wavelength of 8.6 mm is the closest to the corrugation wavelength of 8.9 mm. Figure 7.11f shows the shift of major wavelength components of the lateral force with W3 from 7.4 mm at rotation 1, to 8.3 mm at rotation 5000, and to 9.0 mm at rotation 10500, which leads to their phase difference at some positions in Figure 7.10f, such as in 10.80 - 10.81 m. The wavelength components of 8.3 mm and 9.0 mm may contribute to the corrugation wavelength of 8.9 mm.

In summary, the lateral and vertical forces with W1 and the longitudinal and vertical forces with W3 determine the corrugation development at the dominant wavelength component of 6.4 mm. Although there are no wavelength components of contact forces that exactly match the corrugation wavelength of 8.9 mm, it is observed that the lateral force wavelength of 9.5 mm with W1, vertical force wavelength of 9.3 mm with W1, lateral force wavelengths of 8.3 mm and 9.0 mm with W3, vertical force wavelength of 8.6 mm with W3 are quite close to it. It is thus inferred that the modulation of these wavelength components contributes to the corrugation development at 8.9 mm. The other wavelength components of contact forces (i.e., between 7 and 20 mm) may be related to some minor corrugation wavelengths. In addition, the repetitive wavelength and phase of the contact forces confirm that corrugation consistently grows at certain locations of the rail.

7.4.2. CORRUGATION FREQUENCIES

The characteristic frequency f is the quotient of the running speed ν and a characteristic wavelength λ , as follows.

$$f = \frac{\nu}{\lambda} \quad (7.3)$$

With the running speed of 13 km/h, two corrugation characteristic frequencies are calculated as 564 Hz and 405 Hz, corresponding to the wavelength components of 6.4 mm and 8.9 mm (see Figure 7.8b). This equation also applies to the calculation of characteristic frequencies of the wheel-rail contact forces.

S. L. Grassie[30] reported that all types of corrugation that have been documented to date are essentially constant-frequency phenomena, which are determined by the eigenfrequencies of the vehicle-track system[14]. Track dynamic behaviors characterized by FRFs were obtained by the hammer test to identify the corrugation frequencies. Figure 7.12a, 7.12b, 7.12c shows the measured FRFs in the longitudinal, vertical, and lateral directions, respectively, with the excitations of on-support and mid-span. Some resonance peaks and anti-resonance dips are observed in the FRFs with strong fluctuation amplitudes, corresponding to different rail vibration modes[31][32]. It is found that the corrugation frequency of 564 Hz corresponds well to a longitudinal anti-resonance mode at 574 Hz, a vertical resonance mode at 570 Hz, and a lateral resonance mode at 572 Hz (indicated by arrows in Figure 7.12.). The corrugation frequency of 405 Hz corresponds to a vertical and a lateral resonance mode at 400 Hz (indicated by arrows in Figure 7.12b and 7.12c), while no relevant longitudinal mode is found in Figure 7.12a.

7.4.3. CORRUGATION DEVELOPMENT MECHANISM

To better understand the corrugation development mechanism, the characteristic wavelengths and frequencies of the corrugation, contact forces, and relevant rail vibration modes are summarized in Table 7.2. The numbers are colored depending on their relevance to the corrugation wavelengths and frequencies. Those related to corrugation wavelength of 6.4 mm or frequency of 564 Hz are set to be blue. Numbers related to

corrugation wavelength of 8.9 mm or frequency of 405 Hz are set to be orange. Other numbers are set to be black.

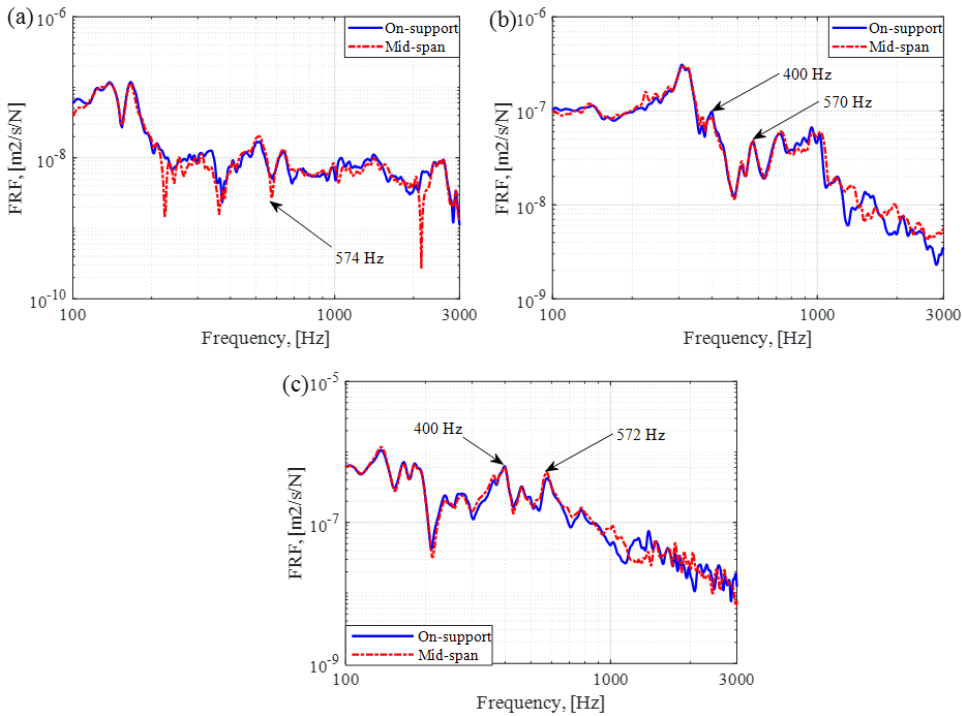


Figure 7.12: Measured FRFs in three directions with the on-support and the mid-span excitations. (a) Longitudinal FRF; (b) vertical FRF; (c) lateral FRF.

A general process for corrugation development is proposed based on observations and measurement results of wheel-rail dynamic contact forces and track dynamic behaviors. First, the imperfect joint, the absent fastening clamps at SL81- SL84, and the loose fastening bolt at SL85 are identified as the initial excitation [14] to the V-Track vehicle-track system, which leads to a weaker constraint to the rail. Hence some rail vibration modes cannot be effectively suppressed, as shown in Figure 7.12. Afterward, when the wheel rolls over the rail, these vibration modes are excited and induce wheel-rail dynamic contact forces with a certain wavelength and phase. With multiple wheel passages, the dynamic contact forces repeat the same wavelength and phase as the previous ones, as shown in Figure 7.10. During this process, the differential wear or plastic deformation caused by the dynamic contact forces continuously accumulates at certain rail locations. Corrugation can thus consistently initiate and grow.

Specifically, for the W1-track system, the lateral mode at 572 Hz and vertical mode at 570 Hz are excited and induce the vertical and lateral dynamic contact forces at 564 Hz, contributing to the corrugation development at 6.4 mm. However, for the W3-track system,

the longitudinal mode at 574 Hz and the induced longitudinal force at 564 Hz are responsible for corrugation wavelength of 6.4 mm, together with the vertical mode at 570 Hz and vertical force at 540 Hz. Despite different wavelength-fixing mechanisms for W1 and W3, the passages of these two wheels both promote the corrugation development at 6.4 mm because of the coupling of rail longitudinal, lateral and vertical modes around the corrugation frequency 564 Hz. The lateral and vertical modes at 400 Hz and the induced lateral and vertical forces determine the corrugation development at 8.9 mm for both wheel-track systems. It is noted that the frequencies of rail vibration modes, contact forces, and corrugation are not identical but with slight deviations (within 5%), which may be influenced by the dynamic behaviors of the wheel that are not analyzed in this work.

Table 7.2: Characteristic wavelengths and frequencies of corrugation, contact forces, and relevant track vibration modes. The numbers are colored depending on their relevance to the corrugation wavelengths and frequencies (in boldface). The numbers related to the corrugation wavelength of 6.4 mm or frequency of 564 Hz are set to be blue. The numbers related to the corrugation wavelength of 8.9 mm or frequency of 405 Hz are set to be orange. Otherwise, they are set to be black.

Dynamic quantities	W1-track system		W1-track system	
	Wavelength(mm)	Frequency(Hz)	Wavelength(mm)	Frequency(Hz)
Corrugation	6.4	564	6.4	564
	8.9	405	8.9	405
Longitudinal contact force	7.7	469	6.4	564
Vertical contact force	6.4	564	6.7	540
	9.3	388	8.6	420
Lateral contact force	6.4	564	7.4	488
			8.3	435
	9.5	381	9.0	401
Longitudinal vibration mode, Hz			574	
Vertical vibration mode, Hz			400	570
Lateral vibration mode, Hz			400	572

7.5. DISCUSSIONS

7.5.1. VALIDATION AND EXTENSION OF THE NEW INSIGHTS IN [7][14]

S. Li et al. [7] and Z. Li et al. [14] numerically studied the development mechanism of short pitch corrugation employing a validated 3D FE vehicle-track interaction model [33][34][35] and indicated that rail longitudinal vibration modes are possibly responsible for corrugation initiation. This insight agrees with the experimental results of the W3-track system that the longitudinal rail mode at 574 Hz contributes to corrugation development at 6.4 mm. The simulation results further inferred that the consistency condition between the longitudinal contact force, vertical contact force, differential wear, and the resulting corrugation need to be satisfied for corrugation can continuous growth. The corrugation experiment in this chapter confirmed this hypothesis. The consistency between the wavelengths of longitudinal force, vertical force, and corrugation is found experimentally for corrugation formation at 6.4 mm of the W3-track system. This consistency condition still holds at the rotation 10500, which suggests corrugation can further grow. The repetitive wavelength and phase of measured contact forces for all rotations confirm

that corrugation consistently develops on the rail.

In addition, the experimental results of the W1-track system show that the rail lateral vibration mode can also dominate the corrugation development. Similarly, the consistency between the frequencies of the lateral force, vertical force, lateral vibration mode, vertical vibration mode, and the corrugation is also observed. In the FE simulation of [7], lateral vibration modes and lateral force were not analyzed because the lateral wheel-rail interaction is generally considered weak on tangent tracks and hence negligible to corrugation formation. Nevertheless, Figure 7.10c shows that the fluctuation amplitude of the lateral force can be considerably large due to a small AoA. That is possible because the V-Track is circular with a small radius (2 m) instead of tangent, and hence the lateral vibration modes can be more easily excited by the AoA. Besides, the track has the largest flexibility in the lateral direction compared to those in the longitudinal and vertical directions, as shown in Figure 7.12, and with the same excitation, the lateral vibration is the strongest.

Overall, the experimental results validated the new insights in [7][14] about longitudinal vibration modes and the consistency condition for corrugation development. Besides, it is found that rail lateral vibration mode and induced lateral dynamic force are responsible for corrugation development in this circular track. This chapter provides the first experimental evidence to the best knowledge of the authors, indicating that rail longitudinal vibration modes contribute to the consistent development of short pitch corrugation.

7.5.2. VERTICAL VIBRATION MODES AND SHORT PITCH CORRUGATION

A widely accepted hypothesis in the literature is that vertical vibration modes induce the varying vertical (normal) force that determines the development of short pitch corrugation [4][5][10][36][37]. This hypothesis is probably based on the fact that the wheel-rail interaction mainly acts in the vertical direction. The longitudinal and lateral vibration modes have not been included in most analytical and numerical studies in the literature. Except for the unawareness of their significance, another possible reason is the limitation of the previous models that cannot directly and instantaneously consider the coupling of 3D structural dynamics and the contact mechanics of the vehicle-track system. For the corrugation simulation, the tangential force in these models is usually assumed to be constant [36] or fluctuate depending on the normal force [37]. Nevertheless, the experimental results in this chapter indicate that the fluctuation of tangential force is independent on but much larger than that of the vertical force. This fluctuation is mainly determined by the longitudinal and lateral vibration modes excited from the vehicle-track dynamic interaction. Although the vertical vibration modes and vertical dynamic forces play a role in the corrugation formation, they seem not as decisive as those in the longitudinal and lateral directions.

7.5.3. THE INITIAL EXCITATION FOR CORRUGATION DEVELOPMENT

Corrugation is not observed everywhere on the track but at some particular locations. Hence, it is reasonable to assume that the track that can develop corrugation has some initial energy input to excite the vehicle-track system called “initial excitation” [14]. With

the initial excitation, rail vibration modes are excited and induce dynamic wheel-rail contact forces. These dynamic forces result in differential wear or plastic deformation that is responsible for corrugation development. In some situations, the initial excitation of corrugation is obvious, for instance, the joint-, the scratch-, and the squat-induced corrugation[2][20][38][39][40], which follows the excitation and often decays out over a finite number of wavelengths. In other situations, the initial excitation seems invisible (i.e., railpad aging), and the corrugation can develop over a much longer distance. The purpose of this work is to reproduce the latter corrugation. Therefore, fastening clamps were installed only every three or four sleepers to simulate the fastening degradation in the field, which may provide a potentially preferred condition for corrugation initiation and growth. The loose fastening bolt at SL85 was unexpected and observed during the corrugation experiment. Four rail joints were used to connect the four rails, and only the joint between SL85 and SL86 used a small piece of rail because of the insufficient length of the adjacent rails. The absent fastening clamps at SL81- SL84, the loose fastening bolt at SL85, and the imperfect joint serve as the initial excitation for the very first corrugation development that is at SL80-SL85. The latter two factors probably play a more important role because corrugation was not observed in the vicinity of the other three joints.

7.5.4. THE LOADING CONDITIONS AND THE EXCITED RAIL VIBRATION MODES

The previous analysis indicates that W1 and W3 excited different rail vibration modes as the wavelength-fixing mechanisms of corrugation. It is noted from Figure 7.10 that the initial loading conditions of W1 and W3 are quite different. For instance, the quasi-static longitudinal load of W3 is around -850 N while W1 is around 0 N. W3 excited the longitudinal vibration mode at 574 Hz while W1 did not, indicating the stronger interaction and coupling is more likely to excite the corresponding vibration modes. The quasi-static lateral forces of both wheels are around 150 N but in different directions. W1 excited the lateral vibration mode at 572 Hz while W3 did not, suggesting that the loading direction could influence the excited vibration modes considering the asymmetrical position of running banding on the rail head. Overall, these experiment results indicate that the values and directions of the initial loadings of the vehicle-track system may influence the excited rail vibration modes, and thus the wavelength-fixing mechanism of corrugation.

7.6. CONCLUSIONS AND FUTURE WORK

In this chapter, an experimental study of short pitch corrugation has been performed using the V-Track test rig. The employed V-Track configuration consists of two wheel assemblies (W1 and W3) and a ring track and can accurately simulate the high-frequency dynamics of the real vehicle-track system, which is crucial to understand the wavelength-fixing mechanism of short pitch corrugation. The loading conditions of the V-Track were first designed and adjusted for the wheel preload, the braking torque, and the angle of attack to simulate the vehicle-track interaction. Short pitch corrugation was successfully reproduced between SL80 and SL85 of the V-Track, and its spatial distribution, wave-

length components, and hardness variation were captured by the 3D HandyScan and the hardness tests. Based on the measurement results of wheel-rail contact forces and track dynamic behaviors and observations, the development mechanism of short pitch corrugation was identified. The main conclusions are summarized as follows.

1. The reproduced rail corrugation in the V-Track has two major wavelengths of 6.4 mm and 8.9 mm, approximately equivalent to 32 mm and 45 mm of corrugation wavelengths in the field considering a scale factor of 1/5, falling in the typical short pitch range. Therefore, the study of its formation mechanism can be applied to understand short pitch corrugation in the field.
2. The process for consistent development of the short pitch corrugation is identified. The imperfect joint, the loose fastening bolt at SL85, and the absent fastening clamps at SL81- SL84 lead to a weaker constraint to the rail, serving as the initial excitation to the V-Track vehicle-track system. Hence some rail vibration modes cannot be effectively suppressed and induce dynamic wheel-rail contact forces with a certain wavelength and phase when the wheel rolls over the rail. With multiple wheel passages, the dynamic contact forces repeat the same wavelength and phase as the previous ones, and the resulting differential wear or plastic deformation can continuously accumulate at certain locations of the rail, causing consistent corrugation growth.
3. Specifically, two types of wavelength-fixing mechanisms of short pitch corrugation at 6.4 mm are identified for the two wheel-track systems with W1 and W3. For the W1-track system, the rail lateral vibration mode at 572 Hz and vertical mode at 570 Hz, and the induced vertical and lateral contact forces at 564 Hz contribute to the corrugation development at 6.4 mm. For the W3-track system, the longitudinal mode at 574 Hz, the induced longitudinal force at 564 Hz, the vertical mode at 570 Hz, and the vertical force at 540 Hz are responsible for a corrugation wavelength 6.4 mm. Despite different wavelength-fixing mechanisms for W1 and W3, the passages of these two wheels both promote the corrugation development at 6.4 mm because of the coupling of rail longitudinal, lateral and vertical modes around the corrugation frequency 564 Hz.
4. The lateral and vertical modes at 400 Hz and the induced lateral and vertical dynamic contact forces determine the corrugation development at 8.9 mm for both wheel-track systems.
5. The experimental results validated the hypotheses in [7][14] about longitudinal vibration modes and the consistency condition for short pitch corrugation development. To the best knowledge of the authors, this chapter provides the first experimental evidence, which indicates that rail longitudinal vibration modes contribute to the consistent development of short pitch corrugation.
6. The experimental results in this work indicate that although they play a role in the corrugation formation, the vertical vibration modes and the induced vertical dy-

dynamic contact forces are not as decisive and dominant as those in the longitudinal and lateral directions.

7. The initial loading conditions of the vehicle-track system may influence the excited rail vibration modes and thus the wavelength-fixing mechanism of short pitch corrugation.

The experimental results and findings can be applied to understand the development mechanism of short pitch corrugation in the field. In future work, the S7 rails will be replaced with the scaled 1/5 rails to better simulate the field wheel-rail dynamic contact. Further metallurgical investigation of rail in the presence of corrugation will be performed to understand the corrugation damage mechanism and explain the measured hardness variation along the corrugation. Besides, mitigation approaches for short pitch corrugation will be designed and validated using the V-Track test rig in future work.

REFERENCES

- [1] P. Zhang and Z. Li, *Experimental study on the development mechanism of short pitch corrugation using a downscale v-track test rig*, Submitted .
- [2] S. Grassie and J. Kalousek, *Rail corrugation: characteristics, causes and treatments*, Proceedings of the Institution of Mechanical Engineers, Part F: Journal of Rail and Rapid Transit **207**, 57 (1993).
- [3] S. Grassie and K. Johnson, *Periodic microslip between a rolling wheel and a corrugated rail*, Wear **101**, 291 (1985).
- [4] K. Hempelmann and K. Knothe, *An extended linear model for the prediction of short pitch corrugation*, Wear **191**, 161 (1996).
- [5] M. Hiensch, J. C. Nielsen, and E. Verheijen, *Rail corrugation in the netherlands—measurements and simulations*, Wear **253**, 140 (2002).
- [6] A. Igeland and H. Ilias, *Rail head corrugation growth predictions based on non-linear high frequency vehicle/track interaction*, Wear **213**, 90 (1997).
- [7] S. Li, Z. Li, A. Núñez, and R. Dollevoet, *New insights into the short pitch corrugation enigma based on 3d-fe coupled dynamic vehicle-track modeling of frictional rolling contact*, Applied Sciences **7**, 807 (2017).
- [8] S. Muller, *A linear wheel-track model to predict instability and short pitch corrugation*, Journal of Sound and Vibration **227**, 899 (1999).
- [9] J. Neilsen, *Evolution of rail corrugation predicted with a non-linear wear model*, Journal of Sound and Vibration **227**, 915 (1999).
- [10] T. Wu and D. Thompson, *An investigation into rail corrugation due to micro-slip under multiple wheel/rail interactions*, Wear **258**, 1115 (2005).

- [11] K. Knothe and A. Groß-Thebing, *Short wavelength rail corrugation and non-steady-state contact mechanics*, *Vehicle system dynamics* **46**, 49 (2008).
- [12] K. Oostermeijer, *Review on short pitch rail corrugation studies*, *Wear* **265**, 1231 (2008).
- [13] S. L. Grassie, *Rail corrugation: advances in measurement, understanding and treatment*, *Wear* **258**, 1224 (2005).
- [14] Z. Li, S. Li, P. Zhang, A. Nunez, and R. Dollevoet, *Mechanism of short pitch corrugation: Initial excitation and wavelength selection for consistent initiation and growth*, Submitted (2021).
- [15] P. Bellette, P. Meehan, and W. Daniel, *Validation of a tangent track corrugation model with a two disk test rig*, *Wear* **271**, 268 (2011).
- [16] A. Matsumoto, Y. Sato, H. Ono, M. Tanimoto, Y. Oka, and E. Miyauchi, *Formation mechanism and countermeasures of rail corrugation on curved track*, *Wear* **253**, 178 (2002).
- [17] X. Jin and Z. Wen, *Rail corrugation formation studied with a full-scale test facility and numerical analysis*, *Proceedings of the Institution of Mechanical Engineers, Part J: Journal of Engineering Tribology* **221**, 675 (2007).
- [18] A. Saulot, S. Descartes, and Y. Berthier, *Sharp curved track corrugation: From corrugation observed on-site, to corrugation reproduced on simulators*, *Tribology International* **42**, 1691 (2009).
- [19] Y. Suda, H. Komine, T. Iwasa, and Y. Terumichi, *Experimental study on mechanism of rail corrugation using corrugation simulator*, *Wear* **253**, 162 (2002).
- [20] M. Naeimi, Z. Li, R. H. Petrov, J. Sietsma, and R. Dollevoet, *Development of a new downscale setup for wheel-rail contact experiments under impact loading conditions*, *Experimental Techniques* **42**, 1 (2018).
- [21] P. Zhang, J. Moraal, and Z. Li, *Design, calibration and validation of a wheel-rail contact force measurement system in v-track*, *Measurement* **175**, 109105 (2021).
- [22] A. Jaschinski, H. Chollet, S. Iwnicki, A. Wickens, and J. Würzen, *The application of roller rigs to railway vehicle dynamics*, *Vehicle System Dynamics* **31**, 345 (1999).
- [23] H. Feller and K. Walf, *Surface analysis of corrugated rail treads*, *Wear* **144**, 153 (1991).
- [24] E. Wild, L. Wang, B. Hasse, T. Wroblewski, G. Goerigk, and A. Pyzalla, *Microstructure alterations at the surface of a heavily corrugated rail with strong ripple formation*, *Wear* **254**, 876 (2003).
- [25] M. Oregui, Z. Li, and R. Dollevoet, *Identification of characteristic frequencies of damaged railway tracks using field hammer test measurements*, *Mechanical Systems and Signal Processing* **54**, 224 (2015).

- [26] Z. Yang, A. Boogaard, R. Chen, R. Dollevoet, and Z. Li, *Numerical and experimental study of wheel-rail impact vibration and noise generated at an insulated rail joint*, International Journal of Impact Engineering **113**, 29 (2018).
- [27] D. Fourie, R. Fröhling, and S. Heyns, *Railhead corrugation resulting from mode-coupling instability in the presence of veering modes*, Tribology International **152**, 106499 (2020).
- [28] N. M. M. Maia and J. M. M. e Silva, *Theoretical and experimental modal analysis* (Research Studies Press, 1997).
- [29] X. Zhao and Z. Li, *A three-dimensional finite element solution of frictional wheel-rail rolling contact in elasto-plasticity*, Proceedings of the Institution of Mechanical Engineers, Part J: Journal of Engineering Tribology **229**, 86 (2015).
- [30] S. Grassie, *Rail corrugation: characteristics, causes, and treatments*, Proceedings of the Institution of Mechanical Engineers, Part F: Journal of Rail and Rapid Transit **223**, 581 (2009).
- [31] P. Zhang, S. Li, A. Núñez, and Z. Li, *Vibration modes and wave propagation of the rail under fastening constraint*, Mechanical Systems and Signal Processing **160**, 107933 (2021).
- [32] P. Zhang, S. Li, A. Núñez, and Z. Li, *Multimodal dispersive waves in a free rail: Numerical modeling and experimental investigation*, Mechanical Systems and Signal Processing **150**, 107305 (2021).
- [33] M. Molodova, Z. Li, A. Núñez, and R. Dollevoet, *Validation of a finite element model for axle box acceleration at squats in the high frequency range*, Computers & Structures **141**, 84 (2014).
- [34] M. Naeimi, S. Li, Z. Li, J. Wu, R. H. Petrov, J. Sietsma, and R. Dollevoet, *Thermo-mechanical analysis of the wheel-rail contact using a coupled modelling procedure*, Tribology International **117**, 250 (2018).
- [35] Z. Yang, X. Deng, and Z. Li, *Numerical modeling of dynamic frictional rolling contact with an explicit finite element method*, Tribology international **129**, 214 (2019).
- [36] S. L. Grassie and J. W. Edwards, *Development of corrugation as a result of varying normal load*, Wear **265**, 1150 (2008).
- [37] H. Ilias, *The influence of railpad stiffness on wheelset/track interaction and corrugation growth*, Journal of Sound and Vibration **227**, 935 (1999).
- [38] Z. Li, R. Dollevoet, M. Molodova, and X. Zhao, *Squat growth—some observations and the validation of numerical predictions*, Wear **271**, 148 (2011).
- [39] X. Deng, Z. Qian, Z. Li, and R. Dollevoet, *Investigation of the formation of corrugation-induced rail squats based on extensive field monitoring*, International Journal of Fatigue **112**, 94 (2018).

- [40] X. Jin, Z. Wen, K. Wang, and W. Zhang, *Effect of a scratch on curved rail on initiation and evolution of rail corrugation*, *Tribology international* **37**, 385 (2004).

8

CONCLUSIONS AND RECOMMENDATIONS

8.1. CONCLUSIONS

This research presented in this dissertation focuses on three aspects to better understand the development mechanism of short pitch corrugation and develop effective solutions for its mitigation. They are 1) to investigate rail vibration modes in free condition and under fastening constraint which determine the wavelength-fixing of short pitch corrugation; 2) to design a new rail constraint to suppress rail vibration modes and mitigate short pitch corrugation; 3) to experimentally validate the corrugation development mechanism using the downscale V-Track test rig. The research questions in Chapter 1 are addressed accordingly.

Q1. How to identify the coupled rail vibration modes to understand and mitigate short pitch corrugation?

Chapter 2 provides the answer to question Q1. This chapter presents an FE solution method to simulate the multimodal dispersive waves in a free rail at 0-5 kHz. Six types of vibrational waves are identified in the longitudinal, vertical and lateral directions. The modal behaviors, phase, and group velocities, and wavenumber-frequency dispersion relations of these waves are obtained to provide useful information to understand wave propagation and dispersion along the rail. The ODS approach is applied to identify different types of vibration modes. The SMAW approach is proposed to investigate the dispersive waves in the free rail. The main conclusions are summarized as follows.

- A better understanding of free rail vibrations is gained with the phase and group velocities of the six types of waves derived in the frequency range of 0-5 kHz.
- The ODS approach can successfully identify coupled rail vibration modes.
- The SMAW approach is capable of experimentally measuring the wave propagation and dispersion characteristics in the rail.

Q2. What is the constraint mechanism of fastening on the rail longitudinal compression modes, which is dominant for short pitch corrugation initiation?

Chapter 3 addresses the question Q2. This chapter proposes a systematic methodology to study rail vibration modes and wave propagation under fastening constraint in three directions. This method includes three steps. In Step 1, an experimental setup is designed in the laboratory, consisting of a rail-fastening system. The ODS and SMAW approaches are employed to identify rail vibration modes and measure wave propagation characteristics. In Step 2, the 3D FE model of rail-fastening is developed and validated with the ODS and SMAW measurement results. In Step 3, insights into the rail vibration control are gained through a sensitivity analysis of fastening dynamic parameters. The main conclusions are drawn as follows.

- Vertical bending modes, longitudinal compression modes and lateral bending modes of the rail under fastening constraint are identified from the ODS measurement

but with shifted frequencies and significantly reduced vibration amplitude compared to a free rail.

- Wave propagation characteristics of the rail-fastening system in terms of group velocities and attenuation coefficients are obtained by SMAW measurement. The fastening constraint considerably increases the wave attenuation along the rail in all three directions. Vertical wave attenuation of the rail-fastening is relatively small between 1800 and 3600 Hz. Lateral wave attenuation of rail-fastening shows a dominant peak at about 3800 Hz.
- The fastening constraint suppresses the longitudinal rail vibrations less strongly, compared to the vertical and lateral directions.
- The change of fastening stiffness and damping can control rail mode frequencies and their vibration amplitude and influence the wave propagation velocities and attenuation along the rail.

Q3. How do the fastening parameters influence the development and mitigation of short pitch corrugation?

Chapter 4 aims at answering Q3. In this chapter, a parametric investigation of fastenings was performed employing a 3D FE vehicle-track interaction model to better understand the corrugation development mechanism and gain insight for its mitigation by fastening design. Fastening models with different configurations, boundary conditions and parameters, representing different service stages of fastenings in the field, were built up and analyzed. The main conclusions are summarised as follows.

- Fastening parameters and modeling play an important role in corrugation development.
- The variation of fastening constraint in the longitudinal dimension (i.e., column number) significantly influences the corrugation development and features. The absence of inner fastening constraint in the lateral dimension (i.e., 2nd and 3rd rows) seems a preferred condition for developing relatively longer-wavelength corrugation.
- The fastening longitudinal constraint to the rail is the major factor determining the corrugation development because the rail longitudinal modes responsible for corrugation initiation are a type of compression/rarefaction vibration in the longitudinal direction. The fastening vertical and lateral constraints influence spatial distribution and wavelength components of corrugation.
- Larger longitudinal stiffness of fastenings shifts the major wavelength components of corrugation to the shorter ones with significantly reduced amplitude. Larger longitudinal damping reduces the corrugation amplitude without changing the wavelength components.

- The increase of fastening constraint in the longitudinal dimension helps to mitigate corrugation. Meanwhile, the inner fastening constraint in the lateral dimension is necessary for corrugation mitigation.
- The increase of fastening longitudinal stiffness and damping can reduce the vibration amplitudes of longitudinal compression modes and thus reduces the track corrugation propensity.
- To effectively mitigate corrugation, fastening constraint should be applied in the proximity of the 'antinodes' of the longitudinal compression mode shape instead of the 'nodes'.

Q4. How to mitigate short pitch corrugation by new design of rail constraint?

Chapter 5 addresses the question Q4. In this chapter, a methodology is proposed to mitigate short pitch corrugation by rail constraint design. This methodology includes four steps. In Step 1, consistent initiation and growth of short pitch corrugation are numerically reproduced employing a 3D FE vehicle-track interaction model. In Step 2, the corrugation initiation mechanism is identified by comparing the ODSs and rail longitudinal compression modes. In Step 3, five types of rail constraints are designed using a 1/5 scaled rail and their influences on rail vibration modes are analyzed. Models of rail constraints types 1, 3 and 5 are built up and their parameters are derived by best fitting the simulations to the measurements. In Step 4, based on the modeling and identified parameters in Step 3, three rail constraint models are established and applied in the 3D FE vehicle-track interaction model, and their validity for corrugation mitigation is evaluated. The main findings are summarized as follows.

- The corrugation initiation mechanism is further explained from the analysis of ODSs. With a particular fastening constraint, rail longitudinal compression modes may not be effectively suppressed. When the wheel rolls over the rail, some of them are excited, and induce longitudinal wheel-rail dynamic contact force with corresponding frequencies, resulting in initial differential wear and corrugation.
- Based on the corrugation initiation mechanism, an approach was proposed to mitigate or even eliminate corrugation. That is to design a new rail constraint that can effectively suppress rail longitudinal compression modes so that the induced longitudinal contact force fluctuates little, differential wear can barely accumulate, and corrugation can hardly initiate.
- Different rail constraints were designed and evaluated, and it is found that a relatively rigid constraint (type 5) can completely restrict the rail longitudinal compression modes. Afterward, this rail constraint model was applied in the FE vehicle-track model and the simulated longitudinal contact force has a significantly small fluctuation amplitude so that corrugation can hardly initiate.
- Fastening longitudinal parameters influence the frequencies of longitudinal compression modes and thus the characteristic wavelengths/frequencies and spatial distribution of short pitch corrugation.

- The fastening constraint (type 3) can effectively suppress vertical bending modes, lateral bending and torsion modes by appropriate parameter design but cannot completely restrict longitudinal compression modes.

Q5. How to measure the wheel-rail contact forces in the downscale V-track test rig for the short pitch corrugation experiment?

Chapter 6 addresses question Q5. In this chapter, a force measurement system named a dynamometer is developed in the V-Track test rig to measure the wheel-rail contact forces in three directions. The dynamometer is comprised of four 3-component piezo-electric force sensors and is installed between the steel frame and the wheel assembly, which is in the load path from the wheel-rail interface to the frame on which the V-Track is mounted. Several static and running tests are performed to examine the reliability and accuracy validity of the dynamometer for measuring the wheel-rail contact forces. The main conclusions are summarized as follows.

- The designed dynamometer can reliably and accurately measure the wheel-rail contact force in the three directions.
- Utilizing the measurement results from the dynamometer, the control of the contact forces in the longitudinal, vertical, and lateral directions was achieved by adjusting the braking torque, wheel preload and angle of attack, respectively.

Q6. How to reproduce short pitch corrugation on the downscale V-track test rig to validate the corrugation development mechanism in[1]?

Chapter 7 provides the answer to Q6. In this chapter, an experimental study of short pitch corrugation is performed using the downscale V-Track test rig. The employed V-Track configuration consists of two wheel assemblies (W1 and W3) and a ring track and can accurately simulate the high-frequency dynamics of the real vehicle-track system, which is crucial to understand the wavelength-fixing mechanism of short pitch corrugation. The loading conditions of the V-Track are first designed and adjusted by the wheel preload, the braking torque, and the angle of attack to simulate the vehicle-track interaction. Short pitch corrugation is successfully reproduced between SL80 and SL85 of the V-Track, and its spatial distribution, wavelength components, and hardness variation were captured by the 3D HandyScan and the hardness tests. Based on the measurement results of wheel-rail contact forces and track dynamic behaviors and observations, the development mechanism of short pitch corrugation is identified. The main conclusions are summarized as follows

- The reproduced rail corrugation in the V-Track has two major wavelengths of 6.4 mm and 8.9 mm, approximately equivalent to 32 mm and 45 mm of corrugation wavelengths in the field considering a scale factor of 1/5, falling in the typical short pitch range. Therefore, the study of its formation mechanism can be applied to understand short pitch corrugation in the field.

- The process for consistent development of short pitch corrugation is identified. The imperfect joint, the loose fastening bolt at SL85, and the absent fastening clamps at SL81- SL84 lead to a weaker constraint to the rail, serving as the initial excitation to the V-Track vehicle-track system. Some rail vibration modes cannot be effectively suppressed and induce dynamic wheel-rail contact forces with a certain wavelength and phase when the wheel rolls over the rail. With multiple wheel passages, the dynamic contact forces repeat the same wavelength and phase as the previous ones, and the resulting differential wear or plastic deformation can continuously accumulate at certain locations of the rail, causing consistent corrugation growth.
- Specifically, two types of wavelength-fixing mechanisms of short pitch corrugation at 6.4 mm are identified for the two wheel-track systems with W1 and W3. For the W1-track system, the rail lateral vibration mode at 572 Hz and vertical mode at 570 Hz, and the induced vertical and lateral contact forces at 564 Hz contribute to the corrugation development at 6.4 mm. For the W3-track system, the longitudinal mode at 574 Hz and the induced longitudinal force at 564 Hz and the vertical mode at 570 Hz and the vertical force at 540 Hz are responsible for the corrugation wavelength 6.4 mm. Despite different wavelength-fixing mechanisms for W1 and W3, the passages of these two wheels both promote the corrugation development at 6.4 mm because of the coupling of rail longitudinal, lateral and vertical modes around the corrugation frequency 564 Hz.
- The experimental results validated the hypotheses in [1] about longitudinal vibration modes and the consistency condition for short pitch corrugation development. To the best knowledge of the authors, this work provides the first experimental evidence, which indicates that rail longitudinal vibration modes contribute to the consistent development of short pitch corrugation.
- The lateral and vertical modes at 400 Hz and the induced lateral and vertical dynamic contact forces determine the corrugation development at 8.9 mm for both wheel-track systems.
- The experimental results in this work indicate that although they play a role in the corrugation formation, the vertical vibration modes and the induced vertical dynamic contact forces are not as decisive and dominant as those in the longitudinal and lateral directions
- The initial loading conditions of the vehicle-track system may influence the excited rail vibration modes and thus the wavelength-fixing mechanism of short pitch corrugation.

8.2. APPLICATIONS OF RESEARCH FINDINGS

The methodologies and findings presented in this dissertation have the following potential applications.

- This work experimentally validated that rail longitudinal compression modes contribute to the short pitch corrugation development and points out a direction for its mitigation in the field by strengthening the rail longitudinal constraint.
- A new rail constraint is designed that may be used in the field track to mitigate short pitch corrugation, which can reduce the related maintenance cost.
- Fastening degradation can induce the initiation of short pitch corrugation. Therefore, the timely monitoring and maintenance of the fastenings in the field are helpful to prevent short pitch corrugation.
- The proposed SMAW approach can be used for the dispersion analysis and defect inspection of the rails and other similar structures, such as steel beams and plates.
- The ODS approach can be applied in the field to identify rail vibration modes and better understand the relevant problems, such as short pitch corrugation, squats, and rolling noise.

8.3. RECOMMENDATIONS FOR FUTURE RESEARCH

Besides the conclusions presented in this dissertation, the following aspects are recommended to be further investigated in future work to better understand and mitigate short pitch corrugation.

- Fastening parameters and modeling play an important role in short pitch corrugation development. To better understand the corrugation features in the field and reliably predict corrugation in the simulation, it is suggested to examine the service stages of fastenings and determine appropriate parameters, such as by hammer test or falling weight test.
- Nine 3D accelerometers are mounted on the rail to identify coupled rail vibration modes in the current ODS approach. It is recommended to use more accelerometers to obtain better spatial resolution and to more accurately identify the rail vibration modes at higher frequencies. More accelerometers could also be used on rail cross-sections (i.e., rail foot, rail web) to capture the cross-section deformation of the wave modes.
- The current fastenings are modeled by multiple linear spring-damper pairs. It is recommended to improve the fastening modeling by, e.g., a more complex Prony series model to consider the nonlinear properties of the railpads to further narrow the gap between measurements and simulations.
- In the current work, a new rail constraint is designed and its validity on short pitch corrugation mitigation is numerically evaluated employing a 3D FE vehicle-track interaction model. In future research, it is recommended to experimentally assess the effect of the new rail constraint on short pitch corrugation mitigation. Besides, it is necessary to investigate the influence of the new rail constraint on other track components, such as sleepers, ballast layers for its field application.

- It is recommended to perform a metallurgical investigation of the rail material in the presence of short pitch corrugation to better understand its damage mechanism.
- In the current V-Track test rig, the commercial S7 rails are used for short pitch corrugation experiments. It is recommended to use 1/5 scaled rails made of field rail materials to better simulate the field wheel-rail dynamic contact. In the field, the rail is made of different steel materials, for instance, bainitic steel B360 and pearlitic steel R260, R260Mn, R350HT. It is recommended to study the relationship between the rail material and short pitch corrugation in future work.

REFERENCES

- [1] Z. Li, S. Li, P. Zhang, A. Nunez, and R. Dollevoet, *Mechanism of short pitch corrugation: Initial excitation and wavelength selection for consistent initiation and growth*, Submitted (2021).

ACKNOWLEDGEMENTS

Time flies so fast. It has been six years since I came to the Netherlands. I remember clearly my first day in Delft, a typical cloudy day with strong wind and a young man full of passions and dreams. At this moment, the passions have faded away and the dream of a doctorate has almost come true. I would like to take this opportunity to thank all the people who help and support me during this long and precious journey.

First, I want to thank my Promotor Prof. Zili Li, who is also my daily supervisor during the entire PhD research. He offered me this valuable chance to do research in TUDelft, and provides me constant guidance and support during the past five years. He gives me sufficient freedom to try my new ideas and keeps me on the right track with his rich knowledge and experience. I am also very grateful for his patience with me. His critical attitude and hardworking have set a good example for my future life.

Many thanks to my copromoter Dr. Alfredo Núñez, who play a key role in my PhD. At work, he always gives me constructive and prompt comments on my research; in life, he encourages and guides me when I feel upset and confusing. Without his support and help, I can hardly imagine finishing this thesis. I also would like to thank Prof. Rolf Dollevoet, my Promotor in the first year, for his inspiring words and helpful discussion at the beginning of my research.

I would also like to appreciate my colleagues Shaoguang Li, Zhen Yang, Li Wang, Zilong Wei, Chen Shen for their kind help and close collaboration in my research. Our joint papers are a good witness to it. Special thanks to the laboratory technician Jan Moraal. Without his help, the experimental work in this dissertation cannot be performed so smoothly. The memory about our tests in the test rig room and Romania is still fresh. Many thanks to Jacqueline Barhoorn, the secretary in our group, who help us solve the administrative problems and make our life easier and happier.

I also want to thank other colleagues in the Railway Engineering group. They are Valeri Markine, Zhiwei Qian, Xiangyun Deng, Xiangming Liu, Hongrui Wang, Lei Xu, Jurjen Hendriks, Evert van Veldhuizen, Haoyu Wang, Lizuo Xin, Yuewei Ma, Ling Chang, Tao Lv, Meysam Naeimi, Omid Hajizad, Ali Jamshidi, Joris van Dijk, Yunlong Guo, Song Liu, Wenqiang Liu, Baifeng An, Bin Zhu, Chunyan He, Yang Jin, Wenli Jia, Siwarak, Wassamon, Fang Ren, Yuanchen Zeng, Taniya, and also our Chinese visiting scholars, Qian Xiao, Xiaoping Wu, Xiubo Liu, Xianmai Chen. We spent a wonderful time together and it is my great pleasure to work with you. Many thanks to Ivan Shevtsov, Greg Lambert, Ruud van Bezooijen for their cooperation in the field experiments in the Dutch Railway. Thanks a lot to my best friends in the Netherlands, Yuxin Liu, Hongjuan Wu, Mingxue Zhen, Ling Jia. I cannot remember how many times we have had dinners and parties together during the past five years. You are like brothers and sisters to me in this foreign country. Wish you all a happy life in China. I am also grateful to my friends in Delft, Yongqiu Zhu, Senlei Wang, Zixia Wu, Bo Li and Chi Jin, Yuqian Tu, Jian Zhang, Na Chen and Yande Jiang, Zhengwu Wang, Yan Song, Dadi Zhang, Yan Song, Bing Huang and

Zongchen Li, Kaiyi Zhu, Meiqi Liu, Yingshan Su, Meng Meng, Yi Song, Xuehui Zhang, Xiaohui Zhang, Qiaochu Fan, Cong Xiao, Xinwei Ma, (sorry I cannot list all the names here). I own my special thanks to friends from the Delft fellowship, Philip and Ting Xin, Weiyuan and Chengcheng, Ou Ku and Jingwen, Andy and Sharon, Chao Lian and Shang Yu, Xiangyu and Xiaoxuan, Tianmu and Yan Li, Meixia and Dahai, Brother Mei and Emily, Guojie Pan, Yuting, Zanni, Hai Yan, Feifei, Yingzhu, Yonghui, Ling Xiong, Maokun, Tianyu, Jingqi, Weiwei, Chenxing Ji and Fei Wu, Gengjing (Sorry I cannot list all the names here). Thanks a lot for your help, sharing and accompany. Life in the Netherlands will be less colorful without you.

Special thanks go to my board-game mates, Zhiwei Qian, Zhen Yang and Lin Xiao, Xiangming Liu and Ting Liu, Xiangyun Deng and Zhao Lian, Xin Tian, Yang Jin and Bowen Li, Chunyan He, Bin Zhu, Yufei Yuan, Haopeng Wang, Kailun Yang. My gratitude also goes to my badminton and tennis mates, Li Wang, Yunlong Guo and Lili Ma, Hao Li, Shiyu Ding, Junhan Wen, Zhangyue Wei, Ziyang Wu, Yun Zeng, Kairui Cui, Tian Tian. I enjoyed our relaxed time together and we are all winners of friendship. I also appreciate my master supervision teams in Southwest Jiaotong University (SWJTU), Prof. Ping Wang, Prof. Kai Wei, Prof. Rong Chen, Prof. Jieling Xiao, Prof. Caiyou Zhao, Prof. Jingmang Xu. They encourage and recommend me to further study abroad for my PhD and give many valuable suggestions on my research and future work. My gratitude also goes to my former colleagues in SWJTU, Fan Yang, Changsheng Zhou, Yingchun Liang, Zixuan Liu, Duo Meng, Menting Xing, Jun Xing, Qiang Yi, Kai Yang, Hongyu Tao, Boyang An, Yuan Gao, Jiayin Chen. Thanks for your caring and encouragement.

Friendship is like wine, and it gets better as it grows older. I would like to thank my old friends, Songnan Chen, Melody Tang, Tao Hu, Can Cui, Kaijun Zhu, Jie Yan, Siyuan Lin, Yilin Wang, Yunfei Wang, Kun Yu, Ruoxu Jia, Jihang Huang, Xiaomeng Wang. The memory with you always makes me smile. Wish our friendship last forever.

Special thanks to my girlfriend Ying Wu, who has accompanied me in the last year of my PhD. You are my best friend and make me the happiest man in the world. You have made significant achievement in not only your master study but also your cooking skills since you came to the Netherlands. My gaining weight (5 kg) in the past year is a good witness. I cannot imagine the life without you in the future. Wish our love forever.

Last but not the least, I want to express my deepest appreciation for my parents. Thanks for your unconditional, selfless and forgiving love! Your endless support gives me the courage to overcome any difficulties in my life. However, it is so hard to accept the fact that I am growing up while you are getting old. Hope the time passes more slowly, so your aging can slow down.

Pan Zhang
November 2022
Delft, Netherlands

致谢

流年似水。倏尔之间，来荷求学已六载。忆初时风华正茂，书生意气；而今沈腰潘鬓沧桑微露。虽韶华易逝，然己志未改。今论文初成，答辩在望，特作此文，致谢各良师益友，父母亲朋。

恩师李自力教授，治学严谨，孜孜不倦；学富五车，誉满中西。高山仰止，景行行止。余虽不能至，然心向往之。恩师不以余为朽木粪墙，悉心传道、授业、解惑，殚精竭虑，呕心沥血。扶持兮若新竹之老干；滋养兮若无声之春雨。恩长纸短，不可胜数。余感激涕零，虽衔环结草，难报万一。借此微文，愿恩师著作等身，桃李芬芳！

尊师 Alfredo，才德兼备，良师益友。余初到时，存急功近利之心，因常感彷徨苦闷，郁郁不得志。恩师 Alfredo 在吾迷途未远之际，解我迷茫之心，抒我抑郁之气，循循善诱，谆谆教导，终使我学业有成。此等恩情，长阔高深，镂心刻骨。

学海初泛舟之际，幸得贤师尊长指点迷津。恩师王平教授顶天立地之训，未尝敢忘；恩师韦凯教授提携入门之恩，铭记在心。尊师陈嵘教授的举荐知遇之情，众师长刘秀波、陈献麦、田春香、吴光芸、赵才友、徐井芒、马道林、肖杰灵、杨帆等教导爱护之心，没齿难忘，他日当报以涌泉。

独学而无友，孤陋而寡闻。吾幸有众同门，交流新闻，探讨学术，增益己所不能。师兄钱智炜之井井有条，李少光之老成持重，邓祥云之持之以恒，杨震之一丝不苟，魏子龙之博闻广识，汪力之细致耐心，沈晨之精益求精，刘向明之豁达乐观，徐磊之废寝忘食，汪宏瑞之聪慧敏捷，余深为敬服，故常师之。同窗郭云龙、刘文强、朱斌、何春燕、金杨、贾文利、任放、曾元辰等帮助扶持，实难忘怀。借此微笔，愿诸位更上一层楼。

千金易得，知己难寻。漫漫求学路，幸有刘宇鑫，吴红娟，郑明雪，贾玲等知己好友为伴，春赏百卉，夏观流星，秋饮甘醇，冬踏初雪。凡此种种，历历在目。然天下无不散之筵席，如今已各奔天涯。离别于歧路之际，方不笑沾巾之儿女！各位海阔凭鱼跃，天高任鸟飞。感恩 Delft 志同道合之黄啸飞、辛婷、熊亮、单美霞、魏威、张巍元、杜成成、库欧、李静雯、Andy、Sharon、商钰、廉超、祁玉婷、张仪、王天子、庄景棋、金谷柳新、陈庚璟、唐露宁、季晨星、吴非等。众人或悟言于一室之内，谈人生哲理；或寄情于自然田园，探宇宙奥秘。由是道路愈通，真理愈明，生命愈盛！感谢忘年之交梅大哥、Emily 大姐，彼此推杯于饭桌之上，游戏在棋盘之间，谈笑关大道，获益匪浅。

独乐乐不如众乐乐。幸得良朋王森磊、张健、吴子夏、肖琳、朱咏秋、李博文、王昊鹏、杨凯伦、刘美岐、廉昭、李博、金赤、李昊、丁世好、文君涵、崔开瑞等相伴异乡，觥筹之间，其乐融融；西南交大之同窗益友梁迎春、刘子煊、邢梦婷、易强、杨

凯、孟铎、陶宏宇、甘元佳、林思源、朱志铭、崔璨、朱恺隼、严劼等，相交多年，情比金坚。挚友陈嵩楠、唐诗光、胡涛、王艺霖、王云飞、余堃、贾若煦等，相知相识已逾十载，虽身隔重洋，然心若比邻。愿吾辈友谊坚如磐石，韧如蒲苇。

弱水三千，只取卿之一瓢。感恩过去一载，有吴莹相依相伴。卿，素若春梅绽白雪，洁似秋兰披重霜；静像老松生空谷，艳如明霞映澄堂。与卿处，常展笑颜；又可叹，相见恨晚！从此不再影只形单。愿余生与卿相濡以沫，白首长伴。

父恩母情，子所恃怙；生我养我，长我育我。常忆儿时，绕膝而戏；今逾花甲，鬓发已稀。父母健在，不应远游；游虽有方，心常怀忧。乌鸦反哺，羊羔跪乳；寸草春心，何太不足！兄弟之义，手足之情；血脉相连，一母而生。同胞共乳，兄友弟恭；及至长成，分散如星。聚渐无时，离别日增。旧情不忘，本心不摒。孝悌忠信，各展程鹏。值此之时，余感激涕零，不知所言。

张攀
壬寅年冬
荷兰 Delft

CURRICULUM VITÆ

Pan ZHANG

12-07-1992 Born in Henan, China.

EDUCATION

2010 - 2014 BSc, Road and Railway Engineering
Southwest Jiaotong University, China

2014 - 2016 MSc, Road and Railway Engineering
Southwest Jiaotong University, China

2016 – 2021 PhD, Railway Engineering
Delft University of Technology, the Netherlands
Thesis: Mechanisms and mitigation of short pitch rail corrugation
Promotor: Prof. dr. ir. Z. Li

2021-Present Postdoc researcher, Railway Engineering
Delft University of Technology, the Netherlands

LIST OF PUBLICATIONS

Thesis-related Journal Papers

1. **P. Zhang**, S. Li, A. Nunez, and Z. Li, *Multimodal dispersive waves in a free rail: Numerical modeling and experimental investigation*, Mechanical Systems and Signal Processing, vol. 150, 2021.
2. **P. Zhang**, S. Li, A. Nunez, and Z. Li, *Vibration modes and wave propagation of the rail under fastening constraint*, Mechanical Systems and Signal Processing, vol. 160, 2021.
3. **P. Zhang**, J. Moraal, and Z. Li, *Design, calibration and validation of a wheel-rail contact force measurement system in V-Track*, Measurement, vol. 175, 2021.
4. **P. Zhang**, S. Li, R. Dollevoet, and Z. Li, *Parametric investigation of railway fastenings into the development and mitigation of short pitch corrugation*, Engineering Structures, under review, 2022.
5. **P. Zhang**, S. Li, and Z. Li, *Short pitch corrugation mitigation by rail constraint design*, International Journal of Mechanical Science, under review, 2022.
6. **P. Zhang**, and Z. Li, *Experimental study on the development mechanism of short pitch corrugation using a downscale V-Track test rig*, Tribology International, under review, 2022.

Other Journal Papers

1. Z. Li and S. Li, **P. Zhang**^{*}, A. Nunez, R. Dollevoet, *Mechanism of Short Pitch Corrugation: Initial Excitation and Frequency Selection for Consistent Initiation and Growth*, International Journal of Rail Transport, under review, 2022.
2. Y. Zhen, **P. Zhang**, and L. Wang, *Wheel-rail impact at an insulated rail joint in an embedded rail system*, Engineering Structures, 246, 2021.
3. Y. Zhen, **P. Zhang**, J. Moraal, and Z. Li, *An experimental study on the effects of friction modifiers on wheel-rail dynamic interactions with various angles of attack*, Railway Engineering Science 30, no. 3 (2022): 360-382.
4. H. Tao, **P. Zhang**^{*}, *Characterization and mitigation of wheel-rail impact at a singular rail defect*, Journal of Vibration and Control, 2022.
5. C. Shen, **P. Zhang**, R. Dollevoet, A. Zoeterman, and Z. Li, *Evaluating railway track dynamic stiffness using axle box accelerations: a digital twin framework*, Mechanical Systems and Signal Processing, under review, 2022.
6. Z. Wei, X. Sun, F. Yang, Z. Ke, T. Lu, **P. Zhang**, and C. Shen, *Carriage interior noise-based inspection for rail corrugation on high-speed railway track*, Applied Acoustics, 196, 2022.

Conference Activities

1. **P. Zhang**, C. Shen, Z. Li, *Numerical and experimental investigation on vehicle-track high frequency dynamic interaction via V-Track test rig*, the 27th IAVSD Symposium on Dynamics of Vehicles on Roads and Tracks, Saint-Petersburg, Russia, August 16-20, 2021.
2. **P. Zhang**, Y. Zhen, J. Moraal, and Z. Li, *Laboratory investigation of effects of a friction modifier on wheel-rail dynamic contact*, the 13th World Congress on Railway Research, Birmingham, the United Kingdom, 6-10 JUNE 2022.
3. **P. Zhang**, Z. Li, *Experimental study of short pitch corrugation using a vehicle-track interaction test rig*, the 12th International Conference on Contact Mechanics and Wear of Rail/Wheel Systems, Melbourne, Australia, 4-7 September 2022.